Dissertation for the Degree of Doctor

Immersive and Interactive Multi-Physics Modeling of Coastal Hazards

Submitted by

Hwang, Sooncheol

Water and Ecosystems Major

Department of Civil, Environmental and Architectural Engineering

In partial fulfillment of the requirements for the degree of Doctor of Philosophy in Civil, Environmental and Architectural Engineering

Korea University

Seoul, Korea

February 2023

博 士 學 位 論 文

Immersive and Interactive Multi-Physics Modeling of Coastal Hazards

高 麗 大 學 校 大 學 院

建 築 社 會 環 境 工 學 科

黃　　淳　　鐵

2023年 2月

孫 尙 永 敎授 指導

博 士 學 位 論 文

Immersive and Interactive Multi-Physics Modeling of Coastal Hazards

이 論文을 工學博士 學位論文으로 提出함

2023年 2月

高 麗 大 學 校 大 學 院

建 築 社 會 環 境 工 學 科

黃 淳 鐵

Certificate of Committee Approval

Korea University

February, 2023

We hereby recommend that the dissertation by:

Hwang, Sooncheol

Entitled:

Immersive and Interactive Multi-Physics Modeling of Coastal Hazards

Be accepted in partial fulfillment of requirements for the degree of:

Doctor of Philosophy in Civil, Environmental and Architectural Engineering

Signatures of Committee on Final Examination

Chairperson
Prof. Sangyoung Son

Committee Member
Prof. Joong Hoon Kim

Committee Member
Prof. Kyungrock Paik

Committee Member
Prof. Jin Hwan Hwang

Committee Member
Prof. Seokkoo Kang

Acknowledgement

First and foremost, I would like to express my deepest gratitude to my advisor and mentor, Dr. Sangyoung Son for his warm guidance, consistent encouragement, patience and support throughout this journey. Without his help, this dissertation could not have been completed.

My sincere appreciation should go to my committee members: Dr. Joong Hoon Kim, Dr. Kyungrock Paik, Dr. Jin Hwan Hwang, Dr. Seokkoo Kang. Their detailed and valuable comments on my works contribute to this dissertation.

I also would like to thank my colleagues in Korea University. Their friendship, support and warm hearts have been an encouragement to my life in school. Especially, I am also grateful to the members of Coastal Hydrodynamics Laboratory, Xiaojuan Qian, Asrini Chrysanti, Junsoo Noh and my intimate mentors: Hannah Jang, Dr. Jungmo Ku, Dr. Jinwook Lee, Dr. Soon Ho Kwon, Chilwoo Lee, Sanghyun Yoo and Oseong Lim for their encouragement and advice.

None of this work would have been possible without unconditional love, trust and support from my family. I would not forget to thank my parents and two brothers, Soonhwan and Chanhee, for giving me love, care and encouragement throughout my life.

Table of Contents

List of Figures

List of Tables

Abstract

This dissertation proposes a multi-physics modeling of coastal hazards which utilizes immersive and interactive simulation systems and GPU acceleration. First, the multi-physics model of coastal hazards is developed based on the Boussinesq-type wave model. Various physical contributors to coastal hazards such as storm surge, tide, rainfall, pollutant, wind stress, and wave breaking are implemented for concurrently simulating these phenomena. The internal source of wave generation and periodic boundary conditions are also implemented. An efficient HLL-based scheme is proposed for scalar transport governed by shallow water flows. An anti-diffusion function is introduced to minimize the numerical diffusion for scalar concentration when solving the advection terms using the HLL Riemann solver. Then, we employ the GPU computation to solve the governing equations. This overcomes the shortcoming of the multi-physics model and enables real-time numerical simulation through GPU acceleration. The immersive and interactive simulation environments are implemented in the developed model. These features allow the end-user to experience the coastal disaster in the immersive simulation environment and alter the terrain while the simulation is running. Finally, the developed model is further coupled with the non-dispersive shallow water model through a one-way coupling. Numerical experiments are performed to validate the accuracy and applicability for all the studied topics. Consequently, we have developed an immersive and interactive multi-physics modeling of coastal hazards.

Chapter 1

Introduction

1.1 Motivation

Recent hazardous coastal hazards have emphasized the importance of understanding hydrodynamic and hydrological processes underlying these disasters, as they caused severe damages (see Figure 1.1). Coastal cities are vulnerable to coastal disasters caused by various physical drivers such as tides, storm surges, wind waves, direct rainfall, river discharge, inland flood, etc. Thus, the importance of accurate modeling for coastal disasters has been highlighted. Another issue associated with coastal disasters is disaster-induced transport problems (e.g., pollutants, wastewater, sewage). A good example can be found during the 2011 Tohoku tsunami when radioactive leakage into the Pacific Ocean occurred due to Fukushima nuclear accident. Therefore, it is vital to concurrently consider these physical drivers threatening coastal residents in order to investigate their interactions and lessen the risk of coastal disasters.

Figure 1.1: Damage in Busan, South Korea after Typhoon Hinnamnor (2022) made landfall (Courtesy of The New York Times)

Three-dimensional Navier-Stokes equations will be the best choice in terms of accuracy for research purposes, but they are computationally too heavy. Thus, many depth-integrated numerical models with different levels of mathematical approximation have been developed for simulating long waves. Owing to high accuracy and efficiency, the non-dispersive shallow water equations (NSWEs) are the most common choice for long wave modeling under hydrostatic and non-dispersive conditions. The numerical implementations solving the NSWEs include Delft3D FM (Flexible Mesh Suite), FVCOM (Finite Volume Community Ocean Model), ADCIRC (Advanced Circulation model), TELEMAC-2D, EFDC (Environmental Fluid Dynamics Code), MIKE21, which have been commonly applied to different shallow water flows (e.g., tides, storm surges, tsunamis). These models neglect the dispersive effects of the wave, resulting in a high computational speed.

In the nearshore region where the relatively short waves may be involved, the dispersive effects of the waves may no longer be neglected. Therefore, the Boussinesq-type equations (BEs), considering both nonlinear and dispersive effects of the waves, should be applied to nearshore dynamics including coastal disasters. The widely used numerical models solving the BEs are FUNWAVE (Fully Nonlinear Boussinesq Wave Model) and COULWAVE (Cornell University Long and Intermediate Wave Modeling Package). Due to the implementations of high-order terms (e.g., dispersive terms), the Boussinesq-type wave models are computationally heavier than the non-dispersive shallow water models. Moreover, the additional considerations for simulating coastal disasters (e.g., rainfall, infiltration, scalar transport, wave breaking, etc.) yield a better approximation to coastal disasters but lessen the computational speed.

To resolve this drawback and further implement real-time numerical simulation, there have been many efforts to enhance the computational speed. First, an efficient numerical scheme for hydrodynamic and scalar transport systems has been developed to retain the high accuracy of the BEs as well as high computational speed. Besides, high-performance computing techniques along with super-computing facilities have been proposed for practical implementation. Parallel computing using Message Passing Interface (MPI) on hundreds of CPU cores enables the real-time numerical simulation of the Boussinesq-type wave models. However, the required facilities are only accessible to a few researchers due to their exorbitant cost. Nowadays, thousands of Graphical Processing Units (GPU) cores are affordable because of the advancements in GPU, which makes GPU computations more attractive in numerical simulations. It can

further democratize real-time numerical simulation of multi-physics modeling within affordable costs.

More than half of the world population (approaching 8 billion people) resides in the urban region and this proportion is projected to grow up to 70 percent by 2050. Besides, more people are attracted to coastal cities. Coastal cities are more vulnerable to coastal disasters due to geographical characteristics (e.g., low-lying regions) and their high impermeability based on urbanization. Therefore, the exacerbated flood risk will threaten more and more urban residents. Recent studies have stressed the importance of public awareness of flood risk. Several authors in previous studies noted that people, whether people have experienced a flood or not, tend to expect that the future flood will replicate the past one, which possibly leads to the underestimation of the consequence of the extreme flood event. Hence, it is another critical issue to alert the public about the possibility of an extreme coastal disasters and its catastrophic result and to improve public awareness of coastal disasters.

Virtual reality (VR) technique may be a practical strategy for visualizing the potential risk of coastal disasters. It enables the modelers to produce lots of dangerous flood scenarios, and the end-user to experience them in a risk-free artificial environment. The informative performance of the VR technique for various disasters has been proven to be more reliable compared to conventional methods. The VR applications for different disasters (e.g., floods, fires, earthquakes, storm surges, etc.) have been developed. These applications require historical data or simulation results for VR visualization since they are unable to simulate disasters. They are effective in depicting the specific event,

but they are limited in visualizing various scenarios under varying disaster and topographic configurations.

There have been pioneering attempts to develop faster-than-real-time hydrodynamic models by harnessing the power of GPU as well as immersive Boussinesq-type wave model for nearshore wave processes. These efforts motivate that the immersive and interactive multi-physics modeling of coastal hazards can be feasible.

1.2 Objectives of Study

The goal of this dissertation is to develop an immersive and interactive multi-physics modeling of coastal hazards (see Fig.1.2). Such a model must enable real-time numerical modeling of coastal disasters governed by the physical interactions among various hydrodynamic and hydrological processes (e.g., tides, storm surges, waves, rainfall, runoff, pollutants). Furthermore, it should support immersive and interactive simulation environments which visualize the simulation results simultaneously and accept user feedback during the simulation. To this end, we extended the Boussinesq-type wave solver, Celeris, in four steps.

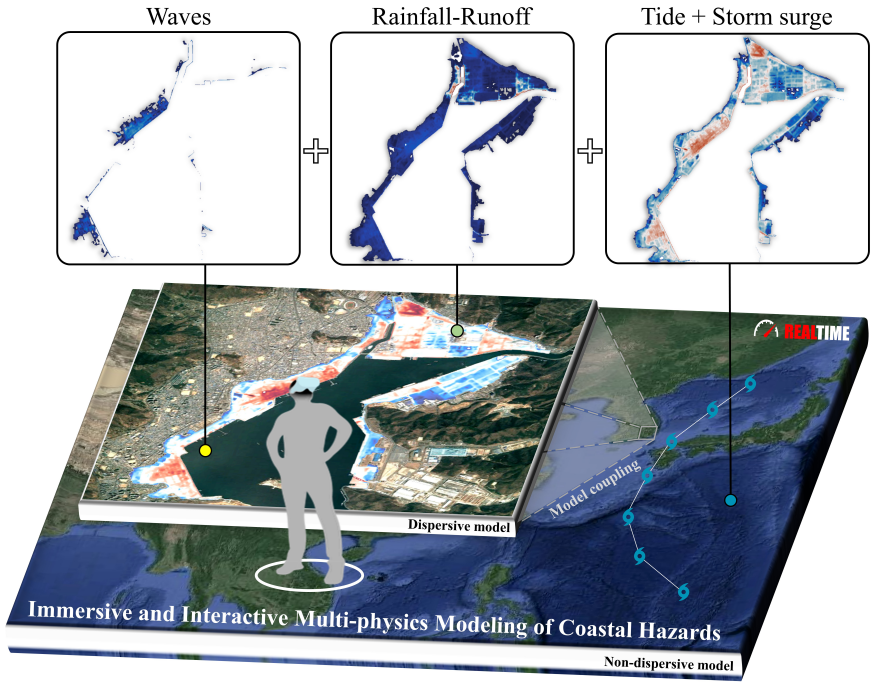

Figure 1.2: Schematic figure of the developed model

1.2.1 Accurate Modeling of Coastal Hazards

The first step in achieving the objective was the development of an accurate numerical model of coastal hazards which can simulate various hydrodynamic and hydrological processes simultaneously. We started with the Boussinesq-type wave model, Celeris. The implementation of wave breaking and wind stress terms along with internal wave generation improved the model accuracy of hydrodynamic processes surrounding coastal cities. Rainfall and infiltration terms were implemented to investigate the rainfall-runoff process in an urban coastal watershed. Besides, the scalar transport model was coupled with the hydrodynamic model to simulate scalar transport (e.g., sewage, pollutants)

governed by shallow water flows.

1.2.2 Real-time Numerical Simulation through Efficient Numerical Scheme and GPU Acceleration

The numerical model becomes computationally expensive as additional terms are implemented, which makes real-time numerical simulation unfeasible. To overcome this shortcoming, we proposed an efficient numerical scheme for the scalar transport model and utilized GPU acceleration for numerical computation. The HLL Riemann solver, commonly used in hydrodynamic models owing to its accuracy and efficiency, is inappropriate for the coupled model solving the hydrodynamic and scalar transport models since it can produce a significant amount of numerical diffusion of scalar concentration. We proposed the efficient HLL-type numerical scheme to minimize the numerical diffusion of scalar concentration, thereby improving the model accuracy without sacrificing efficiency. Furthermore, the governing equations were solved on GPU to provide real-time numerical simulation. The model was developed with C and HLSL languages in Unity3D. The compute shaders written in HLSL, containing the GPU codes (kernels), were implemented for GPU calculation.

1.2.3 Immersive and Interactive Simulation Environment

The model provides simultaneous result visualization while solving the governing equations, hence eliminating the need for post-processing. It also supports an immersive simulation environment where the end-user can move around the numerical domain while the model is running. This provides a special experi-

ence for the end-user to observe the various coastal disaster scenarios, which have the potential to threaten coastal cities, created by the modelers. It further provides an interactive simulation environment where the user can alter the topographical characteristics (e.g., dam break, embankment collapse). The user can directly participate in the numerical simulation, as opposed to passively accepting the situations given by the modelers. Consequently, both modelers and end-users can make up thousands number of hazardous coastal disaster scenarios.

1.2.4 Coupling with Non-Dispersive Shallow Water Model

We coupled the developed model with a non-dispersive shallow water model, Delft3D FM in order to enhance the accuracy and efficiency. Owing to its high efficiency, the non-dispersive model based on non-dispersive and hydrostatic pressure assumptions is superior to the dispersive model for simulating shallow water flows (e.g., tide, storm surge, tsunami) in a wide domain. Thus, we coupled two types of shallow water models using an absorbing-generating boundary condition. This boundary condition generates incoming waves from the outer model (non-dispersive model) to the inner model (dispersive model) and concurrently absorbs outgoing waves without producing the reflected waves at the model boundary, thereby minimizing numerical errors due to model coupling at the interfaces between the two models.

1.3 Organization

In Chapter 2, an efficient numerical scheme for the Saint-Venant system governing scalar transport is proposed based on a hybrid finite volume-finite difference method. An anti-diffusion function is introduced to minimize the numerical diffusion near contact discontinuities when solving the scalar transport problem using the HLL Riemann Solver. The presented model has been tested against the analytical solutions for several numerical experiments and the comparisons between the analytical and numerical solutions in all numerical experiments show good agreement.

In Chapter 3, a GPU-accelerated nearshore scalar transport model is proposed based on the Boussinesq-type nearshore wave solver, Celeris Advent. A modified numerical scheme described in Chapter 2 is adopted instead of the HLL Riemann solver. Several terms (e.g., wave breaking, wind stress, internal wave generation) are implemented along with the periodic boundary condition. Comparisons with two analytical solutions in one- or two-dimensional flow field validate the accuracy of the model. Furthermore, two laboratory experiments were reproduced to evaluate the model performance on scalar transport in complex bathymetry and flow conditions. Finally, a field-scale dye release experiment conducted in Imperial Beach was simulated, which analyze the applicability of the model in the nearshore region.

In Chapter 4, an interactive hydrodynamic rainfall-runoff model with an immersive virtual reality environment is proposed based on the immersive nearshore wave simulation software, Celeris Base. The nonlinear shallow water equations with rainfall and infiltration terms implemented in the continuity

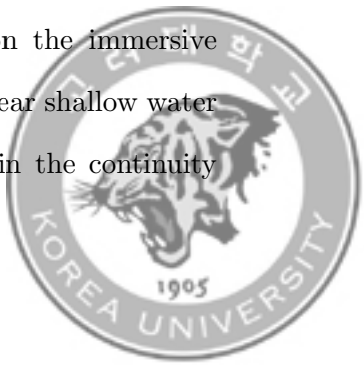

equation are solved. Owing to its simplicity and accuracy, the simplest explicit approximation to the Green-Ampt (GA) model is employed as the infiltration model. The presented model has been tested against the analytical and reference solutions for several numerical experiments. Furthermore, the model is applied to simulate the historical rainfall event in the Goodwin Creek Experimental Watershed (GCEW) and verified against the observed hydrograph at the river outlet. The results show that the model is capable of computing the flood routing process over the natural basin. Other features of the proposed model, immersive and interactive simulation environments, are also introduced.

In Chapter 5, an accurate and efficient modeling system through one-way coupling between non-dispersive and dispersive shallow water models is proposed. An absorbing-generating boundary condition is adopted to integrate two hydrodynamic models without spurious errors. The proposed system has been tested for several wave propagation problems, which validates that the absorbing-generating boundary condition is well implemented. The proposed modeling system is anticipated to contribute to advanced coastal disaster mitigation strategy through accurate and rapid modeling of shallow water waves.

In Chapter 6, storm surge modeling based on Typhoon Maemi (2003) is conducted to investigate the potential risks of future storm-induced flooding under the climate change scenarios suggested by IPCC AR5. The contributions of three primary drivers (i.e., SLR, DR, and TC intensification) on the flooding risk were examined separately and in combination. The results demonstrate that SLR is the most influential single flooding component exacerbating the future flooding risk, followed by TC exacerbation and DR intensification se-

quentially. Future storms with stronger TCs are anticipated to generate more than three times as much flooding damage as the current climate condition. This manuscript was published in Natural Hazards.

In Chapter 7, the conclusions of the dissertation are summarized. Besides, the suggestions for future works are described as well.

Chapter 2

An Efficient HLL-Based Numerical Scheme for Scalar Transport by Shallow Water Flow

An efficient numerical scheme is developed for coupled hydrodynamic and scalar transport systems to guarantee the conservation and the positivity-preserving properties for water depth and scalar concentration. A second-order well-balanced positivity-preserving central-upwind scheme based on the finite volume method is adopted to discretize the Saint-Venant system as well as the advective fluxes in the scalar transport system. In particular, an anti-diffusion modification is augmented in an ad hoc manner to the Harten-Lax-van Leer approximate Riemann solver for the scalar transport system, with the aim of significantly reducing the numerical diffusion near contact discontinuities. The proposed scheme is validated through six numerical experiments, wherein the advection and diffusion processes of scalar transport are considered separately or in combination. Accuracy is measured based on the difference between the numerical results and analytical solutions, and the performance of the proposed scheme is assessed by comparing it with that of the existing scheme. Conver-

gence analysis confirms that the proposed scheme is accurate to the second order. The results for the pure diffusion case reveal that the original scheme has limitations in precisely predicting scalar diffusion when the diffusion coefficient is small. By contrast, the proposed scheme accurately approximates scalar diffusion, even at low diffusivity. The results under flow conditions with various Froude and Peclet numbers confirm that the proposed scheme is more accurate than the existing scheme in solving scalar transport problems over a wide range of shallow water flows.

2.1 Introduction

A passive scalar transport (e.g., pollutants, nutrients, oxygen, chemicals, dyes, etc.) is one of the major issues faced by natural water systems in regard to aquatic environments. Numerical modeling is a common option for evaluating water quality to establish measures to better preserve coastal ecosystems [1]. The Saint-Venant system of shallow water equations (SWEs) based on hydrostatic pressure is generally used to describe flows in rivers and oceans where the horizontal length scale of the particle motion is much greater than its vertical extent, so it can neglect the vertical variations in the flow [e.g. 2, 3]. The SWEs are widely employed in various applications such as free surface flows in oceans, storm surges, and tsunamis [e.g. 4, 5, 6, 7, 8, 9]. Likewise, the scalar concentration whose transport is of interest can be assumed to be vertically homogeneous over the water depth, thus its dynamics can be described in a depth-integrated manner. Under these assumptions, coupled SWEs and scalar

transport equation (STE) can be analyzed using a depth-integrated approach, which provides an advantageous simplification.

Over the past decades, numerical schemes for solving scalar transport by shallow flows have attracted much attention [e.g. 10, 11, 12, 13, 14, 15, 16, 17, 18, 19]. A Godunov-type finite volume method (FVM) for hyperbolic systems [20] has mostly been applied to discretize the coupled SWEs and the STE due to its inherent conservative property. It is typically accompanied by either exact or approximate Riemann solvers to calculate the numerical flux across the interface between two adjacent states. Among various approximate solvers developed so far, Roe solver [21] and Harten-Lax-van Leer (HLL)-type solvers [e.g. 22, 23, 24] are widely used owing to their robustness and efficiency in computation. Ignoring the contact wave, the original HLL scheme assumes a two-wave approximation with a single intermediate wave state, which helps to achieve an improved level of robustness and efficiency. With appropriate choices for the two nonlinear waves (i.e., shock/rarefaction), this scheme automatically satisfies an entropy property, exactly resolves isolated shocks, and preserves positivity [e.g. 25, 26, 27]. However, it is incapable of precisely capturing contact discontinuities, which, in turn, introduces erroneous diffusion around them in handling scalar transport by shallow water flows. Recognizing this issue, another type of HLL solver, named after Harten-Lax-van Leer with Contact (HLLC) solver [24] has been further developed by considering the contact wave in the two-wave structure of the HLL scheme. Although the HLLC scheme is commonly adopted based on its capability of capturing contact discontinuities, it is still prone to numerical instability in the vicinity of strong

shock waves.

Various studies have investigated the reconstruction scheme of the Riemann solver in an attempt to overcome the problem of either numerical instability near strong shocks or numerical diffusion near contact discontinuities. One of the most popular approaches is to hybridize two schemes as first proposed by Quirk [28]. Quirk [28] suggested a framework to resolve the shock instability problems by selectively applying a dissipative scheme (e.g., the HLL scheme) near the strong shock region and a less dissipative scheme (e.g., the Roe scheme or the HLLC scheme) in the remaining areas. Based on Quirk's method, several hybrid schemes have been proposed based on the approach of adopting user-defined switching procedures and parameters suitable for Riemann solver [e.g. 29, 30, 31, 32]. Such hybrid schemes are efficient, but still inadequate in alleviating the dissipation problem. Another approach for handling this issue is to modify the HLL scheme to resolve the contact discontinuities more accurately. Mandal and Panwar [33] decomposed the Euler equations into convective and pressure components, and then reformulated the HLL scheme accordingly. Liu [34] introduced an anti-dissipation function into the HLL scheme to reduce the numerical diffusion arising from scalar advection. Through such a modification, an improved ability to resolve contact discontinuities was achieved. However, despite all previous efforts, there is no agreement on the best solver for achieving both accuracy and robustness near contact discontinuities [35]. Therefore, there is still a need to develop an improved numerical scheme to minimize the numerical diffusion and fluctuation for precisely approximating advective terms in solving the scalar transport system [e.g. 36, 37].

A 'good' numerical scheme for solving a coupled hydrodynamic and scalar transport system should satisfy the conservation property (C-property) [38]. The exact C-property indicates that the numerical scheme can capture the stationary steady state. A numerical method capable of exactly preserving the C-property for both systems should capture the stationary steady state, given by

$$w \coloneqq h + B \equiv \max(\mathrm{Const}_1, B), u \equiv v \equiv 0, c \equiv \begin{cases} \mathrm{Const}_2, & \text{if } h > 0, \\ 0, & \text{otherwise}, \end{cases} \tag{2.1}$$

where w is the water surface elevation, h is the water depth and B is the bottom elevation. u and v are the depth-integrated flow velocities in the x and y directions, respectively, while c is the depth-averaged scalar concentration. Const_1 and Const_2 represent constants for initial state in mass and scalar concentration, respectively.

Another critical property for a reliable numerical scheme is the positivity-preserving property [e.g. 39, 40, 41, 42]. This indicates that the computed water depth and scalar concentration should be non-negative throughout the entire computational domain. In the presence of a dry area, the water depth may become negative at the wet/dry interface owing to numerical oscillations. Then, the numerical computations will immediately break down because the largest and smallest eigenvalues of the Jacobian of the SWEs are $u \pm \sqrt{gh}$, where g is the gravitational constant. Therefore, the positivity-preserving property is important to ensure computational stability when computing numerical simu-

lations at grid points with small water depths.

In summary, a desirable numerical scheme should possess the two properties mentioned above. Various studies have developed many well-balanced positivity-preserving schemes for the SWEs [e.g. 43, 44, 45, 46, 47]. For an accurate approximation of flow and scalar transport, such a numerical scheme should have the desired properties for both hydrodynamic and scalar transport models. Among many possible numerical schemes, a second-order well-balanced positivity-preserving central-upwind scheme [48] was employed for the shallow water model. This scheme (hereafter the Kurganov-Petrova scheme) exhibits the desired properties for the SWEs. It also has the advantages of robustness and the ability to accommodate discontinuous bottom topography. Therefore, it is widely used for the prediction of shallow water flows [e.g. 49, 50, 51, 52, 53]. A special modification was applied to the scalar transport model to guarantee the required properties and minimize the numerical diffusion near the contact discontinuities. Consequently, a modified numerical scheme satisfying the positivity-preserving and C-properties was developed for shallow water flows and scalar transport.

This chapter introduces a modified second-order central-upwind scheme for hydrodynamic and scalar transport models. It preserves the stationary steady state and guarantees the positivity of the computed water depth and scalar concentration throughout the entire computational domain. The FVM was adopted to discretize the governing equations except for the diffusion terms over uniform Cartesian grids. The advective fluxes were discretized using the second-order central-upwind scheme. In particular, an anti-diffusion function

was newly introduced to minimize the numerical diffusion for scalar concentrations in subcritical flows or stationary states. The bottom slope terms were discretized using an appropriate semi-discrete scheme [54], confirming that the scheme is well-balanced and the diffusion terms were discretized based on the finite difference method (FDM). Several analytical cases were numerically reproduced to investigate the performance of the proposed scheme.

The remainder of this chapter is organized as follows. Section 2.2 introduces the proposed numerical scheme for the hydrodynamic and scalar transport systems, and the proof that this scheme guarantees the non-negativity property and the stationary steady state for both water depth and scalar concentration. Section 2.3 presents the simulation results of several numerical experiments to investigate the performance of the proposed scheme. Finally, conclusions are summarized in Section 2.4.

2.2 Numerical Scheme

The depth-averaged scalar transport model coupled with the hydrodynamic model solves the nonlinear SWEs and the depth-averaged advection-diffusion

equation in two dimensions, which can be written in vector form as follows:

$$\mathbf{U}_t + \mathbf{F}\left(\mathbf{U}, B\right)_x + \mathbf{G}\left(\mathbf{U}, B\right)_y + \mathbf{S}\left(\mathbf{U}, B\right) = 0,$$

$$\mathbf{U} = \begin{bmatrix} h \\ hu \\ hv \\ hc \end{bmatrix}, \mathbf{F}\left(\mathbf{U}, B\right) = \begin{bmatrix} hu \\ hu^2 + \dfrac{gh^2}{2} \\ huv \\ huc \end{bmatrix}, \mathbf{G}\left(\mathbf{U}, B\right) = \begin{bmatrix} hv \\ huv \\ hv^2 + \dfrac{gh^2}{2} \\ hvc \end{bmatrix}, \tag{2.2}$$

$$\mathbf{S}\left(\mathbf{U}, B\right) = \begin{bmatrix} 0 \\ ghB_x \\ ghB_y \\ \left(hD_{xx}c_x + hD_{xy}c_y\right)_x + \left(hD_{yx}c_x + hD_{yy}c_y\right)_y \end{bmatrix},$$

where $\mathbf{U}$ is the conservative variable vector, $\mathbf{F}\left(\mathbf{U}, B\right)$ and $\mathbf{G}\left(\mathbf{U}, B\right)$ are the advective flux vectors in the x and y directions, respectively, and $\mathbf{S}\left(\mathbf{U}, B\right)$ is the source term vector including the bottom gradient and diffusion terms. The subscripts x and y denote spatial differentiation and the subscript t denotes temporal differentiation. D_{xx}, D_{xy}, D_{yx} and D_{yy} are the components of the 2D diffusion coefficient tensor. Following the method in [54, 48], the coupled hydrodynamic and scalar transport system (2.2) is recast in an equivalent system in terms of the redefined unknown variables $U := (w, hu, hv, hc)^T$ by substituting water depth h with the difference of surface water elevation and bottom

elevation $w - B$. Here, the bottom elevation B is assumed to be constant over time.

2.2.1 Well-Balanced Numerical Scheme for the Saint-Venant Systems

Finite volume cells $C_{i,j} \coloneqq \left[x_{i-\frac{1}{2}}, x_{i+\frac{1}{2}}\right] \times \left[y_{j-\frac{1}{2}}, y_{j+\frac{1}{2}}\right]$ with uniform grids $x_\alpha \coloneqq \alpha\Delta x$ and $y_\beta \coloneqq \beta\Delta y$ are introduced for discretization. The central-upwind semi-discretization of Eq. 2.2 can be written as follows:

$$\frac{d}{dt}\bar{\mathbf{U}}_{i,j}(t)(t) = -\frac{\mathbf{H}^x_{i+\frac{1}{2},j} - \mathbf{H}^x_{i-\frac{1}{2},j}}{\Delta x} - \frac{\mathbf{H}^y_{i,j+\frac{1}{2}} - \mathbf{H}^y_{i,j-\frac{1}{2}}}{\Delta y} + \bar{\mathbf{S}}_{i,j}(t), \tag{2.3}$$

where $\bar{\mathbf{U}}_{i,j}(t)$ are the cell averages of the solution $\mathbf{U}$:

$$\bar{\mathbf{U}}_{i,j}(t) \approx \frac{1}{\Delta x \Delta y} \iint\limits_{C_{i,j}} \mathbf{U}(x, y, t) dx dt, \tag{2.4}$$

$\bar{\mathbf{S}}_{i,j}(t)$ is an appropriate discretization of the cell averages of the source term:

$$\bar{\mathbf{S}}_{i,j}(t) \approx \frac{1}{\Delta x \Delta y} \iint\limits_{C_{i,j}} \mathbf{S}(\mathbf{U}(x, y, t), \mathbf{B}(x, y)) dx dt. \tag{2.5}$$

A discretization of the bottom gradient terms, which is equal to the numerical fluxes when both terms are applied to the stationary steady-state, was

derived by Kurganov and Levy [54]. It is written as

$$\begin{aligned}
\bar{S}^{(2)}_{i,j}(t) = &- g\frac{B\left(x_{i+\frac{1}{2}}, y_j\right) - B\left(x_{i-\frac{1}{2}}, y_j\right)}{\Delta x} \\
&\cdot \frac{\left(w^{-}_{i+\frac{1}{2},j} - B\left(x_{i+\frac{1}{2}}, y_j\right)\right) + \left(w^{+}_{i-\frac{1}{2},j} - B\left(x_{i-\frac{1}{2}}, y_j\right)\right)}{2}, \\
\bar{S}^{(3)}_{i,j}(t) = &- g\frac{B\left(x_i, y_{j+\frac{1}{2}}\right) - B\left(x_i, y_{j-\frac{1}{2}}\right)}{\Delta y} \\
&\cdot \frac{\left(w^{-}_{i,j+\frac{1}{2}} - B\left(x_i, y_{j+\frac{1}{2}}\right)\right) - \left(w^{+}_{i,j-\frac{1}{2}} - B\left(x_i, y_{j-\frac{1}{2}}\right)\right)}{2}.
\end{aligned} \tag{2.6}$$

This semi-discrete scheme can be applied only if the bottom topography function B is continuous. Therefore, the bottom topography function B is replaced by its continuous piecewise linear approximation $\tilde{B}$, which is defined as

$$\begin{aligned}
\tilde{B}(x,y) = &B_{i-\frac{1}{2},j-\frac{1}{2}} + \left(B_{i+\frac{1}{2},j-\frac{1}{2}} - B_{i-\frac{1}{2},j-\frac{1}{2}}\right)\cdot\frac{x - x_{i-\frac{1}{2}}}{\Delta x} \\
&+ \left(B_{i-\frac{1}{2},j+\frac{1}{2}} - B_{i-\frac{1}{2},j-\frac{1}{2}}\right)\cdot\frac{y - y_{j-\frac{1}{2}}}{\Delta y} \\
&+ \left(B_{i+\frac{1}{2},j+\frac{1}{2}} - B_{i+\frac{1}{2},j-\frac{1}{2}} - B_{i-\frac{1}{2},j+\frac{1}{2}} + B_{i-\frac{1}{2},j-\frac{1}{2}}\right)\frac{(x - x_{i-\frac{1}{2}})(y - y_{j-\frac{1}{2}})}{\Delta x \Delta y}, \\
&(x,y) \in C_{i,j},
\end{aligned} \tag{2.7}$$

where $B_{i\pm\frac{1}{2},j\pm\frac{1}{2}}$ are the values estimated using $\tilde{B}$ at the interfaces of cell $C_{i,j}$, expressed as

$$B_{i\pm\frac{1}{2},j\pm\frac{1}{2}} = B\left(x_{i\pm\frac{1}{2}}, y_{j\pm\frac{1}{2}}\right), \tag{2.8}$$

The cell average of interpolant $\tilde{B}$ over cell $C_{i,j}$ is equal to its value $B_{i,j}$ at the center of the corresponding cell as well as the average value of the approximated values at the cell interfaces:

$$\begin{aligned} B_{i,j} &= \tilde{B}(x_i, y_j) = \frac{1}{\Delta x \Delta y} \iint\limits_{C_{i,j}} \tilde{B}(x,y) dx dy \\ &= \frac{1}{4}\left(B_{i+\frac{1}{2},j} + B_{i-\frac{1}{2},j} + B_{i,j+\frac{1}{2}} + B_{i,j-\frac{1}{2}} \right), \end{aligned} \tag{2.9}$$

where

$$\begin{aligned} B_{i\pm\frac{1}{2},j} &= \tilde{B}(x_{i\pm\frac{1}{2}}, y_j) = \frac{1}{2}\left(B_{i\pm\frac{1}{2},j+\frac{1}{2}} + B_{i\pm\frac{1}{2},j-\frac{1}{2}} \right), \\ B_{i,j\pm\frac{1}{2}} &= \tilde{B}(x_i, y_{j\pm\frac{1}{2}}) = \frac{1}{2}\left(B_{i+\frac{1}{2},j\pm\frac{1}{2}} + B_{i-\frac{1}{2},j\pm\frac{1}{2}} \right), \end{aligned} \tag{2.10}$$

The following relations can be derived using the piecewise linear functions of w and B.

$$\begin{aligned} \bar{w}_{i,j} &= \frac{w_{i+\frac{1}{2},j} + w_{i-\frac{1}{2},j}}{2} = \frac{w_{i,j+\frac{1}{2}} + w_{i,j-\frac{1}{2}}}{2}, \\ B_{i,j} &= \frac{B_{i+\frac{1}{2},j} + B_{i-\frac{1}{2},j}}{2} = \frac{B_{i,j+\frac{1}{2}} + B_{i,j-\frac{1}{2}}}{2}, \end{aligned} \tag{2.11}$$

It follows from Eq. 2.11 that

$$\begin{aligned} h^{\pm}_{i\pm\frac{1}{2},j} &\coloneqq w^{\pm}_{i\pm\frac{1}{2},j} - B_{i\pm\frac{1}{2},j}, \\ h^{\pm}_{i,j\pm\frac{1}{2}} &\coloneqq w^{\pm}_{i,j\pm\frac{1}{2}} - B_{i,j\pm\frac{1}{2}}, \end{aligned} \tag{2.12}$$

Using Eq. 2.11, the discretized source terms can be rewritten as

$$\begin{aligned}\bar{S}^{(2)}_{i,j}(t) &= -g(\bar{w}_{i,j} - B_{i,j})\frac{B\left(x_{i+\frac{1}{2}}, y_j\right) - B\left(x_{i-\frac{1}{2}}, y_j\right)}{\Delta x},\\ \bar{S}^{(3)}_{i,j}(t) &= -g(\bar{w}_{i,j} - B_{i,j})\frac{B\left(x_i, y_{j+\frac{1}{2}}\right) - B\left(x_i, y_{j-\frac{1}{2}}\right)}{\Delta y}.\end{aligned} \tag{2.13}$$

and the central-upwind numerical fluxes H^x and H^y based on the HLL scheme can also be expressed as

$$\begin{aligned}H^x_{i+\frac{1}{2},j} =& \frac{a^+_{i+\frac{1}{2},j}F\left(U^-_{i+\frac{1}{2},j}, B\left(x_{i+\frac{1}{2}}, y_j\right)\right) - a^-_{i+\frac{1}{2},j}F\left(U^+_{i+\frac{1}{2},j}, B\left(x_{i+\frac{1}{2}}, y_j\right)\right)}{a^+_{i+\frac{1}{2},j} - a^-_{i+\frac{1}{2},j}}\\ &+ \frac{a^+_{i+\frac{1}{2},j}a^-_{i+\frac{1}{2},j}}{a^+_{i+\frac{1}{2},j} - a^-_{i+\frac{1}{2},j}}\left[U^+_{i+\frac{1}{2},j} - U^-_{i+\frac{1}{2},j}\right],\\ H^y_{i,j+\frac{1}{2}} =& \frac{b^+_{i,j+\frac{1}{2}}F\left(U^-_{i,j+\frac{1}{2}}, B\left(x_i, y_{j+\frac{1}{2}}\right)\right) - b^-_{i,j+\frac{1}{2}}F\left(U^+_{i,j+\frac{1}{2}}, B\left(x_i, y_{j+\frac{1}{2}}\right)\right)}{b^+_{i,j+\frac{1}{2}} - b^-_{i,j+\frac{1}{2}}}\\ &+ \frac{b^+_{i,j+\frac{1}{2}}b^-_{i,j+\frac{1}{2}}}{b^+_{i,j+\frac{1}{2}} - b^-_{i,j+\frac{1}{2}}}\left[U^+_{i,j+\frac{1}{2}} - U^-_{i,j+\frac{1}{2}}\right],\end{aligned} \tag{2.14}$$

where $U^\pm = (w^\pm, h^\pm \cdot u^\pm, h^\pm \cdot v^\pm, h^\pm \cdot c^\pm)$ represents the values of the solution at the cell interface obtained from a piecewise linear reconstruction $\tilde{U} \equiv (\tilde{w},\ \tilde{hu},\ \tilde{hv},\ \tilde{hc})$,

$$\tilde{U}(x,y) \coloneqq \bar{U}_{i,j} + (U_x)_{i,j}(x - x_i) + (U_y)_{i,j}(y - y_j), (x,y) \in C_{i,j}, \tag{2.15}$$

The numerical derivatives $(U_x)_{i,j}$ and $(U_y)_{i,j}$ are evaluated using a nonlinear

limiter, restricting the solution gradient near discontinuities, to guarantee the non-oscillatory nature of the reconstruction. Among various limiters, a generalized minmod limiter was adopted:

$$
\begin{aligned}
(U_x)_{i,j} &= \text{minmod}\left(\theta\frac{\bar{U}_{i,j}-\bar{U}_{i-1,j}}{\Delta x}, \frac{\bar{U}_{i+1,j}-\bar{U}_{i-1,j}}{2\Delta x}, \theta\frac{\bar{U}_{i+1,j}-\bar{U}_{i,j}}{\Delta x}\right),\\
(U_y)_{i,j} &= \text{minmod}\left(\theta\frac{\bar{U}_{i,j}-\bar{U}_{i,j-1}}{\Delta y}, \frac{\bar{U}_{i,j+1}-\bar{U}_{i,j-1}}{2\Delta y}, \theta\frac{\bar{U}_{i,j+1}-\bar{U}_{i,j}}{\Delta y}\right),
\end{aligned}
\tag{2.16}
$$

where the parameter θ between 1 and 2 determines the level of numerical dissipation. Note that lower values of θ correspond to more dissipation, minimizing the numerical oscillations. Finally, the one-sided local speeds of propagation are obtained using the eigenvalues of the Jacobian $\frac{\partial F}{\partial U}$ and $\frac{\partial G}{\partial U}$, respectively, as follows:

$$
\begin{aligned}
a^+_{i+\frac{1}{2},j} &= \max\left\{u^-_{i+\frac{1}{2},j}+\sqrt{gh^-_{i+\frac{1}{2},j}}, u^+_{i+\frac{1}{2},j}+\sqrt{gh^+_{i+\frac{1}{2},j}}, 0\right\},\\
a^-_{i+\frac{1}{2},j} &= \min\left\{u^-_{i+\frac{1}{2},j}-\sqrt{gh^-_{i+\frac{1}{2},j}}, u^+_{i+\frac{1}{2},j}-\sqrt{gh^+_{i+\frac{1}{2},j}}, 0\right\},\\
b^+_{i,j+\frac{1}{2}} &= \max\left\{v^-_{i,j+\frac{1}{2}}+\sqrt{gh^-_{i,j+\frac{1}{2}}}, v^+_{i,j+\frac{1}{2}}+\sqrt{gh^+_{i,j+\frac{1}{2}}}, 0\right\},\\
b^-_{i,j+\frac{1}{2}} &= \min\left\{v^-_{i,j+\frac{1}{2}}-\sqrt{gh^-_{i,j+\frac{1}{2}}}, v^+_{i,j+\frac{1}{2}}-\sqrt{gh^+_{i,j+\frac{1}{2}}}, 0\right\}.
\end{aligned}
\tag{2.17}
$$

2.2.2 Positivity-Preserving Reconstruction for w

The semi-discrete central-upwind scheme guarantees the C-property but fails to preserve the positivity-preserving property as it may produce a negative water depth near dry areas. This is because the use of a nonlinear limiter for

reconstruction cannot ensure the positivity of the computed water depth, which is obtained from the reconstructed water surface $w^{\pm}$. Figure 2.1 illustrates a typical configuration of a stationary steady state that violates the positivity-preserving property at the wet/dry interface. If there is no spatial difference in the water surface, the reconstructed water surfaces are computed to have the same value as the cell average value by piecewise linear reconstruction. For example, at point $(x, y) = (i, j)$ which is located near the dry cell, the reconstructed water surfaces $w_{i\pm\frac{1}{2},j}$ have a value equivalent to $\bar{w}_{i,j}$ since the numerical derivative $(U_x)_i$ is zero. As a result, the computed water depth may become negative even though the amount of water in this cell is positive $(\bar{w}_{i,j} > B_{i,j})$ as

$$\begin{aligned} h^{+}_{i-\frac{1}{2},j} &\coloneqq w^{+}_{i-\frac{1}{2},j} - B_{i-\frac{1}{2},j} < 0, \\ h^{-}_{i+\frac{1}{2},j} &\coloneqq w^{-}_{i+\frac{1}{2},j} - B_{i-\frac{1}{2},j} > 0. \end{aligned} \tag{2.18}$$

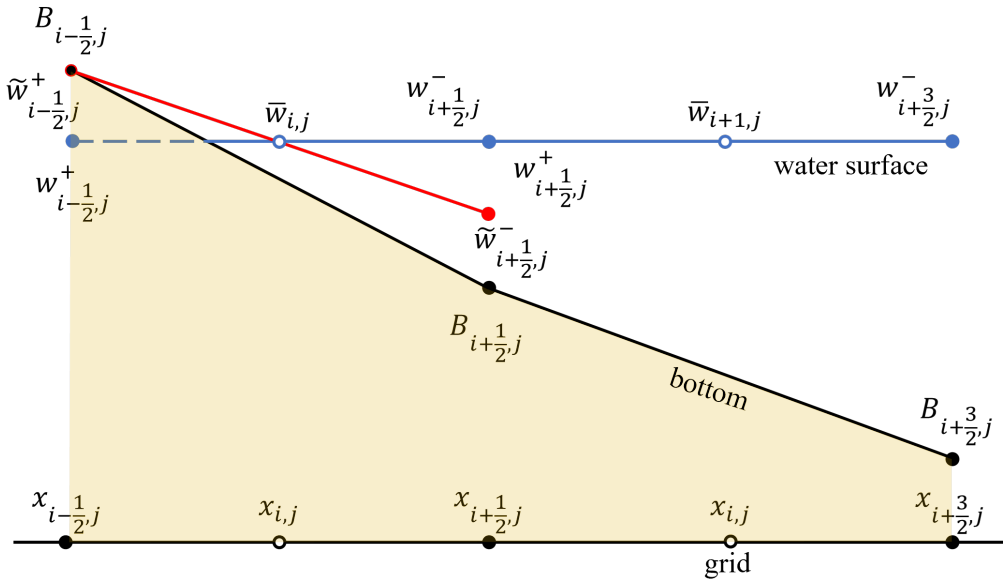

Figure 2.1: Positivity-preserving piecewise linear reconstruction for w

Therefore, the basic piecewise linear reconstruction should be corrected to guarantee that all the computed water depths throughout the computational domain have non-negative values. An additional technique to correct only $\tilde{w}$ while satisfying mass conservation is used as follows.

$$\text{If } w^{+}_{i-\frac{1}{2},j} < B_{i-\frac{1}{2},j}, \text{ then substitute } \bar{w}_{i,j} \text{ with } B_{i-\frac{1}{2},j} \text{ so } (w_x)_{i,j} := \frac{B_{i+\frac{1}{2}} - \bar{w}_i}{\Delta x/2}$$

$$\Rightarrow \tilde{w}^{+}_{i-\frac{1}{2},j} = B_{i-\frac{1}{2},j}, \tilde{w}^{-}_{i+\frac{1}{2},j} = 2\bar{w}_{i,j} - B_{i+\frac{1}{2},j},$$

$$\text{If } w^{-}_{i+\frac{1}{2},j} < B_{i+\frac{1}{2},j}, \text{ then substitute } \bar{w}_{i,j} \text{ with } B_{i+\frac{1}{2},j} \text{ so } (w_x)_{i,j} := \frac{\bar{w}_i - B_{i-\frac{1}{2}}}{\Delta x/2}$$

$$\Rightarrow \tilde{w}^{+}_{i-\frac{1}{2},j} = 2\bar{w}_{i,j} - B_{i-\frac{1}{2},j}, \tilde{w}^{-}_{i+\frac{1}{2},j} = B_{i+\frac{1}{2},j}. \tag{2.19}$$

This correction technique ensures that the corrected values of $\tilde{w}$ will remain

conservative but higher than the piecewise linear approximation of the bottom elevation function $\tilde{B}$. Hence, the corrected water depths $\tilde{h}$ will become non-negative, but they may be very small near the wet/dry interfaces. This modification may trigger unforeseen instability problems or even cancellation problems in cells with a non-positive water depth. To avoid division by extremely small values or zero, a prescribed tolerance value ϵ is introduced for the computation of the flow velocities u and v, and the scalar concentration c, as follows:

$$u = \frac{\sqrt{2}(hu)}{\sqrt{h^4 + \max(h^4, \epsilon)}}, v = \frac{\sqrt{2}(hv)}{\sqrt{h^4 + \max(h^4, \epsilon)}}, c = \frac{\sqrt{2}(hc)}{\sqrt{h^4 + \max(h^4, \epsilon)}}, \tag{2.20}$$

Using Eq. 2.20, all conservative variables except the water depth (i.e., hu, hv, hc) can be decomposed into products of each variable. This allows the reconstructed values (h, u, v, c) to be set at the corners of the cell $C_{i,j}$, where the fluxes are calculated, as

$$(hu) \coloneqq h \cdot u, (hv) \coloneqq h \cdot v, (hc) \coloneqq h \cdot c. \tag{2.21}$$

2.2.3 Anti-Diffusion Modification for the Approximation of the Scalar Advective Fluxes

In the presence of shock waves, an appropriate level of numerical dissipation is employed in various shock-capturing schemes to inhibit the development of unphysical oscillations [34]. The HLL Riemann solver also utilizes the difference

in the reconstructed conservative variables of the solution as a means of adding artificial dissipation. However, in the case of scalar advection, this approach inevitably causes numerical diffusion even in a stationary state over uniform bathymetry. This is because, in the HLL Riemann solver, the scalar concentration gradient can produce a certain amount of advective flux regardless of the flow velocity and bathymetric conditions. Let us assume a 1D configuration in which a scalar concentration is distributed unevenly under stationary flow conditions over a constant water depth h_0. Since the reconstructed water depths are constant and the flow velocities are zero, the advective flux of the scalar concentration in one dimension can be expressed as

$$\begin{aligned}(H^x)^{(4)}_{i+\frac{1}{2}} &= \frac{a^+_{i+\frac{1}{2}} h^-_{i+\frac{1}{2}} u^-_{i+\frac{1}{2}} c^-_{i+\frac{1}{2}} - a^-_{i+\frac{1}{2}} h^+_{i+\frac{1}{2}} u^+_{i+\frac{1}{2}} c^+_{i+\frac{1}{2}}}{a^+_{i+\frac{1}{2}} - a^-_{i+\frac{1}{2}}} \\ &\quad + \frac{a^+_{i+\frac{1}{2}} a^-_{i+\frac{1}{2}}}{a^+_{i+\frac{1}{2}} - a^-_{i+\frac{1}{2}}} \left[h^+_{i+\frac{1}{2}} c^+_{i+\frac{1}{2}} - h^-_{i+\frac{1}{2}} c^-_{i+\frac{1}{2}} \right] \\ &= \frac{a^+_{i+\frac{1}{2}} a^-_{i+\frac{1}{2}}}{a^+_{i+\frac{1}{2}} - a^-_{i+\frac{1}{2}}} h_0 \left[c^+_{i+\frac{1}{2}} - c^-_{i+\frac{1}{2}} \right] \neq 0.\end{aligned} \tag{2.22}$$

This indicates that the numerical flux resulting from the use of the HLL Riemann solver induces undesirable scalar diffusion, which indicates that the numerical scheme cannot guarantee the exact C-property for the scalar concentration. To reduce the numerical diffusion embedded in the numerical scheme and thus guarantee a stationary steady state for scalar transport as well as the Saint-Venant system, we propose an anti-diffusion modification suitable for the Kurganov-Petrova scheme. This modification is made in an ad hoc manner aiming to minimize the numerical diffusion arising from scalar advection

across the contact. Therefore, it is applicable only to the advective terms in the STE. It should be noted that the Saint-Venant system is well-balanced and positivity-preserving. The proposed method is expressed as follows:

$$
\begin{aligned}
(H^x)^{(4)}_{i+\frac{1}{2},j} &= \frac{a^+_{i+\frac{1}{2},j} F\left(U^-_{i+\frac{1}{2},j}, B\left(x_{i+\frac{1}{2}}, y_j\right)\right) - a^-_{i+\frac{1}{2},j} F\left(U^+_{i+\frac{1}{2},j}, B\ \left(x_{i+\frac{1}{2}}, y_j\right)\right)}{a^+_{i+\frac{1}{2},j} - a^-_{i+\frac{1}{2},j}} \\
&\quad + \vartheta\left(\tilde{F}_{r\,i+\frac{1}{2},j}, \delta\right) \frac{a^+_{i+\frac{1}{2},j} a^-_{i+\frac{1}{2},j}}{a^+_{i+\frac{1}{2},j} - a^-_{i+\frac{1}{2},j}} \left[U^+_{i+\frac{1}{2},j} - U^-_{i+\frac{1}{2},j}\right], \\
(H^y)^{(4)}_{i,j+\frac{1}{2}} &= \frac{b^+_{i,j+\frac{1}{2}} F\left(U^-_{i,j+\frac{1}{2}}, B\left(x_i, y_{j+\frac{1}{2}}\right)\right) - b^-_{i,j+\frac{1}{2}} F\left(U^+_{i,j+\frac{1}{2}}, B\left(x_i, y_{j+\frac{1}{2}}\right)\right)}{b^+_{i,j+\frac{1}{2}} - b^-_{i,j+\frac{1}{2}}} \\
&\quad + \vartheta\left(\tilde{F}_{r\,i,j+\frac{1}{2}}, \delta\right) \frac{b^+_{i,j+\frac{1}{2}} b^-_{i,j+\frac{1}{2}}}{b^+_{i,j+\frac{1}{2}} - b^-_{i,j+\frac{1}{2}}} \left[U^+_{i,j+\frac{1}{2}} - U^-_{i,j+\frac{1}{2}}\right],
\end{aligned}
\tag{2.23}
$$

where

$$
\begin{aligned}
\vartheta\left(\tilde{F}_{r\,i+\frac{1}{2},j}, \delta\right) &= \frac{\tilde{F}_{r\,i+\frac{1}{2},j} + \delta}{\tilde{F}_{r\,i+\frac{1}{2},j} + 1}, \\
\vartheta\left(\tilde{F}_{r\,i,j+\frac{1}{2}}, \delta\right) &= \frac{\tilde{F}_{r\,i,j+\frac{1}{2}} + \delta}{\tilde{F}_{r\,i,j+\frac{1}{2}} + 1},
\end{aligned}
\tag{2.24}
$$

in which

$$
\begin{aligned}
\tilde{F}_{r\,i+\frac{1}{2},j} &= \frac{1 + \mathrm{sign}\left(u'_{i+\frac{1}{2},j}\right)}{2} \frac{\left|u^+_{i+\frac{1}{2},j}\right|}{\sqrt{g h^+_{i+\frac{1}{2},j}}} + \frac{1 - \mathrm{sign}\left(u'_{i+\frac{1}{2}}\right)}{2} \frac{\left|u^-_{i+\frac{1}{2},j}\right|}{\sqrt{g h^-_{i+\frac{1}{2},j}}} \\
\tilde{F}_{r\,i,j+\frac{1}{2}} &= \frac{1 + \mathrm{sign}\left(v'_{i,j+\frac{1}{2}}\right)}{2} \frac{\left|v^+_{i,j+\frac{1}{2}}\right|}{\sqrt{g h^+_{i,j+\frac{1}{2}}}} + \frac{1 - \mathrm{sign}\left(v'_{i,j+\frac{1}{2}}\right)}{2} \frac{\left|v^-_{i,j+\frac{1}{2}}\right|}{\sqrt{g h^-_{i,j+\frac{1}{2}}}}
\end{aligned}
\tag{2.25}
$$

where $\delta = 10^{-4}$ is a model parameter that adjusts the minimum value of the anti-diffusion function $\vartheta(\tilde{F}_r, \delta)$ when $\tilde{F}_r = 0$. The magnitude differences in the reconstructed flow velocities at the cell interfaces in the x and y directions are $\left(u^{'}, v^{'}\right) = \left(\left|u^{+}\right| - \left|u^{-}\right|, \left|v^{+}\right| - \left|v^{-}\right|\right)$ and sign(x) is the symbol function which is defined as

$$\text{sign}(x) = \begin{cases} 1, & x \geq 0, \\ -1, & x < 0. \end{cases} \tag{2.26}$$

2.2.4 Numerical Approximation of the Diffusive Fluxes

The diffusive fluxes $\tilde{F}$ are approximated by numerical discretization using the central FDM. The approximation can be expressed as

$$\begin{aligned} \tilde{F} = & \frac{D_{xx}}{\Delta x^2} \left\{ (hc)_{i+1,j} - 2\,(hc)_{i,j} + (hc)_{i-1,j} \right\} \\ & + \frac{D_{xy}}{2\Delta x \Delta y} \left\{ (hc)_{i+1,j+1} - (hc)_{i+1,j-1} - (hc)_{i-1,j+1} + (hc)_{i-1,j-1} \right\} \\ & + \frac{D_{yy}}{\Delta y^2} \left\{ (hc)_{i,j+1} - 2\,(hc)_{i,j} + (hc)_{i,j-1} \right\}, \end{aligned} \tag{2.27}$$

where $D = \begin{bmatrix} D_{xx} & D_{xy} \\ D_{yx} & D_{yy} \end{bmatrix}$ can be estimated as follows [55, 19],

$$
\begin{aligned}
D_{xx} &= D_L \cos^2\theta_d + D_T \sin^2\theta_d, \\
D_{xy} &= D_{yx} = \frac{1}{2}(D_L - D_T)\sin 2\theta_d, \\
D_{yy} &= D_L \sin^2\theta_d + D_T \cos^2\theta_d,
\end{aligned}
\tag{2.28}
$$

in which the flow direction is $\theta_d = \cos^{-1}(\frac{u}{\sqrt{u^2+v^2}}) = \sin^{-1}(\frac{v}{\sqrt{u^2+v^2}})$. The longitudinal and transverse diffusion coefficients D_L and D_T can be calculated as follows [56],

$$
\begin{aligned}
D_L &= \frac{\alpha_L h\sqrt{g(u^2+v^2)}}{C}, \\
D_T &= \frac{\alpha_T h\sqrt{g(u^2+v^2)}}{C}
\end{aligned}
\tag{2.29}
$$

where α_L and α_T are dimensionless constants for longitudinal and transverse dispersion and C is the Chezy coefficient.

2.2.5 Positivity-Preserving Property for the Water Depth and the Scalar Concentration

This section briefly demonstrates the proof that the proposed scheme guarantees the positivity-preserving property for the hydrodynamic model. The confirmation that the proposed scheme preserves the positivity property for the scalar transport model is presented as well. The systems of Eq. 2.2 are

discretized in time, simply using the forward Euler method or a higher-order strong-stability-preserving (SSP) ordinary differential equation (ODE) solver. Subsequently, the first component of Eq. 2.2 can be rewritten as

$$\bar{w}_{i,j}^{n+1} = \bar{w}_{i,j}^{n} - \lambda \left((H^x)^{(1)}_{i+\frac{1}{2},j} - (H^x)^{(1)}_{i-\frac{1}{2},j} \right) - \mu \left((H^y)^{(1)}_{i,j+\frac{1}{2}} - (H^x)^{(1)}_{i,j-\frac{1}{2}} \right), \tag{2.30}$$

where $\lambda := \Delta t/\Delta x, \mu := \Delta t/\Delta y$ and the superscript n represents the discretized time level, with the time level being $t^{n+1} = t^n + \Delta t$ for a time step Δt. The

numerical fluxes at time level $t = t^n$ are expressed as

$$
\begin{aligned}
(H^x)^{(1)}_{i+\frac{1}{2},j} &= \frac{a^+_{i+\frac{1}{2},j}\left(h^-_{i+\frac{1}{2},j}u^-_{i+\frac{1}{2},j}\right) - a^-_{i+\frac{1}{2},j}\left(h^+_{i+\frac{1}{2},j}u^+_{i+\frac{1}{2},j}\right)}{a^+_{i+\frac{1}{2},j} - a^-_{i+\frac{1}{2},j}} \\
&\quad + \frac{a^+_{i+\frac{1}{2},j}a^-_{i+\frac{1}{2},j}}{a^+_{i+\frac{1}{2},j} - a^-_{i+\frac{1}{2},j}}\left[w^+_{i+\frac{1}{2},j} - w^-_{i+\frac{1}{2},j}\right] \\
&= \frac{a^+_{i+\frac{1}{2},j}\left(h^-_{i+\frac{1}{2},j}u^-_{i+\frac{1}{2},j}\right) - a^-_{i+\frac{1}{2},j}\left(h^+_{i+\frac{1}{2},j}u^+_{i+\frac{1}{2},j}\right)}{a^+_{i+\frac{1}{2},j} - a^-_{i+\frac{1}{2},j}} \\
&\quad + \frac{a^+_{i+\frac{1}{2},j}a^-_{i+\frac{1}{2},j}}{a^+_{i+\frac{1}{2},j} - a^-_{i+\frac{1}{2},j}}\left[h^+_{i+\frac{1}{2},j} - h^-_{i+\frac{1}{2},j}\right], \\
(H^y)^{(1)}_{i,j+\frac{1}{2}} &= \frac{b^+_{i,j+\frac{1}{2}}\left(h^-_{i,j+\frac{1}{2}}u^-_{i,j+\frac{1}{2}}\right) - b^-_{i,j+\frac{1}{2}}\left(h^+_{i,j+\frac{1}{2}}u^+_{i,j+\frac{1}{2}}\right)}{b^+_{i,j+\frac{1}{2}} - b^-_{i,j+\frac{1}{2}}} \\
&\quad + \frac{b^+_{i,j+\frac{1}{2}}b^-_{i,j+\frac{1}{2}}}{b^+_{i,j+\frac{1}{2}} - b^-_{i,j+\frac{1}{2}}}\left(w^+_{i,j+\frac{1}{2}} - w^-_{i,j+\frac{1}{2}}\right) \\
&= \frac{b^+_{i,j+\frac{1}{2}}\left(h^-_{i,j+\frac{1}{2}}u^-_{i,j+\frac{1}{2}}\right) - b^-_{i,j+\frac{1}{2}}\left(h^+_{i,j+\frac{1}{2}}u^+_{i,j+\frac{1}{2}}\right)}{b^+_{i,j+\frac{1}{2}} - b^-_{i,j+\frac{1}{2}}} \\
&\quad + \frac{b^+_{i,j+\frac{1}{2}}b^-_{i,j+\frac{1}{2}}}{b^+_{i,j+\frac{1}{2}} - b^-_{i,j+\frac{1}{2}}}\left[h^+_{i,j+\frac{1}{2}} - h^-_{i,j+\frac{1}{2}}\right].
\end{aligned}
\tag{2.31}
$$

Together, Eqs. 2.11 and 2.12 yield

$$
\begin{aligned}
\bar{w}_{i,j} - B_{i,j} &= \frac{1}{4}\left(w^-_{i+\frac{1}{2},j} + w^+_{i-\frac{1}{2},j} + w^-_{i,j+\frac{1}{2}} + w^+_{i,j-\frac{1}{2}}\right) \\
&\quad - \frac{1}{4}\left(B_{i+\frac{1}{2},j} + B_{i-\frac{1}{2},j} + B_{i,j+\frac{1}{2}} + B_{i,j-\frac{1}{2}}\right) \\
&= \frac{1}{4}\left(h^-_{i+\frac{1}{2},j} + h^+_{i-\frac{1}{2},j} + h^-_{i,j+\frac{1}{2}} + h^+_{i,j-\frac{1}{2}}\right).
\end{aligned}
\tag{2.32}
$$

By subtracting $B_{i,j}$ from Eq. 2.30 and substituting Eq. 2.31 into Eq. 2.30, one can obtain

$$
\begin{aligned}
\bar{h}_{i,j}^{n+1} = & \left\{ \frac{1}{4} + \lambda a_{i-\frac{1}{2},j}^{-} \left(\frac{a_{i-\frac{1}{2},j}^{+} - u_{i-\frac{1}{2},j}^{+}}{a_{i-\frac{1}{2},j}^{+} - a_{i-\frac{1}{2},j}^{-}} \right) \right\} h_{i-\frac{1}{2},j}^{+} \\
& + \left\{ \frac{1}{4} - \lambda a_{i+\frac{1}{2},j}^{+} \left(\frac{u_{i+\frac{1}{2},j}^{-} - a_{i+\frac{1}{2},j}^{-}}{a_{i+\frac{1}{2},j}^{+} - a_{i+\frac{1}{2},j}^{-}} \right) \right\} h_{i+\frac{1}{2},j}^{-} \\
& - \lambda a_{i+\frac{1}{2},j}^{-} \left(\frac{a_{i+\frac{1}{2},j}^{+} - u_{i+\frac{1}{2},j}^{+}}{a_{i+\frac{1}{2},j}^{+} - a_{i+\frac{1}{2},j}^{-}} \right) h_{i+\frac{1}{2},j}^{+} + \lambda a_{i-\frac{1}{2},j}^{+} \left(\frac{u_{i-\frac{1}{2},j}^{-} - a_{i-\frac{1}{2},j}^{-}}{a_{i-\frac{1}{2},j}^{+} - a_{i-\frac{1}{2},j}^{-}} \right) h_{i-\frac{1}{2},j}^{-} \\
& + \left\{ \frac{1}{4} + \mu b_{i,j-\frac{1}{2}}^{-} \left(\frac{b_{i,j-\frac{1}{2}}^{+} - v_{i,j-\frac{1}{2}}^{+}}{b_{i,j-\frac{1}{2}}^{+} - b_{i,j-\frac{1}{2}}^{-}} \right) \right\} h_{i,j-\frac{1}{2}}^{+} \\
& + \left\{ \frac{1}{4} - \mu b_{i,j+\frac{1}{2}}^{+} \left(\frac{v_{i,j+\frac{1}{2}}^{-} - b_{i,j+\frac{1}{2}}^{-}}{b_{i,j+\frac{1}{2}}^{+} - b_{i,j+\frac{1}{2}}^{-}} \right) \right\} h_{i,j+\frac{1}{2}}^{-} \\
& - \mu b_{i,j+\frac{1}{2}}^{-} \left(\frac{b_{i,j+\frac{1}{2}}^{+} - v_{i,j+\frac{1}{2}}^{+}}{b_{i,j+\frac{1}{2}}^{+} - b_{i,j+\frac{1}{2}}^{-}} \right) h_{i,j+\frac{1}{2}}^{+} + \mu b_{i,j-\frac{1}{2}}^{+} \left(\frac{v_{i,j-\frac{1}{2}}^{-} - b_{i,j-\frac{1}{2}}^{-}}{b_{i,j-\frac{1}{2}}^{+} - b_{i,j-\frac{1}{2}}^{-}} \right) h_{i,j-\frac{1}{2}}^{-}.
\end{aligned}
\tag{2.33}
$$

where $(hu)_{i\pm\frac{1}{2},j}^{\pm} = (h)_{i\pm\frac{1}{2},j}^{\pm} \cdot (u)_{i\pm\frac{1}{2},j}^{\pm}$ and $(hv)_{i,j\pm\frac{1}{2}}^{\pm} = (h)_{i,j\pm\frac{1}{2}}^{\pm} \cdot (v)_{i,j\pm\frac{1}{2}}^{\pm}$, as given in Eq. 2.21.

The cell average of the water depth at time level $t = t^{n+1}$ is a linear combination of the reconstructed water depths at time level $t = t^{n}$. Since $a_{i\pm\frac{1}{2},j}^{+} \geq 0$, $a_{i\pm\frac{1}{2},j}^{-} \leq 0$, $a_{i\pm\frac{1}{2},j}^{+} - u_{i\pm\frac{1}{2},j}^{+} \geq 0$, $u_{i\pm\frac{1}{2},j}^{-} - a_{i\pm\frac{1}{2},j}^{-} \geq 0$, $b_{i,j\pm\frac{1}{2}}^{+} \geq 0$, $b_{i,j\pm\frac{1}{2}}^{-} \leq 0$, $b_{i,j\pm\frac{1}{2}}^{+} - v_{i,j\pm\frac{1}{2}}^{+} \geq 0$, and $v_{i,j\pm\frac{1}{2}}^{-} - b_{i,j\pm\frac{1}{2}}^{-} \geq 0$, all coefficients are non-negative under the Courant-Friedrichs-Lewy (CFL) restriction $\Delta t \leq \min\left\{ \frac{\Delta x}{4a}, \frac{\Delta y}{4b} \right\}$ with $a \coloneqq \max_{i,j} \left[\max\left\{ a_{i+\frac{1}{2},j}^{+}, -a_{i-\frac{1}{2},j}^{-} \right\} \right]$ and $b \coloneqq \max_{i,j} \left[\max\left\{ b_{i,j+\frac{1}{2}}^{+}, -b_{i,j-\frac{1}{2}}^{-} \right\} \right]$.

Therefore, the cell-averaged water depth at time level $t = t^{n+1}$ is non-negative for all cells.

The full discretization for the STE can also be rewritten in the same manner as for the water depth, as follows:

$$\bar{hc}_{i,j}^{n+1} = \bar{hc}_{i,j}^{n} - \lambda \left((H^x)^{(4)}_{i+\frac{1}{2},j} - (H^x)^{(4)}_{i-\frac{1}{2},j} \right) - \mu \left((H^y)^{(4)}_{i,j+\frac{1}{2}} - (H^y)^{(4)}_{i,j-\frac{1}{2}} \right), \tag{2.34}$$

The numerical fluxes at time level $t = t^n$ are expressed as

$$\begin{aligned}
(H^x)^{(4)}_{i+\frac{1}{2},j} =& \frac{a^+_{i+\frac{1}{2},j}\left(h^-_{i+\frac{1}{2},j}u^-_{i+\frac{1}{2},j}c^+_{i+\frac{1}{2},j}\right) - a^-_{i+\frac{1}{2},j}\left(h^+_{i+\frac{1}{2},j}u^+_{i+\frac{1}{2},j}c^-_{i+\frac{1}{2},j}\right)}{a^+_{i+\frac{1}{2},j} - a^-_{i+\frac{1}{2},j}} \\
&+ \vartheta\left(\tilde{F}r_{i+\frac{1}{2},j}, \delta\right) \frac{a^+_{i+\frac{1}{2},j}a^-_{i+\frac{1}{2},j}}{a^+_{i+\frac{1}{2},j} - a^-_{i+\frac{1}{2},j}} \left[h^+_{i+\frac{1}{2},j}c^+_{i+\frac{1}{2},j} - h^-_{i+\frac{1}{2},j}c^-_{i+\frac{1}{2},j}\right], \\
(H^y)^{(4)}_{i,j+\frac{1}{2}} =& \frac{b^+_{i,j+\frac{1}{2}}\left(h^-_{i,j+\frac{1}{2}}v^-_{i,j+\frac{1}{2}}c^-_{i,j+\frac{1}{2}}\right) - b^-_{i,j+\frac{1}{2}}\left(h^+_{i,j+\frac{1}{2}}v^+_{i,j+\frac{1}{2}}c^+_{i,j+\frac{1}{2}}\right)}{b^+_{i,j+\frac{1}{2}} - b^-_{i,j+\frac{1}{2}}} \\
&+ \vartheta\left(\tilde{F}r_{i,j+\frac{1}{2}}, \delta\right) \frac{b^+_{i,j+\frac{1}{2}}b^-_{i,j+\frac{1}{2}}}{b^+_{i,j+\frac{1}{2}} - b^-_{i,j+\frac{1}{2}}} \left[h^+_{i,j+\frac{1}{2}}c^+_{i,j+\frac{1}{2}} - h^-_{i,j+\frac{1}{2}}c^-_{i,j+\frac{1}{2}}\right],
\end{aligned} \tag{2.35}$$

Substituting Eq. 2.35 into Eq. 2.34, one can obtain

$$
\begin{aligned}
\bar{hc}_{i,j}^{n+1} = & \left[\frac{1}{4} + \lambda a_{i-\frac{1}{2},j}^{-} \left(\frac{\vartheta \left(\tilde{F}_{ri-\frac{1}{2},j}, \delta \right) a_{i-\frac{1}{2},j}^{+} - u_{i-\frac{1}{2},j}^{+}}{a_{i-\frac{1}{2},j}^{+} - a_{i-\frac{1}{2},j}^{-}} \right) \right] h_{i-\frac{1}{2},j}^{+} c_{i-\frac{1}{2},j}^{+} \\
& + \left[\frac{1}{4} - \lambda a_{i+\frac{1}{2},j}^{+} \left(\frac{u_{i+\frac{1}{2},j}^{-} - \vartheta \left(\tilde{F}_{ri+\frac{1}{2},j}, \delta \right) a_{i+\frac{1}{2},j}^{-}}{a_{i+\frac{1}{2},j}^{+} - a_{i+\frac{1}{2},j}^{-}} \right) \right] h_{i+\frac{1}{2},j}^{-} c_{i+\frac{1}{2},j}^{-} \\
& - \lambda a_{i+\frac{1}{2},j}^{-} \left(\frac{\vartheta \left(\tilde{F}_{ri+\frac{1}{2},j}, \delta \right) a_{i+\frac{1}{2},j}^{+} - u_{i+\frac{1}{2},j}^{+}}{a_{i+\frac{1}{2},j}^{+} - a_{i+\frac{1}{2},j}^{-}} \right) h_{i+\frac{1}{2},j}^{+} c_{i+\frac{1}{2},j}^{+} \\
& + \lambda a_{i-\frac{1}{2},j}^{+} \left(\frac{u_{i-\frac{1}{2},j}^{-} - \vartheta \left(\tilde{F}_{ri-\frac{1}{2},j}, \delta \right) a_{i-\frac{1}{2},j}^{-}}{a_{i-\frac{1}{2},j}^{+} - a_{i-\frac{1}{2},j}^{-}} \right) h_{i-\frac{1}{2},j}^{-} c_{i-\frac{1}{2},j}^{-} \\
& + \left[\frac{1}{4} + \mu b_{i,j-\frac{1}{2}}^{-} \left(\frac{\vartheta \left(\tilde{F}_{ri,j-\frac{1}{2}}, \delta \right) b_{i,j-\frac{1}{2}}^{+} - v_{i,j-\frac{1}{2}}^{+}}{b_{i,j-\frac{1}{2}}^{+} - b_{i,j-\frac{1}{2}}^{-}} \right) \right] h_{i,j-\frac{1}{2}}^{+} c_{i,j-\frac{1}{2}}^{+} \\
& + \left[\frac{1}{4} - \mu b_{i,j+\frac{1}{2}}^{+} \left(\frac{v_{i,j+\frac{1}{2}}^{-} - \vartheta \left(\tilde{F}_{ri,j+\frac{1}{2}}, \delta \right) b_{i,j+\frac{1}{2}}^{-}}{b_{i,j+\frac{1}{2}}^{+} - b_{i,j+\frac{1}{2}}^{-}} \right) \right] h_{i,j+\frac{1}{2}}^{-} c_{i,j+\frac{1}{2}}^{-} \\
& - \mu b_{i,j+\frac{1}{2}}^{-} \left(\frac{\vartheta \left(\tilde{F}_{ri,j+\frac{1}{2}}, \delta \right) b_{i,j+\frac{1}{2}}^{+} - v_{i,j+\frac{1}{2}}^{+}}{b_{i,j+\frac{1}{2}}^{+} - b_{i,j+\frac{1}{2}}^{-}} \right) h_{i,j+\frac{1}{2}}^{+} c_{i,j+\frac{1}{2}}^{+} \\
& + \mu b_{i,j-\frac{1}{2}}^{+} \left(\frac{v_{i,j-\frac{1}{2}}^{-} - \vartheta \left(\tilde{F}_{ri,j-\frac{1}{2}}, \delta \right) b_{i,j-\frac{1}{2}}^{-}}{b_{i,j-\frac{1}{2}}^{+} - b_{i,j-\frac{1}{2}}^{-}} \right) h_{i,j-\frac{1}{2}}^{-} c_{i,j-\frac{1}{2}}^{-}.
\end{aligned}
\tag{2.36}
$$

where $(hc)^{\pm}_{i\pm\frac{1}{2},j} = (h)^{\pm}_{i\pm\frac{1}{2},j} \cdot (c)^{\pm}_{i\pm\frac{1}{2},j}$ and $(hc)^{\pm}_{i,j\pm\frac{1}{2}} = (h)^{\pm}_{i,j\pm\frac{1}{2}} \cdot (c)^{\pm}_{i,j\pm\frac{1}{2}}$, as given in Eq. 2.21.

The cell-averaged scalar concentration at time level $t = t^{n+1}$ is a linear combination of the reconstructed scalar concentration at time level $t = t^n$. Since $\vartheta\left(\tilde{F}_{ri\pm\frac{1}{2},j}, \delta\right) \geq 0$, $\vartheta\left(\tilde{F}_{ri,j\pm\frac{1}{2}}, \delta\right) \geq 0$, $\vartheta\left(\tilde{F}_{ri\pm\frac{1}{2},j}, \delta\right) a^{+}_{i\pm\frac{1}{2},j} - u^{+}_{i\pm\frac{1}{2},j} \geq 0$, $u^{-}_{i\pm\frac{1}{2},j} - \vartheta\left(\tilde{F}_{ri\pm\frac{1}{2},j}, \delta\right) a^{-}_{i\pm\frac{1}{2},j} \geq 0$, $\vartheta\left(\tilde{F}_{ri,j\pm\frac{1}{2}}, \delta\right) b^{+}_{i,j\pm\frac{1}{2}} - v^{+}_{i,j\pm\frac{1}{2}} \geq 0$, and $v^{-}_{i,j\pm\frac{1}{2}} - \vartheta\left(\tilde{F}_{ri,j\pm\frac{1}{2}}, \delta\right) b^{-}_{i,j\pm\frac{1}{2}} \geq 0$, all coefficients are also non-negative under the same CFL restriction defined for the positivity of the water depth. Therefore, the cell average of the scalar concentration at the next time level $t = t^{n+1}$ is also non-negative based on the positivity of the reconstructed water depth and scalar concentration.

The positivity-preserving property is still valid if a higher-order SSP ODE solvers such as multistep methods are adopted instead of the forward Euler method. This is because such time discretizations can be decomposed into convex combinations of several forward Euler steps [57]. In the numerical experiments described in Section 2.3, a third-order Adams-Bashforth predictor scheme and an optional fourth-order Adams-Moulton corrector scheme were used.

2.2.6 Exact C-property for Hydrodynamic and Scalar Transport Systems

This section presents the proof that the exact C-property for hydrodynamic and scalar transport systems is satisfied. The stationary steady state (lake at

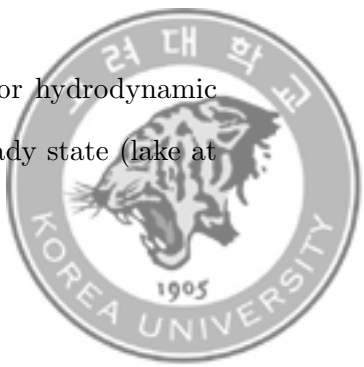

rest), i.e.,

$$h + B = \text{Const}_1, \quad u = v = 0, \quad c = \text{Const}_2 \tag{2.37}$$

are considered.

Starting from Eq. 2.33, the water depth at time level $t = t^n$ under stationary steady state can be written as

$$\bar{h}_{i,j}^{n+1} = \frac{1}{4} h^{+}_{i-\frac{1}{2},j} + \frac{1}{4} h^{-}_{i+\frac{1}{2},j} + \frac{1}{4} h^{+}_{i,j-\frac{1}{2}} + \frac{1}{4} h^{-}_{i,j+\frac{1}{2}} \tag{2.38}$$

Using Eq. 2.11 and Eq. 2.12,

$$\bar{h}_{i,j}^{n+1} = \bar{h}_{i,j}^{n} \tag{2.39}$$

To guarantee exact C-property for SWEs, the momentum flux in Eq. 2.14 should equal to the source terms in Eq. 2.13 under the stationary steady state. Thus, the second and third components of Eq. 2.2 under the stationary steady state can be written as

$$\begin{aligned}
\bar{hu}_{i,j}^{n+1} &= \bar{hu}_{i,j}^{n} - \lambda \left(\left(\frac{1}{2} g h^2 \right)_{i+\frac{1}{2},j} - \left(\frac{1}{2} g h^2 \right)_{i-\frac{1}{2},j} \right) \\
&\quad - \lambda g \left(\bar{w}_{i,j} - B_{i,j} \right) \left(B_{i+\frac{1}{2},j} - B_{i-\frac{1}{2},j} \right) \\
\bar{hv}_{i,j}^{n+1} &= \bar{hv}_{i,j}^{n} - \mu \left(\left(\frac{1}{2} g h^2 \right)_{i,j+\frac{1}{2}} - \left(\frac{1}{2} g h^2 \right)_{i,j-\frac{1}{2}} \right) \\
&\quad - \mu g \left(\bar{w}_{i,j} - B_{i,j} \right) \left(B_{i,j+\frac{1}{2}} - B_{i,j-\frac{1}{2}} \right)
\end{aligned} \tag{2.40}$$

The above equations can be rewritten as

$$\begin{aligned}
\bar{hu}_{i,j}^{n+1} &= \bar{hu}_{i,j}^{n} - \lambda\left(\frac{1}{2}g\left(h_{i+\frac{1}{2},j}\right)^2 - \frac{1}{2}g\left(h_{i-\frac{1}{2},j}\right)^2\right) - \lambda g\bar{h}_{i,j}\left(B_{i+\frac{1}{2},j} - B_{i-\frac{1}{2},j}\right) \\
\bar{hv}_{i,j}^{n+1} &= \bar{hv}_{i,j}^{n} - \mu\left(\frac{1}{2}g\left(h_{i,j+\frac{1}{2}}\right)^2 - \frac{1}{2}g\left(h_{i,j-\frac{1}{2}}\right)^2\right) - \mu g\bar{h}_{i,j}\left(B_{i,j+\frac{1}{2}} - B_{i,j-\frac{1}{2}}\right)
\end{aligned} \tag{2.41}$$

in which

$$\begin{aligned}
\frac{\left(h_{i+\frac{1}{2},j}\right)^2 - \left(h_{i-\frac{1}{2},j}\right)^2}{2} &= \frac{h_{i+\frac{1}{2},j} + h_{i-\frac{1}{2},j}}{2}\left(h_{i+\frac{1}{2},j} - h_{i-\frac{1}{2},j}\right) \\
&= \bar{h_{i,j}}\left(w_{i,j} - B_{i+\frac{1}{2},j} - w_{i,j} + B_{i-\frac{1}{2},j}\right) \\
&= -\bar{h_{i,j}}\left(B_{i+\frac{1}{2},j} - B_{i-\frac{1}{2},j}\right) \\
\frac{\left(h_{i,j+\frac{1}{2}}\right)^2 - \left(h_{i,j-\frac{1}{2}}\right)^2}{2} &= \frac{h_{i,j+\frac{1}{2}} + h_{i,j-\frac{1}{2}}}{2}\left(h_{i,j+\frac{1}{2}} - h_{i,j-\frac{1}{2}}\right) \\
&= \bar{h}_{i,j}\left(w_{i,j} - B_{i,j+\frac{1}{2}} - w_{i,j} + B_{i,j-\frac{1}{2}}\right) \\
&= -\bar{h}_{i,j}\left(B_{i,j+\frac{1}{2}} - B_{i,j-\frac{1}{2}}\right)
\end{aligned} \tag{2.42}$$

Therefore, Eq. 2.2 under stationary steady state can be expressed as

$$\begin{aligned}
(\bar{hu})_{i,j}^{n+1} &= (\bar{hu})_{i,j}^{n} \\
(\bar{hv})_{i,j}^{n+1} &= (\bar{hv})_{i,j}^{n}
\end{aligned} \tag{2.43}$$

which verifies that the numerical scheme guarantees the exact C-property for SWEs.

The scalar concentration at time level $t = t^n$ under stationary steady state

can be expressed using Eq. 2.36 as

$$\begin{aligned}(\bar{hc})_{i,j}^{n+1} &= \frac{1}{4}h^{+}_{i-\frac{1}{2},j}c^{+}_{i-\frac{1}{2},j} + \frac{1}{4}h^{-}_{i+\frac{1}{2},j}c^{-}_{i+\frac{1}{2},j} + \frac{1}{4}h^{+}_{i,j-\frac{1}{2}}c^{+}_{i,j-\frac{1}{2}} + \frac{1}{4}h^{-}_{i,j+\frac{1}{2}}c^{-}_{i,j+\frac{1}{2}} \\ &= \frac{1}{4}h_{i-\frac{1}{2},j}c^{+}_{i-\frac{1}{2},j} + \frac{1}{4}h_{i+\frac{1}{2},j}c^{-}_{i+\frac{1}{2},j} + \frac{1}{4}h_{i,j-\frac{1}{2}}c^{+}_{i,j-\frac{1}{2}} + \frac{1}{4}h_{i,j+\frac{1}{2}}c^{-}_{i,j+\frac{1}{2}}\end{aligned} \tag{2.44}$$

Using $c_{i\pm\frac{1}{2},j} = c_{i,j\pm\frac{1}{2}} = \bar{c}^{n}_{i,j}$, one can obtain

$$\begin{aligned}(\bar{hc})_{i,j}^{n+1} &= \frac{1}{4}h_{i-\frac{1}{2},j}\bar{c}^{n}_{i,j} + \frac{1}{4}h_{i+\frac{1}{2},j}\bar{c}^{n}_{i,j} + \frac{1}{4}h_{i,j-\frac{1}{2}}\bar{c}^{n}_{i,j} + \frac{1}{4}h_{i,j+\frac{1}{2}}\bar{c}^{n}_{i,j} \\ &= \frac{1}{4}\left(h_{i-\frac{1}{2},j} + h_{i+\frac{1}{2},j} + h_{i,j-\frac{1}{2}} + h_{i,j-\frac{1}{2}}\right)\bar{c}^{n}_{i,j} \\ &= \bar{h}^{n}_{i,j}\bar{c}^{n}_{i,j}\end{aligned} \tag{2.45}$$

Substituting Eq. 2.39 into Eq. 2.45, it yields

$$\bar{c}^{n+1}_{i,j} = \bar{c}^{n}_{i,j} \tag{2.46}$$

which proves that the numerical scheme guarantees the exact C-property for the STE.

2.2.7 Stability Condition of the Proposed Numerical Scheme

The combination of advection and diffusion determines the stability condition, so the time step restriction is dominated by both the CFL number and the

Peclet number, Pe, as follows:

$$\mathrm{CFL} + Pe \leq 1, \tag{2.47}$$

where

$$\begin{aligned} \mathrm{CFL} &= \max\left\{\frac{4a}{\Delta x}, \frac{4b}{\Delta y}\right\}\Delta t, \\ Pe &= \max\left\{\frac{D_{xx}+D_{xy}}{\Delta x}, \frac{D_{yx}+D_{yy}}{\Delta y}\right\}\Delta t. \end{aligned} \tag{2.48}$$

Substituting Eq. 2.48 into Eq. 2.47, a time step restriction satisfying the stability condition can be obtained as follows:

$$\Delta t \leq \frac{1}{\max\left\{\frac{4a}{\Delta x}, \frac{4b}{\Delta y}\right\} + \max\left\{\frac{D_{xx}+D_{xy}}{\Delta x}, \frac{D_{yx}+D_{yy}}{\Delta y}\right\}}. \tag{2.49}$$

2.3 Numerical Experiments

In this section, we investigate the performance of the proposed scheme in six problems where the advection and diffusion processes of the scalar are considered individually or together. In all numerical experiments, the minmod parameter θ in Eq. 2.16 is set to 2.0 and $g = 9.81\ m/s^2$

2.3.1 Numerical Order of Accuracy

The purpose of the first case is to examine the numerical order of accuracy of the proposed method. Following Xing and Shu [58], the friction-less bottom

topography and the initial conditions over computational domain [0.1] m are defined by

$$
\begin{aligned}
&B(x,0) = \sin^2(\pi x),\ w(x,0) = B(x,0) + 5 + \exp\{\cos(2\pi x)\},\\
&hu(x,0) = \sin(\cos(2\pi x)), c(x,0) = 0.3\exp\{-0.1(x-0.5)^2\}.
\end{aligned}
\tag{2.50}
$$

Scalar diffusion is not considered, and periodic boundary conditions are imposed on both boundaries of the numerical domain.

Since the exact solution is not known explicitly, we use a second-order scheme with 12,800 cells as a reference solution. This reference solution is then used to compute the numerical errors and corresponding numerical orders of accuracy for w, hu and hc. It is computed up to $t = 0.1$ s and the numerical results listed in Table 2.1 confirm that the proposed scheme has second-order accuracy.

Table 2.1: L^1-errors and numerical orders of accuracy

N	w		hu		hc	
	L^1-error	Order	L^1-error	Order	L^1-error	Order
200	1.46e-04	-	2.59e-03	-	1.65e-04	-
400	3.64e-05	2.00	6.37e-04	2.02	4.07e-05	2.01
800	9.00e-06	2.01	1.58e-04	2.01	1.01e-05	2.01
1600	2.22e-06	2.01	3.90e-05	2.01	2.48e-06	2.02
3200	5.28e-07	2.05	9.31e-06	2.05	5.98e-07	2.04

2.3.2 2D Pure Diffusion

A scalar diffusion experiment investigates the capability of the proposed scheme for a diffusion-only process. The diffusion process of a Gaussian distribution of scalar concentration [e.g. 59, 60] is adopted. A 16 m^2 square tank over a flat and frictionless bottom with a water depth of $h = 0.01$ m is discretized using a uniform grid size of 0.02 m for the x- and y- directions. A Gaussian distribution is employed for scalar concentration. The analytical solution for the diffusion process of the Gaussian distribution with respect to time is expressed as follows:

$$c(x, y, t) = \frac{\sigma^2}{4Dt + \sigma^2} \exp\left(-\frac{(x - x_0)^2 + (y - y_0)^2}{4Dt + \sigma^2}\right), \tag{2.51}$$

where the standard deviation is $\sigma = 0.1$, D is the diffusion coefficient in both the x- and y- directions, and the center of the Gaussian distribution is $(x_0, y_0) = (0, 0)$. The initial scalar distribution is given by

$$c(x, y, 0) = \exp\left(-\frac{(x - x_0)^2 + (y - y_0)^2}{\sigma^2}\right), \tag{2.52}$$

Four numerical cases using diffusion coefficients of $D = 0.001, 0.002, 0.005,$ and 0.01 were simulated to assess the accuracy of the numerical schemes.

Figure 2.2 shows the analytical and numerical scalar distributions at different times when $D = 0.01$. Figure 2.2 (a, c, e) illustrates the scalar distribution at $t = 0, 7.5,$ and 15 s along the cross section $y = 0$, and shows that both numerical schemes are in excellent agreement with the analytical solution throughout the entire simulation. Figure 2.2 (b, d, f) depicting the scalar distributions

over the numerical domain obtained by each solution also indicates that the numerical solutions are highly consistent with the analytical solution. For the maximum scalar concentration at $t = 15$ s, the original numerical scheme has an error of 0.27% and the proposed numerical scheme indicates an error of 0.03%. Figure 2.3 shows the analytical and numerical solutions for the scalar diffusion at two points, one located at the center ($r = 0$) and the other 0.5 m away from the center ($r = 0.5$ m). This figure further confirms that the proposed scheme shows high accuracy at any point within the model domain whereas the original scheme induces a small amount of numerical diffusion in the early stage of the scalar diffusion process.

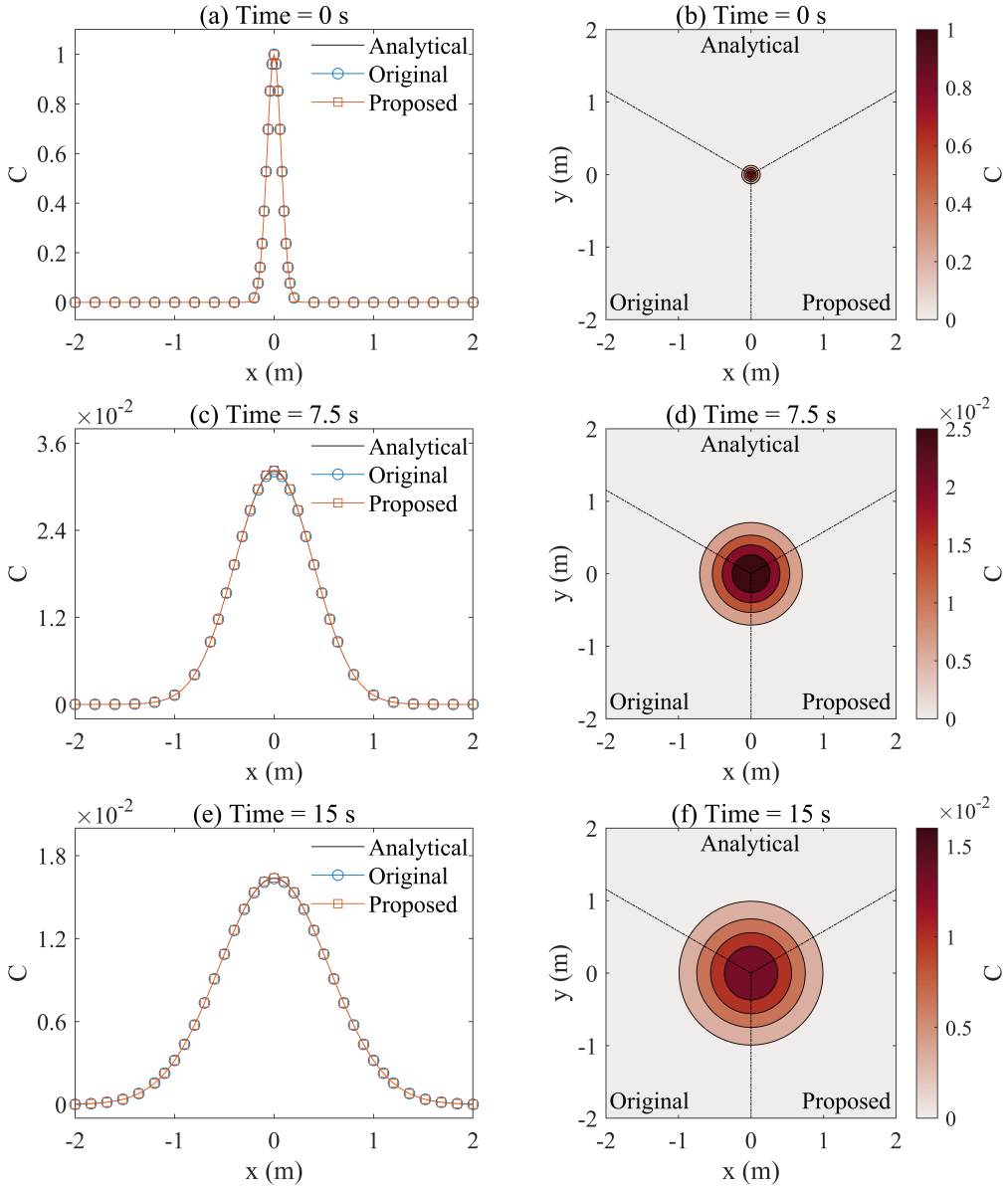

Figure 2.2: Scalar concentration comparisons when $D = 0.01$ at (a, b) $t = 0$ s, (c, d) $t = 7.5$ s, and (e, f) $t = 15$ s

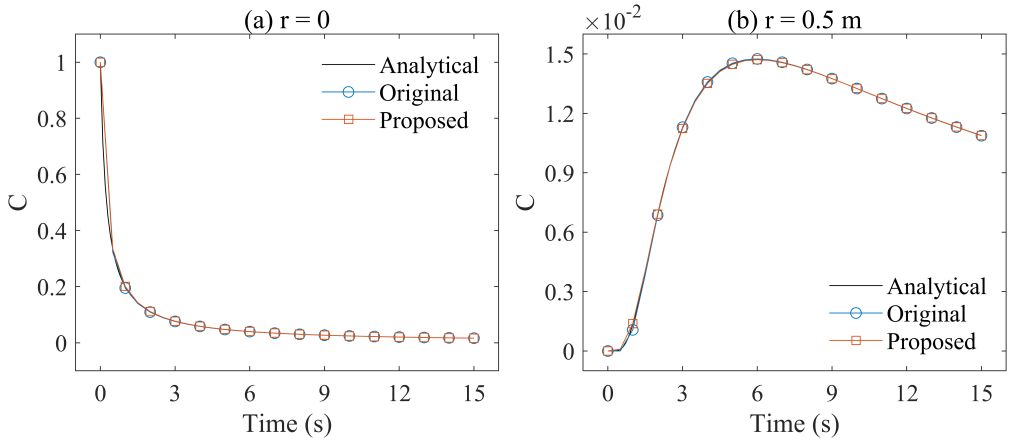

Figure 2.3: Scalar concentration over time when $D = 0.01$: (a) $r = 0$ and (b) $r = 0.5$ m

Let us now consider the minimum value of the diffusion coefficient ($D = 0.001$). Figure 2.4 shows the analytical and numerical solutions at different times when $D = 0.001$. Good agreement is obtained between the proposed scheme and analytical solution. However, unlike in the previous scalar diffusion case, the original scheme causes excessive scalar diffusion. The original scheme shows a relative error of approximately 16.4% in the maximum scalar concentration at $t = 15$ s, whereas the proposed scheme produces less than 0.3% error. Furthermore, the original scheme underestimates the maximum scalar concentration at the center compared to the analytical solution owing to the numerical diffusion throughout the entire simulation time as shown in Figure 2.5 (a). The original scheme shows better agreement with the black dashed line which represents the analytical solution for $D = 1.25 \times 10^{-3}$, than with the black solid line representing the analytical solution for $D = 0.001$. Also, Figure 2.5 (b) shows that the variation of the scalar concentration at a

distance of 0.5 m from the center, calculated by the original scheme, remains constant up to 9 s and subsequently exhibits a sharp increase compared to the analytical solution. These results imply that the original scheme fails to correctly simulate the diffusion process owing to numerical diffusion.

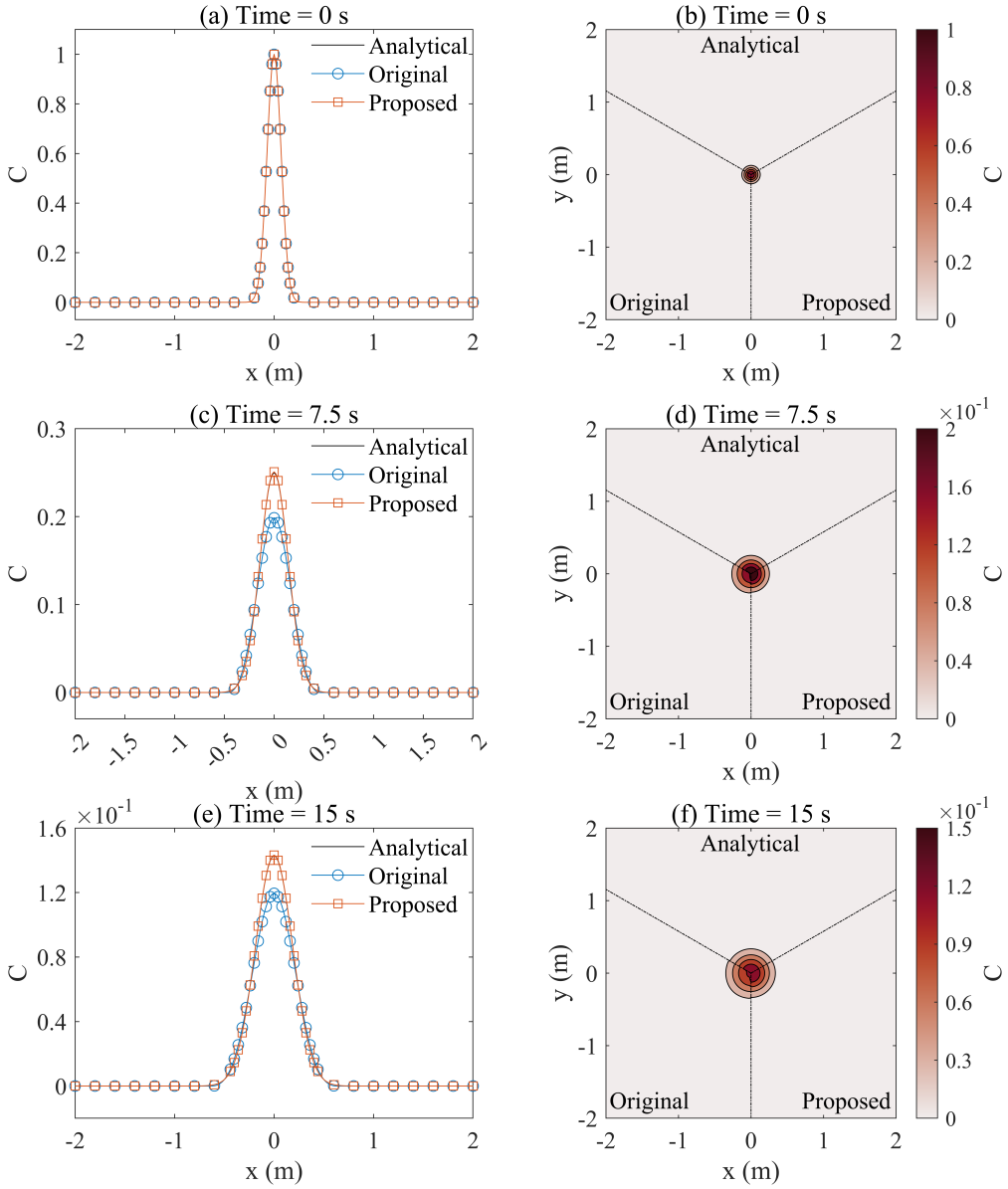

Figure 2.4: Scalar concentration comparisons when $D = 0.001$ at (a, b) $t = 0$ s , (c, d) $t = 7.5$ s , and (e, f) $t = 15$ s

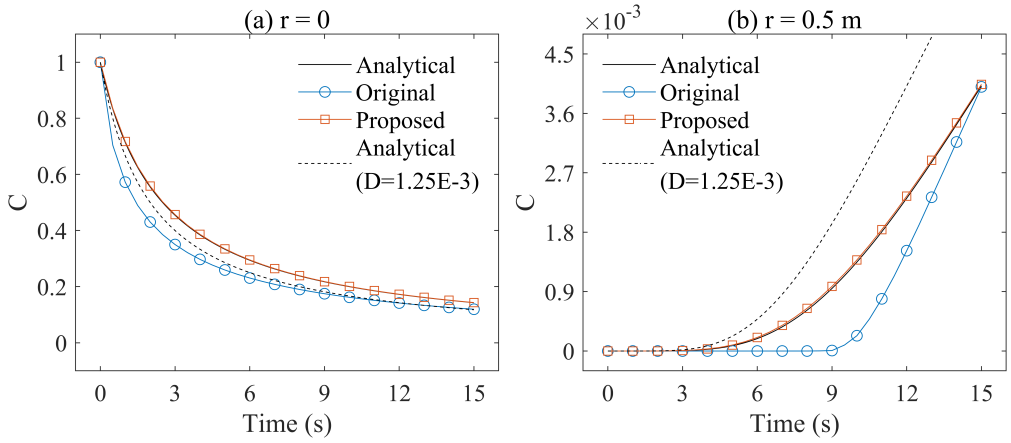

Figure 2.5: Scalar concentration over time when $D = 0.001$: (a) $r = 0$ and (b) $r = 0.5$ m

For a more detailed evaluation of the numerical schemes, the global relative error E_g is adopted following Li and Huang [61], which is defined as

$$E_g = \frac{\sqrt{\sum_i |C_i - C_{ai}|^2}}{\sqrt{\sum_i |C_{ai}|^2}}, \tag{2.53}$$

where C_i and C_{ai} are the scalar concentrations produced by the numerical and analytical solutions, respectively, for the i-th computational cell.

The global relative errors of the numerical solutions for the four numerical cases were calculated for both numerical schemes throughout the numerical domain over time. The black solid and red dotted lines in Figure 2.6 represent the simulation results obtained using the original and proposed schemes, respectively. Lines marked with circles, asterisks, squares, and pentagrams in Figure 2.6 represent the numerical results for the diffusion coefficients of 0.001, 0.002,

0.005, and 0.01, respectively. The results from the original scheme confirm that the global relative error increases as the diffusion coefficient decreases. In contrast, the proposed scheme produces much smaller errors than the original scheme, regardless of the value of the diffusion coefficient. As the diffusion coefficient decreases, the maximum E_g of the original scheme increases from 0.028 to 0.187, whereas the proposed scheme exhibits similar values below 0.004 for all cases.

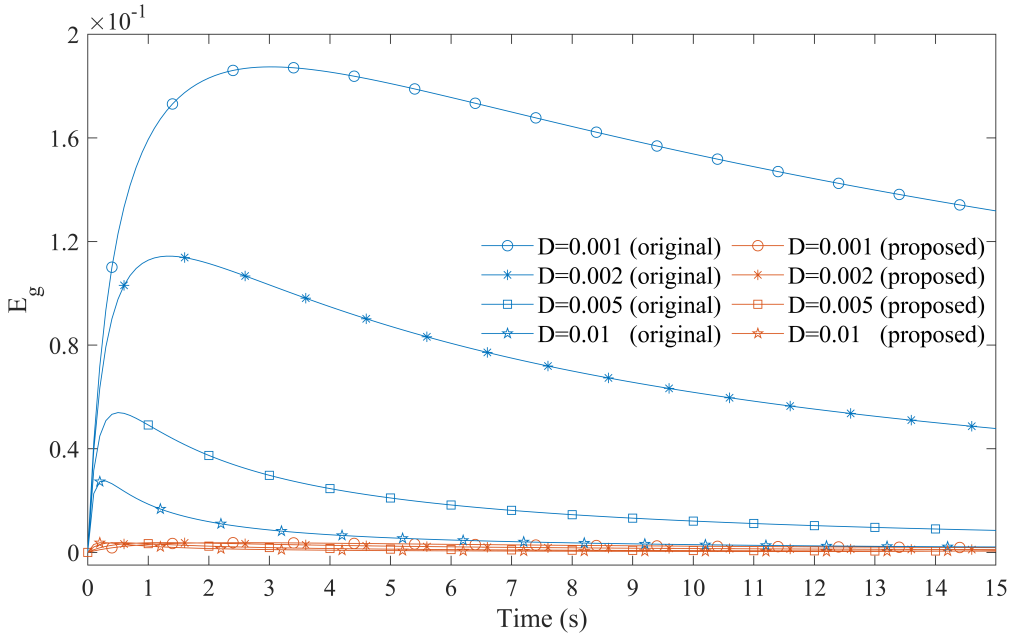

Figure 2.6: Global relative errors (E_g) versus simulation time under various diffusion coefficients

2.3.3 1D Pure Advection in a Uniform Flow

The pure advection of the scalar in a one-dimensional uniform flow field is adopted to validate the proposed scheme. A 25 m channel over a frictionless bottom has a constant depth of 2.5 m. A uniform flow with a velocity of 0.25

m/s is imposed on the computational domain. The initial conditions of the scalar concentration are defined as follows:

$$c(x,0) = \begin{cases} 1, & 1 \le x \le 3, \\ x-4, & 4 \le x \le 5, \\ -x+6, & 5 \le x \le 6, \\ \cos\{0.5\pi(x-8)\}, & 7 \le x \le 9, \\ \exp\{-4.5(x-11)^2\}, & 10 \le x \le 12, \\ 0, & \text{elsewhere.} \end{cases} \tag{2.54}$$

The diffusion terms are not considered to examine the numerical diffusion purely generated from the advection process. The computational domain is divided into 1,251 cells using a uniform grid size of 0.02 m. The total simulation time is 40 s.

Figure 2.7 shows a scalar advection comparison between the numerical and analytical solutions. Numerical diffusion occurs at different levels depending on the scalar concentration profile during scalar advection. Undesirable diffusion is found near the discontinuities of the rectangular scalar profile, although the maximum concentration is maintained. The results computed according to both numerical schemes show good agreement with the analytical solution for the cosine-shaped scalar distribution, without any significant reduction in the maximum scalar concentration. However, the maximum scalar concentration diminishes in accordance with the spatial gradient around the peak scalar con-

centration for the triangular scalar distribution; the original scheme yields a relative error of 10%, while the proposed scheme exhibits a corresponding error of 6%.

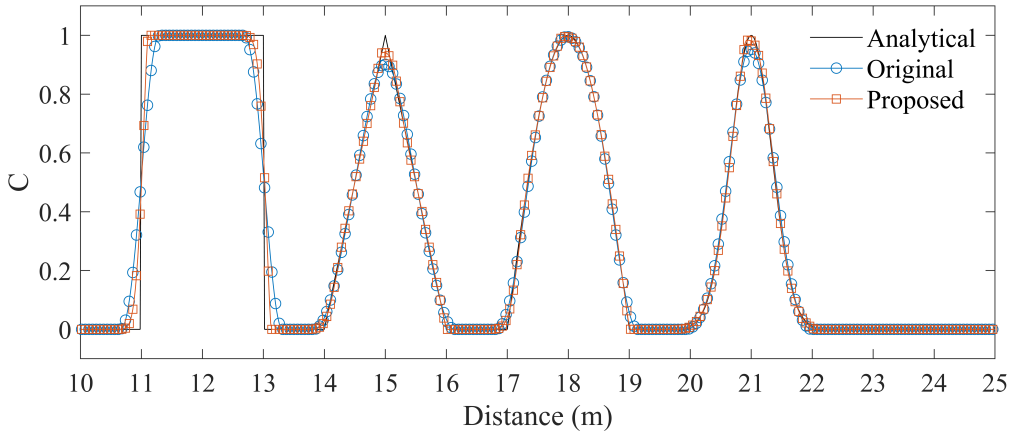

Figure 2.7: Scalar advection comparisons at $t = 40$ s in 1D uniform flow

Further numerical simulations were conducted under different water depth conditions to investigate the influence of the Froude number on the accuracy of the numerical scheme. For a given channel with flow velocity $u = 0.25$ m/s, the Froude numbers are set to 0.05, 0.1, 0.25, 0.5, and 1.01. The time step is restricted depending on the Froude number to maintain a constant CFL number. Table 2.2 shows the global relative errors of the numerical schemes for different Froude numbers. The results imply that the smaller the Froude number, the larger the difference between the errors of the two numerical schemes. When the Froude number is 0.05, the original scheme has an error of 0.131. However the proposed scheme produces an error of 0.095, which is equivalent to 73% of that of the original scheme. It should be noted that for Froude numbers greater than 1, the errors of both schemes converge to the same value because

the advective flux is calculated to be either $h^+u^+c^+$ or $h^-u^-c^-$ without the activation of the anti-diffusion function. Consequently, the comparison of the global relative error across a variety of Froude numbers reveals that the use of the anti-diffusion function is required particularly when the flow regime is subcritical.

Table 2.2: E_g comparison for various F_r conditions

Fr	Original scheme	Proposed scheme
0.05	0.131	0.095
0.10	0.119	0.095
0.25	0.107	0.095
0.50	0.100	0.095
1.01	0.096	0.096

2.3.4 2D Advection and Diffusion in a Diagonal Uniform Flow

An instantaneous release of a passive scalar under a uniform flow conditions is performed. This experiment involves scalar transport due to combined advection and diffusion. The numerical domain extends from 0 to 800 m in both the x and y directions and is sufficiently large; hence, the boundary effects can be neglected. An analytical solution for this experiment in an infinite domain is given by Liang et al. [15]. A generalized form of the analytical solution with an arbitrary flow direction θ_d can be expressed as

$$c(x,y,t) = \frac{M_s}{4\pi th\sqrt{D_L D_T}} \exp\left(-(\delta_x + \delta_y)\right), \tag{2.55}$$

where

$$\delta_x = \frac{\left((x - x_0 - ut)\cos(\theta_d) + (y - y_0 - vt)\sin(\theta_d)\right)^2}{4D_L t},$$
$$\delta_y = \frac{\left(-(x - x_0 - ut)\sin(\theta_d) + (y - y_0 - vt)\cos(\theta_d)\right)^2}{4D_T t}, \tag{2.56}$$

where M_s is the total amount of scalar instantaneously released at the initial location (x_0, y_0) and h is the water depth.

In the numerical test, M_s and h are 233.06 and 1 m, respectively. The flow condition is defined as $u = v = 1/\sqrt{2}$ m/s, so the flow direction is set to $\theta_d = 45°$. The Chezy coefficient is 40 $\mathrm{m}^{1/2}/\mathrm{s}$ and the longitudinal and the transverse diffusion constants in Eq. 2.29 are 13 and 1.2, respectively; accordingly, the diffusion coefficients are calculated to be $D_L = 1$ m^2/s and $D_T = 0.1$ m^2/s. Isotropic diffusion with $D_L = D_T = 1$ m^2/s along with advection was also simulated for comparison. The initial scalar release point is $(x_0, y_0) = (17.58\text{ m}, 17.58\text{ m})$. The numerical simulation starts at $t = 60$ s after the release. The initial scalar concentration is also defined as the analytical solution at $t = 60$ s. A square mesh with a grid size of $\Delta d = 1$ m is used to discretize the computational domain. The total simulation time is set to 600 s after injection of the scalar.

The analytical solution for the temporal evolution of the scalar transport behavior is shown in Figure 2.8. The black dashed diagonal line in Figure 2.8 indicates the flow direction ($\theta_d = 45°$). Figure 2.8 (b) shows that, as a result of the isotropic diffusion property, the same amount of scalar diffusion occurs in both the longitudinal and transverse directions. Meanwhile, anisotropic

diffusion leads to the gradual development of an elliptical distribution of scalar aligned with the diagonal flow direction during the transport process; this is because scalar diffusion along the flow direction (D_L) predominates over transverse diffusion (D_T).

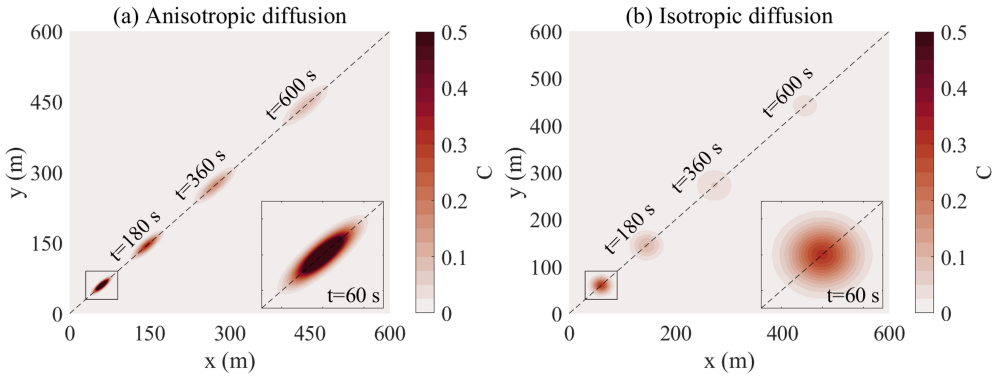

Figure 2.8: Analytical solution of the temporal evolution of the scalar distribution over time. (a) anisotropic diffusion and (b) isotropic diffusion

In case of isotropic diffusion, the numerical solutions from both numerical schemes are in good agreement with the analytical solution without any significant error as shown in Figure 2.9 (b). However, when the diffusion process is anisotropic, the scalar distribution in the early stage of scalar transport exhibits a significant difference in the maximum scalar concentration as shown in Figure 2.9 (a). The discrepancy in the maximum scalar concentration at $t = 90$ s is 6.99% for the original scheme and is reduced to 2.81% when the anti-diffusion function is implemented. Anisotropic diffusion occurs equally with isotropic diffusion in the flow direction but induces a steeper gradient of the scalar concentration in the transverse direction; the reason is that the scalar diffuses less actively along the transverse direction. The sharp concentration gradient con-

sequently leads to an undesirable numerical damping of the peak concentration even though the advection-diffusion process along the flow direction remains constant.

Further numerical simulations were conducted under various Peclet numbers ($P_e = \sqrt{u^2 + v^2}\Delta d/\sqrt{D_L D_T}$) because diverse settings of the longitudinal and transverse diffusion coefficients are likely to affect the accuracy. Here, values of 0.1, 0.2 and 1.0 m^2/s are considered for the transverse diffusion coefficient D_T, while the longitudinal diffusion coefficient D_L remains constant at 1.0 m^2/s. The global relative errors of the numerical solutions for different Peclet numbers calculated for the entire simulation are shown in Figure 2.10. When the Peclet number is 1.0, the two numerical schemes yield similar accuracy. However, As P_e decreases, the results show a significant discrepancy in E_g in the early stage of scalar transport. The ratio between the maximum global relative errors of the two numerical methods (i.e., $E_g^{\text{proposed}}/E_g^{\text{original}}$) is almost 0.9 when $P_e = 1$, but it decreases to 0.45 when $P_e = 3.23$. This implies that the more prevalent the advection process over the diffusion process, the higher the accuracy of the proposed scheme relative to the original scheme. Thus, adopting the proposed scheme is preferable under advection-dominated conditions.

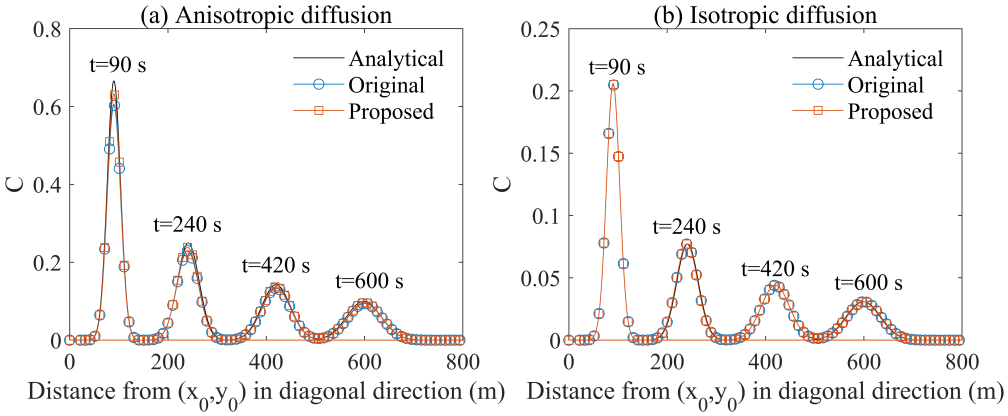

Figure 2.9: Development of scalar concentration profile in the diagonal direction (a) $P_e = 3.23$ and (b) $P_e = 1.0$

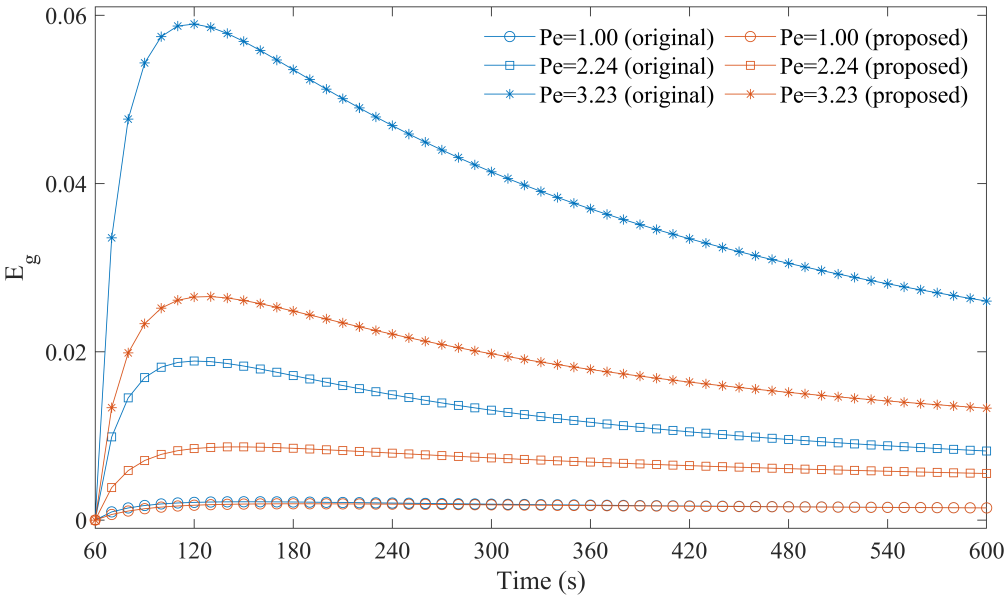

Figure 2.10: Global relative error as a function of simulation time

2.3.5 2D Advection in a Rotating Flow

A circular scalar patch in a 2D rotating flow field is considered to examine the numerical schemes. We assume a square water tank of 80 m × 80 m with a

constant depth of 1 m where the friction effect is ignored. The flow velocity field over the model domain is defined as follows:

$$u(x,y,t) = -\frac{2\pi}{360}(y-40),\ v(x,y,t) = \frac{2\pi}{360}(x-40), \tag{2.57}$$

which represents a clockwise rotating flow field around $(x,y) = (40\text{ m}, 40\text{ m})$, with a rotation period of 360 s. Additionally, the initial conditions of the scalar concentration are defined as

$$c(x,y,0) = \begin{cases} 1, & \text{if } (x-20)^2 + (y-40)^2 \leq 7^2, \\ 0, & \text{otherwise.} \end{cases} \tag{2.58}$$

The diffusion terms, like 1D scalar advection problem, are omitted in this problem. A uniform grid size of 0.8 m is used in the x- and y- directions to discretize the computational domain. The total simulation time is 360 s, which is equivalent to one rotation period.

Figure 2.11 compares the numerical and analytical solutions along two cross-sections: (a) $y = 40$ m and (b) $x = 20$ m, respectively. The peak concentration at $t = 360$ s is not maintained in the original scheme. The original scheme has an error of approximately 18% at the peak scalar concentration. However, the proposed scheme successfully prevents numerical damping, and reduces numerical diffusion near the discontinuities of the scalar concentration distribution, but shows asymmetry of the numerical diffusion in the flow direction. While the original scheme is uniformly dissipative in all directions, the proposed scheme

exhibits a more dissipative effect in the windward direction than in the leeward direction. Additionally, the global relative errors of the numerical solutions are 0.51 for the original scheme and 0.35 for the proposed scheme. These results show that the proposed scheme can significantly reduce the numerical diffusion during scalar transport, even in non-uniform flows.

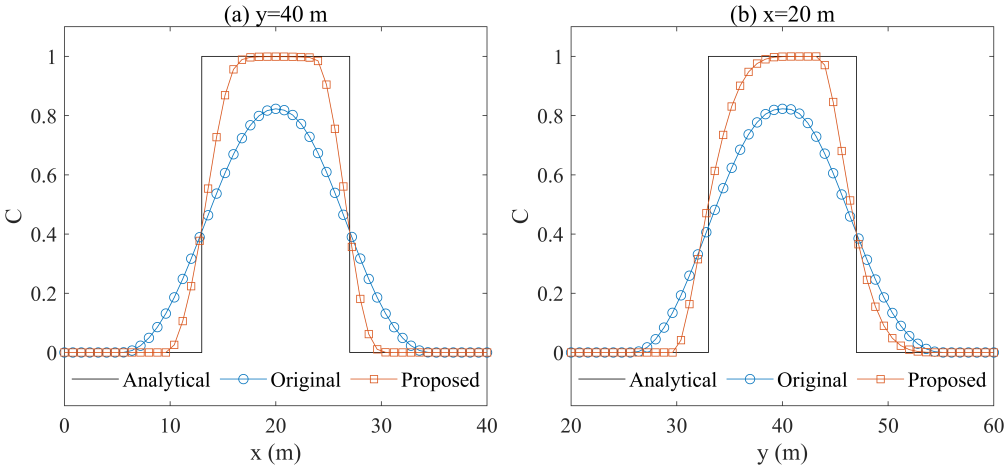

Figure 2.11: Scalar concentration comparisons at $t = 360$ s in a 2D rotating flow: (a) $y = 40$ m and (b) $x = 20$ m

2.3.6 2D Advection in a Cyclogenesis Flow

The final test deals with scalar advection governed by a two-dimensional cyclogenesis flow field [62]. The numerical domain is 8×8 m^2 and a uniform grid size of $\Delta x = \Delta y = 0.01$ m is used to discretize the model domain. The water depth is constant 1 m over a flat, smooth, and frictionless bottom topography,

and the initial conditions governing the flow velocity field are defined as

$$
\begin{aligned}
&p = \operatorname{sech}^2(r)\tanh(r),\\
&\omega(x,y) = \frac{p}{d\max(p)},\\
&u(x,y) = -\omega y, v(x,y) = \omega x,
\end{aligned}
\tag{2.59}
$$

where p is the tangential velocity around the center $(x, y) = (0, 0)$ and $\max(p) = 0.385$ is the maximum tangential velocity. The distance from the center is $r = \sqrt{x^2 + y^2}$, and ω is the frequency. The analytical solution for the scalar concentration in this problem is as follows:

$$
c(x,y,t) = -\tanh\left\{\frac{y}{2}\cos(\omega t) - \frac{x}{2}\sin(\omega t)\right\}, \tag{2.60}
$$

Following Eq. 2.60, the initial condition for the scalar concentration is defined as

$$
c(x,y,0) = -\tanh\frac{y}{2}. \tag{2.61}
$$

The scalar diffusion coefficient is set to zero to avoid scalar diffusion. A total of 641,601 computational cells are constructed using a uniform grid size and the total simulation time is 12 s.

Figure 2.12 shows time evolution of the scalar transport induced by the cyclogenesis flow field obtained using the proposed scheme. The computed results show a vortex of scalar concentration gradually develops over time without significant numerical damping of the scalar concentration. Figure 2.13 shows the

predicted scalar concentration profiles at $t = 3, 6, 9$, and 12 s along the cross section at $y = 0$ represented by the black dotted line in Figure 2.12. The comparison shows that the differences between the analytical solution and the numerical solutions gradually increases over time. The global relative errors of the numerical solutions over the entire computational domain at $t = 3$ s are 5.01×10^{-4} for the original scheme and 4.96×10^{-4} for the proposed scheme. By $t = 12$ s, these errors increases to 2.2×10^{-2} and 8.9×10^{-3}, respectively. The difference in E_g between the two numerical schemes is found to increase from 5.28×10^{-6} at $t = 3$ s to 1.31×10^{-2} at $t = 12$ s. In addition, the maximum error of the scalar concentration is found at the point 0.7 m from the center of the scalar distribution. At $t = 12$ s, the analytical solution for the scalar concentration at this location is 0.33. In comparison, the value calculated using the original scheme is 0.21, corresponding to an error rate of 36.5%. When the anti-diffusion function is applied, it becomes 0.30, and the error rate reduces to 9.8%. This final numerical experiment also verifies that the proposed scheme is in satisfactory agreement with the analytical solution.

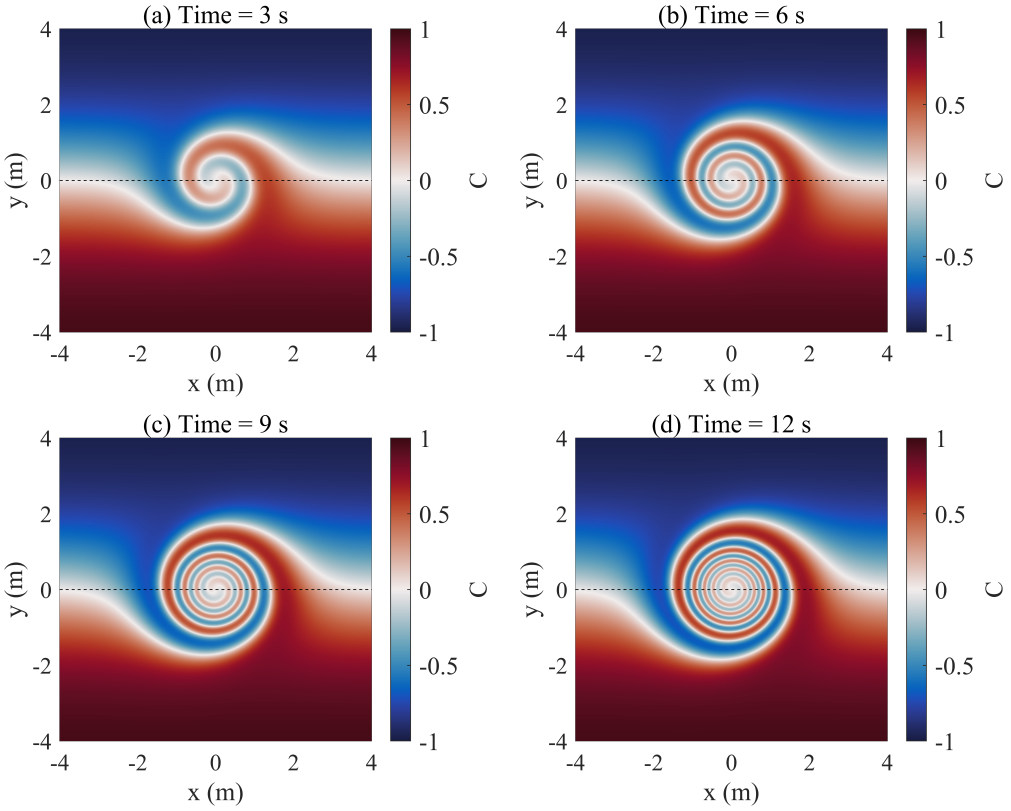

Figure 2.12: Time evolution of the modeled scalar distribution over the model domain at $t = 3, 6, 9$ and 12 s

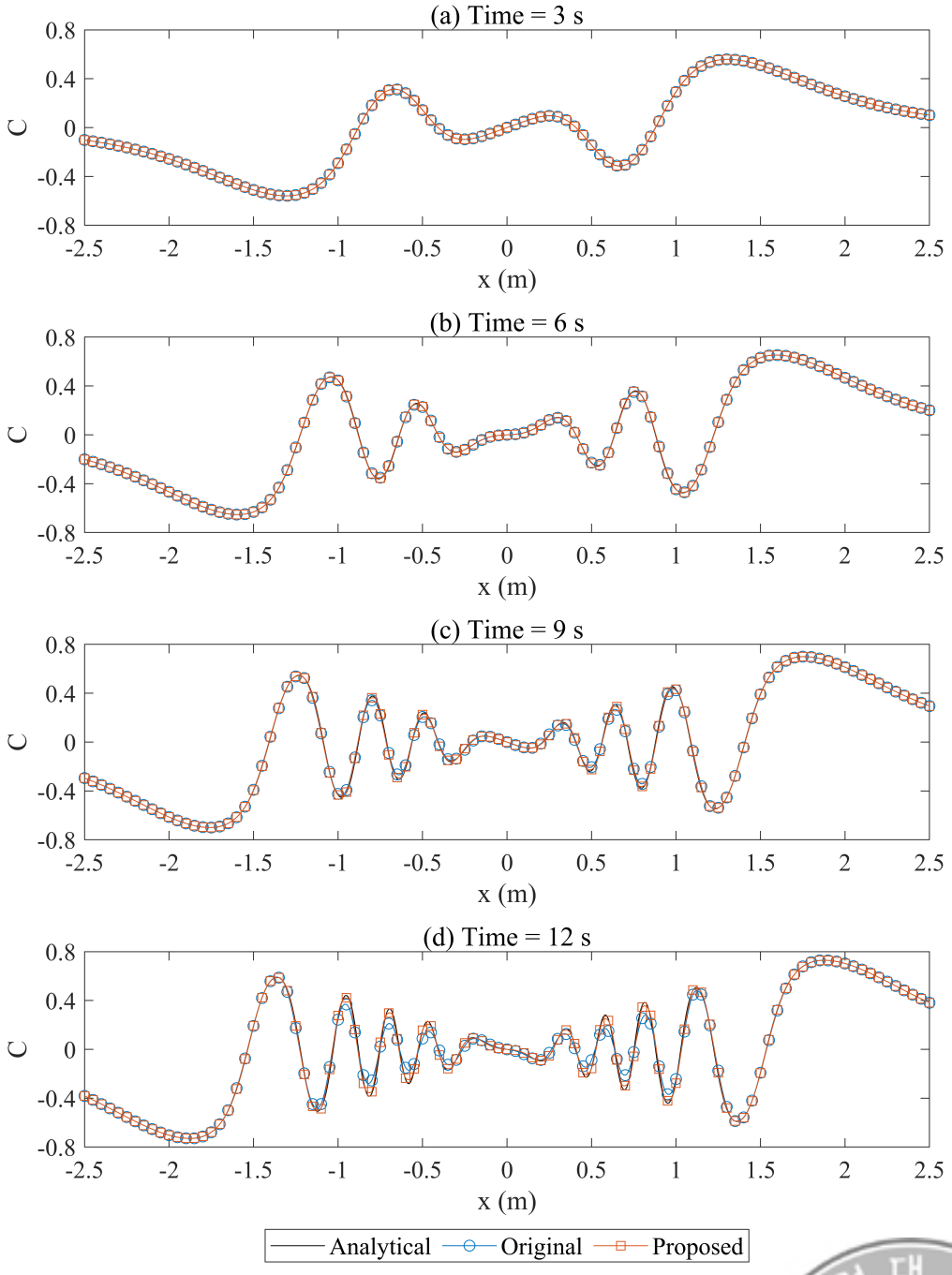

Figure 2.13: Scalar concentration profiles along the cross section at $y = 0$ at $t = 3, 6, 9$ and 12 s

2.4 Conclusions

An efficient numerical scheme for the Saint-Venant system governing scalar transport is proposed based on a hybrid finite volume - finite difference method. The Kurganov-Petrova scheme, commonly used for the SWEs, is employed to simulate both the hydrodynamic and scalar transport systems. Owing to its simplicity and robustness, the HLL Riemann solver is adopted to solve for the numerical flux across the discontinuity to achieve the precise approximation of the advective fluxes. An anti-diffusion modification is introduced in an ad hoc manner to minimize the numerical diffusion near contact discontinuities when solving the scalar transport problem. Time integration using the first-order Euler method theoretically confirms that the proposed scheme ensures non-negativity and the exact C-property for the scalar concentration as well as the water depth. The proposed model has been tested against the analytical solutions for several numerical experiments. Convergence analysis, the first case, guarantees that the proposed scheme is second-order accurate. The second test, considering pure scalar diffusion, verifies that the anti-diffusion function sufficiently reduces the numerical diffusion, making the proposed model suitable for the prediction of scalar diffusion. The third test investigating pure scalar advection shows that anti-diffusion modification is also essential for simulating scalar transport in a subcritical flow. In addition, the experiment involving the scalar advection-diffusion process shows that the proposed scheme is applicable for flows with a wide range of Peclet numbers. In particular, the use of the original scheme is confirmed to be inappropriate for scalar transport in flows where the relative importance of advection versus diffusion is significant. Other

numerical tests using non-uniform flows also verify that the proposed scheme is sufficiently accurate and robust for simulating scalar transport in various flow problems.

Chapter 3

A GPU-Accelerated Scalar Transport Model Based on Boussinesq-Type Equations

A GPU-accelerated scalar transport model based on the Boussinesq-type wave solver called Celeris Advent is proposed. The depth-integrated advection-diffusion equation was combined into Celeris Advent, a firstly-developed open-source Boussinesq wave model equipped with an interactive system supporting simultaneous visualization and data exchange between a user and the computing unit. A hybrid finite volume-finite difference scheme was still used for the numerical consistency, but the modified HLL Riemann solver for preserving the stationary steady state of the scalar as well as mass was adopted for the calculation of advective flux. A simple formula of wave breaking and corresponding eddy viscosity terms are implemented in the model to consider physical dissipation and turbulent mixing within breaking waves. Several benchmark cases were performed to validate the model. Two numerical experiments in the 1D and 2D problems were used to validate the accuracy of the model against the analytical solutions. Besides, two benchmark tests were simulated and vali-

dated against the experimental data. The solitary wave propagation over the complex bathymetry evaluated the accuracy of not only the scalar transport model but also the wave breaking model. The computed results showed good agreement with the observed data for all cases. Finally, field-scale experiments were reproduced through the numerical simulation, which accessed the performance of the model for pollutant transport prediction in nearshore regions.

3.1 Introduction

The understanding of scalar transport mechanism in coastal engineering is of importance for various applications including oil spills [e.g. 63, 64], contaminant spills [e.g. 65, 66], and algal blooms [67]. The growth in both pollutant emissions to the ocean and the contaminant spill accidents by human activities are aggravating the marine ecosystem, and the exacerbation of ocean weather conditions due to global warming makes it even more unpredictable. Since pollutant transport is dominated by ocean currents, ocean hydrodynamics and nearshore dynamics contribute to the prediction of pollutant transport as well as flow. Since field observation of scalar transport using drafters and dyes [e.g. 68, 69, 70] is limited due to cost and relatively narrow research scope, numerical modeling [e.g. 71, 72] is one of the common approaches to investigate the flow and the scalar transport within the ocean. An integrated model solving the nonlinear shallow water (NLSW) equations and the depth-averaged advection-diffusion equation may be a practical choice for predicting shallow water flow and scalar transport. This coupled model has the advantage of high computa-

tion speed and model robustness with acceptable accuracy and has been widely used for a variety of long-wave applications such as tides [e.g. 73, 74], storm surges [e.g. 45, 5], and tsunamis [75]. However, the application of the coupled model is limited to non-dispersive long waves because NLSW equations are derived from the hydrostatic pressure and the wave nonlinearity. Therefore, despite high computational efficiency, NLSW equations are inappropriate for nearshore dynamics since the dispersive effects of the waves have an important role.

As NLSW equations' counterparts, Boussinesq-type equations are mainly used to derive a more accurate approximation rather than efficient computation because they can consider the dispersion of waves. This is because frequency dispersion is no longer negligible, but rather as important in determining phase speed as water depth in solving the Navier-Stokes equations. Boussinesq equations also can consider relatively short waves from deeper water due to non-hydrostatic pressure. They make Boussinesq equations more essential for the investigation of nearshore dynamics where nonlinear, dispersive effects and complex bathymetry are included. However, additional consideration of the higher-order dispersive terms contributes to a rise in computational cost and a reduction of model stability. Also, implicit methods embedded to guarantee the model stability increase the amount of computation more, which aggravates computational efficiency. This inevitably required special computational techniques such as parallel processing using hundreds of both CPU and GPU cores. Tavakkol and Lynett [52] developed the open-source wave simulation software called Celeris Advent which solves Boussinesq equations

using GPU. To achieve high computation speed, Celeris Advent uses a hybrid finite volume-finite difference scheme which guarantees the robustness of the finite volume method (FVM) and high accuracy simultaneously to solve the governing equations.

For the development of the scalar transport model, Celeris Advent was used as a hydrodynamic model and the advection-diffusion equation was coupled with the Boussinesq equations. Since Celeris Advent resolves wave propagation in two-dimensional horizontal space, a depth-integrated advection-diffusion equation was adopted. The hybrid discretization used in Celeris Advent was adopted to solve the advection-diffusion equation, retaining a consistency of numerical schemes. However, the HLL Riemann solver, applied to advective terms, is suitable only for the hydrodynamic model and has the problem of producing excessive numerical dissipation when used in the advection-diffusion equation without any deformation. Therefore, the modified method introducing the anti-diffusion function proposed by Hwang and Son [76] was applied.

The outline of this chapter is as follows. Boussinesq model (Celeris Advent) and the scalar transport model are briefly described with their applied numerical scheme in Section 3.2. Besides, the wave breaking model and a few boundary conditions newly implemented to Celeris Advent are introduced in Section 3.2. Quantitative comparisons of analytical and numerical scalar transport for model validation are discussed in Section 3.3. Section 3.4 focuses on the qualitative comparisons of observed and computed dye transport through the lab- and field-scale benchmark tests with wide-varying flow conditions and complex bathymetry. Finally, conclusions are discussed in Section 3.5.

3.2 Numerical Model

3.2.1 Governing Equations

Celeris Advent [52] which solves the extended Boussinesq equations derived by Madsen and Sørensen [77] is adopted as a hydrodynamic model. A detailed information of the governing equations in Celeris Advent is provided in Tavakkol and Lynett [52]. Celeris Advent considers nonlinear and dispersive effect of waves, and bottom friction based on the theoretically derived physical law. However, numerical dissipation caused by using minmod limiter plays a role in energy dissipation due to wave breaking. Restricting gradient using flux limiters can mimic physical dissipation, but there are limitations to physical discussions through results, especially in areas with large turbulent kinetic energy, such as surf zones. Hence, a simple formulation using eddy viscosity [78] was employed for the consideration of momentum reduction due to wave breaking to account for the energy transformation process from wave energy to turbulent kinetic energy. In addition, the depth-averaged advection-diffusion equation is solved together to simulate scalar transport by shallow water flows.

Therefore, the governing equations are given by

$$
\begin{aligned}
&\frac{\partial h}{\partial t}+\frac{\partial hu}{\partial x}+\frac{\partial hv}{\partial y}=0\\
&\frac{\partial hu}{\partial t}+\frac{\partial}{\partial x}\left(hu^2+\frac{gh^2}{2}\right)+\frac{\partial huv}{\partial y}+ghz_x+\psi_1+f_1+hR_{bx}=0\\
&\frac{\partial hv}{\partial t}+\frac{\partial huv}{\partial x}+\frac{\partial}{\partial y}\left(hv^2+\frac{gh^2}{2}\right)+ghz_y+\psi_2+f_2+hR_{by}=0\\
&\frac{\partial hc}{\partial t}+\frac{\partial huc}{\partial x}+\frac{\partial hvc}{\partial y}-\frac{\partial}{\partial x}\left(Kh\frac{\partial c}{\partial x}\right)-\frac{\partial}{\partial y}\left(Kh\frac{\partial c}{\partial y}\right)\\
&\qquad -C\delta\left(x-x_s\right)\delta\left(y-y_s\right)=0
\end{aligned}
\tag{3.1}
$$

where h is the total water depth. t is the time. u and v are the depth-averaged flow velocities along with x and y coordinates, respectively. c is the depth-integrated scalar concentration. g is the gravitational acceleration coefficient. z_x and z_y are the bottom elevation gradient along with x and y directions, ψ_1 and ψ_2 are the modified dispersive terms and f_1 and f_2 are the bottom friction terms [52]. K is the diffusivity coefficient involving molecular diffusivity K_0 and breaking wave eddy diffusivity K_{br}, which becomes equal to the eddy viscosity (ν) by setting the Schmidt number to 1. C is the source/sink term in scalar concentration at some location (x_s, y_s) due to dye release, oil spill, and so on. δ is the Kronecker delta function. R_{bx} and R_{by} are the additional eddy viscosity

terms due to wave breaking defined as

$$
\begin{aligned}
R_{bx} &= \frac{1}{h}\left(\frac{\partial}{\partial x}\left(\nu\frac{\partial}{\partial x}(hu)\right) + \frac{1}{2}\frac{\partial}{\partial y}\left(\nu\frac{\partial}{\partial y}(hu)\right) + \frac{1}{2}\frac{\partial}{\partial y}\left(\nu\frac{\partial}{\partial x}(hv)\right)\right) \\
R_{by} &= \frac{1}{h}\left(\frac{\partial}{\partial y}\left(\nu\frac{\partial}{\partial y}(hv)\right) + \frac{1}{2}\frac{\partial}{\partial x}\left(\nu\frac{\partial}{\partial y}(hu)\right) + \frac{1}{2}\frac{\partial}{\partial x}\left(\nu\frac{\partial}{\partial x}(hv)\right)\right)
\end{aligned}
\tag{3.2}
$$

where the eddy viscosity ν is calculated by using a wave breaking model, which is described in Section 3.2.3

3.2.2 Numerical Scheme

Celeris Advent uses a hybrid finite-volume/finite-difference scheme in solving the governing equations to simultaneously satisfy high accuracy and model robustness. The governing equations are recast in terms of the water surface elevation $w := h + B$, following the approach in Kurganov and Levy [54]. The bottom elevation B is assumed to remain constant over time. Discretization based on a second-order well-balanced positivity preserving central-upwind scheme [48] (hereafter KP07) enables advective terms to be solved with the finite volume method. KP07 preserves stationary steady states and guarantees the positivity of the computed water depth under discontinuous bottom topography. In 1D case, the central-upwind numerical fluxes H_{i*} at the interface $x = i*$ between grid points $x = i$ and its neighboring cell $(x = i+1)$ discretized

by KP07 is given by

$$H_{i*}(t) = \frac{a_{i*}^{+} F\left(U_{i*}^{-}, B\left(x_{i*}\right)\right) - a_{i*}^{-} F\left(U_{i*}^{+}, B\left(x_{i*}\right)\right)}{a_{i*}^{+} - a_{i*}^{-}} + \frac{a_{i*}^{+} a_{i*}^{-}}{a_{i*}^{+} - a_{i*}^{-}}\left(U_{i*}^{+} - U_{i*}^{-}\right) \tag{3.3}$$

where $a_{i*}^{\pm}$ are local speed from each direction (+: right,-: left) calculated as the largest and the smallest eigenvalues of the Jacobian $\partial F/\partial U$. U is the conservative variable term and F is the advection term, which are given by

$$U = (w, hu, hc)^T$$
$$F(U, B) = \left(hu, \frac{(hu)^2}{w - B} + \frac{g}{2}(w - B)^2, huc \right)^T \tag{3.4}$$

The central finite difference method discretizes the rest of the terms including eddy viscosity terms. A detailed information of the numerical scheme applied to Celeris Advent can be found on Tavakkol and Lynett [52].

Unlike mass, scalar concentration can be over-dissipated when approximating the numerical flux by using Eq. 3.3 since it can cause excessive diffusion even at the stationary state over the flat topography. Thus, Hwang and Son [76] proposed an anti-diffusion modification method to preserve the stationary steady state of the scalar concentration by introducing a dimensionless function in the last term of Eq. 3.3. Thus, the advective terms are discretized by using

the modified central-upwind method [76]. The modified scheme is given by

$$H_{i*}(t) = \frac{a^+_{i*}F\left(U^-_{i*}, B\left(x_{i*}\right)\right) - a^-_{i*}F\left(U^+_{i*}, B\left(x_{i*}\right)\right)}{a^+_{i*} - a^-_{i*}} + \vartheta\left(\tilde{F}_r, \epsilon\right)\frac{a^+_{i*}a^-_{i*}}{a^+_{i*} - a^-_{i*}}\left(U^+_{i*} - U^-_{i*}\right) \tag{3.5}$$

where non-dimensional anti-diffusion function $\vartheta\left(\tilde{F}_r, \epsilon\right)$ is defined as

$$\vartheta\left(\tilde{F}_r, \epsilon\right) = \frac{\tilde{F}_r + \epsilon}{\tilde{F}_r + 1} \tag{3.6}$$

in which

$$\tilde{F}_r = \frac{1 + \mathrm{sign}(u')}{2}\frac{u^+}{\sqrt{gh^+}} + \frac{1 - \mathrm{sign}(u')}{2}\frac{u^-}{\sqrt{gh^-}} \tag{3.7}$$

where $\epsilon = 10^{-4}$ is a numerical parameter to control the amount of the artificial diffusion at the stationary state. u' is the magnitude difference in the reconstructed flow velocities at the cell interface and $\mathrm{sign}(x)$ is the symbol function which is given by

$$\mathrm{sign}(x) = \begin{cases} 1, & x \geq 0, \\ -1, & x < 0. \end{cases} \tag{3.8}$$

Diffusive terms are discretized simply by using a central finite difference

scheme, which is the same method as source terms except for the bottom slope term in the governing equations.

3.2.3 Wave Breaking

Wave breaking is implemented in Celeris Advent by introducing a simple eddy viscosity formulation [78] representing the turbulent mixing and physical dissipation caused by wave breaking. The implement of the wave breaking model in Celeris Advent eliminated the necessity to employ the minmod limiter to imitate the physical dissipation due to wave breaking, which led the use of the minmod limiter to be optional. The eddy viscosity ν is given by

$$\nu = B_b \delta_b^2 h \frac{\partial h}{\partial t} \tag{3.9}$$

where δ_b is the dimensionless mixing length coefficient. B_b is the linear proportional factor varying between 0 and 1 that indicates a continuous change in kinetic energy reduction during wave breaking event, which is given by

$$B_b = \begin{cases} 1, & \dfrac{d\eta}{dt} > 2\dfrac{d\eta^*}{dt}, \\ \dfrac{d\eta/dt}{d\eta^*/dt} - 1, & \dfrac{d\eta^*}{dt} < \dfrac{d\eta}{dt} \leq 2\dfrac{d\eta^*}{dt}, \\ 0, & \dfrac{d\eta}{dt} < \dfrac{d\eta^*}{dt}, \end{cases} \tag{3.10}$$

where η is the free surface elevation. The parameter η^* determines the initiation and termination of wave breaking. The evolution of η^* was estimated based

on a linear assumption and used three parameters to account for the temporal decrease of the wave breaking threshold after wave breaking initiated, which is given by

$$\frac{d\eta^*}{dt} = \begin{cases} \dfrac{d\eta^{(F)}}{dt}, & t \geq T^* \\ \dfrac{d\eta^{(I)}}{dt} + \dfrac{t - t_0}{T^*}\left(\dfrac{d\eta^{(F)}}{dt} - \dfrac{d\eta^{(I)}}{dt}\right), & 0 \leq t - t_0 < T^* \end{cases} \tag{3.11}$$

where T^* is the transition time. t_0 is the time when breaking began. $d\eta^{(I)}/dt$ is the initial threshold value for the initiation of wave breaking and $d\eta^{(F)}/dt$ is the last threshold value remaining until the end of the wave breaking after the transition time of the beginning of the wave breaking. Since the values assigned for these parameters are not derived from physical theory, it is necessary to estimate appropriate parameters through result comparisons with experimental measurements.

3.2.4 Boundary Conditions

The latest released version of Celeris Advent included five types of boundary conditions: sinusoidal wavemaker, random directional irregular wavemaker, Dirichlet boundary condition using time series data, fully reflective solid wall, and sponge layer. Two types of boundary conditions are implemented in Celeris Advent: internal wave generation and periodic boundary condition.

Internal Wave Generation

Internal wave generation is implemented in Celeris Advent to minimize the effects of a reflected wave exiting the model domain. Sufficient consideration for offshore propagating wave has not been made when the two layers of the ghost cells located at the model boundary generated the waves. However, waves can be gradually attenuated until the wave that passes through the internal wavemaker reaches the boundary by placing the sponge layer behind the internal wavemaker. Following Wei et al. [79], a source-function internal wavemaker is considered and the modified mass conservation is as follows

$$\frac{\partial w}{\partial t} + \frac{\partial hu}{\partial x} + \frac{\partial hv}{\partial y} = f(x, y, t) \tag{3.12}$$

where $f(x, y, t)$ represents mass source function wavemaker and can be expressed in two functions according to the independent variable of space-time coordinates.

$$f(x_\alpha, x_{1-\alpha}, t) = G(x_\alpha, x_{\alpha_W M}) F(x_{1-\alpha}, t) \tag{3.13}$$

where subscript α denotes spatial coordinates such as cross-shore $\alpha = 0$ and alongshore $\alpha = 1$ directions. Since mass source function wavemaker can be applied in both horizontal directions, spatial coordinates are expressed by using tensor notation. $x_{\alpha_W M}$ is the centerline of the wavemaker. $G(x_\alpha, x_{\alpha_W M})$ is a function that determines the width of the wavemaker with respect to the wavelength and spatial energy distribution along the cross-shore direction.

$G(x_\alpha, x_{\alpha_W M})$ is a time-invariant function which simply manipulates the spatial distribution because time is not a variable.

$$G(x_\alpha, x_{\alpha_W M}) = \begin{cases} exp\left(-\beta\left(x_i - x_{i_W M}\right)^2\right), & x_i - x_{i_W M} \geq W \\ 0, & x_i - x_{i_W M} < W \end{cases} \tag{3.14}$$

where β is a shape parameter to control the energy reduction rate with respect to the distance from the centerline. W is the width of mass source function wavemaker and is given by

$$W = \frac{1}{2}\delta\lambda \tag{3.15}$$

where δ is a dimensionless wavemaker width and λ is a characteristic wavelength. Unlike $G(x_\alpha, x_{\alpha_W M})$, alongshore wavemaker source function $F(x,t)$ is time-dependent and given by

$$F(x,t) = \sum_i D_i \sum_j d_{ij} \cos\left(k_y^{(ij)} y - \omega_i t\right) \tag{3.16}$$

where subscript i, j correspond to frequency and direction, respectively. D_i is the frequency-dependent coefficient. d_{ij} is the directional weight factor. Alongshore wavenumber $k_y^{(ij)} = k_i \sin\theta^j$ where k^i is the wavenumber corresponding to the frequency ω^i and θ^j is the jth wave angle. Φ_{ij} is uniformly randomly distributed phase along the direction θ^j at the same frequency ω^i.

Periodic Boundary Condition

Periodic boundary condition allows the physical quantity in the numerical domain that passed through one side to appear on the opposite side in order to preserve the total amount in the system. Celeris Advent has two layers of ghost cells on each side for boundary condition, along with $nx \times ny$ computational grids. The ghost cells on one side must equal the interior cell ahead of the boundary cell of the computational grid because the interior boundary cells on both sides must be equal to each other under the periodic boundary condition. If the entire model domain including the multiple layers of ghost cells is $(nx + 4) \times (ny + 4)$ grid, The first and second grid points corresponding to the ghost cells should be assigned values of points n and n+1, respectively. Artificial treatment should be conducted in the wave direction when the irregular wave conditions and periodic boundary conditions were used simultaneously. As mentioned above, in the periodic boundary condition, ghost cells imitated the interior cell next to the boundary cell on the opposite side in order to equalize the information that the boundary cell on both sides had. However, since irregular wave boundary conditions force the grid points to enter the specified value with respect to the time and space, unintended oscillation occurs at the corners of the model domain when wave direction is not manipulated artificially. Therefore, the wave direction should be adjusted so that the wavenumber and the alongshore length of the wavemaker are integer multiples. A more detailed procedure about this treatment was described in Suanda et al. [80].

3.3 Numerical Validations

3.3.1 Pure Advection in a 1D Dam Break

A scalar advection in the 1D idealized dam break problem [81] is considered. A dam is located at the 10 m downstream of the inlet of a frictionless flume with 50 m in length. The flume is divided into upstream and downstream regions according to its relative position with the dam, and two static states are imposed on the each side. The upstream state ($0 \leq x \leq x_0$) is defined by water depth $h_u = 1.0$ m, flow velocity $u_u = 2.5$ m/s and scalar concentration $c_u = 1.0$. The downstream state ($x_0 \leq x \leq 50$) is characterized by water depth $h_d = 0.1$ m, flow velocity $u_d = 0$ m/s and scalar concentration $c_d = 0$. The diffusion coefficients and the eddy viscosity are set to zero. The grid size of 0.05 m is adopted to discretize the numerical domain.

The result comparisons between the analytical and numerical solutions at $t = 7$ s are shown in Figure 3.1. A negligible amount of spurious oscillations in water depth and flow velocity due to the shock are captured at a point downstream of 10 m from the dam. However, the computed results show good agreement with the analytical solution without any significant errors in the presence of the discontinuities in the water depth, flow velocity and scalar concentration. Therefore, the results confirm that the present model is able to resolve sharp discontinuities without significant numerical oscillations in the vicinity of steep gradient.

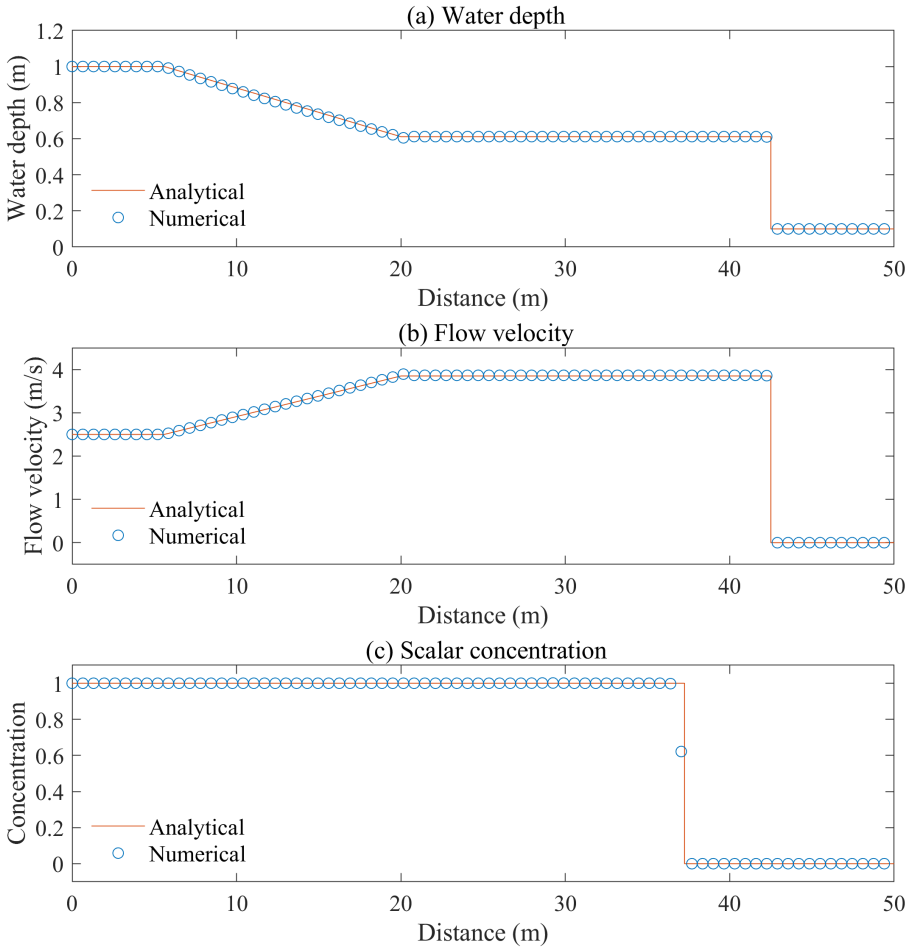

Figure 3.1: Comparison of the analytical solution with the compuated (a) water depth, (b) flow velocity and (c) scalar concentration at $t = 7$ s

The performance of the GPU implementation in comparison to the CPU is measured by the comparison of computational speed using the CPU and GPU, respectively. The time for main scripts of solving governing equations and visualizing results except for model initialization and variable declaration is measured. Yuan et al. [82] noted that it is fairly challenging to verify the competitive advantage of GPU acceleration over GPU, given that the compu-

tations are based mostly on the hardware, algorithm and computational load. Following Yuan et al. [82], we investigate the efficiency of the GPU acceleration by running the dam break case at several grid resolutions. Here, an Intel Core 3.1 GHz i9-9900 processor is employed for CPU computation and an Intel Core 3.7 GHz i7-8700k processor and NVIDIA Geforce GTX 1070 Ti are used for GPU computation. Different numbers of computational cells for x- direction (N_x) are set as follows: 100, 200, 400, 800, 1600, 3200, 6400. The number of cells for y- direction is fixed as 5, thus the domain size can be expressed as $5N$. For simplicity, the governing equations for hydrodynamic systems switches to nonlinear shallow water equations by neglecting dispersive terms. The time step is constrained based on the Froude number in order to maintain a constant CFL number.

Table 3.1 compares the CPU and GPU computation times for different grid resolutions. When $N_x = 100$, computation time using CPU (T_{CPU}) took 0.61 and computation time using GPU (T_{GPU}) took 0.48 s. Thus, the speedup factor, ratio between T_{CPU} and T_{GPU}, was about 1.27. As the grid resolution refines, the difference between T_{CPU} and T_{GPU} increases. When $N_x = 6400$, T_{CPU} was about 20 mins, whereas T_{GPU} is 27 s. Besides, the speedup factor rises to approximately 46. These results imply that the GPU-accelerated numerical model becomes more attractive as it requires heavier computational nodes (e.g., high-resolution grids, dispersive effects).

Table 3.1: Comparison of computation times for different computational cells

Unit	The number of computational cells in x- direction						
	100	200	400	800	1600	3200	6400
CPU	0.61	1.94	6.00	19.56	75.20	284.71	1218.12
GPU	0.48	0.62	1.41	2.55	5.18	10.53	26.68

3.3.2 Combined Advection and Diffusion in a 2D Rotating Flow

Model validation is expanded to a scalar transport in a two-dimensional flow velocity field. The second case is the combined scalar advection and diffusion in the 2D rotating flow with a constant angular velocity ω. A square water tank of 100 m $\times$ 100 m where friction effect can be ignored has a constant depth of 1 m, and the flow velocity field over the model domain is defined as

$$u(x,y,t) = -\frac{2\pi}{360}(y-y_0), \quad v(x,y,t) = \frac{2\pi}{360}(x-x_0), \tag{3.17}$$

which represents a clockwise rotating flow around $(x_0, y_0) = (50, 50)$ and the rotation period is 360 s. Thus, the angular velocity is $\omega = 0.017$. A Gaussian distribution is adopted for the scalar concentration. An analytical solution for the combined advection and diffusion process of the Gaussian distribution in a 2D rotating flow is given by Wang et al. [83] as follows:

$$c(x,y,t) = \frac{2\sigma^2}{4\gamma t + 2\sigma^2} \exp\left(-\frac{(\bar{x}-x_c)^2 + (\bar{y}-y_c)^2}{4\gamma t + 2\sigma^2} \right) \tag{3.18}$$

where $\bar{x} = x\cos(\omega t) + y\sin(\omega t)$ and $\bar{y} = -x\sin(\omega t) + y\cos(\omega t)$. The standard deviation is $\sigma = 3.5$, the isotropic diffusion coefficient is $\gamma = 0.05$ and a center of the initial Gaussian distribution is $(x_c, y_c) = (25, 50)$. Following Eq. 3.18, The initial scalar distribution can be expressed by

$$c(x, y, 0) = \exp\left(-\frac{(\bar{x} - x_c)^2 + (\bar{y} - y_c)^2}{2\sigma^2}\right) \tag{3.19}$$

The total number of 40,401 computational cells using a uniform grid size of 0.5 m for both $x-$ and $y-$axis were constructed. Total simulation time is 360 seconds equivalent to the rotating period.

Figure 3.2 compares the computed results with the analytical solutions at $t = 360$ s. Figure 3.2 (a) showing the contours of the numerical and analytical solutions confirms that the computed results agree well with the exact solutions overall. The maximum scalar concentration at $t = 360$ s in Figure 3.2 (b) is 0.253 as an exact solution and it is calculated as 0.254, which shows an error of about 0.5%. Hence, the present model is expected to investigate the scalar transport under complex two-dimensional flow fields.

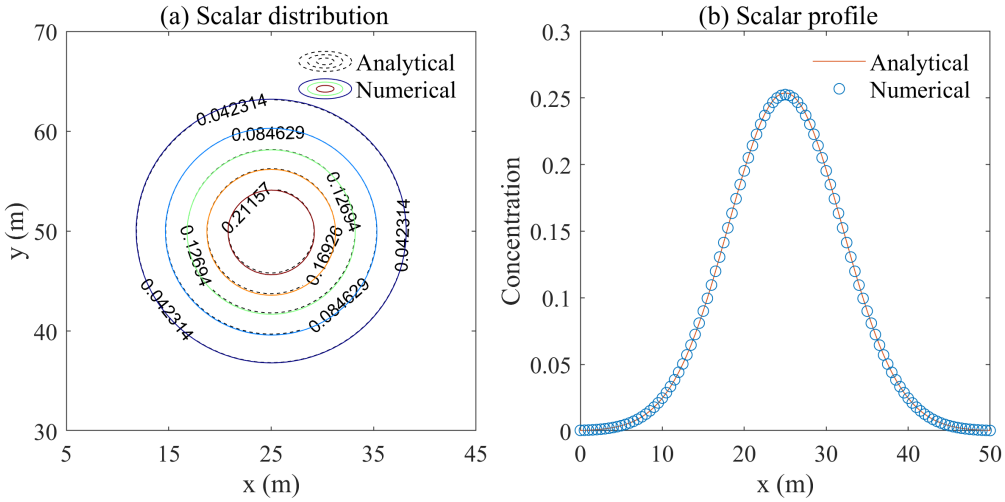

Figure 3.2: Scalar concentration comparison at $t = 360$ s. (a) Contours of scalar concentration and (b) scalar profile along the cross section $y = 0$

3.4 Model Applications

3.4.1 Development of Vortex Shedding in the Wake behind a Submerged Island

As a first benchmark test to validate the present model qualitatively, we dealt with the experiment investigating a vortex shedding in the wake behind a submerged conical island conducted by Lloyd and Stansby [84] (hereafter LS97). LS97 studied various vortex formations in the wake according to the design conditions of submerged conical islands under shallow water flow. LS97 also performed a dye release experiment to trace the vortex structure's generation process and vorticity pattern visually. This experiment and the result dataset have been used widely for numerical validation by many studies [30, 85, 86].

The experiment domain consists of a flume and the conical model island. The flume is 9.75 m in length and 1.52 m in width. The conical island located at 5.00 m downstream of the inlet and centerline in width has various model geometry options according to side slope angle θ. Two particle tracking velocimetry (PTV) gauges, one located at the center of the flume and the other 0.27 m away from the center in width, are deployed at 1.02 m behind the island (see Figure 3.3). We choose theta at 8.0° among 33.1, 22.2, 12.6, and 8.0°. The base diameter of the conical island is 0.75 m, which is half the width of the channel. Also, the upper plane of the conical island has a diameter of 5 mm. The flume and the island were designed to have spatially uniform surface roughness. Finally, our benchmark case is set to SB4_02 in LS97: Mean velocity $U_0 = 0.115$ m/s; Water depth $h = 0.054$ m; Ratio of the water depth to the island height $h/h_i = 1.10$; Figure 3.3 depicts the model bathymetry and gauge location in LS97. The model grid size of 0.015 m was adopted uniformly to the $x-$ and $y-$axis. The model domain is 9.75 m in length and 1.52 m in width, which is identical to the flume size.

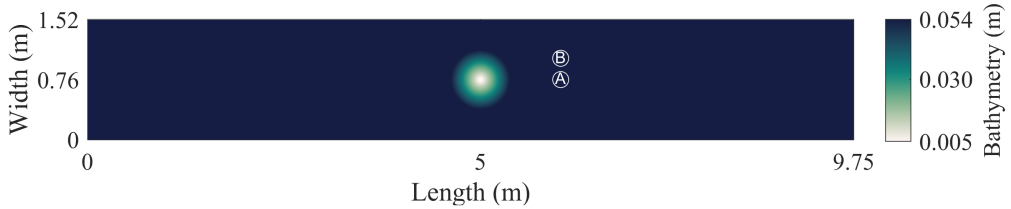

Figure 3.3: Model bathymetry and the location of PTV gauges in LS97

While the Manning's roughness coefficient recommended by LS97 is 0.01 $s/m^{1/3}$, the majority of researchers found that a larger value was necessary [86]. Lynett et al. [86] summarized the numerical models, grid resolutions,

bottom friction models and friction coefficients used by modelers for this numerical experiment. Manning's n value ranging from 0.01 to 0.02 $s/m^{1/3}$ was adopted. The BOSZ model solving the weakly nonlinear Boussinesq equations with similar numerical approach as the present model adopted $n = 0.02$ $s/m^{1/3}$ with the grid resolution of 0.015 m. In the present study, the same friction coefficient ($n = 0.02$) was employed as the optimal value. The upstream boundary condition is set to generate a steady discharge the open boundary condition is imposed on the downstream.

Figure 3.4 shows a comparison of surface velocities at gauges A and B between the modeled result and the observed data. The results at the two gauges agree well with the observed data for the v velocity, although the u velocity shows an error between the observed and the modeled results. These errors are found larger at gauge A, located at the centerline of the flume, than gauge B, located away from the centerline. These results represents that the vortex shedding is well generated by the development process of a complex vortex structure created while a constant flow field passes through a three-dimensional structure, but the wake behind the three-dimensional structure is not sufficiently reflected. Such results were commonly shown in many previous studies such as LS97 and Zhang et al. [85] where LS97 was tested by using the depth-averaged model.

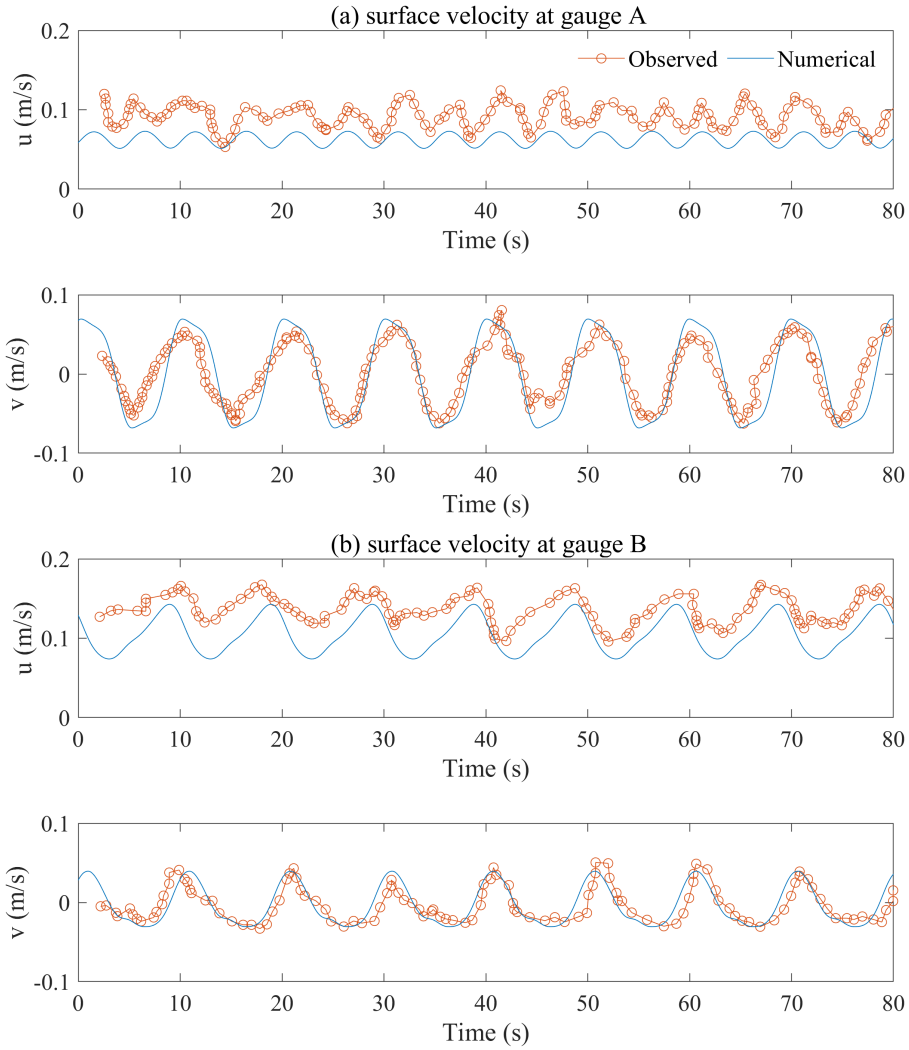

Figure 3.4: Comparisons of surface flow velocities at (a) gauge A and (b) gauge B

Figure 3.5 shows the development of vortex shedding behind the submerged island in different times. The vorticity appears as a straight line in the downstream direction in the early stage of the wave development. However, it gradually turns into a meandering formation over time (see Figures 3.5 (b)~(c)).

Finally, the vortex formation is fully developed after 200 seconds. Therefore, the computed results are analyzed after 200 s once mean square vorticity equilibrated.

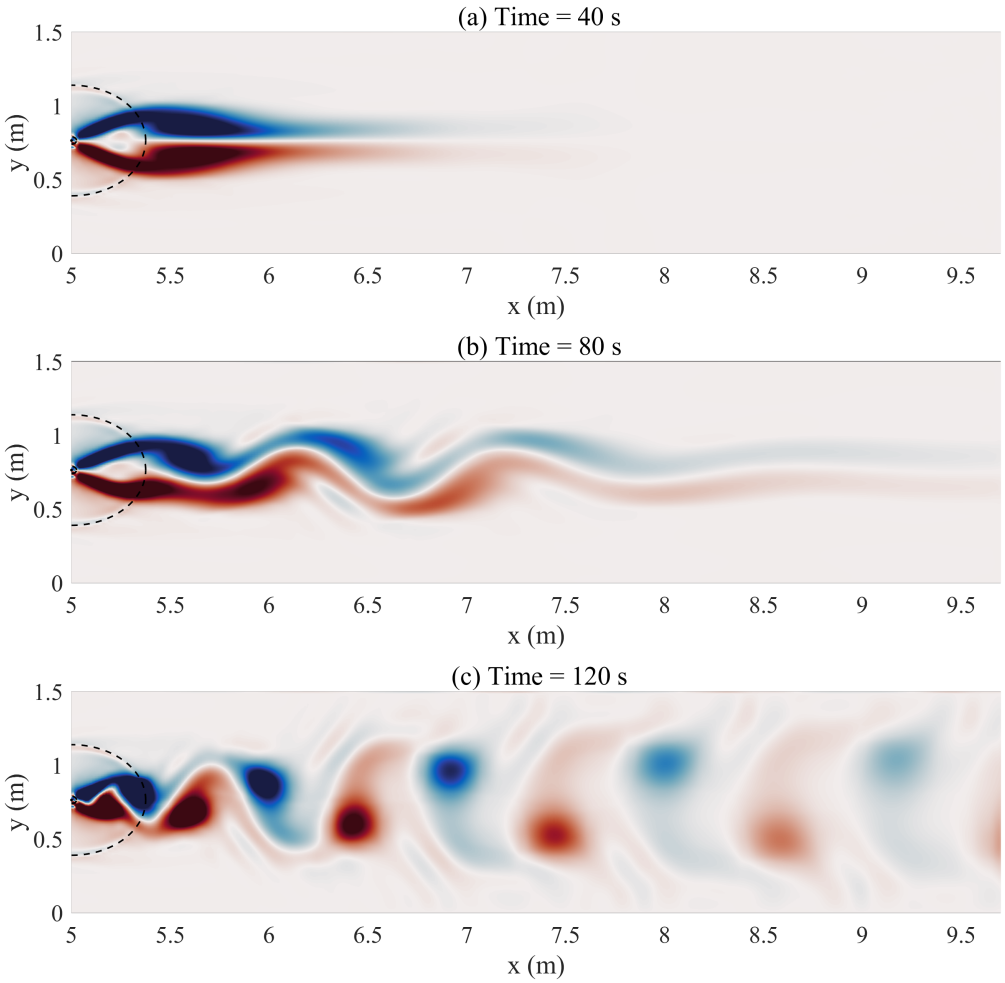

Figure 3.5: Temporal evolution of vortex shedding behind the island in different times

The simulated results for the LS97 experiment is shown in Figure 3.6. The 2D coherent structures behind the submerged island are well generated. The scalar concentration is governed by these structures, hence the patterns of vor-

ticity and scalar concentration are comparable. The computed results of the velocity field and dye transport agree well with the observations in LS97 experiment (see Figure 3.7). Therefore, the LS97 experiment was well reproduced in numerical simulation, although it didn't use a fully matched condition due to the limitation of the depth-integrated model.

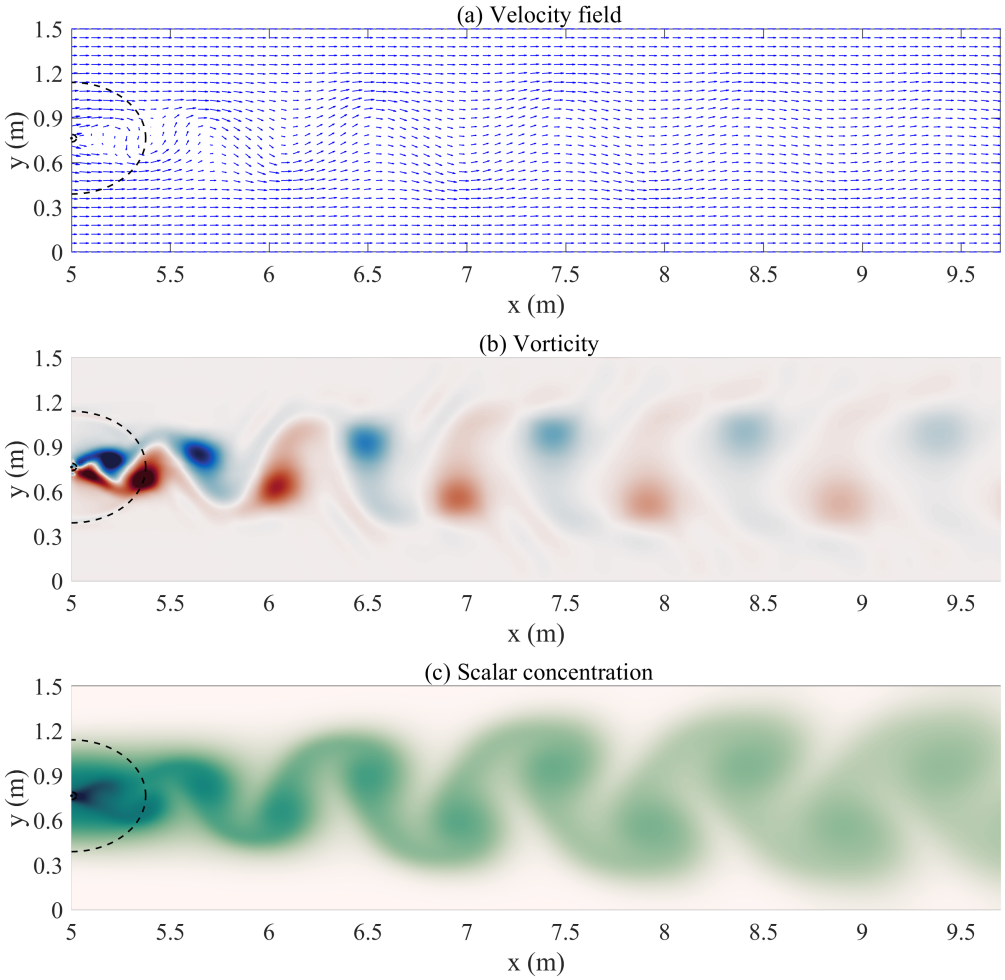

Figure 3.6: The results of (a) velocity field, (b) vorticity and (c) scalar concentration behind the island

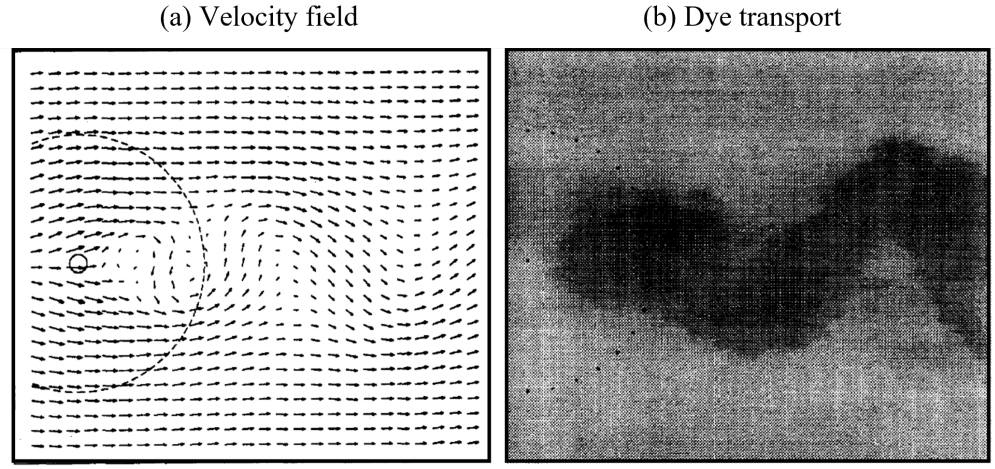

Figure 3.7: Experimental data from LS97. (a) Flow velocity field and (b) dye transport (reprinted from Lloyd and Stansby 1997)

3.4.2 A Breaking Solitary Wave Runup on a Slope with a Conical Island

The second benchmark test dealt with Lynett et al. [87] experiment (hereafter LP19), which has more complicated bathymetry within its experiment domain. LP19 studied kinematic changes of a breaking solitary wave propagating over the three-dimensional shelf installed in an irregular shallow water bathymetry. LP19 examined three-dimensional turbulence caused by various experimental conditions such as the bathymetry complexity and the wave breaking and tried to broaden the understanding of three-dimensional hydrodynamics through this experiment. LP19 also performed a dye experiment continuously released at a fixed location to identify the advection and dispersion process visually. Many previous studies where the Boussinesq model was employed [e.g. 88, 89, 53]

computed this experiment to validate the accuracy of the model. The experiment domain involves a channel where the length is 48.8 m, the width is 26.5 m and the maximum water depth is 0.78 m with a conical island. With $X = 0$ m, a wavemaker is located and a flat bottom gradient continues to $X = 10.20$ m. A three-dimensional shelf with a steep depth gradient and y-axis symmetry is located from $X = 10.20$ m to $X = 25.5$ m. Water depth at the apex located at $X = 12.6$ m is 0.07 m. Then, a planar beach with mild slope extends to $X = 31$ m, and the bottom profile intersects the still water level at $X = 25.75$ m. Finally, the conical island with a radius of 3.0 m and a height of 0.45 m is located at $X = 17.0$ m. The experiment observed the transport of the dye released at a fixed point in the wave propagation process by generating a solitary wave with 0.39 m of wave height in the channel. A total of 14 resistance-type, wire wave gauges (rWGs) and 5 ultrasonic wave gauges (usWGs) were used to measure a temporal change of the free surface elevation as solitary wave propagated over the three-dimensional shelf. Among the total number of 19 measurement devices, observations from 9 rWGs were used for numerical validation, and the locations of gauges 1 9 are as follows: (7.5,0.0), (7.5,5.0), (13.0,0.0), (13.0,5.0), (21.0,0.0), (21.0,5.0), (25.0,0.0), (25.0,5.0), (25.0,10.0). Figure 3.8 shows the experiment setup which depicts the basin, the bathymetry, and the rWGs locations. The dimensionless friction coefficient for the quadratic friction formula was considered as 0.0025. Further details on the experiment are provided in LP19. The model domain was constructed with a total number of 531×265 grids using 0.1 m grid size for both $x-$ and $y-$axis.

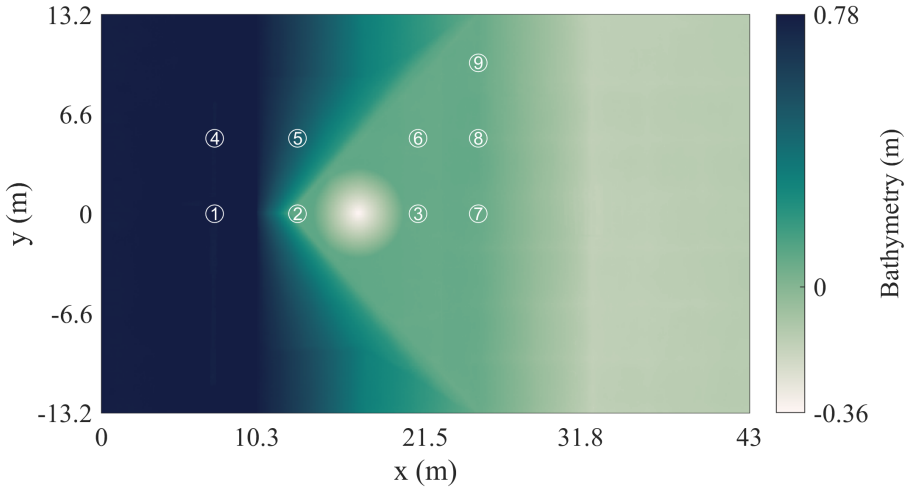

Figure 3.8: Model bathymetry and gauge locations in LP19

Figure 3.9 shows the comparison between the computed and observed water levels at 9 gauges during solitary wave propagation. The navy blue and yellow solid lines represent the computed results using the minmod limiter and the wave breaking model, respectively. Also, the orange solid line represents the observed water level in LP19. As mentioned, numerical dissipation through the minmod limiter scheme mimicked physical dissipation since the wave breaking was not implemented in Celeris Advent. However, the wave breaking using the eddy viscosity is implemented in the model, so the results computed by each model were quantitatively compared. The results of two methods were very similar to those of the observations, but in case of maximum water level at each gauge, the breaking model was closer to the observed data than the minmod limiter. Two simulation results were almost identical at gauges 1, 2, 4, and 5, located before the wave breaking zone and where the solitary wave did not break yet. However, the difference between the two methods gradually

widened as the solitary wave approached the shoreline. At gauge 3, complex hydrodynamic process induced by wave breaking, hydraulic jump and bore formation around the island makes both methods At gauges 6, 7, 8, 9 installed behind the surfzone, the maximum water level decreased by 4.8, 7.6, 7.6, 4.1%, respectively, as the wave breaking model was applied instead of the minmod limiter. This result indicates that a complex flow characteristics of a wake behind the conical island were reproduced well as the wave breaking model was considered. In areas where the role of physical dissipation is of great importance, the use of the wave breaking model is more essential. Besides. the simulation results showed that the numerical dissipation by using the flow limiter scheme is no longer essential, but optional.

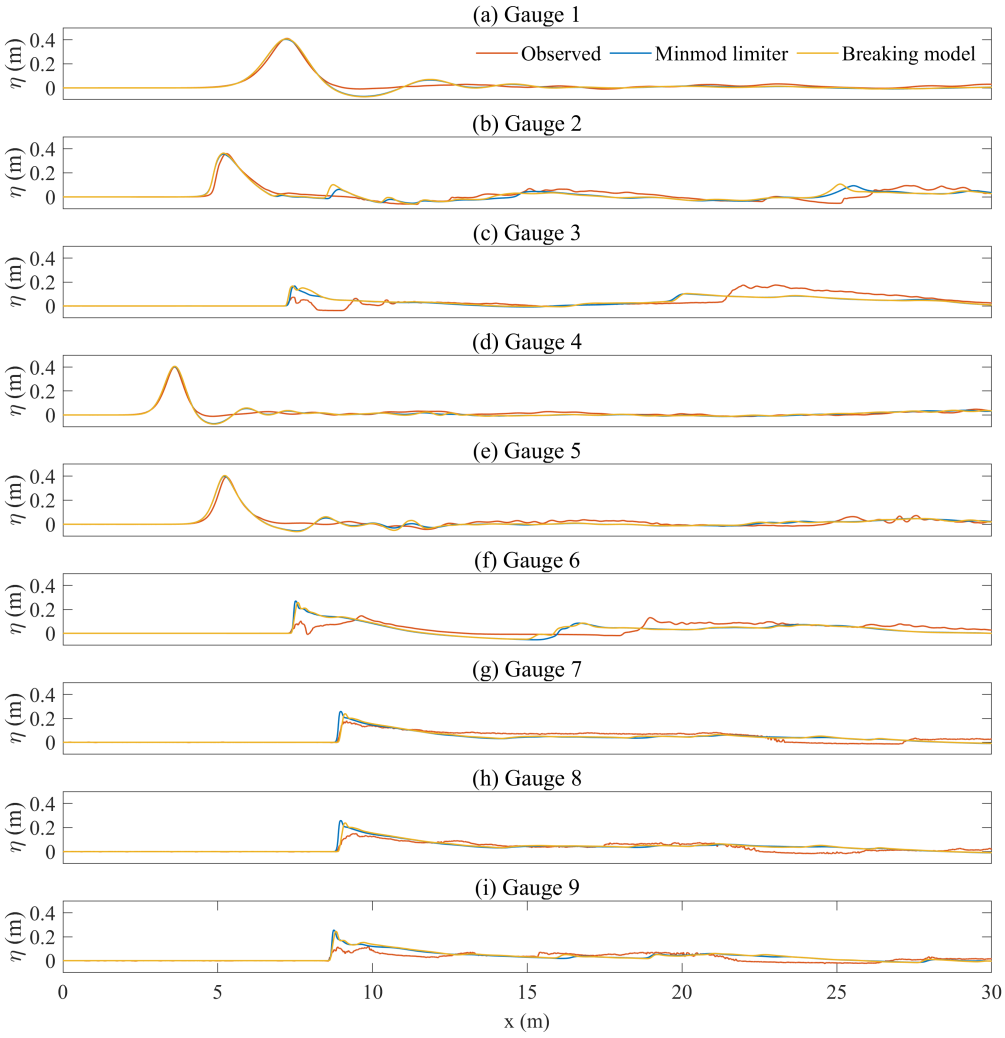

Figure 3.9: Free surface elevation comparison at gauges 1∼9. The black dashed line indicates the observed data from the LP19 experiment. Red solid and blue dashed lines indicate the simulation results using explicit and implicit methods, respectively

Figure 3.10 shows the dye transport comparison between LP19 experiment and the numerical results. The pictures on the left side of Figure 3.10 are the observed results of the dye release experiment performed by LP19, and

the description of white boxes that pointed out the hydrodynamic activities is provided in LP19. The white and black arrow indicate the onshore and offshore mean flow direction, respectively. Also, the figures on the right side of Figure 3.10 show the computed dye transport result. The ivory-colored area in the figures located on the right side of Figure 3.10 indicates the dye concentration is zero and the green-colored area refers to areas where dyes are present. Quantitative analysis is not available since the exact dye concentration was not measured in the dye release experiment by the LP19. Figure 3.10- (a) shows (1) observed and (2) computed result of dye release at 6.2 s. At 6.2 s, the solitary wave passed through the apex of the triangle shelf, and the wave started to break at the edge of the conical island. The dye remains stationary as the solitary wave did not propagate to the dye release point yet. Observed dyes were shown to be spread slightly due to molecular diffusion of the dye, but the computed dyes showed that initial concentration conserved without any deformation since the molecular diffusivity was not considered. Figure 3.10 (b) shows the results at 8 s when solitary wave passed through the dye release point. Due to the dominant onshore direction flow, the dye began to be transported toward the shoreline. After the propagation of the solitary wave through the conical island, the water level rose behind the island, and flow with offshore direction occurred at the onshore edge of the island. Besides, some of the water bodies, which propagated and ran up the slope, returned by restoring force. Therefore, the offshore flow began to grow behind the island. The offshore flow interfered with the onshore flow at 20 s, thus the dye is concentrated in the border area, as shown in Figure 3.10 (c). Then, the dye

was split into two parts and transported with the direction of each flow (see Figure 3.10 (d)). Overall, dye transport during the solitary wave propagation was well reproduced.

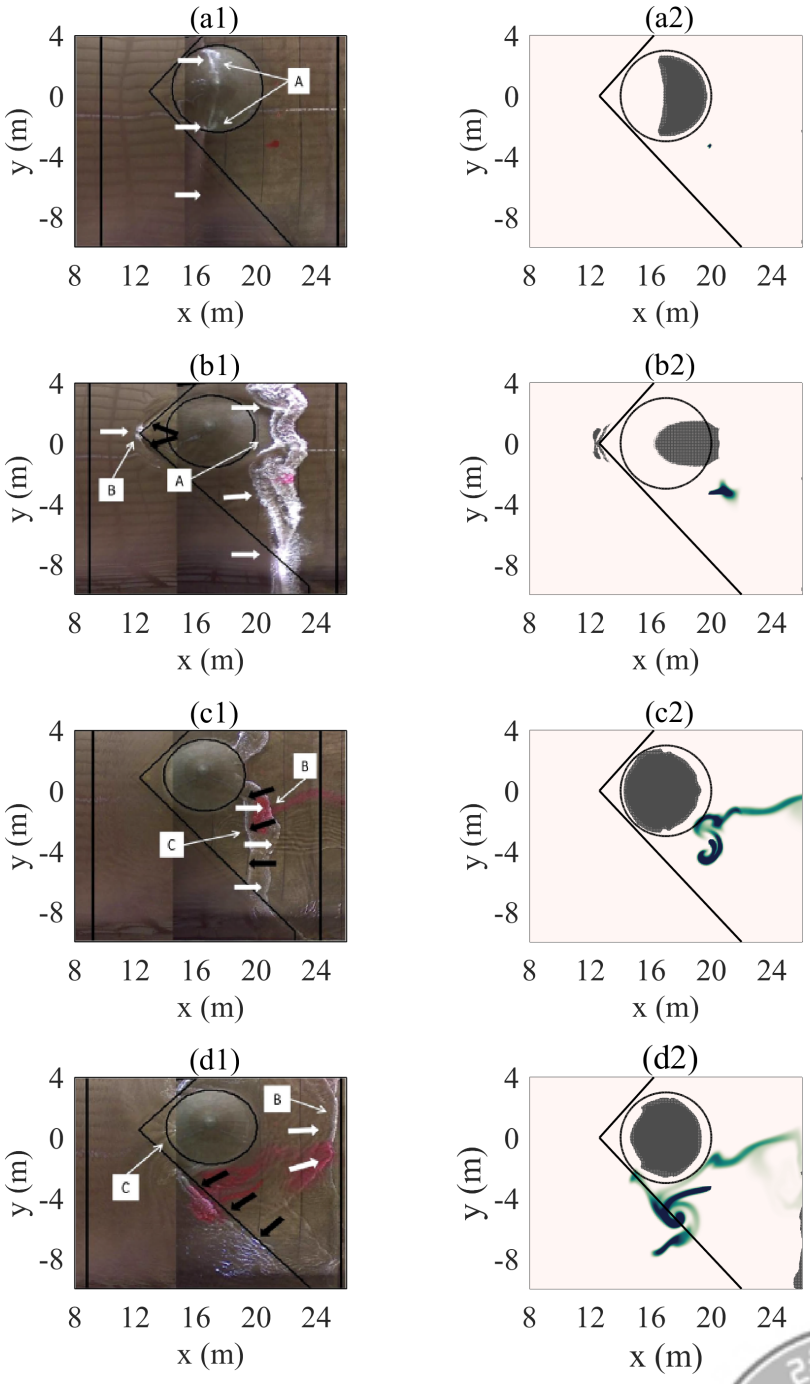

Figure 3.10: Dye transport comparison between (left) LP19 experiment and (right) the present model at (a) 6.2 s, (b) 8 s, (c) 20 s and (d) 27.4 s (reprinted from Lynett et al. 2019)

3.4.3 A Near-Shoreline Scalar Transport Forced by Wave-Breaking as well as Wind-Driven Currents

As a part of the Imperial Beach pollutant transport and dilution experiment conducted on 13 October 2009 (IB09), Hally-Rosendahl et al. [90] (hereafter HR15) performed a dye release experiment to investigate the complicated hydrodynamic processes within surf zone. Based on the field measurement, Hally-Rosendahl and Feddersen [91] (hereafter HF16) reproduced this field-scale dye release experiment by using a funwaveC model solving both the Boussinesq equations [92] and the advection-diffusion equation, and analyzed hydrodynamic phenomena in surf zones. The total model domain is 650 m in cross-shore direction (x) and 2,025 m in alongshore direction (y). The grid sizes are 1 and 1.35 m in $x-$ and $y-$directions, respectively. Thus, the model domain consists of 650×1500 grids with a time step of 0.01 s. Figure 3.11 shows the model domain and bathymetry used in this experiment, which was adopted in HR15 as well. The bathymetry is assumed alongshore uniform, which enables use to get rid of the effects of bathymetrically controlled rip currents. Six near-bottom frames were deployed on the 125 m long cross-shore direction at $y = 248$ m to measure the waves, currents and dye concentration.

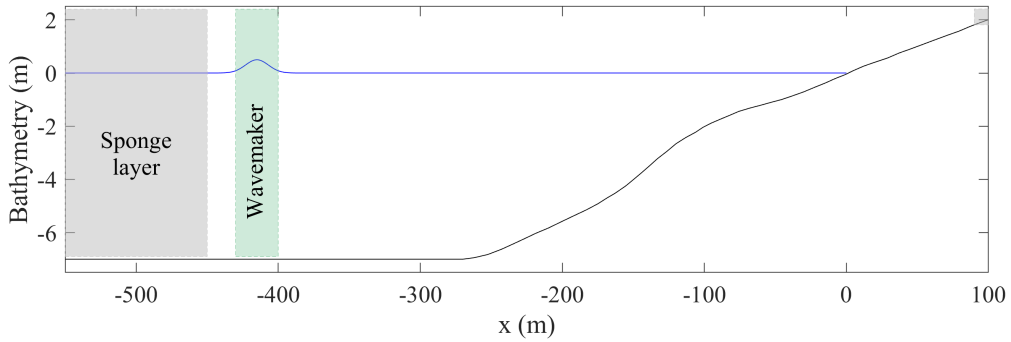

Figure 3.11: Model domain and bathymetry in HR15

A wavemaker with the length of 30 m in the offshore direction was installed on a flat region with a depth of 7 m. It generates a directionally spread random frequency wave spectrum [80] with 801 random frequencies ranging from 0.04 to 0.25 Hz. A sponge layer was installed at the offshore boundary to minimize the effects of the reflective waves from the shoreline. For the alongshore boundaries, periodic boundary condition was applied for surface water level and flow velocities and open boundary condition was used for scalar concentration. To avoid numerical errors due to the simultaneous use of irregular wave conditions and periodic boundary conditions, artificial treatment of wave direction with respect to wave frequency [80] was considered to satisfy the integer ratio of domain length and wave number. A dye with a constant discharge $Q = 512$ ppb m^3/s was released at (x, y) = (-10, 0) m. For the bottom friction, dimensionless friction coefficient for quadratic friction formula was considered as 2.25×10^{-3}. Besides, a constant wind drag coefficient of 8.5×10^{-5} m^2/s^{-2} in the alongshore direction (+y) was applied to account for the wind-driven currents as HF16 did.

During the IB09 dye release experiment, significant wave height and along-

shore velocity at six observation points are shown as a circle symbol in Figure 3.12. Besides, solid line represents the numerical results. The simulated alongshore velocity was underestimated in the inner-shelf, but good agreement was obtained in the surf zone. The simulated significant wave height showed a profile to the observed data with a slight underestimation within the surf zone. Overall, the wave and current conditions in the Imperial Beach were reasonably reproduced.

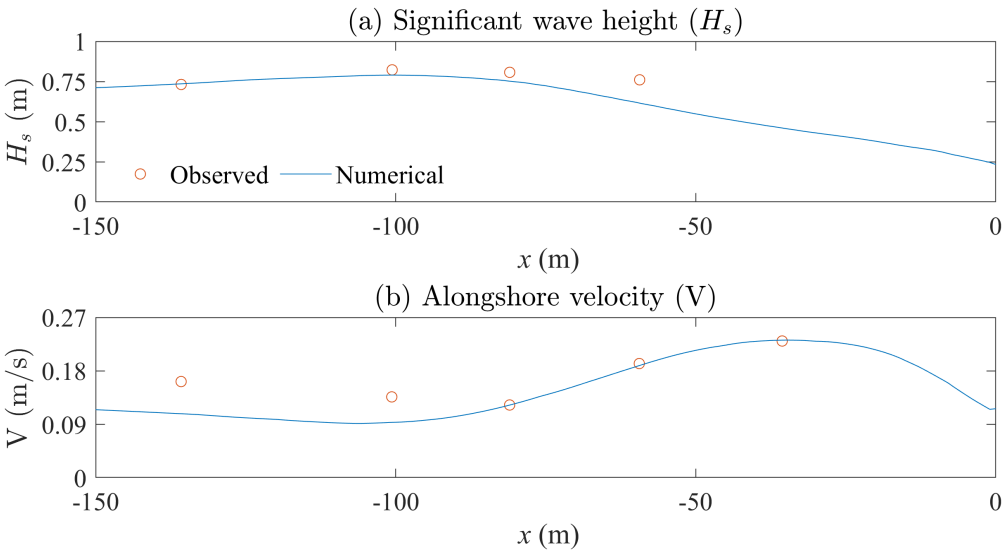

Figure 3.12: Comparisons of (a) significant wave height and (b) alongshore velocity perpendicular to a shoreline at $y = 248$ m

Figure 3.13 shows an aerial images of dye concentration at different times observed in HR15. The black color region indicated unspecified regions due to bubble from wave breaking. During the experiment, the dye was transported by various nearshore processes such as irregular waves, wind-driven currents and wave breaking. Especially, the cross-shore dye transport was driven by

the transient rip current which result from the wave breaking. The transient rip current induces a cross-shelf exchange from the surf zone to the inner-shelf. Thus, the dye was advected about 300 m offshore from the shoreline while it approached the alongshore boundary by the waves and wind-driven currents.

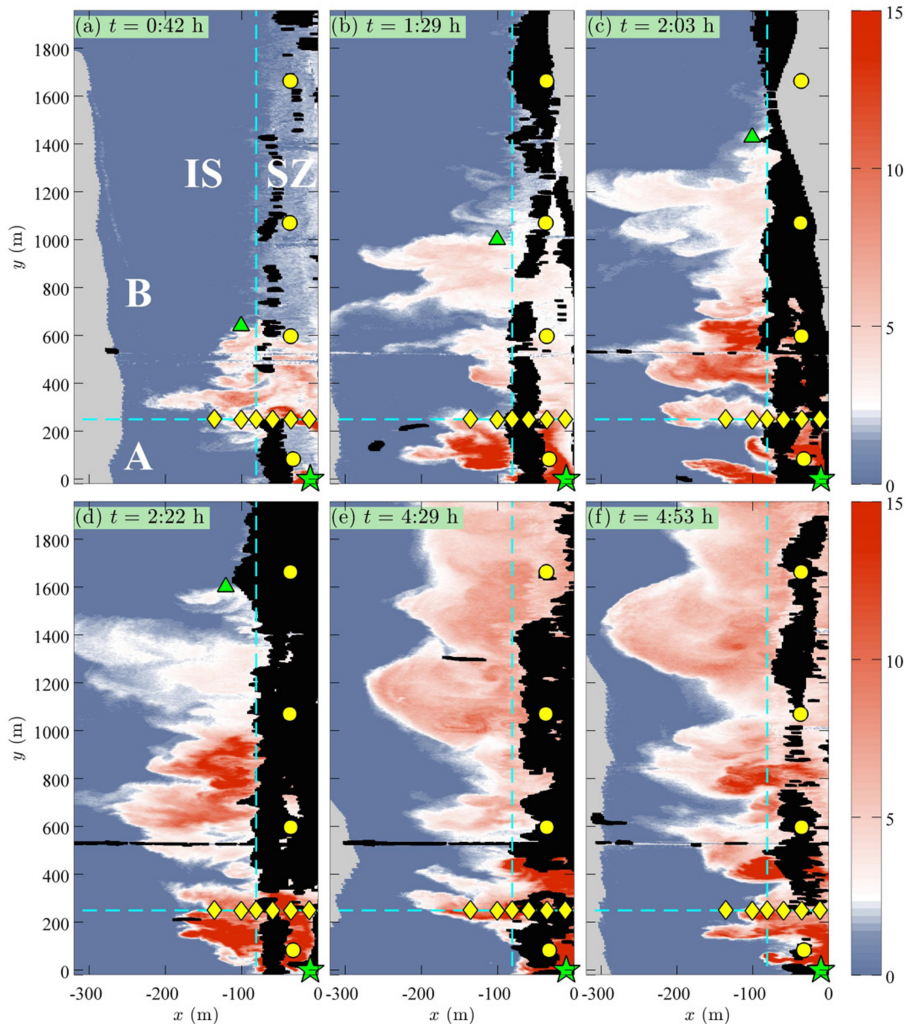

Figure 3.13: Aerial images of dye concentration from HF16 for IB09 experiment at different times. The cyan dashed line divides the inner-shelf and the surf zone (reprinted from Hally-Rosendahl and Feddersen 2016)

Figure 3.14 shows the simulated dye concentration distributions at different simulation times. it is difficult to accurately match the locations of the transient rip currents, caused by wave breaking, with these from the experimental data since the wave breaking occurs randomly due to the complex interaction of the irregular waves. Therefore, the reference simulation time was set as $t_r = 0:42$ h when the leading alongshore edge of the dye advected about 600 m, as shown in Figure 3.14 (a). The numerical results showed less diffusive distribution compared to the observations, which may result from the underestimation of the eddy viscosity calculated from the wave breaking model. The dye mixing within the surf zone can be better estimated through the parameter calibration of the wave breaking model. Nevertheless, the scalar transport in both cross-shore and alongshore directions shows good agreement with the observations. The comparison of leading alongshore edge of the dye, plotted in Figure 3.15, confirms that the alongshore dye advection was well simulated until the dye passed out the model domain. Besides, the dye ejection from the surf zone to inner-shelf by transient rip currents was accurately captured. Figure 3.16, showing the snapshot of vorticity distribution, captures the transient rip current developed from the surf zone to the inner-shelf. In summary, the results verify that the model can predict the hydrodynamic processes and the resulting scalar transport in the nearshore region.

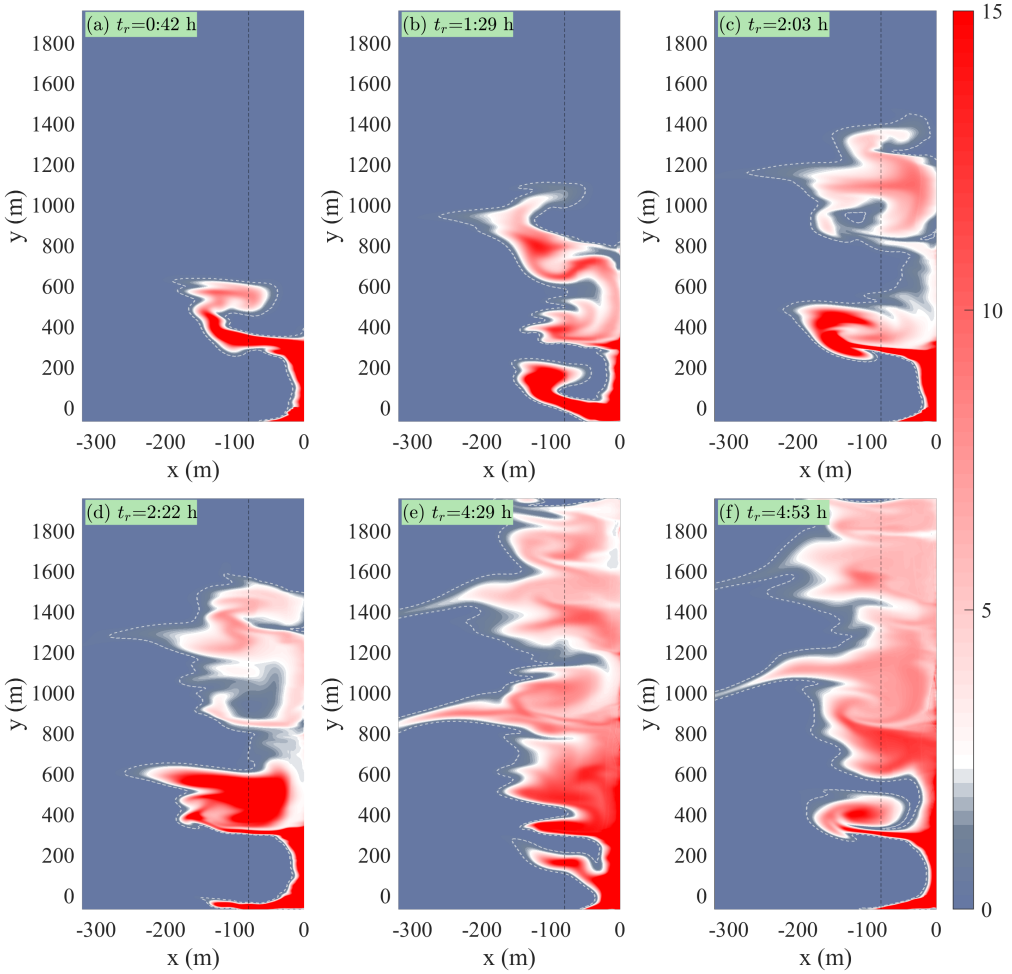

Figure 3.14: The simulated results of dye concentration at different times. The white dashed line represents a dye concentration more than 0.5 ppb

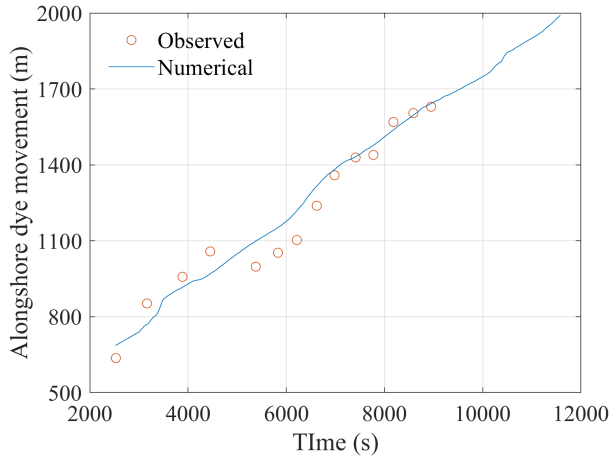

Figure 3.15: Comparison of leading alongshore edge of dye

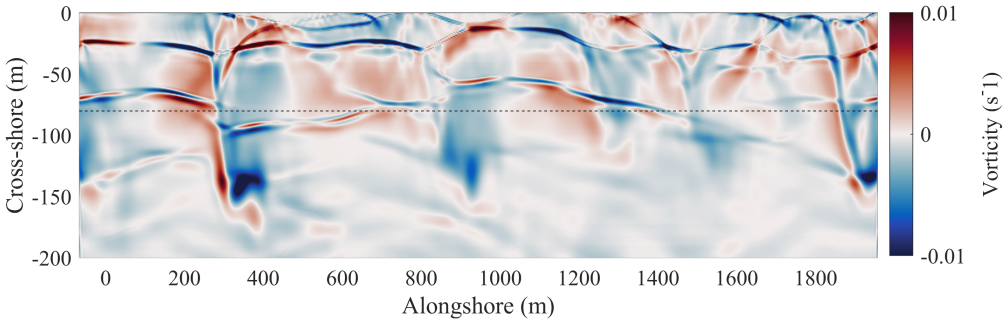

Figure 3.16: Snapshot of vorticity distribution over the Imperial Beach

3.5 Conclusions

A GPU-accelerated nearshore scalar transport model is proposed based on the Boussinesq-type nearshore wave solver, Celeris Advent. A modified numerical scheme using an anti-diffusion function to guarantee the conservation property for scalar concentration is employed instead of the original HLL Riemann solver. Besides, various boundary conditions applicable to different nearshore

problems are implemented in the model. Comparisons with two analytical solutions in one- or two-dimensional flow field validate the accuracy of the model. Furthermore, two laboratory-scale benchmark tests were performed to evaluate the model performance on the scalar transport in complex bathymetry and flow conditions. In the experiment investigating a breaking solitary wave runup on a slope with a conical island, the wave breaking model was validated against the experimental data, and the results confirmed that the consideration of physical dissipation using the wave breaking model showed a better approximation to the observed data than the numerical dissipation through the use of the minmod limiter. Finally, a field-scale dye release experiment in Imperial Beach was simulated to examine the applicability of the model in the nearshore region. We did our best to match the simulation environments within the limited available data. The simulation result showed that waves, wind-driven currents and transient rip currents occurring in the surf zones were reasonably reproduced by the model. Correspondingly, the dye transport, especially including dye advection from the surf zone to the inner-shelf by the transient rip currents due to the wave breaking, was well predicted.

Chapter 4

Virtual Reality-Based Hydrodynamic Rainfall-Runoff Model for Simultaneous Flood Simulation and Experience

Urban flood risk has been exacerbated due to various factors including global warming and urbanization. In order to minimize the flood risk, development of accurate, fast flood simulation model has been demanded and the importance of public awareness in flood risk has been highlighted. We introduce virtual reality-based hydrodynamic rainfall-runoff model which can simulate and visualize the flood in an immersive simulation environment simultaneously. The presented model solves the 2D nonlinear shallow water equations, including rainfall and infiltration terms in a continuity equation, to simulate rainfall-runoff process. An explicit approximation to the implicit GA model is employed to simulate infiltration. The governing equations are discretized using hybrid finite volume–finite difference method. Several numerical experiments with different rainfall, roughness and topography conditions were performed

to verify the accuracy of the presented model. The model is further applied to simulate historical rainfall event on the Goodwin Creek Experimental Watershed. Good agreement with the analytical solution or the observation was obtained. The model supports an immersive and interactive simulation environment where the user can travel around the simulation field in virtual reality and alter the terrain during the simulation. The model is expected to be helpful for flood education and advanced hazard mitigation strategy such as real-time countermeasures in case of flash flood.

4.1 Introduction

Storm-induced urban flooding has been a topic of interest since it causes disastrous damages such as human casualties, economic losses and industrial damages. Global warming leads to the intensification of extreme rainfall over various regions of the globe [e.g. 93, 94, 95, 96, 97], resulting in significant increase in extreme rainfall events [e.g 98, 99, 100, 101]. Urbanization, characterized by expansion in impervious area, increases runoff volume with the shorten peak time, which in turn aggravates flood risk [e.g. 102, 103, 104, 105]. More than half of the world population (approaching 8 billion people) resides in the urban area [e.g. 106, 107, 108, 109, 110] and this proportion is projected to rise up to 70 percent by 2050 [e.g 111, 112, 113]. Therefore, the exacerbated flood risk will threaten more and more urban residents [114].

The importance of public awareness in flood risk has been emphasized in recent studies [e.g 115, 116, 117]. Burningham et al. [115] pointed out that

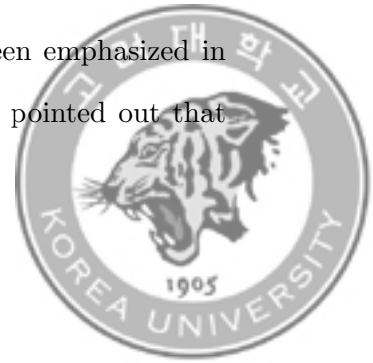

flood experience along with the length of time in residence is significant for public awareness of the flood risk. A lack of direct experience with the risk leads to underestimation of the possibility, thus people generally under-prepare for the flood. They also noted that the public with knowledge and experience of flood risk does not necessarily protect their poverty against the flooding. Similarly, Green et al. [118] mentioned that those who have experienced flooding or not tend to have common expectation that the future flood will replicate the past one, which possibly leads to the underestimation of the consequence of the extreme flood event. Thus, it is a challenge for experts and policy makers to inform people about the possibility of the extreme flood event and its devastating consequence, and raise the public awareness of future flood risk.

Virtual reality (VR) application to the disaster is a new technology that can be a useful strategy for training and educational purposes. The VR application enables users to reproduce a variety of hazardous scenarios, and people to experience these scenarios in a computer-generated realistic environment without risk [e.g 119, 120, 121, 122]. The performance of the VR training in terms of knowledge acquisition and retention, compared to the traditional methods, has been emphasized. Previous researches have proposed the VR applications of various fields including flood, fire [123], earthquake [124], storm surge [122] and so on [e.g 125, 126]. Sermet and Demir [117] proposed a VR framework, Flood Action VR, which visualizes a realistic three-dimensional environment with disaster scenarios. Fujimi and Fujimura [127] presented a VR application that encourages people to decide early evacuations from flash flood. However, historical data or simulation results are needed ahead of the VR simulation

since these applications are unable to produce the results, but only visualize the input disaster data passively.

Advances in graphical processor units (GPU) and VR technology enables real-time simulation of real-world physics and simultaneous visualization within affordable costs. There have been many efforts to achieve real-time numerical simulation of shallow flows using GPU [e.g 128, 129, 130, 82]. Tavakkol and Lynett [52] developed Celeris Advent, real-time interactive Boussinesq-type wave model. It solves the extended Boussinesq equations and visualizes the results simultaneously using GPU, which enables faster than real-time simulations. Tavakkol and Lynett [131] further developed Celeris Base as a successor to Celeris Advent. Celeris Base is an immersive nearshore wave simulation software which utilizes VR environment. It allows users who mount an VR device to jump into the numerical domain while the simulation is running. Thus, users can travel virtual world, which is updated every time step, and even interact with the environment using the VR controllers. This achievement motivates that the real-time flood routing VR simulation, standalone model without requiring the flood simulation results from other hydrodynamic or hydrological models, can be applicable.

The most appropriate method to automatically represent the rainfall-induced overland flows is to solve the two-dimensional (2D) nonlinear shallow water equations (NSWEs) since the 2D NSWEs describe dynamic processes of different overland flows, ranging from subcritical to supercritical, over natural or complex topography [132]. Various studies have proposed infiltration models of different degree of complexity to represent the infiltration mechanism, and

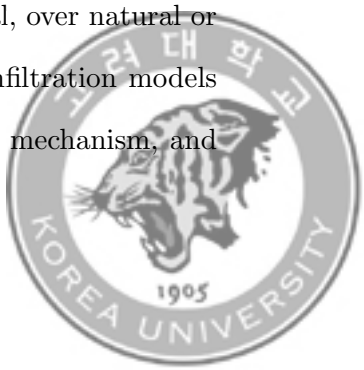

these models can be classified into three categories: (1) empirical, (2) semi-empirical, and (3) physically based models [133]. The empirical models [e.g 134, 135], derived from experimental data, use straightforward mathematical equation without any physical representation. The semi-empirical models [e.g 136, 137, 138, 139] adopt simplified expression of continuity equation and simple assumption of the relationship between the infiltration rate and cumulative infiltration [140]. The physically based models [e.g 141, 142, 143, 144], relying on the law of Darcy's law and mass conservation, employ mathematical expression which can fully describe the infiltration process whereas the empirical and semi-empirical models are restricted.

We aims to develop a VR-based interactive flood routing numerical model to simulate rainfall-induced overland flows over complex topography with different types of soil characteristics and land uses. The presented model is based on Celeris Base [131], but its governing equations reduce to the 2D NSWEs by neglecting the dispersive terms. Owing to its simplicity and accuracy, the explicit approximation to the Green-Ampt (GA) model, derived from [145], is adopted as the infiltration model. A hybrid finite volume-finite difference (FVM-FDM) scheme [52] is adopted to solve the governing equations. The interactive system that the users can alter the bottom topography using the VR controllers is implemented to enhance the model's interactivity. It enables users to simulate a dam or embankment failure or an installation of the disaster prevention structure, which can be represented by terrain change, while the model is running.

The remainder of this chapter is organized as follows. Section 4.2 introduces

mathematical model including governing equations, numerical model, rainfall-infiltration terms and VR application. Section 4.3 presents the simulation results of the analytical scale cases. Section 4.4 describes model application to historical rainfall event in natural watershed. Section 4.5 summarizes the conclusions.

4.2 Mathematical Model

4.2.1 Governing Equations

The conservative form of the 2D NSWEs, including rainfall and infiltration terms in a continuity equation, is solved to describe surface flow, which can be expressed as

$$\begin{aligned}
&\frac{\partial h}{\partial t}+\frac{\partial (hu)}{\partial x}+\frac{\partial (hv)}{\partial y}=r-f \\
&\frac{\partial hu}{\partial t}+\frac{\partial}{\partial x}\left(hu^2+\frac{1}{2}gh^2\right)+\frac{\partial (huv)}{\partial y}=-gh\frac{\partial B}{\partial x}-S_{fx} \\
&\frac{\partial hv}{\partial t}+\frac{\partial (huv)}{\partial x}+\frac{\partial}{\partial y}\left(hv^2+\frac{1}{2}gh^2\right)=-gh\frac{\partial B}{\partial y}-S_{fy}
\end{aligned} \tag{4.1}$$

where h is the water depth and B is the bottom elevation. u and v are the depth-averaged flow velocities in the x and y directions, respectively. g is the gravitational coefficient, r is the rainfall intensity and f is the infiltration capacity. S_{fx} and S_{fy} are the bottom stress friction terms in x and y directions,

respectively.

Following the technique in [e.g. 54, 48, 52, 131], the governing equations are rewritten in terms of the surface water elevation $w \coloneqq h + B$. Assuming that the bottom elevation B is constant over the time, h_t is substituted into w_t. Finally, the governing equations in terms of unknown variables w, hu and hv are numerically discretized.

4.2.2 Numerical Model

The governing equations are discretized using a hybrid FVM-FDM scheme [52] and the details of the scheme can be also found in Tavakkol and Lynett [131]. Following the previous methods [e.g. 146, 147, 148], the governing equations are rearranged and solved using a hybrid FVM-FDM discretization on a uniform Cartesian grid. Each cell represents a control volume in FVM and cell average over the cell is adopted as a grid point for FDM discretization. A second-order well-balanced positivity preserving central-upwind method [48] is used to discretize the advective terms. The bottom gradient terms are discretized following Kurganov and Levy [54]. The bottom friction terms are discretized using a central FDM and the rainfall and infiltration terms are considered as cell averages of water depth h in source terms. A third-order Adams-Bashforth scheme is used for time integration. A first-order Euler method is also adopted for the very first two time steps of the simulation (i.e. $n = 1, 2$) since the conservative variables at those time steps are not defined [52]. Special attention is paid to the consideration of the rainfall and infiltration terms as the numerical scheme is implemented in single precision on GPU.

4.2.3 Rainfall Intensity

The reciprocal distance squared method [149] is adopted to estimate spatial rainfall distribution in numerical domain with measured data at the rain gauges. The rainfall intensity R at point (x, y) is calculated as

$$R(x,y) = \frac{\sum_{n=1}^{\mathrm{NRG}} R_n / {D_n}^2}{\sum_{n=1}^{\mathrm{NRG}} 1/{D_n}^2} \tag{4.2}$$

where R_n is the measured rainfall intensity at rain gauge n, D_n is the distance between rain gauge n and point (x, y), and NRG is the number of rain gauges. If NRG is 1, then rainfall distribution is assumed to be uniform over the numerical domain.

4.2.4 Green-Ampt Model

Infiltration process represents that a certain amount of rainfall on the surface enters the soil when rainfall occurs. The GA model assumes that a wetting front, present in a homogeneous soil profile with a spatially uniform initial soil water content, divides the soil profile into upper wetted zone and underlying dry zone. The GA model is based on the mathematical formulation, derived from Darcy's law, with physical infiltration parameters to represent soil characteristics. Owing to its accurate approximation and simplicity, it has been widely used either alone or together with the SWEs [e.g. 150, 151, 152, 153, 154, 155, 156]. The infiltration capacity f_p, estimated using

the GA model, can be expressed as

$$f_p(t) = K_s + \frac{K_s \Psi \Delta\theta}{F(t)} \tag{4.3}$$

where K_s is the saturated hydraulic conductivity, Ψ is the average suction head at the wetting front and $\Delta\theta$ is the difference between the soil porosity θ_s and the initial volumetric water content θ_i. The cumulative infiltration $F(t)$ can be calculated by integrating f as

$$F(t) = K_s t + \Psi\Delta \log\left(1 + \frac{F(t)}{\Psi\Delta\theta}\right) \tag{4.4}$$

Since the Equation 4.4 is an implicit solution, iterative procedure with corresponding convergence criteria is required to solve it numerically, which increase the computational effort. Over the decades, various studies have derived the simplified approximate solutions to overcome this problem [e.g. 157, 158, 159, 160, 161, 162, 163, 164]. Each model has its own merits and demerits as to mathematical complexity, numerical accuracy and computational efficiency. Li et al. [145] (LI) derived one of the simplest explicit solution to the GA model by employing a power series expansion. LI model is adopted as an alternative to improve the numerical efficiency, which can be expressed following [e.g. 145, 165] as

$$f_p(t) = \frac{1}{2\Delta t}\left[P_1 + \left(P_1^2 + 8P_2\Delta t\right)^{0.5}\right] \tag{4.5}$$

where the variables P_1 and P_2 are written as

$$P_1 = K_s \Delta t - 2F(t) \tag{4.6}$$

$$P_2 = K_s \Delta t + K_s \Psi \Delta \theta \tag{4.7}$$

in which the accumulative infiltration depth is $F(t) = 0$ at $t = 0$ and then calculated as $\Delta F(t) = f(t)\Delta t$. Note that the infiltration rate $f(t)$ is not equal to the infiltration capacity $f_p(t)$. It will be explained in the following section.

4.2.5 Infiltration Rate

The infiltration capacity f_p represents the maximum rate at which a soil can absorb water [166]. The infiltration capacities in Eqs. 4.3, 4.5 are valid only if the water supply including rainfall and ponded water (h_p) exceeds the infiltration capacity. In this case, the infiltration rate f equals to the infiltration capacity ($f(t) = f_p(t)$). Otherwise, the infiltration rate f is dependent on the water supply. In the absence of surface ponding ($h_p(t) = 0$), all the rainfall will infiltrate into the soil ($f(t) = R(t)$) if the rainfall intensity is weak compared to the infiltration capacity ($R(t) \leq f_p(t)$). if $R(t) > f_p(t)$, however, the surface will be ponded, and the infiltration capacity can be applied to the infiltration rate. The infiltration can continue even if there is no rainfall until the surface becomes dry. The cumulative infiltration $F(t)$ can be obtained by integrating the infiltration rate $f(t)$.

4.2.6 Source Code Structure

Unity3D is one of the most famous cross-platform engine which supports a variety of VR platforms. A Unity3D project includes hundreds of scripts, written by JavaScript, C# and high-level shader language (HLSL), within numerous folders. Celeris Base is developed in Unity3D using C# as main programming language and HLSL to support compute shaders to solve the governing equations using GPU. A Celeris consist of several Assets folders with hundreds of scripts. The Celeris folder contains the bulk of the source code which drives the GPU, create the solver, solve the equations and render the shaders. Figure 4.1 shows the directory structure of the Celeris folder with the primary source files. GameManager.cs handles the main flow of the source code. The KP07Driver.cs and TL17Driver.cs contain the codes to solve the shallow water equations and the optional Boussinesq equations, respectively. The ControllerInteraction.cs governs the interactive system where the user can change the terrain during the simulation.

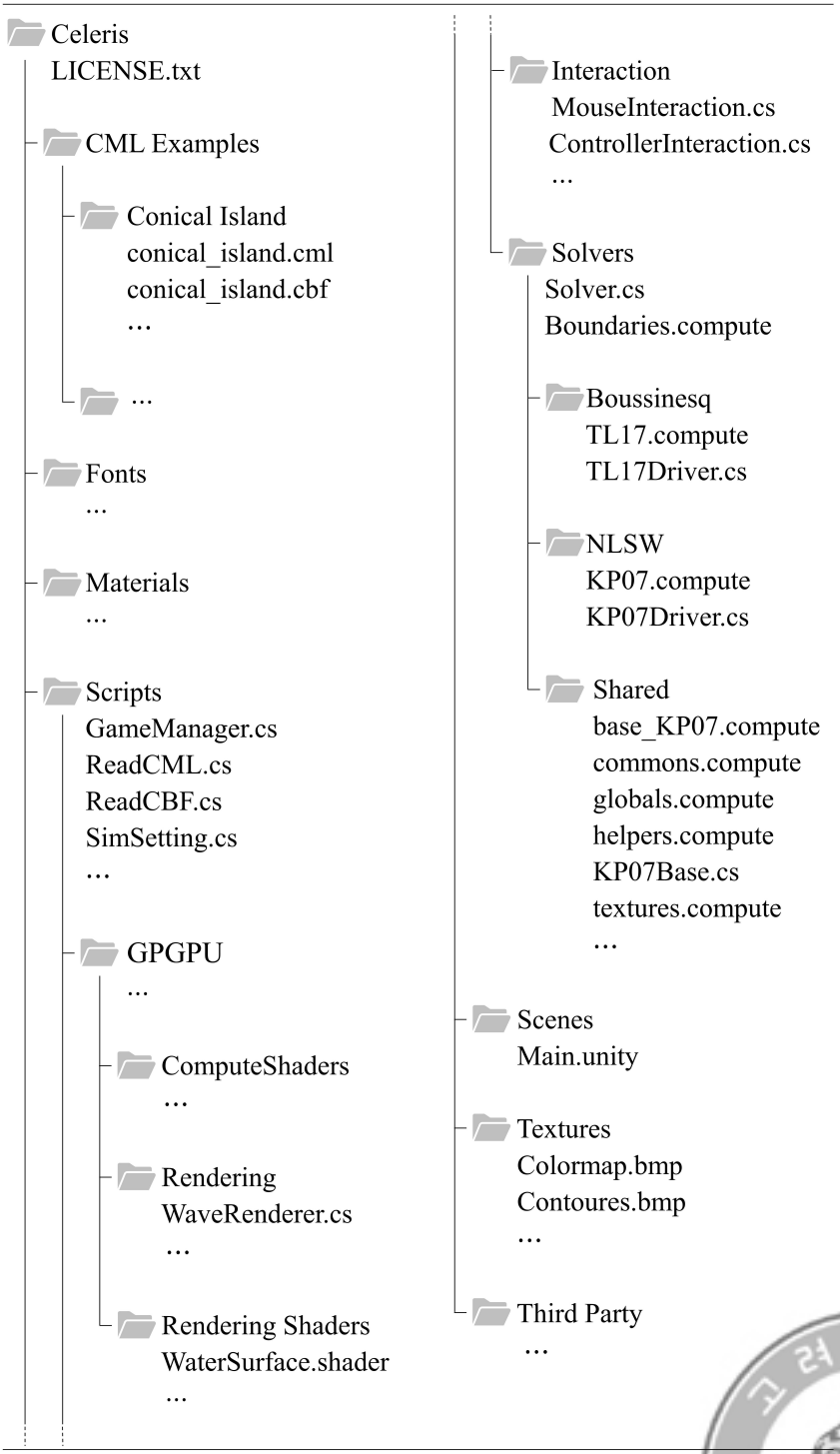

Figure 4.1: Directory structure of the Celeris folder

There are five primary GameObjects in the scene: Main Camera, GameManager, Engine, OVRPlayerController, Interaction. The Main Camera renders the user's view in the scene, which contains a script that enables the user to alter the camera's movement. The GameManager controls the main flow of the source code such as reading the input file, defining parameters, solving the governing equation using the GPU, rendering the results. The Engine with sub-objects (e.g., Wave Surface, Terrain Surface, Rendering Steps, etc.) renders the wave and terrain surfaces. The OVRPlayerController enables the user equipped with the VR device to move in the virtual world. The user's view can be changed by either physically turning the user's head (the VR headset) or pressing the VR controller. It also lets the developer to assign any button on the VR controller to a user-defined function (see Figure 4.2). The Interaction supports the interactive system which can modify the terrain while the simulation is running. It contains a script that reads the user's position, viewpoint and button input and affects the simulation environment through the GameManager GameObject.

The details of implementation, shaders, rendering and compilation in Celeris Base can be found in Tavakkol and Lynett [131].

Figure 4.2: Control of VR device in the presented model

4.2.7 Terrain change

The presented model implements an interactive system, where the user can alter the bottom topography. The feature is implemented in a similar manner to the mouse pointer gauge and buoy features in Celeris Base. When the user press the button which actives terrain change (see Figure 4.2), the ControllerInteraction.cs reads the user's current position and the activation signal. To identify the location that the user points on the simulation field, the software draws an imaginary line along the heading direction of the user equipped with VR headset. Then, the target point on a horizontal plane located on the mean sea level are calculated based on the user's current position and the viewpoint. Through the GameManager Object, The activation signal and target point on the numerical domain is then entered into the solvers (e.g., Solver.cs, KP08Driver.cs, TL17Driver.cs). While the user activates the terrain change, the terrain uplift in the form of an exponential function centered on the target point is continuously applied every timestep (see Figure 4.3).

(a) Before uplift

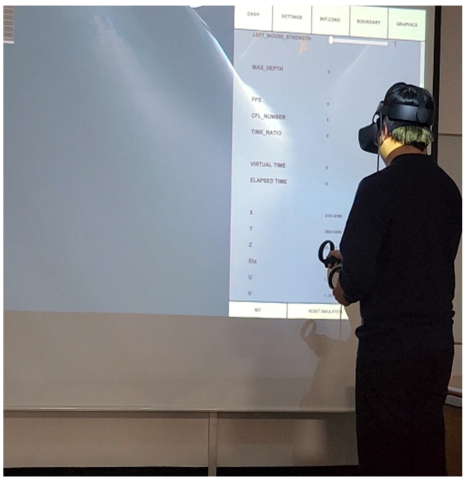

(b) After uplift

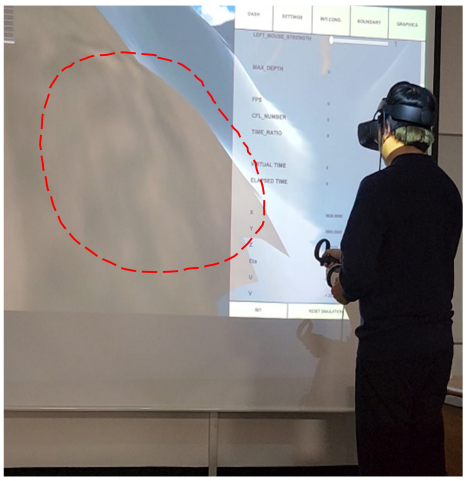

Figure 4.3: Example of terrain uplift using the interactive system during VR experience. The area closed with a red-dashed line represents terrain uplift region

4.3 Model Validations

Several numerical cases with rainfall, roughness and topography variations are considered to investigate the performance of the model. The accuracy of the model is assessed by comparing the simulation results with either analytical solutions or those calculated using the implicit GA model, which is used as reference solution. The analytical case of one-dimensional overland flow over a sloping bottom subject to excessive rainfall is performed. Following the test cases and soil characteristics in Fernández-Pato et al. [167], three numerical cases to evaluate the infiltration model are further simulated and the infiltration parameters in the GA model, which match to a sandy soil, are set as follows: $K_s = 3.272 \times 10^{-5}$ m/s, $\Psi = 0.0495$ m and $\Delta\theta = 0.38$.

4.3.1 A Steady, Uniform Excessive Rainfall

The one-dimensional overland flow on a sloping plane subjected to a steady, uniform excessive rainfall [168] is adopted. The excessive rainfall of 300 mm/h during a duration of 1,600 s is applied over the inclined plane with a length of 1,000 m and slope of 0.01. A uniform grid size of $\Delta x = 20$ m is used to discretize the computational domain and the Manning's roughness coefficient is set to 0.02. The initial conditions of the model domain are set to be dry: $h = 0$ and $u = 0$ at $t = 0$. The upstream boundary conditions are dry surface conditions as $h = 0$ and $u = 0$ and the open boundary conditions are imposed on the downstream.

Figure 4.4 compares the analytical and numerical results with respect to time at outlet for the case of steady, uniform excessive rainfall event. The water depth at the outlet increases linearly and reaches the peak value under the constant rainfall condition until $t = 1600$ s. After 1600 s, the water depth slowly decreases as rainfall stops. Good agreement between analytical and numerical solutions is obtained. The relative error (RE) between analytical and numerical solutions in the maximum water depth is calculated as 0.03 %. The results verify the accuracy of the model for the runoff due to the excessive rainfall against the analytical solution.

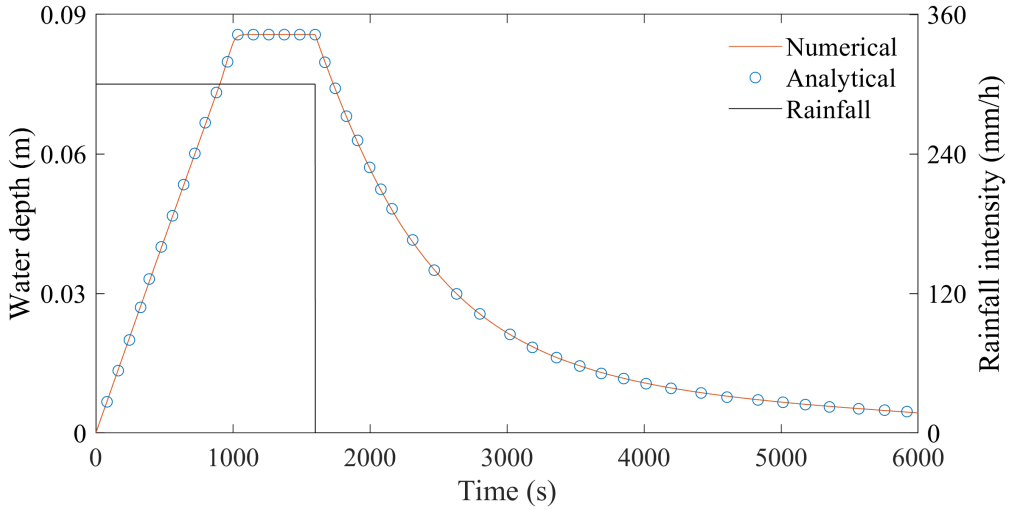

Figure 4.4: Comparison of water depth at outlet between the analytical and numerical solutions for steady, uniform excessive rainfall event

4.3.2 Different Rainfall Conditions

The runoff on a plane (2000 m in length and 20 m in width) with a uniform slope of 0.005 under different rainfall conditions are employed. Four rainfall scenarios with diverse rainfall hyetographs are considered, which are listed in Table 4.1. Case a has steady rainfall condition whereas Cases b-d have unsteady rainfall conditions. All cases except for Case d ensure full water availability until $t =$ 300 min. Besides, all rainfall conditions are uniform in space. The numerical domain is discretized using a grid size of 1 m for the $x-$ and $y-$directions. The Manning's roughness coefficient of $n = 0.03$ is used. The dry initial conditions are imposed on the model domain as $h = 0$, $u = 0$ and $v = 0$ at $t = 0$. The open boundary conditions are applied along the downstream side and the reflective boundary conditions are applied on the rest of the boundaries.

Figure 4.5 compares the simulated runoff hydrographs at the outlet under

Table 4.1: Rainfall hyetograph for various rainfall scenarios

Time (s)	Rainfall intensity (mm/s)			
	Case a	Case b	Case c	Case d
0-2,500	1.25	2.5	1.875	1.875
2,500-5,000	1.25	1.25	0.9375	0.375
5,000-7,500	1.25	0.75	0.5625	1.75
7,500-10,000	1.25	0.2	0.375	0
10,000-12,500	1.25	0.75	0.5625	0.5625
12,500-15,000	1.25	1.75	1.3125	1.3125
Total volume (m^3)	75,000	75,000	56,250	43,000

various rainfall conditions. The results are in satisfactory agreement with the reference solutions for all cases. Specifically, Case a, characterized by uniform rainfall event, shows the RE of about 0.39% in peak discharge and Cases b d with unsteady rainfall events commonly show the RE of about 0.01%. These results imply that the model is applicable for various rainfall conditions including steady, unsteady, single, and multiple rainfall events.

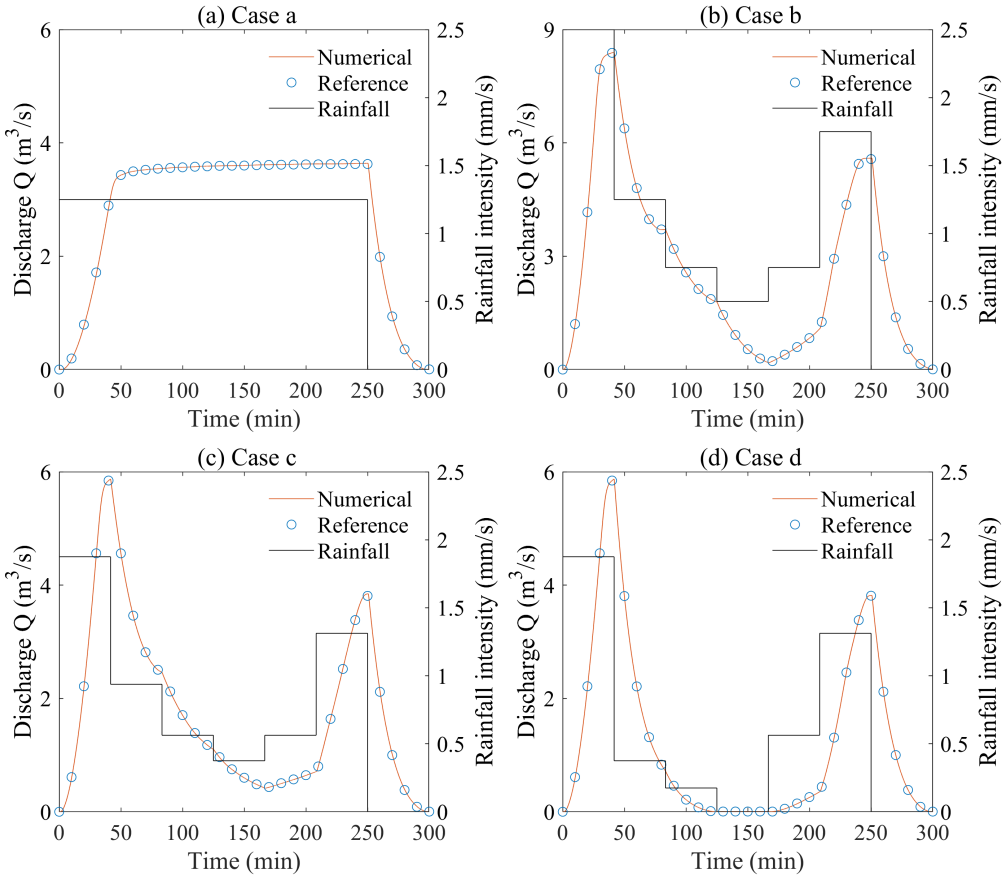

Figure 4.5: Comparison of runoff hydrographs under various rainfall conditions

4.3.3 Various Roughness and Slope Conditions

Various combinations of roughness and slope are investigated to identify their contributions on the runoff. The ratio ϕ between normal and critical depths, which represents the mildness fraction of the sloping plane, is employed to explain the effects of these parameters. Three different ϕ values are adopted as 0.79, 1.43 and 2.16. A uniform, steady rainfall with the intensity of 1.25 mm/s is applied on a sloping plane of 2,000 m length during 250 min. The uniform

grid with 401 cells is adopted. As with the previous cases, the initial and upstream boundary conditions are dry surface conditions and the downstream boundary conditions are the open boundary conditions.

The comparison of simulated and reference solutions with different ϕ values is shown in Figure 4.6. The peak discharge remains constant regardless of the mildness fraction, as seen in Figure 4.6 (a). However, the mildness fraction affects the speed of the overland flow, the duration for which surface ponding lasts on the surface and the infiltration volume, which is shown in Figure 4.6 (b). It can be seen that the numerical solutions match well with the reference solutions. The results show that the RE of peak discharge are 0.2, 0.72, and 0.75% for ϕ =0.79, 1.43 and 2.16, respectively. Besides, the RE of the maximum runoff volume are 0.13, 0.04, and 0.14%, respectively. These results indicate that the model can accurately predict the runoff generation on plains with varying roughness and slopes.

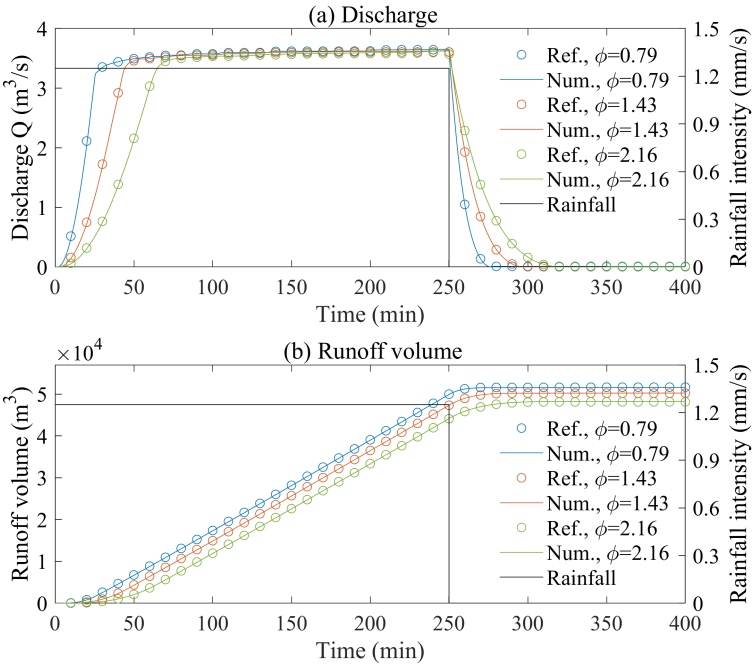

Figure 4.6: Comparison of (a) runoff hydrographs and (b) runoff volume with respect to time under different slope and roughness conditions

4.3.4 Irregular Topography

The inclined plain with sinusoidal topography subject to the steady, uniform rainfall is studied to examine the effects of irregular topography in infiltration. A constant rainfall with the intensity of 0.25 mm/s during 125 min is applied on the sinusoidal topography with slope, which is given by

$$B(x) = 21.0 - \sin\left(\frac{\pi}{10}\right) - 0.005x \tag{4.8}$$

The grid size of $\Delta x = 0.32$ m and the Manning's roughness coefficient of 0.03 are used in the numerical simulation. The initial and boundary conditions are

same as the case presented in Section 4.3.2.

Figure 4.7 describes the temporal evolution of the water surface elevation over irregular topography. As shown in Figure 4.7 (a), the water depth in each depression storage increases during rainfall. When rainfall stops ($t = 125$ min), the water surface elevation exceeds the local maxima (see Figure 4.7 (b)) and the surface water beyond the local maxima moves downstream, which varies the amount of water stored in each depression storage. Then, the water level decreases as water continues to infiltrate in the ponded regions even in the absence of rainfall (see Figure 4.7 (c)). In this case, a spatial difference in the cumulative infiltration appears since the local minima remains ponded but the local maxima have different duration of surface ponding (see Figure 4.8). As shown in Figures 4.7∼4.8, the simulated water surface elevation and cumulative infiltration show good agreement with the reference solutions. The average RE of water surface elevation and cumulative infiltration over the numerical domain at $t = 180$ min are 0.03% and 0.18%, respectively. Therefore, the results guarantee that the model is suitable for simulating runoff in the irregular topography.

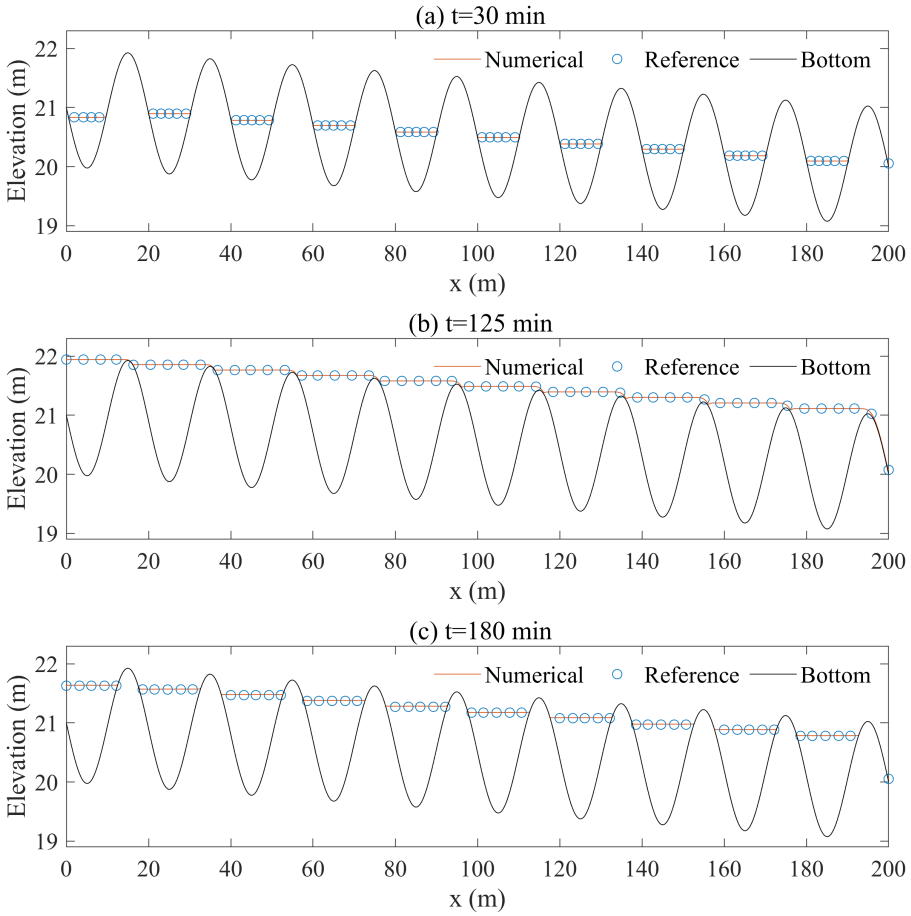

Figure 4.7: Comparison of water surface elevation over irregular topography at (a) $t = 30$ min, (b) $t = 125$ min and (c) $t = 180$ min

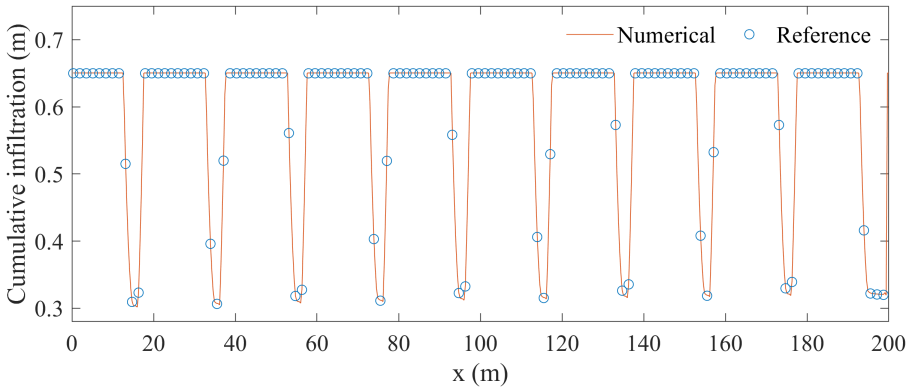

Figure 4.8: Comparison of cumulative infiltration over irregular topography at (a) $t = 180$ min

4.4 Model Application

The Goodwin Creek Experimental Watershed (GCEW) located in Mississippi, which has a drainage area of 21.3 km^2 [169], is simulated for model application. The GCEW has been operated by the United States Department of Agriculture Agricultural Research Service (USDA-ARS) National Sedimentation Laboratory (NSL) since 1981. Research studies conducted in the watershed include land surface processes, gully erosion, sediment transport, fluvial geomorphology, and stream restoration and stabilization [170]. The watershed elevation ranges from 69 m to 127 m with an average slope of 0.004 for the main channel network. A detailed description of the GCEW and the data is available in Blackmarr [171] and Rojas [172]. The land use of the GCEW consists of pasture (59.3%), forest (26.3%), cultivated (13.92%) and water (0.47%). The soil type of the GCEW is classified into loring (45.47%), coliins (17.59%), gullied land (16.18%), fallaya (6.72%), memphis (6.53%), grenada (5.00%) and

calloway (2.50%). The topographical, land use and soil type maps are shown in Figure 4.9.

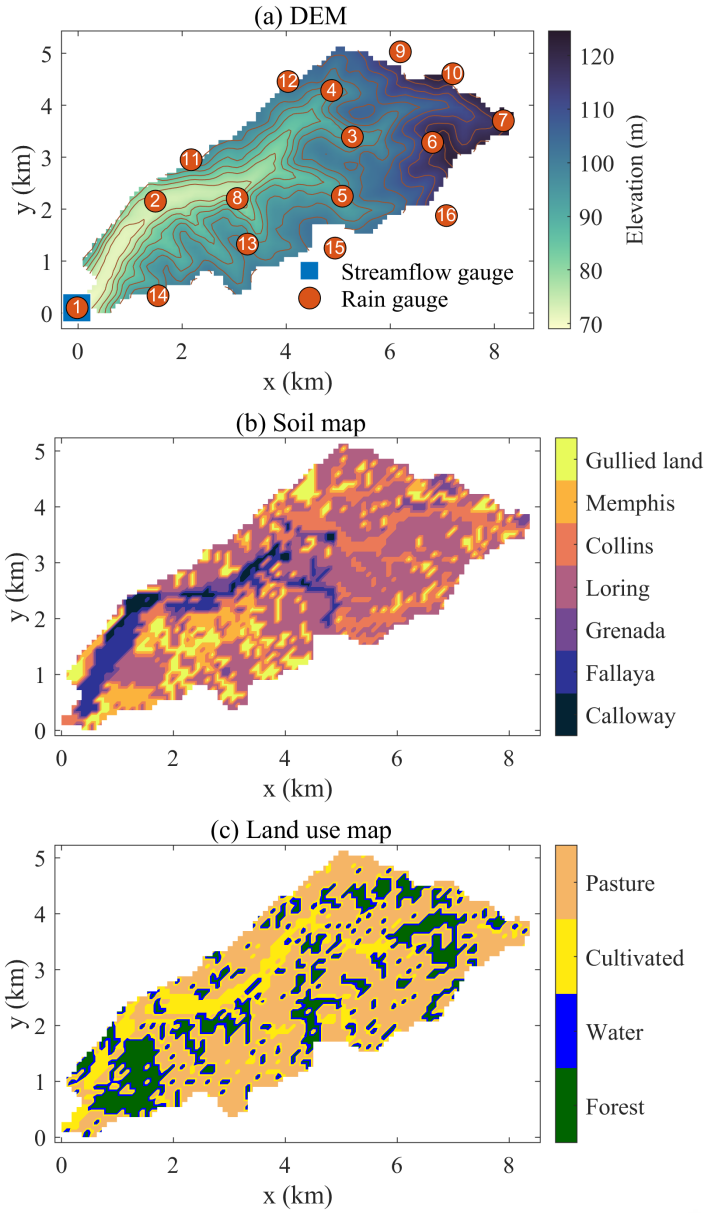

Figure 4.9: (a) DEM with streamflow and rain gauges; (b) soil map; (c) land use map of the GCEW

31 rain gauges is located in or near the watershed and 14 streamflow gauges is located at subcatchment outlets, which have been monitored by USDA-ARS NSL. The precipitation data from 16 rain gauges and the discharge data from one streamflow gauge located at the outlet of the GCEW are used, as shown in Figure 4.9 (a). The rainfall event of October 17, 1981 is adopted for model application. This event with a duration of 4.8 hours started at 9:19 p.m. There was very little rainfall ahead of this event. Precipitation data with 30-minute rain rate, taken from sixteen rain gauges displayed in Figure 4.9 (a), are presented in Figure 4.10. Gauge2 showed a maximum rain rate of 51.6 mm/h and the average rain rate was 14.7 mm/h. The total amount of rainfall ranged from 66.0 mm at Gauge15 to 78.7 mm at Gauge6 with an average depth of 73.5 mm.

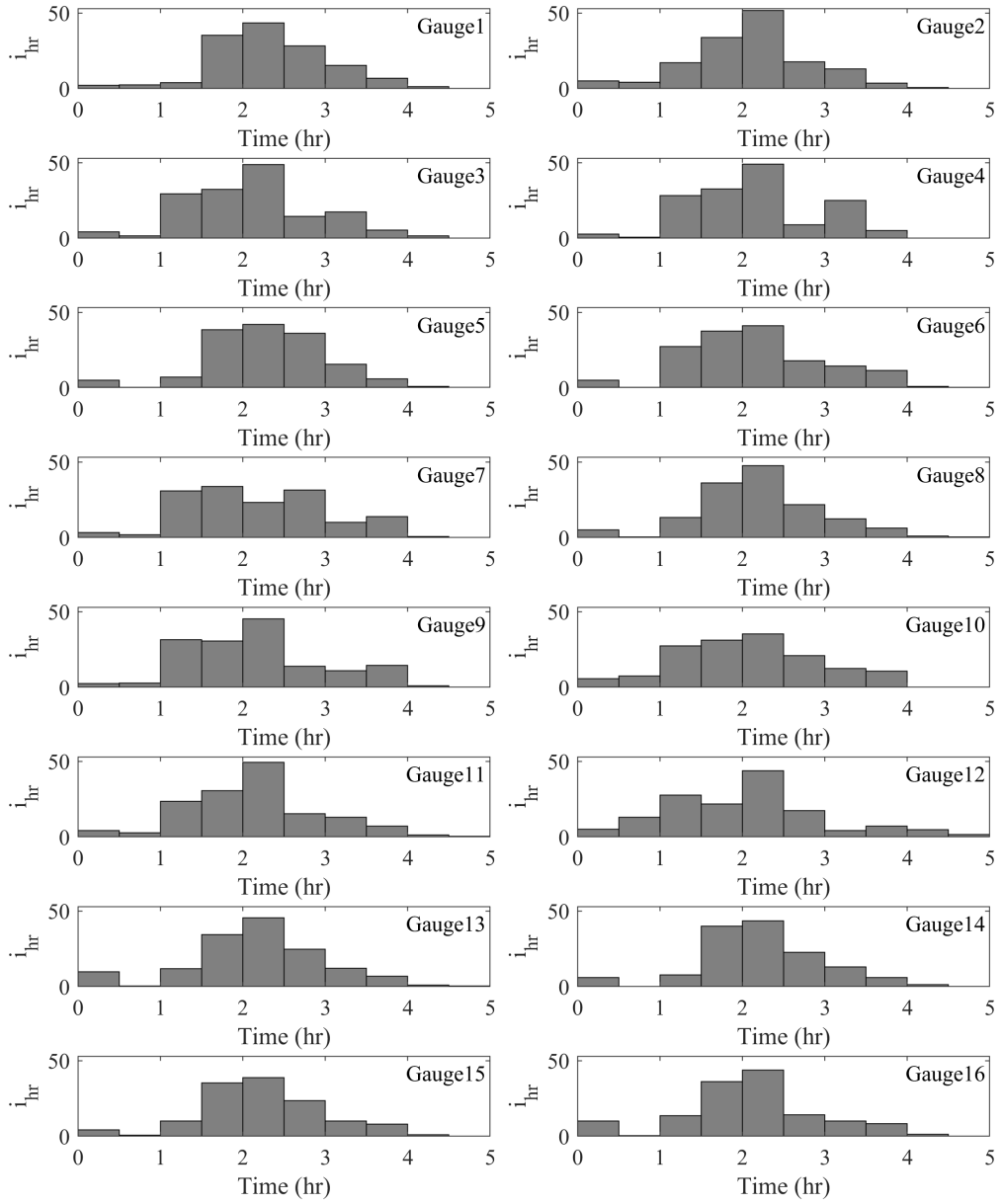

Figure 4.10: Hyetographs at 16 rain gauges for the rainfall event of October 17, 1981 in the GCEW (unit:mm/h)

A grid size of 90 m is adopted in the x- and y- directions to discretize the computational domain. The infiltration parameters for various soil types are

listed in Table 4.2. Also, the Manning's roughness n for different land uses are listed in Table 4.3. The initial condition of the numerical domain is assumed to be dry. The open boundary conditions are applied on the west boundaries where the outlet of the GCEW is located. The reflective boundary conditions are imposed on the rest of the boundaries.

Table 4.2: Infiltration parameters for various soil types

Soil type	Infiltration parameters		
	K_s	Φ	$\Delta\theta$
Calloway	0.336	22	0.29
Fallaya	0.307	14	0.29
Grenada	0.355	17	0.29
Loring	0.365	22	0.29
Collins	0.346	18	0.29
Memphis	0.432	22	0.29
Gullied land	0.384	15	0.29

Table 4.3: Manning's roughness n for different land use

Land use	Manning's roughness n
Forest	0.050
Water	0.010
Cultivated	0.021
Pasture	0.030

The comparison between observed and simulated runoff hydrographs along with the hyetograph at the outlet of the GCEW calculated using the reciprocal distance squared method, is shown in Figure 4.11. The simulated results are in

satisfactory agreement with the observed data in terms of peak discharge and time to peak. The observed peak discharge is 7.06 mm/hr occurring at $t = 280$ min. The computed peak discharge is 7.03 mm/hr, showing a RE of 0.43%. Besides, the time to peak is calculated as $t = 284$ min, which shows a RE of 1.43%.

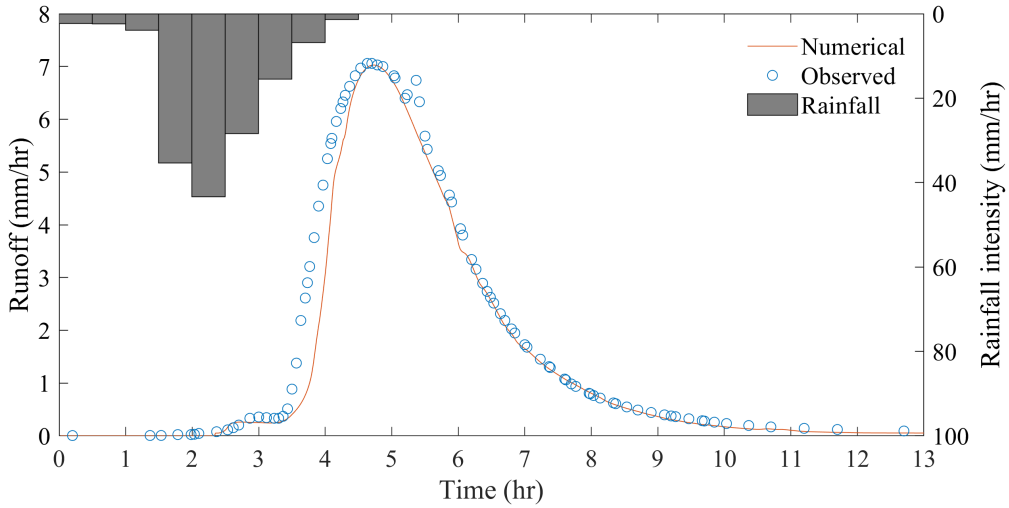

Figure 4.11: Comparison of runoff hydrograph at the outlet of the GCEW on rainfall event dated October 17, 1981

The simulated rainfall intensity, water depth and infiltration depth at different times after the rainfall event started are presented in Figures 4.12∼4.14. In the early stage of rainfall event (see Figure 4.12 (a)), the infiltration rate depends on the rainfall intensity rather than soil characteristics since the rainfall intensity is weak, as shown in Figure 4.14 (a). Consequently, the surface is not ponded since all the rainfall infiltrates into the soil (see Figure 4.13 (a)). As rainfall increases, the infiltration rate is determined by the infiltration capacity governed by soil characteristics and the surface starts to be ponded. During the

rising limb, the water depth gradually rises in the watershed. more water flows toward the river outlet, which contributes to increase in the discharge at the river outlet. At this time, the river network including main channel and tributaries can be easily identified (see Figure 4.13 (b)). When $t = 284$ min, peak discharge occurs at the river outlet. Some tributaries vanish or shrink in length as the rainfall decreases (see Figures 4.12 (c)∼4.13 (c)). During the recession limb, all the tributaries disappear and the length of the main channel is shorten since rainfall ended (see Figures 4.12 (d)∼4.13 (d)). Thus, peak discharge at the river outlet is also reduced. After rainfall stops, channels remains ponded for a while, but hillslope areas become dry. Hence, the infiltration depth is intensified in areas corresponding to the river network (see Figure 4.14 (d)).

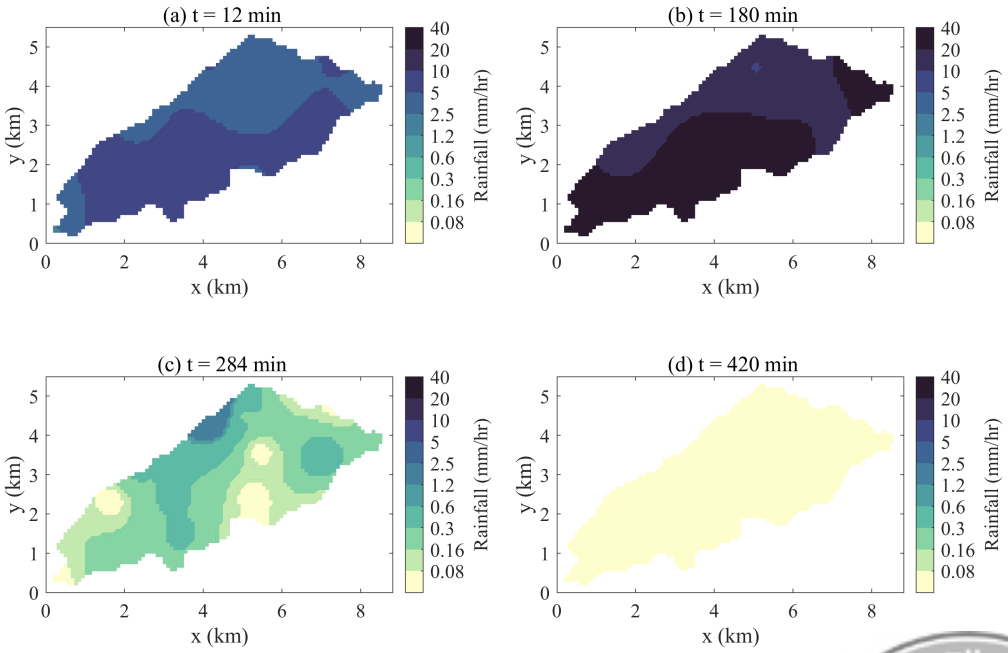

Figure 4.12: Simulated map of rainfall intensity over the GCEW at different times after the initiation of the rainfall event dated October 17, 1981

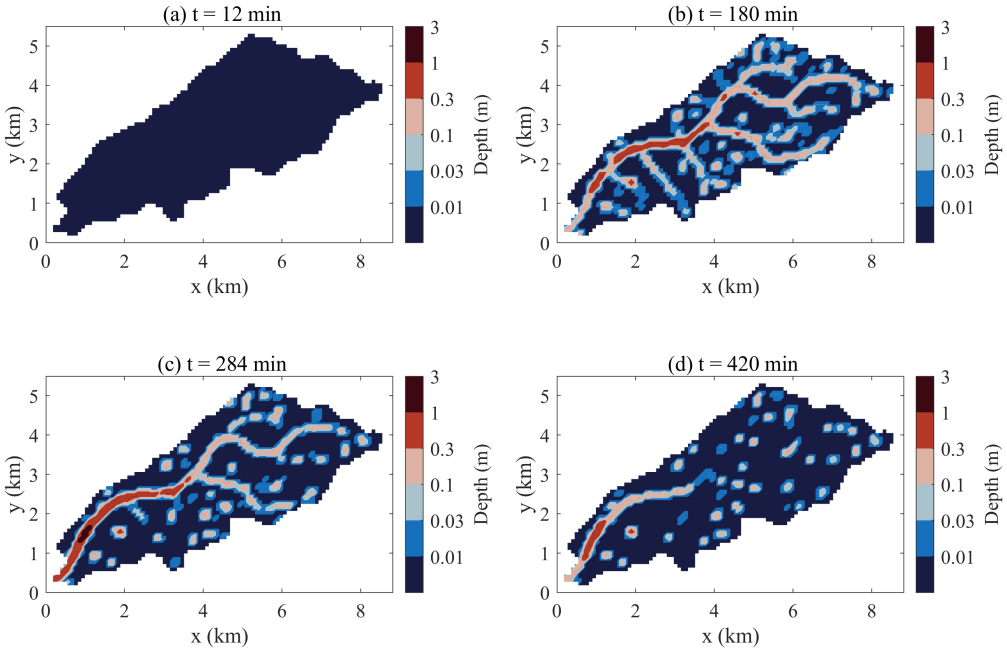

Figure 4.13: Simulated map of water depth over the GCEW at different times after the initiation of the rainfall event dated October 17, 1981

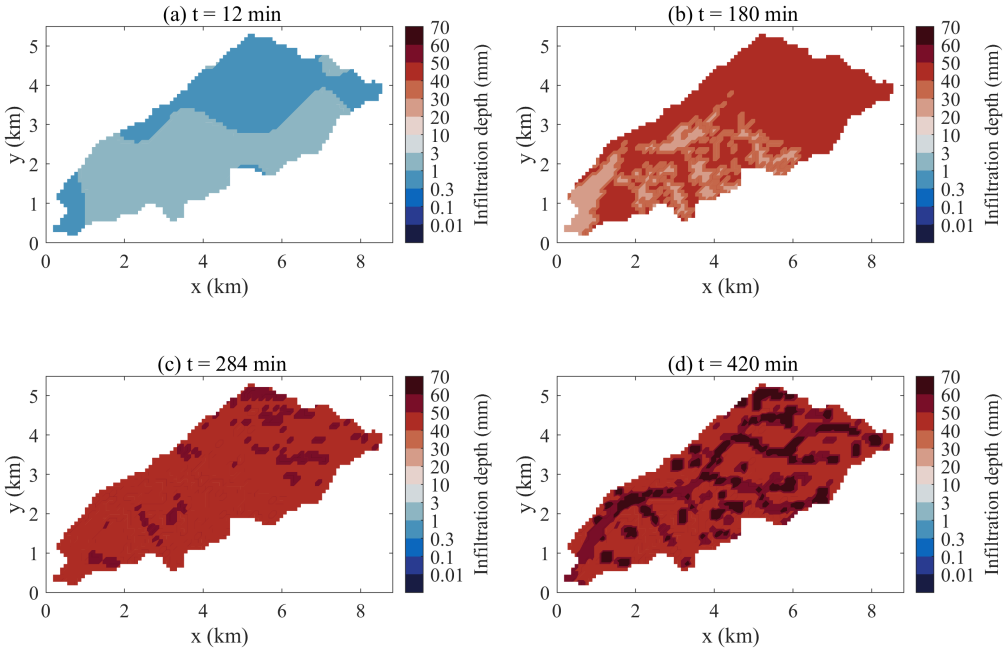

Figure 4.14: Simulated map of infiltration depth over the GCEW at different times after the initiation of the rainfall event dated October 17, 1981

Figure 4.15 depicts the VR experience during the simulation on the GCEW for the rainfall event dated October 17, 1981. the user equipped with the VR device can move around the numerically-reproduced GCEW and closely observe the temporal change of the water depth at a desired point in the GCEW. Besides, the user can alter the bottom topography by entering button on the VR controller. This feature may enable the user to simulate various situations related to the bottom change such as the collapse of dams or embankments or the installation of disaster prevention structure according to real-time countermeasures.

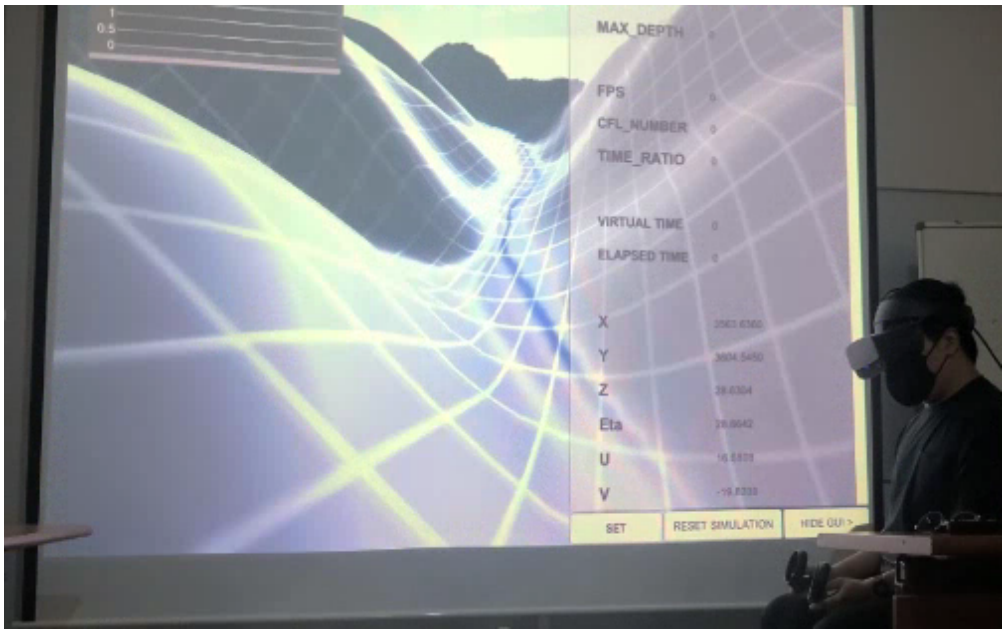

Figure 4.15: Snapshot of the VR experience within the numerical domain during the rainfall-runoff simulation on the GCEW

4.5 Conclusions

Interactive hydrodynamic rainfall-runoff model with an immersive virtual reality (VR) environment is proposed based on the immersive nearshore wave simulation software, Celeris Base. Neglecting the dispersive terms, the nonlinear shallow water equations (NSWEs) are adopted as the governing equations. Rainfall and infiltration terms are implemented in mass conservation to account for the rainfall-runoff process. The reciprocal distance squared method is adopted to consider the spatial distribution of rainfall intensity. Owing to its simplicity and accuracy, the explicit approximation to the Green-Ampt (GA) model, derived from Li et al. [145], is employed. The presented model has

been tested against the analytical and reference solutions for several numerical experiments. A steady, uniform excessive rainfall test verifies the accuracy of the model for simulating the direct runoff entered as source term in the continuity equation. Several rainfall-runoff cases under various rainfall, roughness, bottom slope and topography conditions were performed to validate the infiltration model. The validation results show that the explicit GA model is quite accurate compared to the implicit GA model without significant error. Furthermore, the model is applied to simulate historical rainfall event in the Goodwin Creek Experimental Watershed (GCEW) and verified against the observed hydrograph at the river outlet. Based on the soil and land use maps of the GCEW, the spatial distribution of the roughness coefficient and infiltration parameters is applied to consider the soil and land use characteristics. The results show that the model is capable of computing the flood routing process over the natural basin as well as the simplified plain. Since it is difficult to collect soil characteristics necessary to estimate infiltration parameters in the GA model, other infiltration models (e.g., Horton model, NRCS-CN model) are implemented. Other features of the presented model, immersive and interactive simulation environments, are also introduced. VR simulation environment is anticipated to improve the proposed model's usability by enabling researchers and engineers to access the potential risk of an extreme flood while people are experiencing it simultaneously. Besides, interactive system capable of altering the bottom topography during the simulation may consider unexpected terrain changes such as dam or embankment collapse or installation of disaster prevention structure during the flood event. This feature is expected to open a new

era for advanced hazard mitigation strategy such as real-time countermeasures in case of flash flood.

Chapter 5

Model Coupling with Non-Dispersive Shallow Water Model

An accurate and efficient modeling system through one-way coupling between two different shallow water models, i.e., non-dispersive shallow water model (Delft3D FM) and dispersive Boussinesq model (Celeris) is proposed. The two shallow water models are briefly introduced focusing on the governing equations. Besides, the numerical scheme of Celeris is introduced since the data exchange between two models are preformed on the model boundary in Celeris. An absorbing-generating boundary condition is implemented to integrate two models without spurious errors at the model boundary. Special treatment is applied to maintain the wave property and thus match the boundary condition at the model boundary. The proposed system has been tested for 1D and 2D long wave propagation. The comparison results show an acceptable errors for both 1D and 2D problems, which validates the absorbing-generating boundary condition is well implemented. The proposed system is expected to contribute to advanced coastal disaster mitigation strategy through accurate

and fast modeling of shallow water waves.

5.1 Introduction

Storm surges have caused catastrophic damage to coastal areas, including severe causalities and property losses [e.g. 173, 174, 5]. For example, typhoon-induced storm surges, such as Typhoon Maemi (2003), Typhoon Haiyan (2013) and Hurricane Harvey (2017), have caused many hazardous loss of property and life in coastal regions. Typhoon Maemi (2003), which landed on the Korean Peninsula in 2003, resulted in more than 100 casualties and a property loss of five billion dollars [5]. Furthermore, the rise in sea surface temperature due to global warming has been observed to exacerbate the storm surge [e.g. 175, 176, 177]. Thus, in order to mitigate typhoon-induced disasters in coastal areas, it is crucial to develop an accurate and effective storm surge model.

Various hydrodynamic models such as Delft3D [5], ADCIRC [178], POM [179], FVCOM [180] and MIKE21 [181] have been applied to predict storm surge. These hydrodynamic models, developed based on long-wave assumptions, adopted different numerical schemes and have been validated for a variety of shallow water waves (e.g., tides, storm surges, tsunamis, riverine flows). These models, adopting depth-integrated approach, usually solve the two-dimensional horizontal shallow water equations. Besides, the external forces for considering storm surge are wind, pressure and Coriolis force.

Many studies have emphasized the key role of waves in storm surge and its inundation modeling in coastal regions, mostly via the wave-induced radiation

stress. Xie et al. [182] found that the waves contributed 0.76 m to the total surge elevation in Charleston Harbor during Hurricane Hugo (1989). Kim et al. [183] reported that, during the Typhoon Anita (1970), the waves contributed 40% (∼0.5 m) along the coast of Tosa Bay. Sheng et al. [184] noticed that the contribution of the waves was up to 36% along the north-eastern Gulf of Mexico during Hurricane Ivan (2004). He et al. [185] found that the waves contributed 14.4% in the Yangshan Deep-Water Harbor during typhoon Chan-hom (2015). Wuxi et al. [174] noted that the coupling effect between surge and wave will significantly impact the accuracy of storm surge prediction. Therefore, for accurate prediction of storm surge and inundation damage, the effects of the waves, especially in nearshore regions, should be considered.

Up to now, the spectral phase-averaged models (e.g., WAM and SWAN) have been developed and been been integrated with the hydrodynamic models to accurately predict storm surge. These coupled models have provided reliable results for both deep water areas and coastal regions with shallow water. However, the phase-averaged models are limited to be applied for nearshore regions [186]. Therefore, the phase-resolving wave models should be used for accurate prediction of storm surge propagation as well as nearshore physics. Since these phase-resolving models are more vulnerable to numerical instability and are computationally more expensive than the phase-averaged models, the super-computing facilities or high performance computing techniques are required.

Therefore, this chapter aims to develop the one-way coupled modeling system where dispersive and non-dispersive wave models are coupled through

the absorbing-generating boundary condition. This approach enables to increase the accuracy while maintaining the computational efficiency by adopting the non-dispersive model in deep-water areas, while predicting wave components using the dispersive model in nearshore regions. Besides, the absorbing-generating boundary condition is applied for data exchange between the two models without spurious errors at the model boundary.

The outline of this chapter is as follows. Section 5.2 introduces two different wave models, Delft3D FM and Celeris. Besides, one-way coupling using the absorbing-generating boundary condition is presented. Section 5.3 presents the simulation results of several numerical experiments to investigate the performance of the coupled model. Conclusions are discussed in Section 5.4.

5.2 Numerical Models

5.2.1 Dispersive Boussinesq Model with Non-characteristic Form: Celeris

Celeris [e.g. 52, 131] is a GPU-accelerated Boussinesq-type wave model considering the nonlinear and weakly dispersive effects of the wave. It solves the

extended Boussinesq equation [77], which is given by

$$\begin{aligned}
&\frac{\partial h}{\partial t}+\frac{\partial hu}{\partial x}+\frac{\partial hv}{\partial y}=0\\
&\frac{\partial hu}{\partial t}+\frac{\partial}{\partial x}\left(hu^2+\frac{gh^2}{2}\right)+\frac{\partial huv}{\partial y}+ghz_x+\psi_1=0\\
&\frac{\partial hv}{\partial t}+\frac{\partial huv}{\partial x}+\frac{\partial}{\partial y}\left(hv^2+\frac{gh^2}{2}\right)+ghz_y+\psi_2=0
\end{aligned} \tag{5.1}$$

where h is the total water depth. t is the time. u and v are the depth-averaged flow velocities along with x and y coordinates, respectively. g is the gravitational acceleration coefficient. z is the bottom elevation. ψ_1 and ψ_2 are the modified dispersive terms [52], which are defined as

$$\begin{aligned}
\psi_1 =& -\left(B_0+\frac{1}{3}\right)d^2\left(P_{xxt}+Q_{xyt}\right)-B_0gd^3\left(\eta_{xxx}+\eta_{xyy}\right)\\
&-dd_x\left(\frac{1}{3}P_{xt}+\frac{1}{6}Q_{yt}+2B_0gd\eta_{xx}+B_0gd\eta_{yy}\right)-dd_y\left(\frac{1}{6}Q_{xt}+B_0gd\eta_{xy}\right)\\
\psi_2 =& -\left(B_0+\frac{1}{3}\right)d^2\left(P_{xyt}+Q_{yyt}\right)-B_0gd^3\left(\eta_{yyy}+\eta_{xxy}\right)\\
&-dd_x\left(\frac{1}{3}Q_{yt}+\frac{1}{6}P_{xt}+2B_0gd\eta_{yy}+B_0gd\eta_{xx}\right)-dd_x\left(\frac{1}{6}P_{yt}+B_0gd\eta_{xy}\right)
\end{aligned} \tag{5.2}$$

where $P=hu$ and $Q=hv$ are the depth-integrated mass fluxes in x and y coordinates, respectively. d is the still water depth and η is the water surface elevation measured from the still-water elevation. $B_0=1/15$ is the calibration parameter for dispersive properties in the governing equations. The governing equations are rewritten in terms of the surface water elevation $w:=h+B$. Assuming that the bottom elevation B is constant over the time, h_t is substituted

into w_t. Finally, the governing equations with the unknown variables (w, hu and hv) are discretized.

The governing equations are discretized using a hybrid finite volume-finite difference (FVM-FDM) scheme [131]. A second-order well-balanced positivity preserving central-upwind scheme [48] to discretize the advective terms along with the bottom gradient terms in shallow water equations. The advective flux $\mathcal{F}^{HLL}$ based on the HLL approximate Riemann solver [22] is defined as

$$\mathcal{F}^{HLL} = \frac{a_R F_L - a_L F_R + a_L a_R \left(U_R - U_L\right)}{a_R - a_L} \tag{5.3}$$

where U is the conservative variable vector and F is the advective flux vector. The subscripts L and R represent the reconstructed variables at the cell interface calculated using a generalized minmod limiter. The one-sided local speeds (a_L,a_R) are obtained using the eigenvalues of the Jacobian $\frac{\partial F}{\partial U}$, as follows:

$$\begin{aligned} a_R &= \max\left\{u_L + \sqrt{gh_L}, u_R + \sqrt{gh_R}, 0\right\} \\ a_L &= \min\left\{u_L - \sqrt{gh_L}, u_R - \sqrt{gh_R}, 0\right\} \end{aligned} \tag{5.4}$$

The rest of the terms (e.g., dispersive terms) are discretized based on the central FDM. A third-order Adams-Bashforth scheme is adopted as the predictor time step for time integration. A first-order Euler method is employed only for the very first two time steps of the simulation (i.e. n = 1, 2) since the conservative variables at those time steps are not defined [53].

5.2.2 Non-dispersive Shallow Water Model with Characteristic Form: Delft3D FM

Delft3D Flexible Mesh Suite (Delft3D FM) developed by Deltares [187], is widely used for the prediction of long waves (e.g., tides, tsunamis, storm surges). It solves two-dimensional nonlinear shallow water equations (2D NSWEs), which is defined as

$$\begin{aligned}
&\frac{\partial h}{\partial t} + \frac{\partial hu}{\partial x} + \frac{\partial hv}{\partial y} = 0 \\
&\frac{\partial u}{\partial t} + u\frac{\partial u}{\partial x} + v\frac{\partial u}{\partial y} + g\frac{\partial h}{\partial x} = g\frac{\partial d}{\partial x} \\
&\frac{\partial v}{\partial t} + v\frac{\partial u}{\partial x} + v\frac{\partial v}{\partial y} + g\frac{\partial h}{\partial y} = g\frac{\partial d}{\partial y}
\end{aligned} \tag{5.5}$$

The 2D NSWEs are then divided into two sets of 1D SWEs using some manipulations [188] in order to efficiently solve the Saint-Venant systems. The resulting two sets of 1D SWEs are given by

$$\begin{aligned}
&\frac{\partial h}{\partial t} + \frac{\partial hu}{\partial x} = 0 \\
&\frac{\partial u}{\partial t} + u\frac{\partial u}{\partial x} + g\frac{\partial h}{\partial x} = g\frac{\partial d}{\partial x} \\
&\frac{\partial v}{\partial t} + v\frac{\partial u}{\partial x} = 0
\end{aligned} \tag{5.6}$$

and

$$\begin{aligned}
&\frac{\partial h}{\partial t} + \frac{\partial hv}{\partial y} = 0 \\
&\frac{\partial u}{\partial t} + v\frac{\partial u}{\partial y} = 0 \\
&\frac{\partial v}{\partial t} + v\frac{\partial v}{\partial y} + g\frac{\partial h}{\partial y} = g\frac{\partial d}{\partial y}
\end{aligned} \tag{5.7}$$

As the two sets of above equations are quasi-linear hyperbolic systems that the eigenvalues of the Jacobian matrix are real, the equations along the x direction can be recast in characteristic form as follows:

$$\begin{aligned}
&\frac{\partial p}{\partial t} + \lambda_1\frac{\partial p}{\partial x} = g\frac{\partial d}{\partial x} \\
&\frac{\partial q}{\partial t} + \lambda_2\frac{\partial q}{\partial x} = g\frac{\partial d}{\partial x} \\
&\frac{\partial r}{\partial t} + \lambda_3\frac{\partial r}{\partial x} = 0
\end{aligned} \tag{5.8}$$

where Riemann invariants (p,q,r) along a characteristic are defined as

$$\begin{aligned}
&p = u + 2\sqrt{gh} \\
&q = u - 2\sqrt{gh} \\
&r = v
\end{aligned} \tag{5.9}$$

and the three different eigenvalues (λ_1,λ_2,λ_3) are defined as

$$\begin{aligned}\lambda_1 &= u + \sqrt{gh} \\ \lambda_2 &= u - \sqrt{gh} \\ \lambda_3 &= u\end{aligned} \tag{5.10}$$

These characteristic variables with respect to distinct characteristic speeds represent that their quantities remain constant along the characteristic. λ_1 has a positive value whereas λ_2 has a negative value in subcritical flow. The absorbing-generating boundary condition can be simplified owing to these propagation characteristics.

5.2.3 Absorbing-Generating Boundary Condition

The absorbing-generating boundary condition is designed to generate the incoming waves while allowing the outgoing waves not to be reflected into the model domain. It allows the outgoing waves to pass through the model boundary with minimal reflection. In other words, the outgoing characteristic have to pass the model boundary without affecting the inner domain. Therefore, the absorbing boundary condition should force the absence of the incoming waves. For subcritical flow, q propagates propagates in the negative x-direction so it reaches the left boundary. Similarly, p and r propagate in the positive $x-$ and $y-$ directions, respectively. The Riemann invariants propagating along the characteristic should be constant at the model boundary even considering the incoming waves. The equations in characteristic form (5.8) for a 2D space

can be rewritten as

$$\begin{aligned}
\frac{\partial p}{\partial t} &= -(u+c)\frac{\partial p}{\partial x} - v\frac{\partial p}{\partial y} - c\frac{\partial v}{\partial y} + g\frac{\partial h}{\partial x} \\
\frac{\partial q}{\partial t} &= -(u-c)\frac{\partial q}{\partial x} - v\frac{\partial q}{\partial y} + c\frac{\partial v}{\partial y} + g\frac{\partial h}{\partial x} \\
\frac{\partial r}{\partial t} &= -u\frac{\partial r}{\partial x} - v\frac{\partial r}{\partial y} - g\frac{\partial \eta}{\partial y}
\end{aligned} \tag{5.11}$$

To simultaneously generate the incoming waves and absorb the outgoing waves, the total flux along the model boundaries at next time step should be determined. The conservative variables (w, hu and hv) are given for the entire numerical domain including model boundary at the time level $t = t^n$. At the time level $t = t^{n+1}$, the components of the incoming wave (η_i, $Q_{x,i}$ and $Q_{y,i}$) is specified along the boundaries. Then, the wave components (η, Q_x and Q_y) in the interior points can be calculated by the integration of the governing equations (5.1). The challenge, however, is to estimate the equivalent total fluxes along the model boundaries and determine the components of the outgoing waves at $t = t^{n+1}$. To solve this problem, the absorbing-generating boundary condition [189] is adopted.

In the following, the first order expansion of the absorbing-generating boundary condition for the $x = 0$ boundary, derived from Van Dongeren and Svendsen [189], is described. Based on the linear superposition assumption of the incoming and outgoing waves $Q_x = Q_{x,i} + Q_{x,r}$ and $\eta_x = \eta_{x,i} + \eta_{x,r}$ (subscripts i and r, respectively), the Riemann invariant q outgoing through boundary can be

expressed by

$$\frac{q}{c_0} = \frac{Q_{x,i}}{c_0 d}\left(1+\frac{\eta_i+\eta_r}{d}\right)^{-1} + \frac{Q_{x,i}}{c_0 d}\left(1+\frac{\eta_i+\eta_r}{d}\right)^{-1} - 2\sqrt{1+\frac{\eta_i+\eta_r}{d}} \tag{5.12}$$

where

$$c_0 = \sqrt{gd} \tag{5.13}$$

For simplicity, the incoming and outgoing waves can be expressed by

$$\begin{aligned} Q_{x,i} &= c\eta_i \cos\theta_i \\ Q_{x,r} &= -c\eta_r \cos\theta_r \end{aligned} \tag{5.14}$$

where θ_i and θ_r are the angles of the incoming and outgoing waves from the x-axis. Substituting Eq. 5.14 into Eq. 5.12, one can obtain

$$\begin{aligned} \frac{q}{c_0} = &\frac{Q_{x,i}}{c_0 d}\left(1+\frac{Q_{x,i}}{cd\cos\theta_i}-\frac{Q_{x,r}}{cd\cos\theta_r}\right)^{-1} + \frac{Q_{x,i}}{c_0 d}\left(1+\frac{Q_{x,i}}{cd\cos\theta_i}-\frac{Q_{x,r}}{cd\cos\theta_r}\right)^{-1} \\ &- 2\left(1+\frac{Q_{x,i}}{cd\cos\theta_i}-\frac{Q_{x,r}}{cd\cos\theta_r}\right)^{-0.5} \end{aligned} \tag{5.15}$$

Expanding this term to the first order with respect to $Q_x/c_0 d$, it yields

$$c_3 = c_1 Q'_{x,i} + b_1 Q'_{x,r} + O\left(\frac{Q_x}{c_0 d}\right)^2 \tag{5.16}$$

where

$$Q_{x,i}^{'} = \frac{Q_{x,i}}{c_0 d},\ Q_{x,r}^{'} = \frac{Q_{x,r}}{c_0 d},\ b_1 = \frac{\cos\theta_r + 1}{\cos\theta_r},\ c_1 = \frac{\cos\theta_i - 1}{\cos\theta_i},\ b_3 = \frac{q}{c_0} + 2 \tag{5.17}$$

The first order expansion of the absorbing-generating boundary condition (5.17) has two unknown variables $Q_{y,r}^{'}$ and θ_r, which can be calculated by

$$\theta_r = \arctan\left(\frac{Q_{y,r}^{'}}{Q_{x,r}^{'}}\right) \tag{5.18}$$

where the unknown variable $Q_{y,r}^{'}$ can be calculated from g using the linear superposition assumption of the incoming and outgoing waves as

$$Q_{y,r}^{'} = \frac{r\,(d + \bar{\eta}) - Q_{y,i}}{c_0 d} \tag{5.19}$$

where the y-component of the incoming wave $Q_{y,i}$ is given and r is determined by integration of the characteristic equations (5.11).

The Riemann invariant q at the next time step is determined by the integration of the the characteristic equations (5.11) as well. Here, the Riemann invariant gradients $\partial q/\partial x$ and $\partial q/\partial y$ are calculated using the q values in the interior points. After iteratively solving the Eqs. 5.17, 5.18 and 5.19 with the specification of incoming wave, the outgoing wave ($\eta_r,\ Q_{x,r},\ Q_{y,r}$) at the next time step can be determined.

5.2.4 Model Coupling

This section presents the one-way coupling method to integrate non-dispersive wave model, Delft3D FM and dispersive wave model, Celeris. Previous studies [e.g. 188] generally coupled two different models without appropriately considering the outgoing waves from the inner domain. The internal wave generation with sponge layer has been an available alternative. It requires an additional model domain behind the internal wavemaker where a sponge layer for absorbing the outgoing waves is applied, thus lessening the computational efficiency. In this chapter, we employed the absorbing-generating boundary to generate the incoming waves from non-dispersive model and absorb the outgoing waves from the inner domain in dispersive model without unnecessarily extending the model domain.

Since the two wave models have different governing equations and correspondingly distinct wave characteristics, special treatment in Celeris is necessary to exchange variables from Delft3D FM without significant errors. Celeris solves the extended Boussinesq equations which includes dispersive terms (higher order terms). The equations in characteristic form in Eq. 5.8 are not valid for Celeris since these equations are derived from the shallow water equations. Thus, the implementation of characteristic boundary condition can cause spurious error due to the dispersive terms. To avoid this problem, the wave properties at the domain boundary should remain constant. Thus, the dispersive terms in Celeris should be ignored at the model boundary, which enables the implementation of the characteristic boundary condition in Celeris. Therefore, the governing equations reduce to the nonlinear shallow water equations at the

grid points near the domain boundary.

5.3 Numerical experiments

5.3.1 One-dimensional Sinusoidal Wave Propagation

A train of sinusoidal waves with a small amplitude is investigated to validate the absorbing-generating boundary condition. A 2,000 m channel with a width of 2,000 m over a frictionless bottom has a constant depth of 10 m. A train of sinusoidal waves with an amplitude of 0.001 m and a period of 60 s are generated at the left boundary and propagated to the right boundary where reflective boundary condition is imposed. The reflected waves travel toward the left boundary, and the left boundary condition generates a sinusoidal incoming waves and absorbs the reflected waves simultaneously. The simulation is computed up to 600 s when 10 sinusoidal waves are generated. A uniform grid size of 10 m and a time step of 0.01 s are adopted.

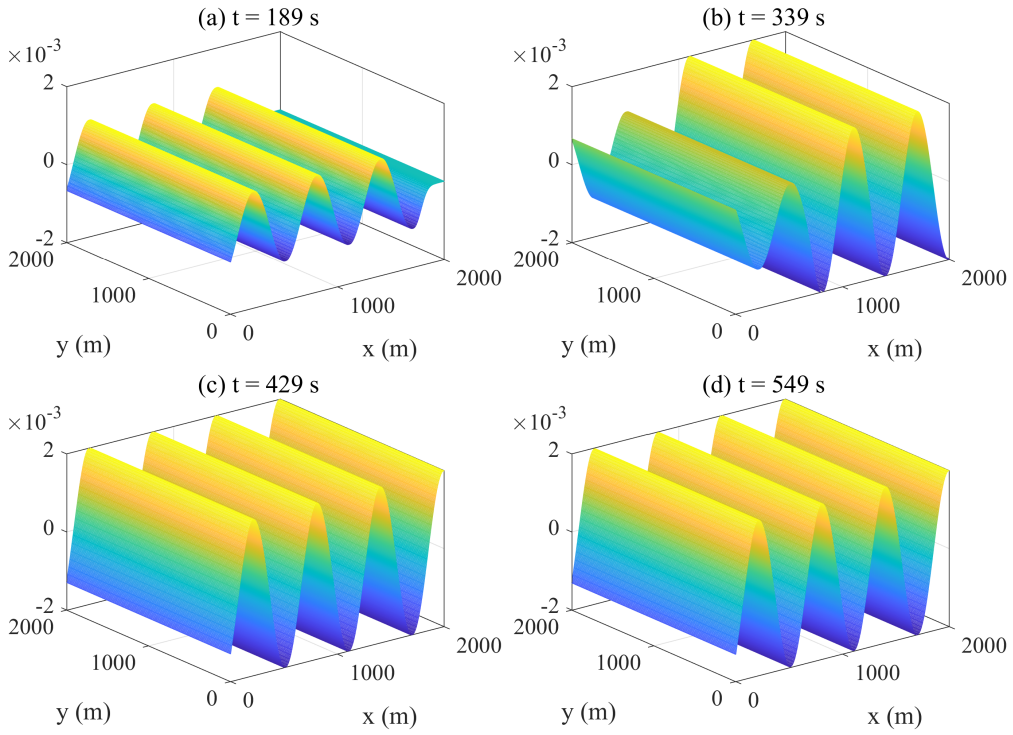

Figure 5.1: Water surface elevation profile at various times

Figure 5.1 illustrates the water surface elevation profile at various times. A train of incident waves, generated at the left boundary, propagates in the positive x-direction as shown in Figure 5.1 (a). After 210 seconds, waves reaching the right boundary are reflected, which propagates in the negative x-direction and overlaps incident waves (see Figure 5.1 (b)). Thus, the surface water elevation becomes twice due to the superposition of incident and reflected waves. After $t = 400$ s, reflected waves reach the left boundary and then are transmitted through the boundary without significant errors. Therefore, the water surface elevation profile is repeated with respect to the period of the incident wave as shown in Figures 5.1 (c)-(d).

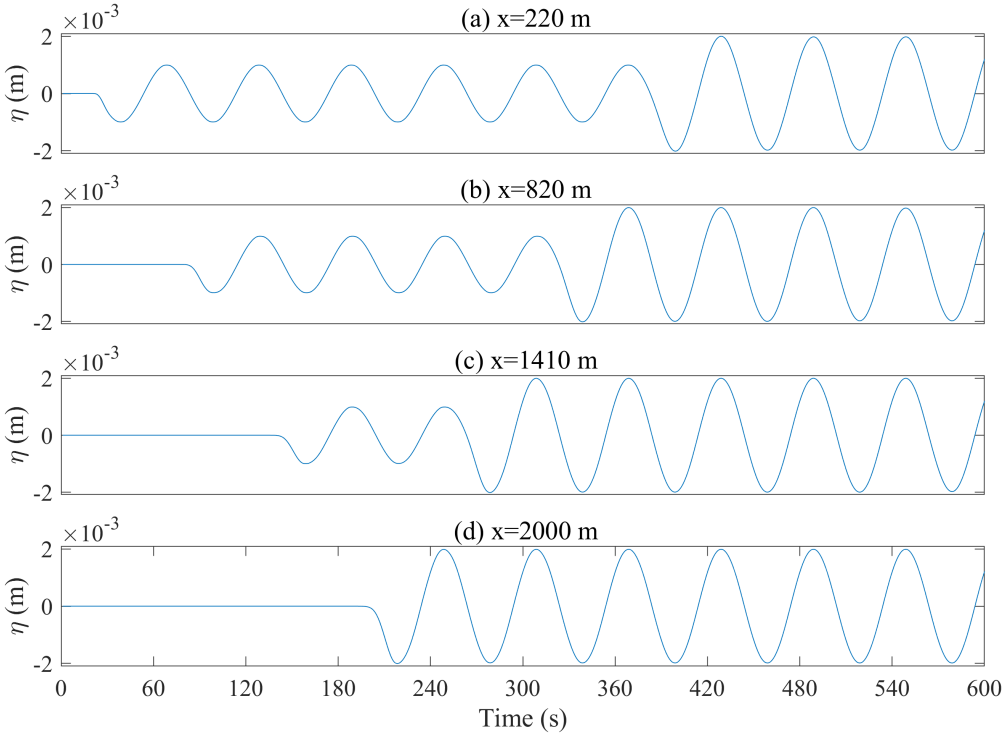

Figure 5.2: Temporal evolution of water surface elevation at several locations

Figure 5.2 shows the temporal evolution of water surface elevation at several locations. Figures 5.2 (a)-(c) show that a train of the incoming waves with an amplitude of 0.001 m is well generated at the left boundary. As shown in Figure 5.2 (d), incident waves reaching the right reflective boundary are reflected. Along the propagation of reflected waves, the water surface displacement becomes twice at different times at x=220, 820 and 1410 m (see Figures 5.2 (a)-(c)). The numerical results at $t = 549$ s show good agreement with the analytical solutions with an error of 0.13%. The results validate that the outgoing (reflected) waves are successfully transmitted through the absorbing-generating boundary without significant errors.

5.3.2 Two-dimensional Sinusoidal Wave Propagation

A train of sinusoidal waves with angle is considered to examine the model performance for the two-dimensional wave problems. A frictionless water tank of 1,000 m $\times$ 1,000 m with a constant depth of 10 m is assumed. A train of the incoming waves with an amplitude of 0.0005 m, a period of 60 s and an angle of 45° is generated at the west and south boundaries. The absorbing boundary condition is imposed on the east and north boundaries. The simulation is continued until 6 sinusoidal waves are generated. A uniform grid size of 10 m and a time step of 0.01 s are adopted.

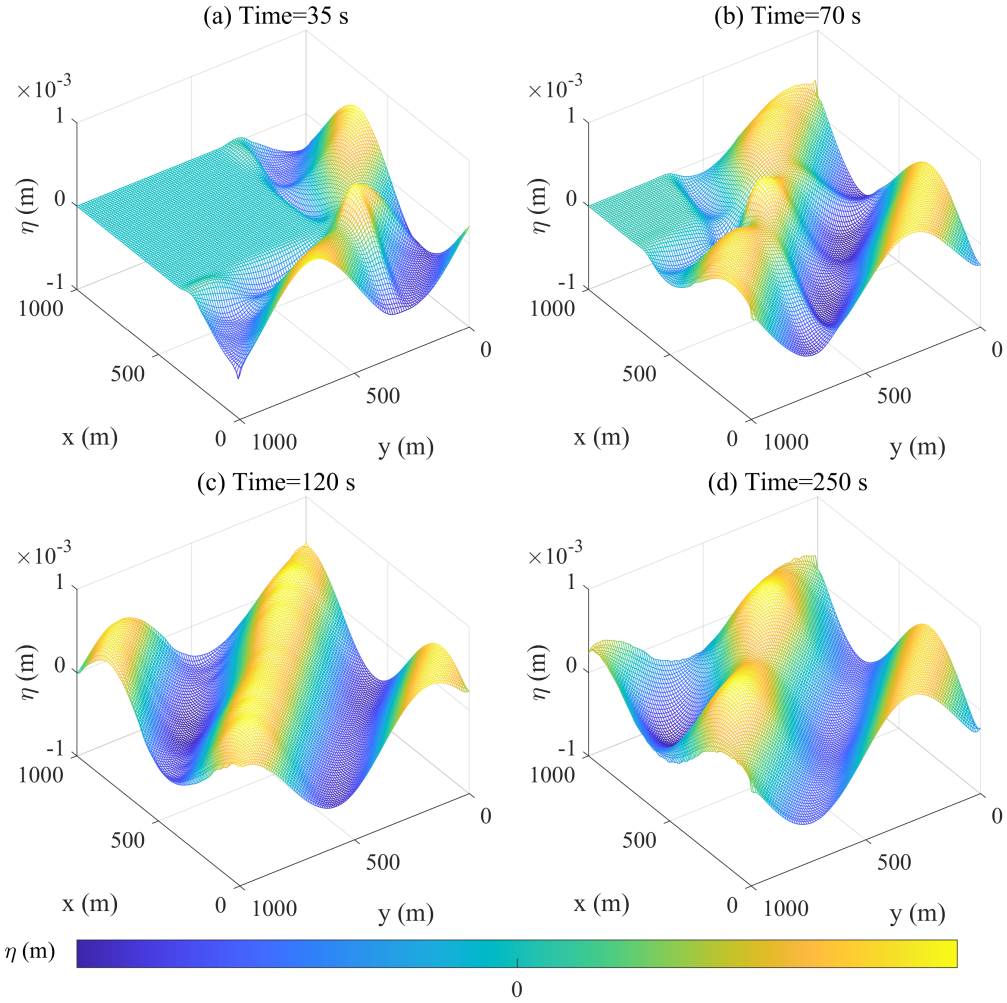

Figure 5.3: Temporal evolution of water surface elevation at different times

Figure 5.3 shows the temporal evolution of water surface elevation at different times. An incident wave with an angle of 45°, generated at the south and west boundaries, propagates in $x-$ and $y-$ directions, as shown in Figures 5.3 (a)-(b). At $t = 120$ s, the leading edge of the incoming waves reach the intersection of the east and north boundaries (see Figure 5.3 (c)) and then the water surface profile is repeated every wave period. Along the wave crest line normal

to the direction of incident wave, a negligible amount of spurious oscillation can be found if the reflected wave is successfully absorbed at the absorbing-generating boundary conditions imposed on the all boundaries. However, figure 5.3 (d) depicts that the outgoing waves are not sufficiently absorbed, which induces the reflected waves within the numerical domain. Therefore, the numerical implementation of the absorbing-generating boundary condition should be further improved.

5.4 Conclusions

An accurate and efficient modeling system through one-way coupling between non-dispersive and dispersive wave solvers is proposed. The Delft3D FM, commonly used for simulating long waves (e.g., tides, storm surges, tsunamis) is adopted as non-dispersive shallow water model whereas the Celeris, capable of simulating relatively short-waves, is employed as dispersive Boussinesq model. The absorbing-generating boundary condition is implemented in Celeris to integrate two models without spurious error at the model boundary. It enables incident waves from non-dispersive model to be generated at the model boundary in dispersive model. Besides, it simultaneously allows the outgoing waves not to be reflected into the inner domain in dispersive model. Special treatment is applied to maintain the wave property and thus match the boundary condition at the model boundary. The proposed system has been tested for 1D and 2D sinusoidal wave propagation. The comparison results show an good agreement for 1D wave propagation, which validates the absorbing-generating

boundary condition can be applied for 1D problems. However, the wave propagation in 2D space shows spurious error due to reflected waves induced at the model boundary. Therefore, the advanced numerical implementations of both absorbing-generating boundary condition and integration of derivatives of Riemann invariant should be necessary. Future study will investigate the contribution of the waves in storm surge and coastal inundation by applying the proposed system to storm surge inundation simulation. The proposed system is expected to contribute to advanced coastal disaster mitigation strategy through accurate and fast modeling of shallow water waves.

Chapter 6

Assessment of Future Storm Surge Flooding Risks

Storm surge modeling based on Typhoon Maemi (2003) was performed to evaluate the potential risks of future storm-induced flooding under the general climate change scenarios suggested by IPCC AR5. The three physical contributors affecting the expected exacerbation of flooding damage in a coastal region (i.e., sea-level rise (SLR), direct runoff (DR), and tropical cyclones (TCs)) were examined separately and in combination in the modeling. Using a coupled hydrologic-hydrodynamic model, the flooding extent during the storm event under current and year 2100 climatic conditions was analyzed, and the influence of each component on the flooding risk was determined. Comparing the results indicated that SLR was the most influential single flooding component exacerbating the future flooding risk, and that TC intensifcation was two-thirds as significant as SLR. Despite its significant expected growth in the future, it was anticipated that DR will have a minor contribution and limited influence. Apart from their contributions to the aggravation of the flooding level, the impacts of these drivers on the flooding danger were quite distinct. In addition,

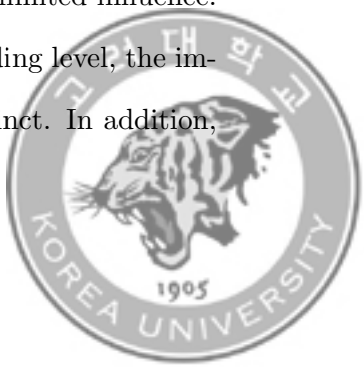

the results considering the combination of both SLR and TC intensification indicated that nonlinear interactions between the components might occur and further exacerbate the damage caused by flooding. Finally, depending on the level of global warming, future storms with amplified TC attributes are likely to worsen the maximum flooding damage in the study area by up to 28.7% in flooding extent and 236.6% in flooding volume compared to current conditions without changing the spatial pattern of the flooding depth distribution.

6.1 Introduction

Under the continuing global warming, storm surge flooding and its related dangers in coastal regions have been seen to grow [190]. Sea level rise (SLR), tropical cyclone (TC) strengthening, and enhanced direct runoff (DR) as a result of intensified typhoon rainfall are among the various variables that aggravate the likelihood of flooding [e.g. 191, 192, 193, 5]. All of these variables are associated with the well known global temperature changes. According to the Fifth Assessment Report (AR5) of the Intergovernmental Panel on Climate Change [194], the global average temperature has risen by 0.85°C from 1880 to 2012, causing the global mean sea level to rise by roughly 0.19 m [195]. Similarly, the global water cycle change caused by climatic warming has led to an increase in the average rainfall in the mid-latitude region of the Northern Hemisphere since 1900.

It has been shown that the increasing trend in sea surface temperature (SST) affects the development and occurrence patterns of TCs. For instance,

the strength of TCs has been rising globally, but the frequency of extreme TCs are becoming has decreased. This indicates that future TCs are more likely to exhibit amplified typhoon rainfall as well as intensified pressure and wind fields [e.g. 196, 197]. One intriguing research warns that global SLR can surpass 2 m by 2100 if the melting ice sheets contribution under high greenhouse gas (GHG) emissions scenarios is considered [198].

As a result of its location in the pathway of frequent TCs, the Korean Peninsula is frequently exposed to catastrophic storm damage; hence, forecasting storm risks has received much attention. Typhoon Maemi (also known as Typhoon Pogi in the Philippines) is the most devastating typhoon to have ever struck the Korean Peninsula, according to [199]. As listed in Table 6.1, with a minimum central pressure of 910 hPa and a maximum instantaneous wind gust of 60 m/s, it was the most destructive typhoon to ever strike the Korean Peninsula. The historical TC records for the Korean Peninsula from 1937 to 2019 are ranked by maximum wind speed in Table 6.1. As it landed in conjunction with the flood tide, massive storm surges were created and caused major flooding damage in the low-lying floodplain [e.g. 200, 180, 201, 202, 5, 203]. This event caused 132 deaths or disappearances, about 61,000 individuals to be impacted, and approximately 5 billion in property loss.

In addition to the rise in surge levels caused by pressure and wind, rainfall-induced runoff may further exacerbate flooding damage during TC event. [e.g. 204, 205, 206, 193, 207, 5]. In particular, When a storm surge is accompanied by rainfall, the combined impact of higher sea level and rapid riverine flow at the basin outlet exacerbates the flooding damage. [e.g. 208, 209, 210].

This indicates that river runoff from heavy rainfall associated with a TC might contribute to flooding processes interactive with tides and storm surges [e.g. 211, 212, 206]. Storm surges and DR owing to typhoon rainfall in coastal regions including river basins are not mutually exclusive processes, according to [e.g. 211, 212, 206, 213, 214]. In addition, several studies [e.g. 215, 216, 217] evaluated river discharge and storm surge to assess the flooding risk during typhoons. Recent research by Lee et al. [5] developed a coupled hydrologic-hydrodynamic model to evaluate the role of DR to storm surge flooding. Employing this model to a historical typhoon, it has been verified that the serious flooding damage was caused not only by the increased surge level but also by the DR. Given that storm surge flooding is essentially reliant on these hydrodynamic conditions, it is pretty apparent that future climatic changes will aggravate storm surge flooding even more.

In general, the flooding risk ralated with storm surges has been analyzed by modelling hypothetical TC events that have been statistically extrapolated from historical data. This conventional method does not account for all flooding sources, including as SLR, DR during TCs, and their interactions, limiting its ability to assess the consequences of climate change completely. Since strengthened typhoons with greater rainfalls are likely to emerge in the mid-latitude region of the Northern Hemisphere, it is insufficient to estimate future flooding damage in coastal regions by evaluating each flooding driver independently. In assessing future storm surge hazards, it is essential to take climatic factors, particularly SLR, enhanced DR, and TC, into account thoroughly.

Different studies examining the future TC strength have yielded conflicting

Table 6.1: Historical typhoons on the Korean Peninsula (1937-2019)*

Rank	Name (year)	Max. instantaneous wind speed (m/s)
1	Maemi (2003)	60.0
2	Prapiroon (2000)	58.3
3	Rusa (2002)	56.7
4	Chaba (2016)	56.5
5	Lingling (2019)	54.4
6	Nari (2007)	52.4
7	Bolaven (2012)	51.8
8	Ted (1992)	51.0
9	Vera (1986)	49.0
10	Nabi (2005)	57.3

*These data are from the Korea Meteorological Administration (`https://www.weather.go.kr`).

conclusions on its tendency, although the majority of scientists agreed that global warming would increase the worldwide mean intensity of TCs. In addition, several studies have analyzed storm surge threats in East Asia under future climate change. Using a stochastic typhoon model, Yasuda et al. [218] studied typhoon characteristics under present and anticipated future climatic conditions. On this basis, scientists ran simulations by feeding the stochastic model results into an atmospheric general circulation model (AGCM), which indicated that the likelihood of stronger typhoons arriving in Japan would rise. According to the four scenarios given by IPCC AR5, Nakamura et al. [219] used SST, atmospheric air temperature, and relative humidity as variables. Using the Advanced Research Weather Research and Forecasting model (ARW-WRF), they created the climatic conditions of Typhoon Haiyan (2013)

that struck the Philippines in 2013. Based on the numerical simulation using a finite volume community ocean model (FVCOM), they predicted that typhoons would be more intense, so the Philippines will experience greater surge heights. Kim et al. [220] split climatic periods surrounding the Korean peninsula into the present (1979–2003), near-future (2015–2039), and future (2075–2099) climate periods and generated climate conditions based on varying SSTs conditions in an AGCM. Using the Surge, WAve, and Tide (SuWAT) model, they performed a numerical simulation to assess the potential risks in surge levels under a future SLR of 0.6 m. They revealed that the future climate would effect storm surges by reducing the height of storm surges on the west coast of the Korean Peninsula while increasing the height of storm surges on the south coast. Therefore, previous research associated with storm surges in East Asia under future climatic scenarios have shown that strengthened typhoons would strike the south coast of the Korean Peninsula, and the height of the storm surge will surely grow. However, research on future storm surge flooding that addresses all flooding factors is quite uncommon. Few studies have studied storm surge flooding by including both storm surge and river runoff concurrently, which is particularly significant for coastal communities that incorporate rivers. Even in such instances, climate change-caused flooding damage has seldom been assessed.

The coupled hydrologic-hydrodynamic model was employed to simulate storm surge flooding under climatic conditions of the year 2100. To sufficiently account for the changing climate and the related changes to SLR, DR, and TC, numerous future storm surge scenarios based on Typhoon Maemi (2003) that

had been adjusted under generic climatic circumstances were constructed. The representative concentration pathway (RCP) scenarios published by IPCC AR5 were used to generate the future climatic conditions based on the established physical properties of typhoons in the year 2100. RCP4.5 (i.e., intermediate emissions) and RCP8.5 (i.e., extremely high emissions) were utilized to give typical climatic conditions across the four RCP scenarios indicating the growth of GHG emissions and their atmospheric concentrations. Typhoon Maemi (2003) and its features were chosen as a model TC. Changing the path of a typhoon is anticipated to change not only the amount of flood damage but also the territory that will be impacted. Several research [e.g. 219, 220, 221] have shown that the strength and path of the TCs would vary as a result of climate change, however Nayak and Takemi [197] suggested that the current TC tracks are expected to stay substantially constant with a greater intensity as the climate warms. Karim and Mimura [177] studied storm surges using a 1D hydrodynamic model excluding the TC track change in order to predict the future flooding risk in Bangladesh resulting from climate change and SLR. Similarly, the primary objective of this research is to examine the impacts of future changes in sea level, DR, and TC strength on storm inundation, and not the change in typhoon paths, which is known to have a significant impact on storm surge heights [219].

Consequently, the TC intensity was modified according to generic climate conditions, while the TC track was isolated without any adjustment [177]. The SLR and an increasing rainfall intensity were projected to constitute the storm environment in the future.

The contents of this chapter are as follows. Section 6.2 introduces the coupled hydrodynamic-hydrologic model and the generic climatic scenarios employed in the present study. Section 6.3 describes the input data, the climatic conditions classification utilized by the model for the numerical simulations and the numerical model setup. Finally, Section 6.4 and Section 6.5 present the simulation results and the conclusions, respectively.

6.2 Modeling Methods

6.2.1 Coupled Hydrodynamic-Hydrologic Model

the coupled hydrodynamic-hydrologic model, developed by Lee et al. [5], was applied to predict storm surge flooding under current and future climatic conditions. This comprehensive modelling framework was developed in order to account for the cumulative impacts of tides, surges, and DR on flooding during the storm event. Therefore, the combined model integrates hydrodynamic (Delft3D Flexible Mesh Suite) and hydrologic (HEC-HMS) models to permit a simultaneous analysis of several storm-induced flooding drivers (i.e. tides, surges, and riverine flows) and their interactions. Each component is detailed briefly below, followed by the coupling technique.

Delft3D Flexible Mesh Suite (Delft3D FM), developed by Deltares [187], is a multidimensional model applicable to unsteady flow and transport phenomena under various oceanic configurations, such as storm surges, tsunamis, density variations, sediment transport, and pollutant dispersion. In Delft3D FM, unsteady nonlinear shallow water equations (NSWEs) are solved in both

2D and quasi-3D spaces by employing a σ coordinate system [e.g. 222, 223]. A depth-integrated hydrodynamic model has advantage of computational efficiency for simulating long waves such as tides and storm surges was employed. The governing equations for two-dimensional horizontal flow are given by:

$$
\begin{aligned}
&\frac{\partial \zeta}{\partial t}+\frac{1}{G_\xi G_\eta}\frac{\partial\left\{u(d+\zeta)G_\eta\right\}}{\partial \xi}+\frac{1}{G_\xi G_\eta}\frac{\partial\left\{v(d+\zeta)G_\xi\right\}}{\partial \eta}=(d+\zeta)Q \\
&\frac{\partial u}{\partial t}+\frac{u}{G_\xi}\frac{\partial u}{\partial \xi}+\frac{v}{G_\eta}\frac{\partial u}{\partial \eta}+\frac{uv}{G_\xi G_\eta}\frac{\partial G_\xi}{\partial \eta}-\frac{v^2}{G_\xi G_\eta}\frac{\partial G_\eta}{\partial \xi}+\frac{g}{G_\xi}\frac{\partial \zeta}{\partial \xi}-fv \\
&\quad=-\frac{1}{\rho_0 G_\xi}\frac{\partial P_a}{\partial \xi}+\frac{(\tau_{s\xi}-\tau_{b\xi})}{\rho_0(d+\zeta)}+F_\xi+M_\xi \\
&\frac{\partial v}{\partial t}+\frac{u}{G_\xi}\frac{\partial v}{\partial \xi}+\frac{v}{G_\eta}\frac{\partial u}{\partial \eta}+\frac{uv}{G_\xi G_\eta}\frac{\partial G_\eta}{\partial \xi}-\frac{u^2}{G_\xi G_\eta}\frac{\partial G_\xi}{\partial \eta}+\frac{g}{G_\eta}\frac{\partial \zeta}{\partial \eta}+fu \\
&\quad=-\frac{1}{\rho_0 G_\eta}\frac{\partial P_a}{\partial \eta}+\frac{(\tau_{s\eta}-\tau_{b\eta})}{\rho_0(d+\zeta)}+F_\eta+M_\eta
\end{aligned}
\tag{6.1}
$$

where ζ is the surface elevation above the datum level; d is the water depth under the datum level; $\sqrt{G_{\xi\xi}}$ and $\sqrt{G_{\eta\eta}}$ are conversion factors used in the curvilinear coordinate system; ξ and η are the horizontal axes; Q is the additional source or sink of water due to inflow or outflow, rainfall, and evaporation; u and v are the horizontal flow velocity in the ξ and η directions, respectively; M_ξ and M_η are terms originating from Q; ρ_0 refers to the reference density of water; P_a is the atmospheric pressure at a free surface; f refers to the Coriolis parameter; F_ξ and F_η represent the horizontal turbulent stresses; $\tau_{s\xi}$ and $\tau_{s\eta}$ refer to the wind-driven shear stress on the free surface; and $\tau_{b\xi}$,and $\tau_{b\eta}$ represent the frictional stress on the bed. It should be noted that the additional

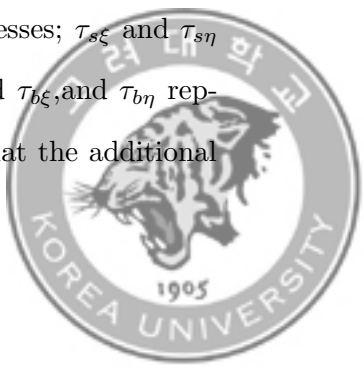

source terms Q, M_ξ and M_η are responsible for accommodating the runoff discharge at the river outlet calculated from the hydrologic model.

HEC-HMS, the hydrologic model consisting of the coupled model, was developed by the U.S. Army Corps of Engineers to track the hydrological response of the basin during a rainfall event [224]. It is capable of analyzing urban floods, frequency of flooding, and reservoir spillway capacity and producing a hydrograph at river outlet. Therefore, the runoff discharge at the basin exit during the severe rainfall event under future climatic circumstances can be calculated through HEC-HMS.

The integration of Delft3D FM with HEC-HMS was performed through a one-way data exchange method. The runoff estimation was carried out by applying the hyetograph corresponding to the simulation period in HEC-HMS, which subsequently generated a hydrograph at the basin outlet. The hydrograph then provide Delft3D FM with the discharge conditions at the river outflow border. Throughout this communication between the models, their spatio-temporal resolutions were set to be the same; otherwise, discontinuous dataflow might result in an undesirable error. The time interval of data exchange between Delft3D FM and HEC-HMS was adjusted to one minute. Lee et al. [5] provides further information on the integrated model and the data exchange method.

6.2.2 Scenario Setup

Storm surge flooding under future climate scenarios can be evaluated by modifying hydrodynamic and meteorological characteristics in the model based on

future climate conditions (see Figure 6.1). The IPCC AR5 and Korean Meteorological Administration (KMA) climate scenarios were used to estimate the SLR due to climate change [225]. Based on HadGEM2-AO, a coupled atmosphere-ocean general circulation model developed by the United Kingdom Met Office Hadley Centre [226], IPCC AR5 forecasts global climate information until the year 2100 with a geographic resolution of $1,875° \times 1,250°$. Using a regional climate model (HadGEM3-RA), KMA [225] projects more precise global climate information at a regional scale of 12.5 km for the Korean Peninsula. Over the northwest Pacific, including the Korean Peninsula. The impact of SLR on storm surge development is fairly significant. Consequently, the SLR anticipated at the global scale was included into the model domain (see Figure 6.2). Under RCP4.5 and RCP8.5 scenarios, the sea level is projected to increase by 0.706 m and 0.885 m, respectively. Moreover, both scenarios predict that the increases in SLR during the first half of the century would be relatively rapid compared to those in the second half of the century.

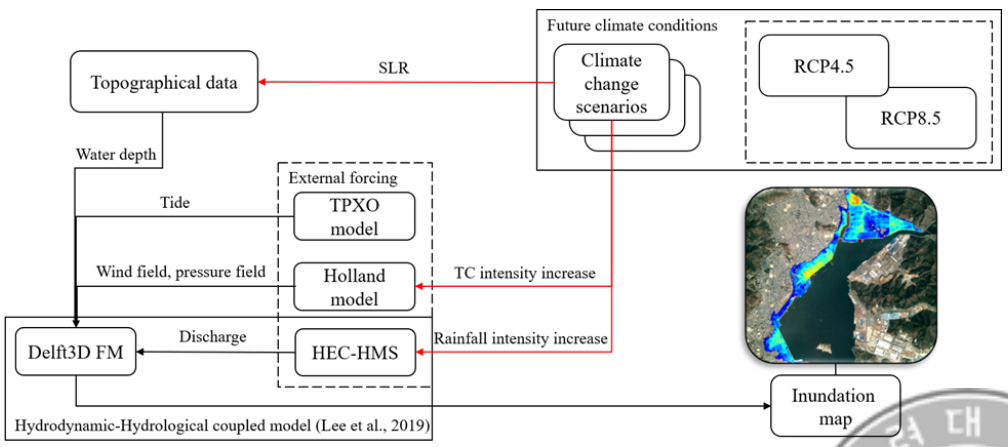

Figure 6.1: A schematic overview of the storm surge simulation under future climate scenarios

The SST change is a primary issue in TC studies since they account for the continuance and development of future TCs. There is a direct relationship between TCs and climate change, however it is difficult to precisely define the changes in TCs. Various types of research have been conducted to examine future changes in the frequency and intensity of TCs using a variety of methods, such as stochastic approaches based on probability assessment and numerical experiments involving global and regional climate models alone or in combination [e.g. 177, 227, 228, 229, 230, 219, 231]. Nevertheless, it is generally accepted that the rise in SST due to climate change is the primary driver of the rising frequency and intensity of tropical cyclones [e.g. 175, 176, 177]. For instance, Mei et al. [230] examined the patterns of intensifying typhoons in the northwest Pacific as a result of a rise in SST. On the Saffir-Simpson scale, they determined that the strength of typhoons will increase from Category 2 to Category 5 under the RCP4.5 scenario. According to IPCC AR5, although the frequency of typhoons would not rise globally by the end of the 21st century, their strength is predicted to increase, indicating that the growth rate of typhoons will reach between 2 and 11% at the end of the century [232].

Despite several studies have conducted future TCs simulation based on future SST conditions, the application of the predicted TC strength varies [e.g. 177, 230, 219, 231]. Similarly, diverse results have been achieved from relevant research due to the application of individual approaches [e.g. 219, 231]. Therefore, we determined a generic value for the TC intensification due to future climate change by examining data sets from previous rsearch; the rise in the maximum wind speed and the drop in the central pressure of TCs intensified

Table 6.2: Climate configurations of SLR, DR and TC in each scenario

Scenario ID	SLR	DR	TC intensity
S0DR0TC0	Current^{+}	Current	Current
S1DR0TC0	RCP4.5	Current	Current
S0DR1TC0	Current	RCP4.5	Current
S0DR0TC1	Current	Current	RCP4.5
S1DR1TC0	RCP4.5	RCP4.5	Current
S1DR0TC1	RCP4.5	Current	RCP4.5
S0DR1TC1	Current	RCP4.5	RCP4.5
S1DR1TC1	RCP4.5	RCP4.5	RCP4.5
S2DR2TC2	RCP8.5	RCP8.5	RCP8.5

$^{+}$'Current' condition refers to the climate at the time of Typhoon Maemi (2003)

by SST changes were estimated accordingly [e.g. 177, 219, 230].

Karim and Mimura [177] studied the effects of SST rise and SLR on the TC intensity based on Emanuel [233] and Ali [234] utilizing 1991 cyclone. As the SST rose 2 and 4 °C, the maximum wind speed rose by 9.3 and 21.8%, and the central pressure deficit rose by 2 and 5 hPa. Nakamura et al. [219] estimated future typhoons depending on the four RCP scenarios using the ARW-WRF model for Typhoon Haiyan (2013). In the RCP4.5 and RCP8.5 scenarios, the average SST rose by 0.92 and 2.16°C, respectively. Accordingly, the maximum wind speed rose by 6.5 and 11.8%, and the minimum central pressure dropped by 14 and 22 hPa. Mei et al. [230] employed TC data from the Joint Typhoon Warning Center (JTWC) best-track dataset to examine the upward trend in the seasonal mean lifetime peak strength of typhoons during 1951∼2010. In 2100, according to the RCP4.5 scenario, the severity of typhoons is anticipated to

rise by around 14%. Typhoon Haiyan (2013) is the most intensely comparable to Typhoon Maemi (2003) among the typhoons adopted in previous research [e.g. 177, 219, 230]; hence, the results from Nakamura et al. [219] were applied to Typhoon Maemi (2003).

Rainfall related to typhoon is predicted to rise as a result of climate change, however it is difficult to predict with precision [e.g. 235, 236, 237, 238, 239]. Choi et al. [240] studied the effects of meteorological factors on maximizing rainfall associated with TC based on Typhoon Maemi (2003) adopting the WRF model. They suggested that the total amount of precipitation on the Korean Peninsula would grow randomly in conjunction with the rise in SST and surface air temperature (SAT). According to Choi et al. [240] and the projected SST rise under RCP4.5 and RCP8.5 would increase typhoon rainfall on the Korean Peninsula by roughly 50 and 67.5%, respectively. Consequently, the rainfall intensity increases in 2100 under the two scenarios were set to 50 and 67.5%, respectively.

A time lag between storm surge and rainfall significantly affects the inundation risk [e.g. 241, 242]. Previous studies [e.g. 243, 244, 245, 246] have assumed the time lag between storm surge and rainfall as constant in order to evaluate the contribution of rainfall intensification under different conditions (e.g., climate change scenario, return period) on the inundation risk. Thus, the temporal patterns of rainfall events in future climatic scenarios were determined to be identical to those observed during Typhoon Maemi (2003). The increased DR was determined by a rainfall-runoff analysis taking into account the amplified typhoon rainfall under future climatic circumstances.

As a result, nine scenarios were developed in which three of the parameters (i.e., SLR, DR, and TC intensities) were manipulated separately or in combination to assess their influence on storm-induced overland flooding. The climatic conditions at the time of Typhoon Maemi (2003), were referred to as current conditions. Table 6.2 outlines the specific conditions of each scenario. It should be noted that the scenario IDs in the table accurately represent the features and important circumstances of each scenario. SLR is thus abbreviated as S in the scenario ID, where represents the severity of the situation. Similarly, DR and typhoon intensity are denoted as DR and TC, respectively. As a result, the number '0' corresponds to the current climatic conditions, while '1' and '2' represent the conditions corresponding to RCP4.5 and RCP8.5 scenarios, respectively. For example, scenario S1DR0TC0 depicts the projected sea level under RCP4.5 and current state of DR and TC intensity. In each scenario, the different combinations of RCPs were designed to quantify the influence of each component relative to the effects of the others. In other words, comparing S0DR0TC1 and S0DR1TC1 will illustrate the consequences of a rise in DR with increasing typhoon rainfall. The physical properties of SLR, TC, and precipitation may be calculated based on the situations outlined in Table 6.2.

6.3 Model Application

6.3.1 Bathymetry and Model Typhoon

A single layer of varying grid sizes was arranged using an unstructured grid with different polygons, enabling the numerical model to compute simultaneously

from the coarse grids of the outside region to the high-resolution grids of the inner region of interest (see Figure 6.2). To incorporate the impacts of wind and pressure fields during the typhoons over the entire domain, grid sizes were constructed to span from large (dx = 35 km) on the northwestern Pacific region, to small (dx = 8 m) focusing on the target area.

The model's stability was improved by minimizing errors caused by the abrupt reduction in grid size by reducing the grid sizes by a factor of $3sim5$ in six stages from the outermost region to the srudy area. In addition, a curvilinear and flexible grid was employed for the finest local domain in order to simulate the flooding process with river flow conditions at Masan Bay precisely and effectively. The global datasets including the General Bathymetric Chart of the Oceans (GEBCO) and the Shuttle Radar Topography Mission (SRTM) 4.0 [247], the digital nautical chart from the Korea Hydrographic and Oceanographic Agency, and the LiDAR DEM from the National Geographic Information Service in Korea were combined to provide bathymetry. For accurate modeling of storm-surge flooding, the hydrodynamic methodology that considers overland physical interactions between topography and water should be used; the so-called 'bathtub' approach is incapable of reflecting the dynamic nature of coastal inundation, such as hydrodynamic processes and bottom frictions, and is therefore known to overestimate the flooding extent [248].

Typhoon Maemi (2003) was adopted as the model typhoon and various scenarios were simulated based on the model typhoon. The reference tide was designed as the state of the tide during the model typhoon. The hydrological data from Lee et al. [5] were used as inputs to HEC-HMS in order to assess

the rainfall-runoff and hence predict riverine discharges at river outlets located in the finest domain.

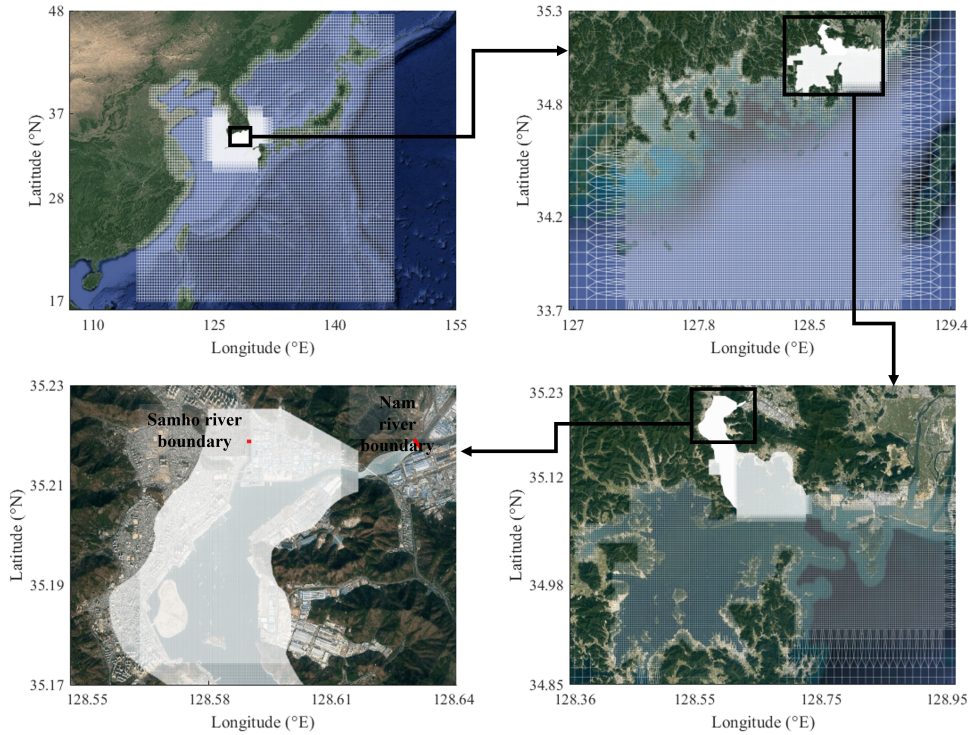

Figure 6.2: Different levels of detail on the constructed flexible mesh. The solid red lines indicate river boundary where boundary conditions for Nam and Samho rivers were imposed

6.3.2 SLR, DR and TC Conditions

Changes on a centennial scale in SLR, DR, and TC intensity as a result of climate change are very important factors. For the quantitative evaluation and comparison of the impacts of SLR, DR, and TC characteristics on storm surge flooding, projected climatic conditions since Typhoon Maemi (2003) were used to define different SLR, DR, and TC properties. As indicated in Table 6.3, the

SLRs for the 'S0' scenario series were set to zero to represent the continuation of the current climatic conditions. Under RCP4.5 ('S1' series) and RCP8.5 ('S2' series), the SLR for the year 2100 was estimated to be 0.706 and 0.885 m, respectively.

According to Choi et al. [240], the cumulative rainfall during Typhoon Maemi (2003) is expected to rise by 50 and 67.5% in 2100 under the RCP4.5 and RCP8.5 scenarios, respectively. The increased rainfall intensities in 2100 were determined by multiplying the measured rainfall records during Typhoon Maemi (2003) by the increase rate under future scenarios. Then, the strengthen DR was approximated by rainfall-runoff analysis utilizing 50 ('DR1' series) and 67.5% ('DR2' series) greater rainfall under RCP4.5 and RCP8.5, respectively. Figure 6.3 shows the current (equivalent to recorded) and future rainfall intensities under the two RCP scenarios. The resulting hyetographs were entered into the HEC-HMS to generate hydrographs for the Nam and Samho River mouths in Masan Bay. Figure 6.4 illustrates the HEC-HMS-calculated runoff levels (i.e. discharges) at outputs. Future variations in rainfall will be significantly distinct from the current condition.

As seen in Figure 6.3, the rainfall event during Typhoon Maemi (2003) may be generally sub-divided into two storm events (Event R_1 and R_2). Former event R_1 had two-thirds of the entire quantity of typhoon rainfall and had no meaningful impact on the flooding process. It did, however, contribute to the high moisture conditions of the soil in the research location, which were expected to enable the subsequent Event R_2 to generate DR without a large lag period. Figure 6.4 demonstrates that Events R_1 and R_2 had distinct reaction

times of DR; Event R_1 required around 3 hours to initiate DR, while Event R_2 created DR nearly instantly due to the preceding rainy circumstances. Consequently, the DR induced by Event R_2 might interact with the storm surge instantaneously, hence exacerbating the flooding damage.

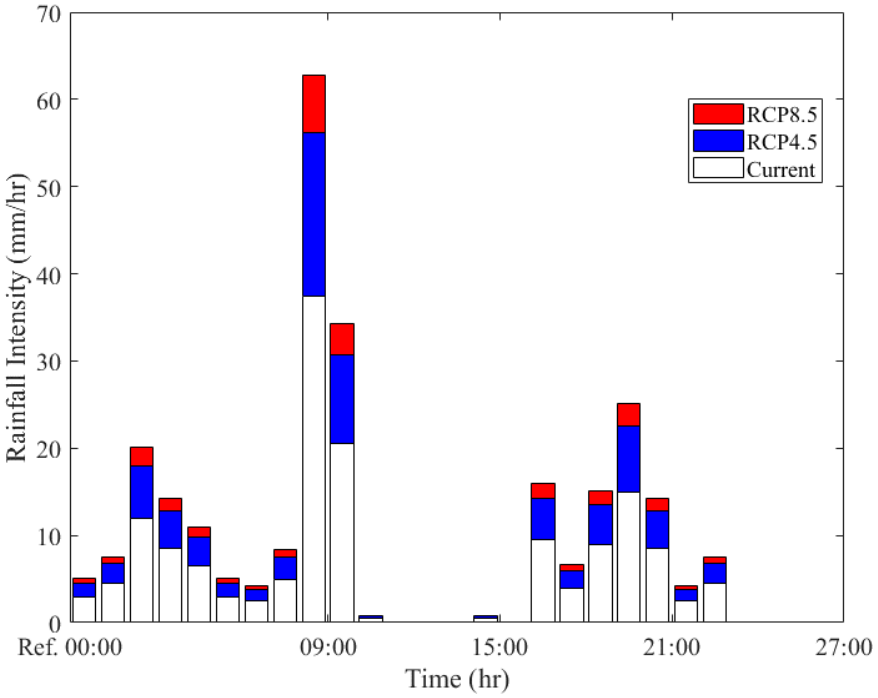

Figure 6.3: Stacked hyetograph of Typhoon Maemi (2003) under current and future climate conditions. Reference time is set to 15:00 on September 11, 2003.

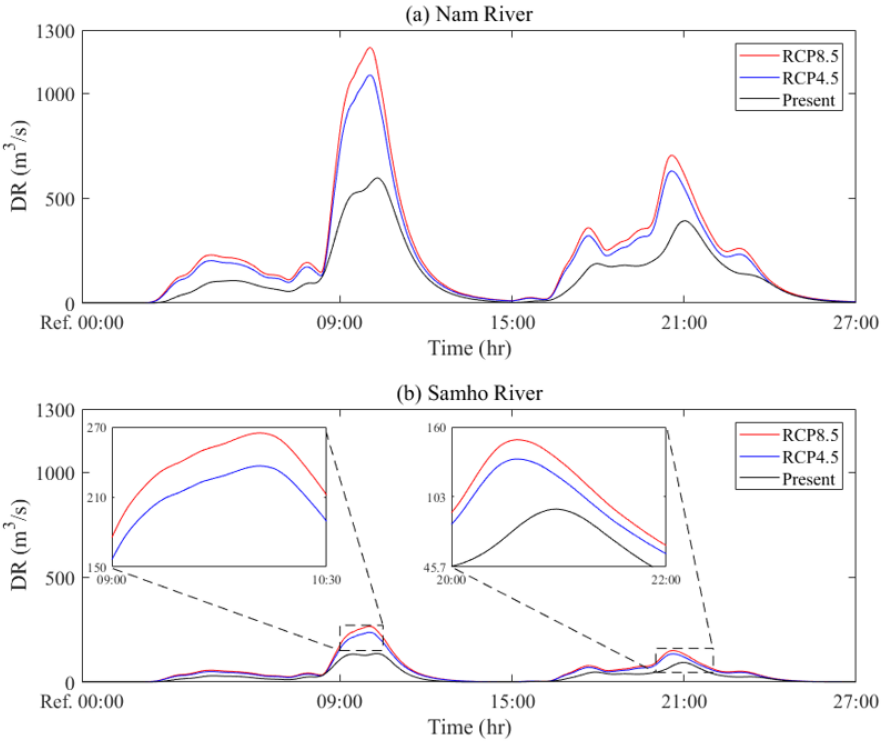

Figure 6.4: Calculated hydrographs at basin outlets during Typhoon Maemi (2003) under current and future climate conditions. Reference time is set to 15:00 on September 11, 2003. (a) Nam River, (b) Samho River

The TC properties are subject to alter depending on future climatic conditions. The highest wind speed and lowest central pressure of Typhoon Maemi (2003) were measured at 54 m/s and 910 hPa, respectively, at the time of its landfall, marked as 'TC0'. Based on the examination of several data sets from previous research [e.g. 177, 230, 219], the maximum wind speed of model typhoon is projected to increase to 57 or 60 m/s, while the lowest central pressures are projected to decrease to 896 or 888 hPa under RCP4.5 ('TC1' series) and RCP8.5 ('TC2' series), respectively. Table 6.3 provides detailed informa-

tion on the TC properties for each scenario. On the basis of this data, future storm surge simulations were performed, and the maximum flooding extent and volume were determined [248]. The following section provides detailed on the entire simulation results.

Table 6.3: Generic characteristics of current and future SLR, TCs and DR

Scenario ID	Max. wind speed (m/s)	Min. central pressure (hPa)	SLR (m)	Increase rate of rainfall intensity (%)
S0DR0TC0	54	910	0	0
S1DR0TC0	54	910	0.706	0
S0DR1TC0	54	910	0	50
S0DR0TC1	57	896	0	0
S1DR1TC0	54	910	0.706	50
S1DR0TC1	57	896	0.706	0
S0DR1TC1	57	896	0	50
S1DR1TC1	57	896	0.706	50
S2DR2TC2	60	888	0.885	67.5

6.3.3 Storm Surge Numerical Modeling Setup

The model bathymetry was altered to account for the SLR. Since all bathymetry and topography datasets were set based on the mean sea level (MSL), it was necessary to adjust the MSL to account for the anticipated SLR at a global scale. To account for SLR, the rise in sea level must be incorporated in the model bathymetry. The overall bathymetry and topography data for scenarios S1 and S2 were 0.706 and 0.885 m lower than those for the current climatic conditions.

The wind and pressure fields of the TC were computed using Holland's model (1980) to account for the surge effects due to wind and pressure gradient in the Delft3D FM. The track data of model typhoon obtained from the KMA was updated according to the T1 and T2 series and input into Holland's model (1980) to calculate the wind and pressure fields of the strengthened typhoon. The wind drag coefficient of 0.0012, used in Lee et al. [5], was adopted, regardless of the climate condition. Then, the wind and pressure fields were entered as external shear stresses on the surface into the Delft3D FM.

Two boundary conditions for applying the riverine flows from the Nam and Samho rivers were employed. Unless DR occurs as a result of typhoon rainfall, the surface water level of the river changes along with the tide, so the tide dominates the baseflow. Therefore, the Riemann boundary condition is applied such that the river border's sea level oscillates in the same manner as the tide. In the case of DR, the discharge boundary condition is applied in order to allocate the DR determined by the rainfall-runoff analysis. For the DR1 and DR2 series, the DR computed using the amplified typhoon rainfall was used. As a consequence of the strengthened intensity of typhoon rainfall under the RCP4.5 and RCP8.5 scenarios, the peak flow rates of the Nam River rose by 82.4 and 104.4%, respectively.

The Manning's roughness coefficient n, which accounts for bottom friction effects, can be dependent on land surfaces (e.g., forest, road covering of concrete, sand, etc.). Nevertheless, the Manning's roughness coefficient is often adopted as a constant to inhibit uncertainties derived from the consideration of empirical values for diverse land types [e.g. 249, 250, 251, 252]. Therefore,

we adopted a constant bottom friction coefficient of $n = 0.026$ s/m$^{1/3}$ in the Manning's formula for the entire numerical domain, as used in Lee et al. [5].

6.3.4 Reference Scenario under the Current Climate Conditions (S0DR0TC0)

Prior to the future storm surge simulations, a storm surge under the current climatic conditions (a reference scenario, S0DR0TC0) was simulated to give a fundamental foundation for the quantitative evaluation of the future flooding risk. This scenario was designed specifically to illustrate the devastation caused by flooding at Masan Bay, where the worst flooding damage was reported when Typhoon Maemi struck in 2003. Therefore, the reference scenario was simulated under the reference tide, typhoon, and rainfall conditions (cf. SLR = 0). Figure 6.5 compares the observed and simulated water elevations at Masan tide station under the reference scenario. The reference scenario shows good agreement with the observed data in terms of maximum water elevation and its occurrence time. The simulated results produced a maximum elevation of 2.87 m, indicating relative error of 6.8% with the observed maximum elevation of 3.08 m. Besides, its occurrence time was calculated as 12:47 on September 12, which is almost equal to the observed one. The tidal condition during the Typhoon Maemi (2003) was accurately reproduced either. Therefore, the reference scenario was found to reasonably reproduce the hydrodynamic conditions near the Masan Bay during Typhoon Maemi (2003).

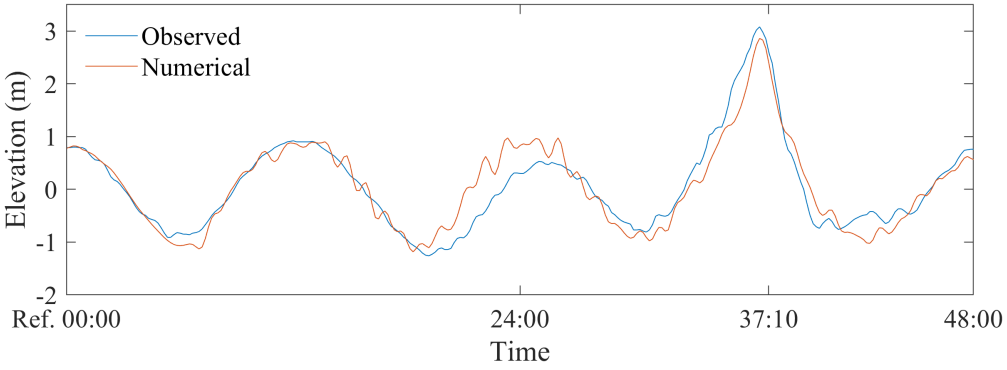

Figure 6.5: Comparison of the observed and numerical water elevations at Masan tide station under the reference scenario. Reference time is set to September 11, 2003

Figure 6.6 depicts the maximum flooding depth induced by the storm surge, tide, and DR during the storm surge event, which is in excellent agreement with the provided data [5]. By comparing this results with those under future scenarios, it is possible to quantify the influence of these variables on overland floods.

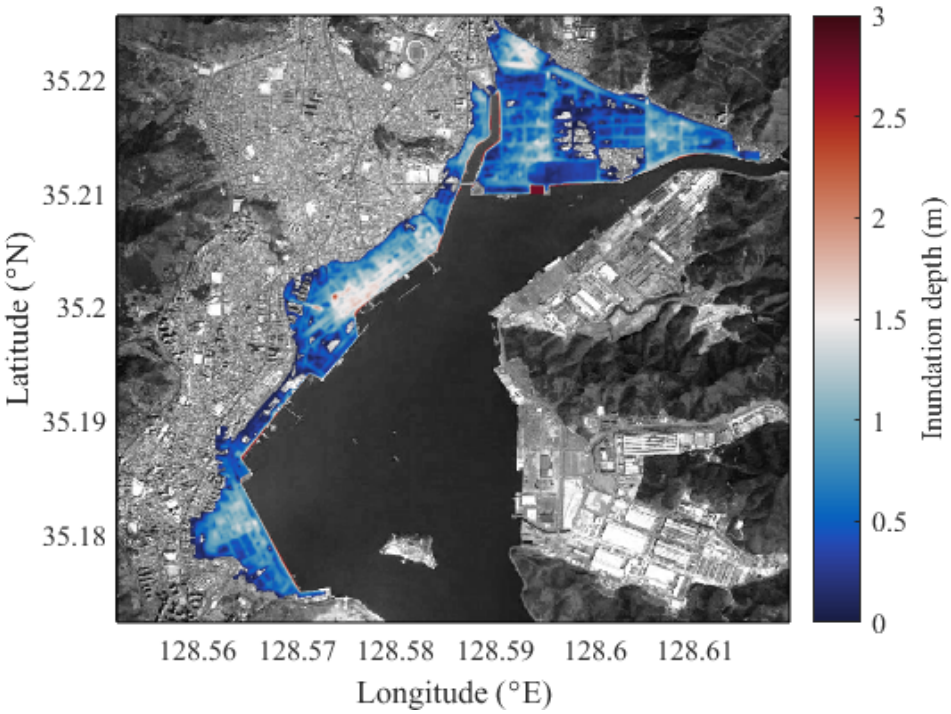

Figure 6.6: Simulated maximum inundation depth by Typhoon Maemi (2003) (S0DR0TC0)

6.4 Results and Discussion

To evaluate the potential flooding damage caused by climate change, numerical simulations were performed on nine scenarios developed with the combination of different SLR, DR, and TC conditions in the present or future. Maximum flooding area and volume were determined for each scenario in order to quantify the flooding damage for each scenario. Consequently, the maximum flooding volume (V_F) was computed as the product of the maximum flooding depth

$(d_{i,j})$ and the mesh area $(\Delta x_{i,j} \times \Delta y_{i,j})$ [253] as follows.

$$V_F = \sum_{i=1}^{N} \sum_{j=1}^{M} \left(d_{i,j} \times \Delta x_{i,j} \times \Delta y_{i,j} \right) \tag{6.2}$$

where i and j are grid indices with their maxima as N and M, respectively. The flooding depth was calculated only for overland areas where the initial water depth was null and changed as the typhoon evolved. The maximum flooding depth $(d_{i,j})$ represents the maximum depth of flooding at each grid point during the entire simulation period.

Table 6.4 provides a summary of the simulation results as well as the increase rate compared to the reference scenario, which will imply any further flooding damage under the future climatic conditions. The dashed lines in the table divide the situations according to the number of adjusted drivers; for instance, the third category consists of cases with two manipulated factors. The subsequent subsections will detail the analyzed results based on these categories. In Figure 6.7, a violin plot was used to effectively illustrate the relative influence of each component on flooding. It demonstrates that the combined S-TC condition (i.e., S1DR0TC1) contributed the most to the potential flooding, while the rise in DR (i.e., S0DR1TC0) contributed the least. This is because S and TC contribute to the increase in sea level throughout the entire target region, resulting in greater direct flooding damage. In addition, scenario S1DR0TC1 revealed that their nonlinear interaction had a significant influence on the danger of flooding, which will be examined in further detail later. It was also discovered that only the S1 series moved toward a negatively skewed distribu-

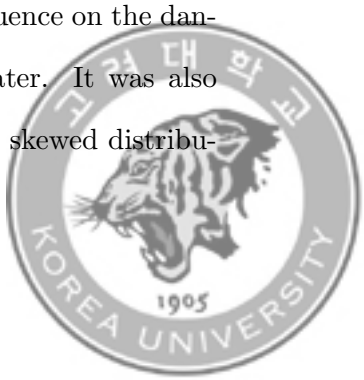

tion, indicating that the majority of flooded locations were severely impacted by flooding. In the following subsections, a more in-depth examination will be given.

Table 6.4: Statistics on the flooding damage

Scenario ID	Max. flooding area (km^2)	Rate of increase in Max.area (%)	Max. flooding volume (m^3)	Rate of increase in Max.V_F (%)
S0DR0TC0	3.73	-	2,602,000	-
S1DR0TC0	4.34	16.35	4,899,000	88.28
S0DR1TC0	3.74	0.27	2,611,000	0.35
S0DR0TC1	4.22	13.14	4,317,000	65.91
S1DR1TC0	4.33	16.09	4,889,000	87.89
S1DR0TC1	4.63	24.13	6,817,000	161.99
S0DR1TC1	4.22	13.14	4,318,000	65.94
S1DR1TC1	4.63	24.13	6,817,000	161.99
S2DR2TC2	4.80	28.69	8,758,100	236.59

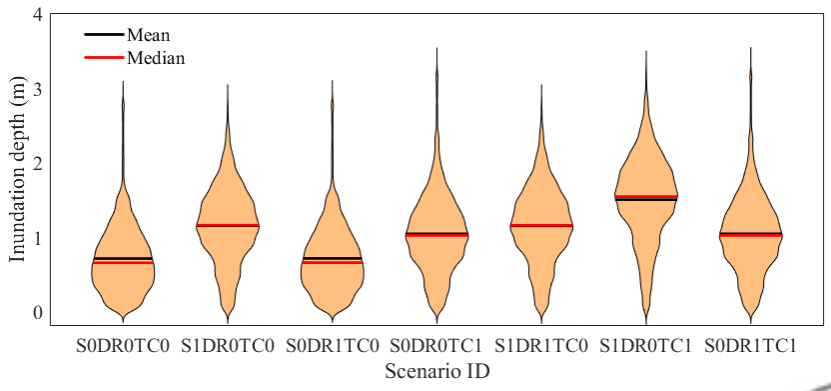

Figure 6.7: Violin plot of seven scenarios

6.4.1 Effects of a Single Factor on Flooding Risk

First, each factor that exacerbates the future flooding risk was considered individually in scenarios. Therefore, the results for S1DR0TC0, S0DR1TC0 and S0DR0TC1 were compared to identify additional damage caused by each factor: SLR (S), direct runoff (DR) or TC intensity (TC). Figure 6.8 depicts the maximum inundation depth of each scenario with the differences from the reference scenario (S0DR0TC0). Among them, S1DR0TC0, which considered SLR only, produced the most extensive damage, with increases of 16.35% in the maximum flooding area and of 88.28% in the flooding volume. These results demonstrate that as a single driver, SLR is the most influential factor in aggravating inundation from future storm surges. The second largest was caused by TC, which led to 13.14% and 65.91% increases in area and volume, respectively; this amounts to three-fourth of the effect of SLR. Throughout the S1DR0TC0 and S0DR0TC1 results, a newly inundated area attributed to SLR and TC intensification appeared and is featured in Figure 6.9 (a).

Unlike SLR and TC intensification, the increased DR had a significantly limited influence on aggravating flooding risk. As shown in Figure 6.9 (b), the DR1 series produced similar but slightly different levels of inundation depth depending on how the storm surge, riverine flow, and topographical characteristics interacted. The magnified riverine runoff resulting from the intensified rainfall worsened the local flooding process only near the outlet [206]. Lee et al. [5] explained that the colliding flow patterns that formed around the outlet led to the elevated water level and flow attenuation, which in turn caused more severe flooding in the low-lying lands nearby. As a result, the areas adjacent

to the two rivers, as shown in Figure 6.9 (b), were further inundated even though the change in the flooding volume was almost negligible. It was noted that the additional inundation damage tended to diminish as the distance from both rivers increased. Moreover, the intensified DR also caused minor changes in the inundation depth in areas far from the two rivers, indicating that the damage was mitigated in some areas.

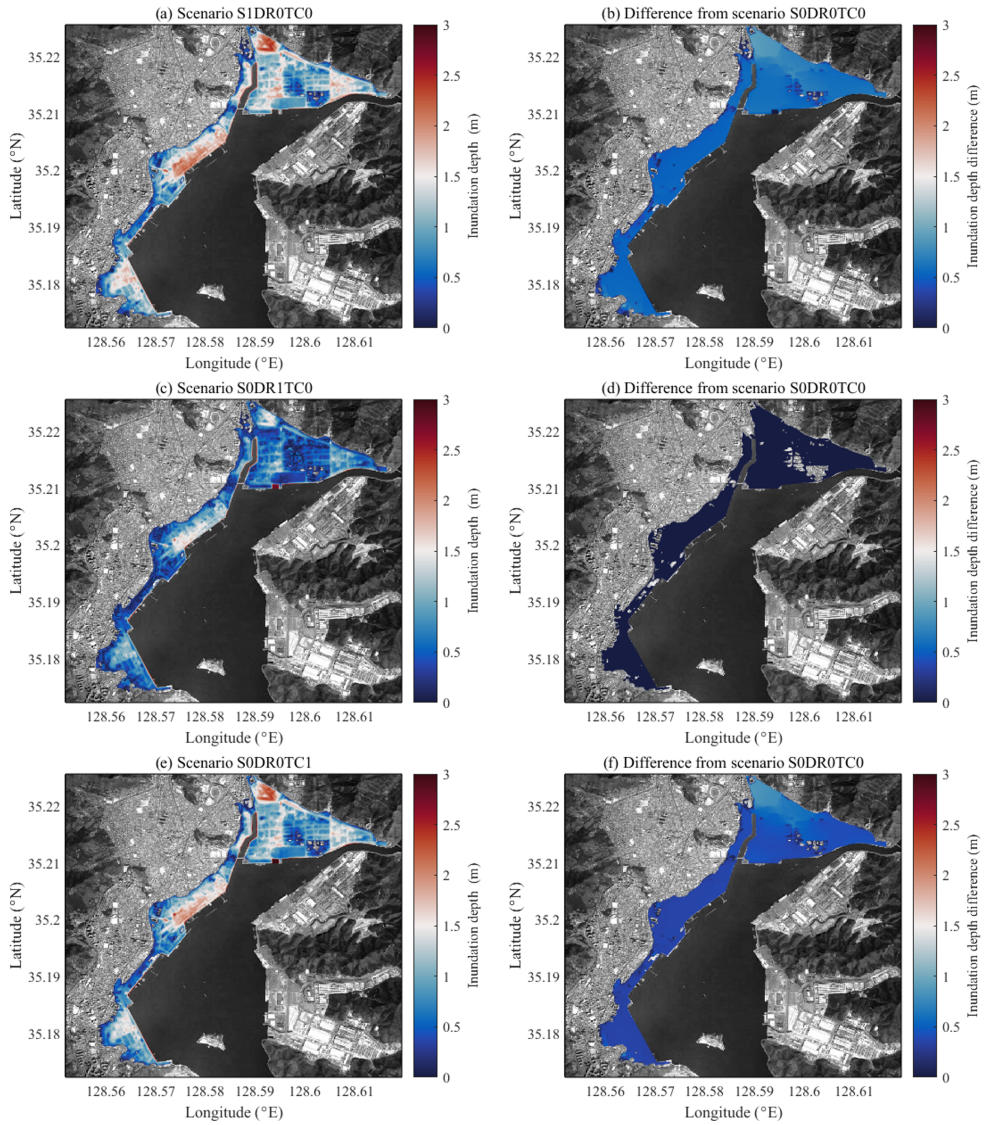

Figure 6.8: Maximum inundation depth of each scenario considering each single factor (left panels) and its discrepancy from the reference scenario, S0DR0TC0 (right panels). (a) and (b) for S1DR0TC0, (c) and (d) for S0DR1TC0, (e) and (f) for S0DR0TC1

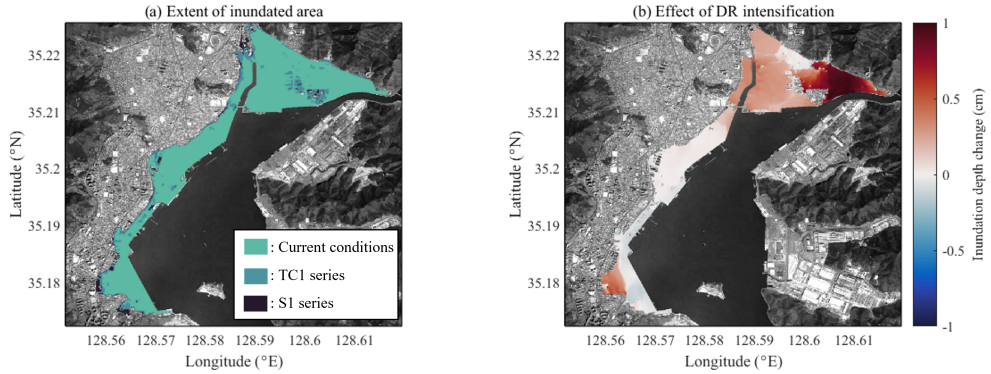

Figure 6.9: (a) Overlapped maximum extents of the flooding area under the current conditions, S1 and TC1 series and (b) the change in the maximum inundation depth due to DR intensification

6.4.2 Effects of Two Coupled Factors on Flooding Risk

As single contributors, SLR was the most influential, while DR was the least influential. When multiple factors are involved at the same time, each impact is presumed to interact with the others and produce additional risk. The influence of the two combined factors on the flooding risk can be examined by comparing the S1DR1TC0, S1DR0TC1, and S0DR1TC1 scenarios. Figure 6.10 depicts the maximum inundation depths of those scenarios and their differences from the reference scenario.

The result of S1DR0TC1, in which both SLR and TC intensification were configured according to the RCP4.5 condition, indicated that the maximum flooding area and volume were increased by 24.13% and 166.2%, respectively. Compared with the linear sum of the S1DR0TC0 and S0DR0TC1 results, this scenario produced higher flooding risk, which demonstrates the nonlinear interaction between SLR and TC intensification that results in aggravated inun-

dation. Consequently, to accurately predict future flooding damage, SLR and TC intensification must be considered simultaneously in the simulation, as the inundation damage is likely to be underestimated when both components are considered separately and then the increases in damage from each factor are combined.

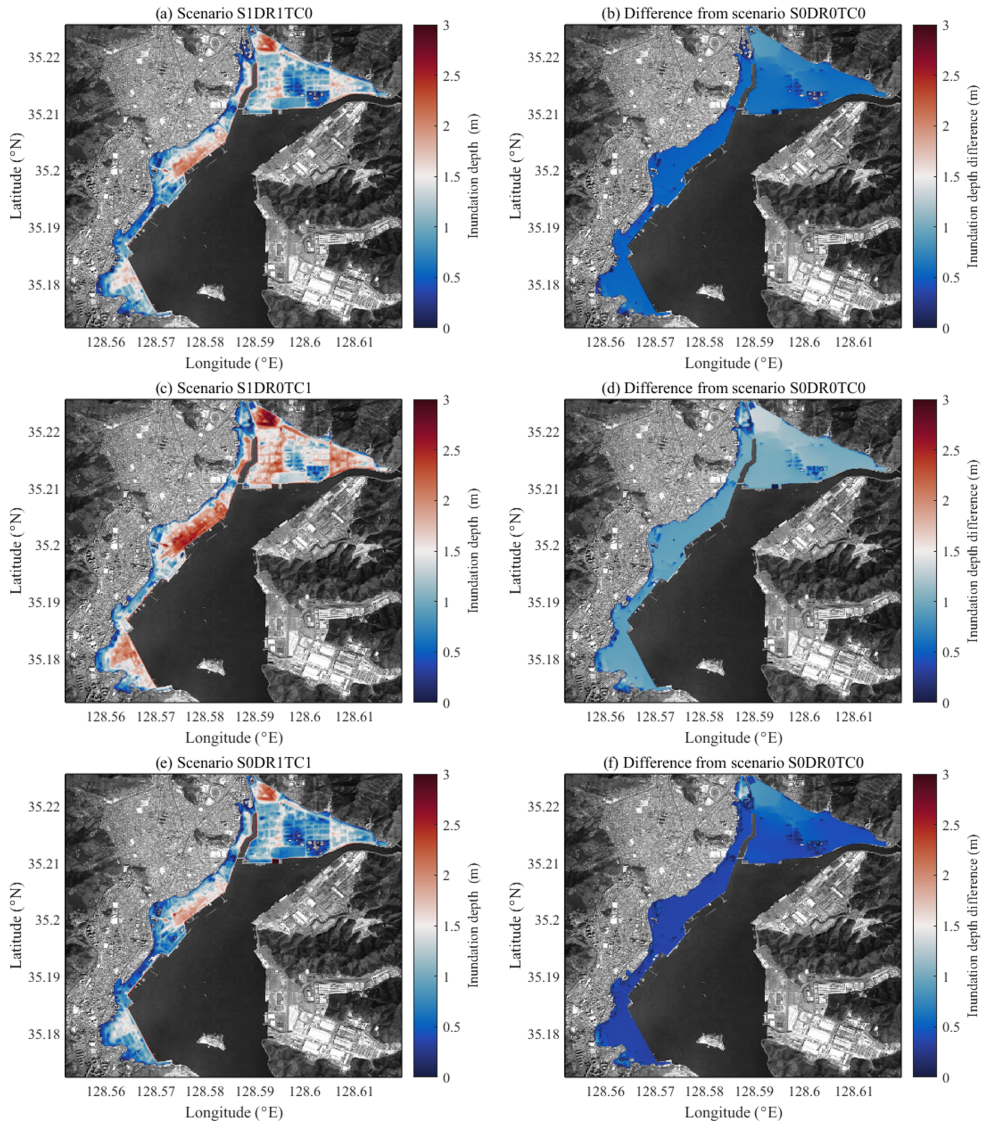

Figure 6.10: Maximum inundation depth of each scenario considering the interactions between two factors (left panels) and the differences from the reference scenario, S0DR0TC0 (right panels). (a) and (b) for S1DR1TC0, (c) and (d) for S1DR0TC1, and (e) and (f) for S0DR1TC1

Meanwhile, when SLR was combined with the DR increase, their effects on the flooding risk were underestimated than that of the S1 series; both the

maximum flooding area and volume of S1DR1TC0 were lower than those of S1DR0TC0. The areas where the inundation depth decreased as DR increased, as shown in Figure 6.9 (b), had a lower flooding risk as the sea level rose. The rates of increase in the maximum flooding area and volume of S0DR1TC1 were found to be 13.14% and 65.94%, respectively, which was very similar with those of S0DR0TC1. It suggests that the inundation damage is dominated by TC intensification when TC and DR are exacerbated simultaneously. These results indicate that the flooding risk is rarely affected by the projected future DR intensification under RCP4.5, as it was observed in S0DR1TC0 to increase the risk much less than the other factors. Therefore, DR intensification is likely to have a minimal impact on flooding risk.

6.4.3 Effects of All Factors on Flooding Risk

Last, all the factors that aggravate future flooding damage (i.e., the intensification of SLR, DR and TC) were considered at the same time, and S1DR1TC1 and S2DR2TC2 were analyzed to identify the relative impacts of all factors under the different climate conditions. Figure 6.11 illustrates the maximum inundation depth and its difference from that in the reference scenario. This configuration enables us to directly assess the comprehensive climate change effects on future coastal flooding hazards depending on the different GHG emission scenarios.

In S1DR1TC1 for the future climate conditions under RCP4.5, the maximum flooding area and volume were predicted to increase by 24.13% and 162.0%, respectively, which are quite comparable to the increases in S1DR0TC1

due to the negligible contribution of DR. As seen in the previous section, however, a nonlinear interaction between SLR and TC intensification can still be observed by comparing S1DR1TC0 with S0DR0TC1 and S0DR1TC1 with S1DR0TC0. When the RCP8.5 scenario is imposed, S2DR2TC2, with an extreme configuration, resulted in the highest level of flooding risk, as shown in Figure 6.11, producing an flooding area increase of 28.69% and a volume increase of 236.7%.

To assess the different GHG emissions effects on the future flooding risk, the results under the current, RCP4.5 and RCP8.5 conditions were intercompared. Figure 6.12 provides a histogram of the inundation depth in S0DR0TC0, S1DR1TC1, and S2DR2TC2 [254]. Figure 6.12 demonstrates that the higher level of GHG emissions will further accelerate the flooding damage without altering the spatial pattern of the inundation depth distribution, that is, the shape of the probabilistic distribution. Climate change only increases the severity of the inundation depth, which is related to the skewness of the distribution; the histogram under the current conditions was positively skewed, but it changed to negatively skewed and its skewness increased as GHG emissions continued to develop. Therefore, it is anticipated that the characteristics of the inundation depth distribution may be locked based in specific TC evolution and geometric conditions. If global warming persists under the RCP8.5 scenario without any reduction in GHG use, low-lying floodplains are likely to be considerably exposed to flooding risk. More specifically, only 1.48% of the total inundated area had more than 2 m inundation depth under the current climate conditions, while 44.22% of the area is expected to be flooded more

than 2 m in 2100 under the RCP8.5.

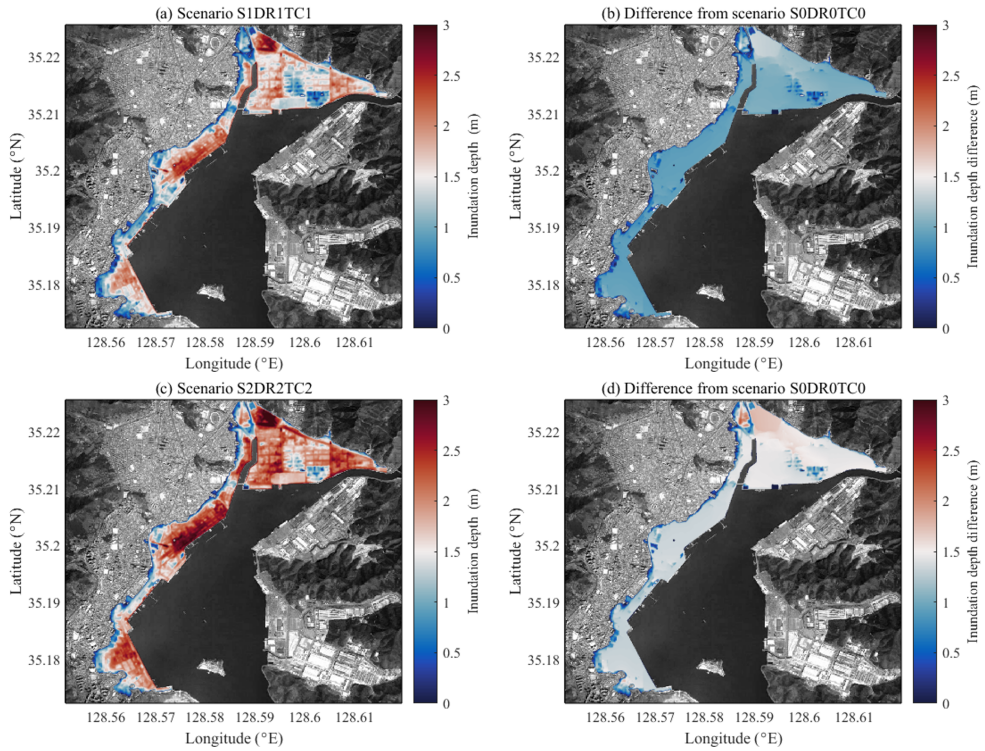

Figure 6.11: Maximum inundation depth in the RCP4.5 and RCP8.5 scenarios (left panels) and its difference from the reference scenario, S0DR0TC0 (right panels). (a) and (b) for S1DR1TC1, (c) and (d) for S2DR2TC2

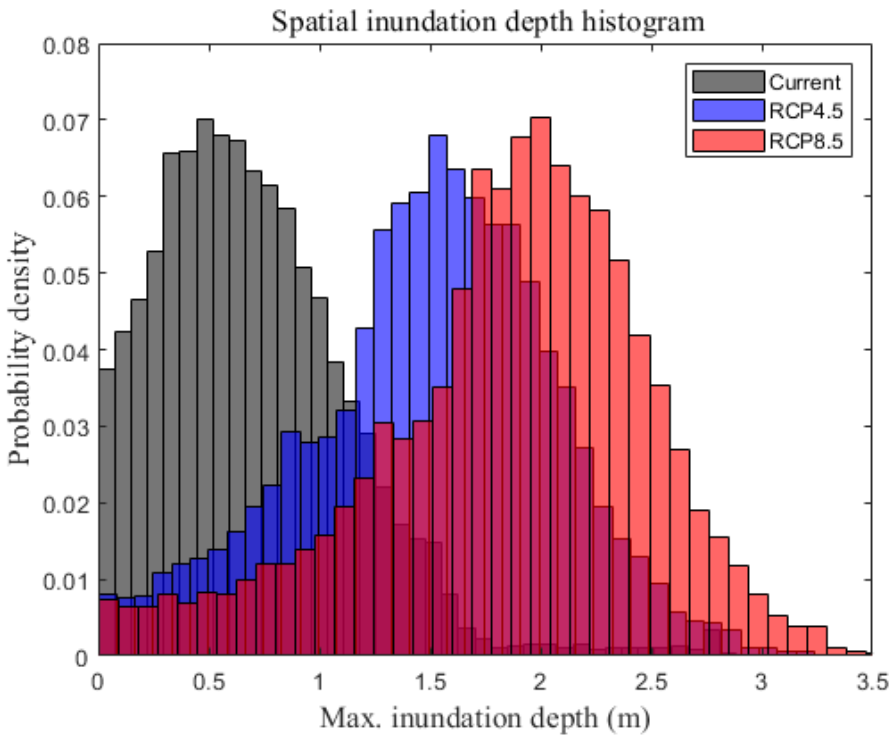

Figure 6.12: Histogram of the maximum inundation depth under the current and future climate conditions (RCP4.5 and RCP8.5)

6.5 Conclusions

The future storm surge flooding risk in a coastal region was assessed by modeling storm surge based on Typhoon Maemi (2003) under future climatic conditions. The effects of three components (i.e., SLR, DR, and TC intensification) on the flooding risk were investigated by the application of a coupled hydrologic-hydrodynamic model to quantify the extent of storm-related flooding under both current and future climatic conditions.

By comparing scenarios in which each component was assessed separately,

the relative contribution of each component to the future flooding risk was determined. The SLR was determined to be the most significant single contributor of future flooding damage, followed by the strengthening of tropical cyclones. However, DR intensification had little effect despite the significant rise in typhoon rainfall (about a 50 to 67.5% increase). In addition to the contributions of these variables to the aggravation of flooding, the mechanisms in which they cause flooding are also fairly diverse. Figures 6.8 (b) and 6.8 (e) illustrate the effect of SLR and TC intensification on the flooding depth over the whole floodplain, while Figure 6.9 (b) illustrates the effect of DR intensification on the flooding level in the region near the river. Besides, the simulated results of the coupled SLR and TC aggravation revealed that a nonlinear interaction might occur and exacerbate the flooding damage. In order to effectively anticipate future flooding damage, both components must be included concurrently in simulations; otherwise, the flooding damage would likely be overestimated.

Future storms with strengthened rainfall and TC features are predicted to generate the highest flooding damage in the study region, with increases of up to 28.69% in the flooding extent and 236.59% in the flooding volume compared to those under the current conditions. Although the scenario with the most severe GHG emissions (i.e., RCP8.5) resulted in the most severe flooding damage, it had no effect on the the spatial pattern of the flooding depth distribution.

Despite the findings above, it is evident that our conclusions were obtained based on case-specific and site-sensitive characteristics; hence, their generalizability is limited. For instance, simulation results are heavily influenced by the topographical features of the target area; hence, the implications of these

simulations may need to be modified by taking into account different kinds of coasts and floodplains. Certain non-included TC properties, such as trajectories, are an additional variable that might affect modeling results. In addition, it is difficult to extrapolate from a single TC to additional TCs [221].

Nonetheless, it is expected that the storm surge modeling with future climatic variables would provide a useful framework for investigating future storm surge threats and aiding in the development of countermeasures against them. Future study will investigate other physical processes affecting floods (e.g., direct rainfall, inland flood, sewage from industrial or urban residential regions).

Chapter 7

Conclusions and Future Works

7.1 Conclusions

This dissertation studies the immersive and interactive multi-physics modeling of coastal hazards, focusing on the hydrodynamic modeling with the rainfall-runoff process, hydrodynamic and transport modeling, interactive numerical simulation with an immersive simulation environment, and model coupling with non-dispersive shallow water model. The following summarizes the major conclusions from each section of this dissertation.

In Chapter 2, an efficient numerical scheme for the Saint-Venant system governing scalar transport is proposed based on a hybrid finite volume - finite difference method. An anti-diffusion function is introduced to minimize the numerical diffusion near contact discontinuities when solving the scalar transport problem using the HLL Riemann Solver. Time integration using the first order Euler method theoretically confirms that the proposed scheme ensures non-negativity and the exact C-property for the scalar concentration as well

as the water depth. The presented model has been tested against the analytical solutions for several numerical experiments and the comparisons between the analytical and numerical solutions in all numerical experiments show good agreement as the anti-diffusion function was applied.

In Chapter 3, a GPU-accelerated nearshore scalar transport model is proposed based on the Boussinesq-type nearshore wave solver, Celeris Advent. A modified numerical scheme described in Chapter 2 is applied instead of the HLL Riemann solver. Besides, various features including periodic boundary condition applicable to different nearshore problems are implemented. Comparisons with two analytical solutions in one- or two-dimensional flow field validate the accuracy of the model. Furthermore, two laboratory experiments were simulated to assess the model performance on scalar transport in complex bathymetry and flow conditions. Finally, a field-scale dye release experiment conducted in the Imperial Beach was simulated to examine the applicability of the model in the nearshore region. The results indicated that waves, wind-driven currents and transient rip currents occurring in the surf zones were reasonably reproduced. Correspondingly, the dye transport, especially including dye advection from the surf zone to the inner shelf by the transient rip currents due to the wave breaking, was well predicted.

In Chapter 4, an interactive hydrodynamic rainfall-runoff model with an immersive virtual reality environment is proposed based on the immersive nearshore wave simulation software, Celeris Base. The nonlinear shallow water equations are adopted as the governing equations, and rainfall and infiltration terms are implemented in mass conservation to consider the rainfall-runoff pro-

cess. Owing to its simplicity and accuracy, the simplest explicit approximation to the Green-Ampt (GA) model is employed as the infiltration model. The proposed model has been tested against the analytical and reference solutions for several numerical experiments. The validation results show that the explicit GA model is quite accurate compared to the implicit GA model without significant error. Furthermore, the model is applied to simulate historical rainfall event in the Goodwin Creek Experimental Watershed (GCEW) and verified against the observed hydrograph at the river outlet. The results show that the model is capable of computing the flood routing process over the natural basin as well as the simplified plain. Other features of the proposed model, immersive and interactive simulation environments, are also introduced. These features are expected to open a new era for advanced hazard mitigation strategies such as real-time countermeasures in case of a flash flood.

In Chapter 5, an accurate and efficient modeling system through one-way coupling between non-dispersive and dispersive wave solvers is proposed. By employing an absorbing-generating boundary condition, it is possible to integrate two shallow water models without significant error. The proposed coupling method has been tested for several wave propagation problems. The results show that the absorbing-generating boundary condition generates incident waves while successfully absorbing the reflected waves in 1D space. However, the numerical implementation of absorbing-generating boundary condition should be further improved for more accurate modeling in 2D space. The suggested coupling method is projected to contribute to an advanced strategy for reducing the impact of coastal disasters (e.g., storm surge, tsunami) through

its accurate and rapid simulation of shallow water waves.

In Chapter 6, the future flooding risk due to storm surge in a coastal region was evaluated through storm surge modeling based on Typhoon Maemi (2003) under future climatic conditions. The contributions of three primary drivers (i.e., SLR, DR, and TC intensification) on the flooding risk were examined by the application of a coupled hydrologic-hydrodynamic model to quantify the storm-related flooding damage under current and future climatic conditions. The results demonstrate that SLR is the most influential single flooding component exacerbating the future flooding risk, followed by TC exacerbation and DR intensification sequentially. Besides, the combination of SLR and TC exacerbation resulted in nonlinear interactions, which might exacerbate flood damage. Future storms with exacerbated TC characteristics are predicted to generate the highest flooding damage, with increases of up to 28.69% in the flooding extent and 236.59% in the flooding volume compared to those under the current conditions in the study area.

7.2 Future Works

Extending the simulation environment to augmented reality (AR) or mixed reality (MR) is another future challenge. Beyond inviting the users into a virtual reality environment, configuration and simulation of numerical setup based on what the users are seeing will make the numerical model more attractive. It will be especially seductive in visualizing flooding due to sudden rainfall in urban basins. Finally, source code compilation using the Unreal Engine provides more

realistic and immersive visualization for various simulation environments such as VR, AR, and XR. It is expected to improve the informative and educational effects through a realistic simulation view.

Current techniques commonly include wave-induced radiation stress in the non-dispersive shallow water model through coupling with the phase-averaged models. Since the phase-averaged models are limited to be applied for nearshore regions, the phase-resolving models applicable to simulate coastal disasters are necessary. Consideration of several physical terms (e.g., wind-driven shear stress, atmospheric pressure, Coriolis force) may be a valuable effort for simulating storm surge. Furthermore, the coupling method can be used for evaluating the role of waves in coastal disaster and inundation damage.

References

[1] A. L. Horn, F. J. Rueda, G. Hörmann, and N. Fohrer, "Implementing river water quality modelling issues in mesoscale watershed models for water policy demands—-an overview on current concepts, deficits, and future tasks," *Physics and Chemistry of the Earth, Parts A/B/C*, vol. 29, no. 11-12, pp. 725–737, 2004.

[2] G. S. Stelling, *On the construction of computational methods for shallow water flow problems*. PhD thesis, Delft University of Technology, Delft, The Netherlands, 1983.

[3] C. B. Vreugdenhil, *Numerical methods for shallow-water flow*, vol. 13. Springer Science & Business Media, 1994.

[4] F. X. Giraldo, J. S. Hesthaven, and T. Warburton, "Nodal high-order discontinuous galerkin methods for the spherical shallow water equations," *Journal of Computational Physics*, vol. 181, no. 2, pp. 499–525, 2002.

[5] C. Lee, S. Hwang, K. Do, and S. Son, "Increasing flood risk due to river runoff in the estuarine area during a storm landfall," *Estuarine, Coastal and Shelf Science*, vol. 221, pp. 104–118, 2019.

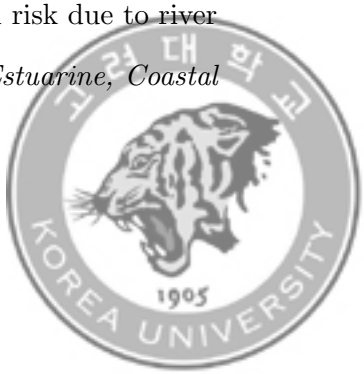

[6] B. Bonev, J. S. Hesthaven, F. X. Giraldo, and M. A. Kopera, "Discontinuous galerkin scheme for the spherical shallow water equations with applications to tsunami modeling and prediction," *Journal of Computational Physics*, vol. 362, pp. 425–448, 2018.

[7] S. Hwang, S. Son, C. Lee, and H.-D. Yoon, "Quantitative assessment of inundation risks from physical contributors associated with future storm surges: a case study of typhoon maemi (2003)," *Natural Hazards*, vol. 104, no. 2, pp. 1389–1411, 2020.

[8] J.-A. Yang, S. Kim, S. Son, N. Mori, and H. Mase, "Correction to: Assessment of uncertainties in projecting future changes to extreme storm surge height depending on future sst and greenhouse gas concentration scenarios," *Climatic Change*, vol. 162, no. 2, p. 443–444, 2020.

[9] B. Na, S. Son, and J.-C. Choi, "Modeling of accidental oil spills at different phases of lng terminal construction," *Journal of Marine Science and Engineering*, vol. 9, no. 4, p. 392, 2021.

[10] E. S. Gross, J. R. Koseff, and S. G. Monismith, "Evaluation of advective schemes for estuarine salinity simulations," *Journal of hydraulic engineering*, vol. 125, no. 1, pp. 32–46, 1999.

[11] J. Murillo, J. Burguete, P. Brufau, and P. García-Navarro, "Coupling between shallow water and solute flow equations: analysis and management of source terms in 2d," *International journal for numerical methods in fluids*, vol. 49, no. 3, pp. 267–299, 2005.

[12] L. Begnudelli and B. F. Sanders, "Unstructured grid finite-volume algorithm for shallow-water flow and scalar transport with wetting and drying," *Journal of hydraulic engineering*, vol. 132, no. 4, pp. 371–384, 2006.

[13] J. Murillo, P. García-Navarro, J. Burguete, and P. Brufau, "A conservative 2d model of inundation flow with solute transport over dry bed," *International journal for numerical methods in fluids*, vol. 52, no. 10, pp. 1059–1092, 2006.

[14] F. Benkhaldoun, I. Elmahi, and M. Seaı¨d, "Well-balanced finite volume schemes for pollutant transport by shallow water equations on unstructured meshes," *Journal of Computational Physics*, vol. 226, no. 1, pp. 180–203, 2007.

[15] D. Liang, X. Wang, R. A. Falconer, and B. N. Bockelmann-Evans, "Solving the depth-integrated solute transport equation with a tvd-maccormack scheme," *Environmental Modelling & Software*, vol. 25, no. 12, pp. 1619–1629, 2010.

[16] Q. Liang, "A well-balanced and non-negative numerical scheme for solving the integrated shallow water and solute transport equations," *Communications in Computational Physics*, vol. 7, no. 5, p. 1049, 2010.

[17] L. Cea and M. Vázquez-Cendón, "Unstructured finite volume discretisation of bed friction and convective flux in solute transport models linked to the shallow water equations," *Journal of Computational Physics*, vol. 231, no. 8, pp. 3317–3339, 2012.

[18] F. Benkhaldoun, I. Elmahi, S. Sari, and M. Seaid, "An unstructured finite-volume method for coupled models of suspended sediment and bed load transport in shallow-water flows," *International Journal for Numerical Methods in Fluids*, vol. 72, no. 9, pp. 967–993, 2013.

[19] D. Vanzo, A. Siviglia, and E. F. Toro, "Pollutant transport by shallow water equations on unstructured meshes: Hyperbolization of the model and numerical solution via a novel flux splitting scheme," *Journal of Computational Physics*, vol. 321, pp. 1–20, 2016.

[20] S. K. Godunov and I. Bohachevsky, "Finite difference method for numerical computation of discontinuous solutions of the equations of fluid dynamics," *Matematičeskij sbornik*, vol. 47(89), no. 3, pp. 271–306, 1959.

[21] P. L. Roe, "Approximate riemann solvers, parameter vectors, and difference schemes," *Journal of computational physics*, vol. 43, no. 2, pp. 357–372, 1981.

[22] A. Harten, P. D. Lax, and B. v. Leer, "On upstream differencing and godunov-type schemes for hyperbolic conservation laws," *SIAM review*, vol. 25, no. 1, pp. 35–61, 1983.

[23] B. Einfeldt, "On godunov-type methods for gas dynamics," *SIAM Journal on Numerical Analysis*, vol. 25, no. 2, pp. 294–318, 1988.

[24] E. F. Toro, M. Spruce, and W. Speares, "Restoration of the contact surface in the hll-riemann solver," *Shock waves*, vol. 4, no. 1, pp. 25–34, 1994.

[25] S. Davis, "Simplified second-order godunov-type methods," *SIAM Journal on Scientific and Statistical Computing*, vol. 9, no. 3, pp. 445–473, 1988.

[26] P. Batten, N. Clarke, C. Lambert, and D. M. Causon, "On the choice of wavespeeds for the hllc riemann solver," *SIAM Journal on Scientific Computing*, vol. 18, no. 6, pp. 1553–1570, 1997.

[27] E. F. Toro, *Riemann solvers and numerical methods for fluid dynamics: a practical introduction*. Springer Science & Business Media, 2013.

[28] J. J. Quirk, "A contribution to the great riemann solver debate," in *Upwind and High-Resolution Schemes*, pp. 550–569, Springer, 1997.

[29] H. Nishikawa and K. Kitamura, "Very simple, carbuncle-free, boundary-layer-resolving, rotated-hybrid riemann solvers," *Journal of Computational Physics*, vol. 227, no. 4, pp. 2560–2581, 2008.

[30] S. D. Kim, B. J. Lee, H. J. Lee, and I.-S. Jeung, "Robust hllc riemann solver with weighted average flux scheme for strong shock," *Journal of Computational Physics*, vol. 228, no. 20, pp. 7634–7642, 2009.

[31] K. Huang, H. Wu, H. Yu, and D. Yan, "Cures for numerical shock instability in hllc solver," *International journal for numerical methods in fluids*, vol. 65, no. 9, pp. 1026–1038, 2011.

[32] H. Wu, L. Shen, and Z. Shen, "A hybrid numerical method to cure numerical shock instability," *Commun. Comput. Phys.*, vol. 8, pp. 1264–1271, 2010.

[33] J. Mandal and V. Panwar, "Robust hll-type riemann solver capable of resolving contact discontinuity," *Computers & fluids*, vol. 63, pp. 148–164, 2012.

[34] X. Liu, "A robust numerical model for shallow water governing solute transport with wet/dry interfaces," *Computer Methods in Applied Mechanics and Engineering*, vol. 351, pp. 85–108, 2019.

[35] X. Deng, P. Boivin, and F. Xiao, "A new formulation for two-wave riemann solver accurate at contact interfaces," *Physics of Fluids*, vol. 31, no. 4, p. 046102, 2019.

[36] A. Rubio, A. Zalts, and C. El Hasi, "Numerical solution of the advection–reaction–diffusion equation at different scales," *Environmental Modelling & Software*, vol. 23, no. 1, pp. 90–95, 2008.

[37] J. Kong, P. Xin, C.-J. Shen, Z.-Y. Song, and L. Li, "A high-resolution method for the depth-integrated solute transport equation based on an unstructured mesh," *Environmental modelling & software*, vol. 40, pp. 109–127, 2013.

[38] A. Bermudez and M. E. Vazquez, "Upwind methods for hyperbolic conservation laws with source terms," *Computers & Fluids*, vol. 23, no. 8, pp. 1049–1071, 1994.

[39] B. Perthame and C. Simeoni, "A kinetic scheme for the saint-venant system with a source term," *Calcolo*, vol. 38, no. 4, pp. 201–231, 2001.

[40] E. Audusse, F. Bouchut, M.-O. Bristeau, R. Klein, and B. Perthame, "A fast and stable well-balanced scheme with hydrostatic reconstruction for shallow water flows," *SIAM Journal on Scientific Computing*, vol. 25, no. 6, pp. 2050–2065, 2004.

[41] M. Ricchiuto and A. Bollermann, "Stabilized residual distribution for shallow water simulations," *Journal of Computational Physics*, vol. 228, no. 4, pp. 1071–1115, 2009.

[42] J. Dong, "A robust second-order surface reconstruction for shallow water flows with a discontinuous topography and a manning friction.," *Advances in Computational Mathematics*, vol. 46, no. 2, 2020.

[43] J. M. Greenberg and A.-Y. LeRoux, "A well-balanced scheme for the numerical processing of source terms in hyperbolic equations," *SIAM Journal on Numerical Analysis*, vol. 33, no. 1, pp. 1–16, 1996.

[44] E. Audusse and M.-O. Bristeau, "A well-balanced positivity preserving "second-order" scheme for shallow water flows on unstructured meshes," *J. Comput. Phys.*, vol. 206, p. 311–333, June 2005.

[45] D.-H. Kim, Y.-S. Cho, and H.-J. Kim, "Well-balanced scheme between flux and source terms for computation of shallow-water equations over irregular bathymetry," *Journal of engineering mechanics*, vol. 134, no. 4, pp. 277–290, 2008.

[46] V. Michel-Dansac, C. Berthon, S. Clain, and F. Foucher, "A well-

balanced scheme for the shallow-water equations with topography," *Computers & Mathematics with Applications*, vol. 72, no. 3, pp. 568–593, 2016.

[47] X. Liu, "A new well-balanced finite-volume scheme on unstructured triangular grids for two-dimensional two-layer shallow water flows with wet-dry fronts," *Journal of Computational Physics*, vol. 438, p. 110380, 2021.

[48] A. Kurganov and G. Petrova, "A second-order well-balanced positivity preserving central-upwind scheme for the saint-venant system," *Communications in Mathematical Sciences*, vol. 5, no. 1, pp. 133–160, 2007.

[49] I. Nikolos and A. Delis, "An unstructured node-centered finite volume scheme for shallow water flows with wet/dry fronts over complex topography," *Computer Methods in Applied Mechanics and Engineering*, vol. 198, no. 47-48, pp. 3723–3750, 2009.

[50] J. Singh, M. S. Altinakar, and Y. Ding, "Two-dimensional numerical modeling of dam-break flows over natural terrain using a central explicit scheme," *Advances in Water Resources*, vol. 34, no. 10, pp. 1366–1375, 2011.

[51] A. Bollermann, G. Chen, A. Kurganov, and S. Noelle, "A well-balanced reconstruction of wet/dry fronts for the shallow water equations," *Journal of Scientific Computing*, vol. 56, no. 2, pp. 267–290, 2013.

[52] S. Tavakkol and P. Lynett, "Celeris: A gpu-accelerated open source software with a boussinesq-type wave solver for real-time interactive simu-

lation and visualization," *Computer Physics Communications*, vol. 217, pp. 117–127, 2017.

[53] S. Tavakkol, S. Son, and P. Lynett, "Adaptive third order adams-bashforth time integration for extended boussinesq equations," *Computer Physics Communications*, vol. 265, p. 108006, 2021.

[54] A. Kurganov and D. Levy, "Central-upwind schemes for the saint-venant system," *ESAIM: Mathematical Modelling and Numerical Analysis*, vol. 36, no. 3, pp. 397–425, 2002.

[55] R. Preston, "Representation of dispersion in two-dimensional water flow," *Central Electricity Research Laboratories, Leatherhead, England, Report No. TPRD/L/2783 N*, vol. 84, pp. 1–13, 1985.

[56] J. Elder, "The dispersion of marked fluid in turbulent shear flow," *Journal of fluid mechanics*, vol. 5, no. 4, pp. 544–560, 1959.

[57] S. Gottlieb, C.-W. Shu, and E. Tadmor, "Strong stability-preserving high-order time discretization methods," *SIAM review*, vol. 43, no. 1, pp. 89–112, 2001.

[58] Y. Xing and C.-W. Shu, "High order finite difference weno schemes with the exact conservation property for the shallow water equations," *Journal of Computational Physics*, vol. 208, no. 1, pp. 206–227, 2005.

[59] F. Behzadi, B. Shamsaei, and J. C. Newman, "Solution of fully-coupled shallow water equations and contaminant transport using a primitive-

variable riemann method," *Environmental Fluid Mechanics*, vol. 18, no. 2, pp. 515–535, 2018.

[60] H. Karjoun, A. Beljadid, and P. G. LeFloch, "A structure-preserving algorithm for surface water flows with transport processes," *Advances in Computational Mathematics*, vol. 48, no. 1, pp. 1–32, 2022.

[61] Y. Li and P. Huang, "A coupled lattice boltzmann model for advection and anisotropic dispersion problem in shallow water," *Advances in Water Resources*, vol. 31, no. 12, pp. 1719–1730, 2008.

[62] P. Tamamidis and D. N. Assanis, "Evaluation of various high-order-accuracy schemes with and without flux limiters," *International Journal for Numerical Methods in Fluids*, vol. 16, no. 10, pp. 931–948, 1993.

[63] M. De Dominicis, N. Pinardi, G. Zodiatis, and R. Lardner, "Medslik-ii, a lagrangian marine surface oil spill model for short-term forecasting–part 1: Theory," *Geoscientific Model Development*, vol. 6, no. 6, pp. 1851–1869, 2013.

[64] A. Al Shami, G. Harik, I. Alameddine, D. Bruschi, D. A. Garcia, and M. El-Fadel, "Risk assessment of oil spills along the mediterranean coast: A sensitivity analysis of the choice of hazard quantification," *Science of the Total Environment*, vol. 574, pp. 234–245, 2017.

[65] M. J. Olascoaga and G. Haller, "Forecasting sudden changes in environmental pollution patterns," *Proceedings of the National Academy of Sciences*, vol. 109, no. 13, pp. 4738–4743, 2012.

[66] J. Rivord, L. Saito, G. Miller, and S. S. Stoddard, "Modeling contaminant spills in the truckee river in the western united states," *Journal of Water Resources Planning and Management*, vol. 140, no. 3, pp. 343–354, 2014.

[67] M. Rowe, E. Anderson, T. T. Wynne, R. Stumpf, D. Fanslow, K. Kijanka, H. Vanderploeg, J. Strickler, and T. Davis, "Vertical distribution of buoyant microcystis blooms in a lagrangian particle tracking model for short-term forecasts in lake erie," *Journal of Geophysical Research: Oceans*, vol. 121, no. 7, pp. 5296–5314, 2016.

[68] M. S. Spydell, F. Feddersen, and R. Guza, "Observations of drifter dispersion in the surfzone: The effect of sheared alongshore currents," *Journal of Geophysical Research: Oceans*, vol. 114, no. C7, 2009.

[69] K. Hally-Rosendahl, F. Feddersen, and R. Guza, "Cross-shore tracer exchange between the surfzone and inner-shelf," *Journal of Geophysical Research: Oceans*, vol. 119, no. 7, pp. 4367–4388, 2014.

[70] J. Choi, C. Troy, N. Hawley, M. McCormick, and M. Wells, "Lateral dispersion of dye and drifters in the center of a very large lake," *Limnology and Oceanography*, vol. 65, no. 2, pp. 336–348, 2020.

[71] K. N. Dimou and E. E. Adams, "A random-walk, particle tracking model for well-mixed estuaries and coastal waters," *Estuarine, coastal and shelf science*, vol. 37, no. 1, pp. 99–110, 1993.

[72] J. C. Warner, C. R. Sherwood, R. P. Signell, C. K. Harris, and H. G. Arango, "Development of a three-dimensional, regional, coupled

wave, current, and sediment-transport model," *Computers & geosciences*, vol. 34, no. 10, pp. 1284–1306, 2008.

[73] S. K. Kang, K. T. Jung, K.-D. Yum, K.-S. Lee, J.-S. Park, and E. J. Kim, "Tidal dynamics in the strong tidal current environment of the uldolmok waterway, southwestern tip off the korean peninsula," *Ocean Science Journal*, vol. 47, no. 4, pp. 453–463, 2012.

[74] M. M. Rahman, G. C. Paul, and A. Hoque, "An efficient tide-surge interaction model for the coast of bangladesh," *China Ocean Engineering*, vol. 34, no. 1, pp. 56–68, 2020.

[75] S. Son, P. J. Lynett, and D.-H. Kim, "Nested and multi-physics modeling of tsunami evolution from generation to inundation," *Ocean Modelling*, vol. 38, no. 1-2, pp. 96–113, 2011.

[76] S. Hwang and S. Son, "A robust hll-based scheme for capturing contact-discontinuity in scalar transport by shallow water flow," (in preparation).

[77] P. A. Madsen and O. R. Sørensen, "A new form of the boussinesq equations with improved linear dispersion characteristics. part 2. a slowly-varying bathymetry," *Coastal engineering*, vol. 18, no. 3-4, pp. 183–204, 1992.

[78] A. B. Kennedy, Q. Chen, J. T. Kirby, and R. A. Dalrymple, "Boussinesq modeling of wave transformation, breaking, and runup. i: 1d," *Journal of waterway, port, coastal, and ocean engineering*, vol. 126, no. 1, pp. 39–47, 2000.

[79] G. Wei, J. T. Kirby, and A. Sinha, "Generation of waves in boussinesq models using a source function method," *Coastal Engineering*, vol. 36, no. 4, pp. 271–299, 1999.

[80] S. Suanda, S. Perez, and F. Feddersen, "Evaluation of a source-function wavemaker for generating random directionally spread waves in the sea-swell band," *Coastal Engineering*, vol. 114, pp. 220–232, 2016.

[81] E. F. Toro, *Shock-capturing methods for free-surface shallow flows*. Wiley-Blackwell, 2001.

[82] Y. Yuan, F. Shi, J. T. Kirby, and F. Yu, "Funwave-gpu: Multiple-gpu acceleration of a boussinesq-type wave model," *Journal of Advances in Modeling Earth Systems*, vol. 12, no. 5, p. e2019MS001957, 2020.

[83] H. Wang, H. K. Dahle, R. E. Ewing, M. S. Espedal, R. C. Sharpley, and S. Man, "An ellam scheme for advection-diffusion equations in two dimensions," *SIAM Journal on Scientific Computing*, vol. 20, no. 6, pp. 2160–2194, 1999.

[84] P. M. Lloyd and P. K. Stansby, "Shallow-water flow around model conical islands of small side slope. ii: Submerged," *Journal of Hydraulic Engineering*, vol. 123, no. 12, pp. 1068–1077, 1997.

[85] Y. J. Zhang, G. Priest, J. Allan, and L. Stimely, "Benchmarking an unstructured-grid model for tsunami current modeling," in *Global Tsunami Science: Past and Future, Volume I*, pp. 4075–4087, Springer, 2016.

[86] P. J. Lynett, K. Gately, R. Wilson, L. Montoya, D. Arcas, B. Aytore, Y. Bai, J. D. Bricker, M. J. Castro, K. F. Cheung, *et al.*, "Inter-model analysis of tsunami-induced coastal currents," *Ocean Modelling*, vol. 114, pp. 14–32, 2017.

[87] P. J. Lynett, D. Swigler, H. El Safty, L. Montoya, A. S. Keen, S. Son, and P. Higuera, "Three-dimensional hydrodynamics associated with a solitary wave traveling over an alongshore variable shallow shelf," *Journal of Waterway, Port, Coastal, and Ocean Engineering*, vol. 145, no. 6, p. 04019024, 2019.

[88] F. Shi, J. T. Kirby, J. C. Harris, J. D. Geiman, and S. T. Grilli, "A high-order adaptive time-stepping tvd solver for boussinesq modeling of breaking waves and coastal inundation," *Ocean Modelling*, vol. 43, pp. 36–51, 2012.

[89] K. Fang, Z. Liu, and Z. Zou, "Efficient computation of coastal waves using a depth-integrated, non-hydrostatic model," *Coastal Engineering*, vol. 97, pp. 21–36, 2015.

[90] K. Hally-Rosendahl, F. Feddersen, D. B. Clark, and R. Guza, "Surfzone to inner-shelf exchange estimated from dye tracer balances," *Journal of Geophysical Research: Oceans*, vol. 120, no. 9, pp. 6289–6308, 2015.

[91] K. Hally-Rosendahl and F. Feddersen, "Modeling surfzone to inner-shelf tracer exchange," *Journal of Geophysical Research: Oceans*, vol. 121, no. 6, pp. 4007–4025, 2016.

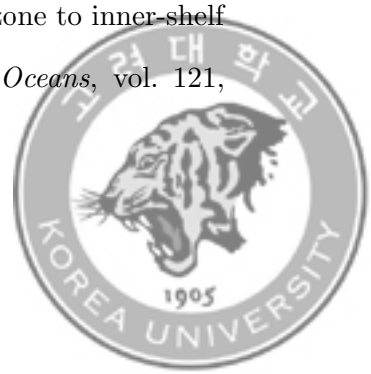

[92] O. Nwogu, "Alternative form of boussinesq equations for nearshore wave propagation," *Journal of waterway, port, coastal, and ocean engineering*, vol. 119, no. 6, pp. 618–638, 1993.

[93] S.-K. Min, X. Zhang, F. W. Zwiers, and G. C. Hegerl, "Human contribution to more-intense precipitation extremes," *Nature*, vol. 470, no. 7334, pp. 378–381, 2011.

[94] K. E. Kunkel, T. R. Karl, D. R. Easterling, K. Redmond, J. Young, X. Yin, and P. Hennon, "Probable maximum precipitation and climate change," *Geophysical Research Letters*, vol. 40, no. 7, pp. 1402–1408, 2013.

[95] J. Lehmann, D. Coumou, and K. Frieler, "Increased record-breaking precipitation events under global warming," *Climatic Change*, vol. 132, no. 4, pp. 501–515, 2015.

[96] M. G. Donat, A. L. Lowry, L. V. Alexander, P. A. O'Gorman, and N. Maher, "More extreme precipitation in the world's dry and wet regions," *Nature Climate Change*, vol. 6, no. 5, pp. 508–513, 2016.

[97] H. Tabari, "Climate change impact on flood and extreme precipitation increases with water availability," *Scientific reports*, vol. 10, no. 1, pp. 1–10, 2020.

[98] B. N. Goswami, V. Venugopal, D. Sengupta, M. Madhusoodanan, and P. K. Xavier, "Increasing trend of extreme rain events over india in a warming environment," *Science*, vol. 314, no. 5804, pp. 1442–1445, 2006.

[99] A. C. Costa and A. Soares, "Trends in extreme precipitation indices derived from a daily rainfall database for the south of portugal," *International Journal of Climatology: A Journal of the Royal Meteorological Society*, vol. 29, no. 13, pp. 1956–1975, 2009.

[100] M. A. Sarr, M. Zoromé, O. Seidou, C. R. Bryant, and P. Gachon, "Recent trends in selected extreme precipitation indices in senegal–a changepoint approach," *Journal of hydrology*, vol. 505, pp. 326–334, 2013.

[101] X. Zhou, Z. Bai, and Y. Yang, "Linking trends in urban extreme rainfall to urban flooding in china," *International Journal of Climatology*, vol. 37, no. 13, pp. 4586–4593, 2017.

[102] N. Nirupama and S. P. Simonovic, "Increase of flood risk due to urbanisation: a canadian example," *Natural Hazards*, vol. 40, no. 1, pp. 25–41, 2007.

[103] B. Saghafian, H. Farazjoo, B. Bozorgy, and F. Yazdandoost, "Flood intensification due to changes in land use," *Water resources management*, vol. 22, no. 8, pp. 1051–1067, 2008.

[104] S. Suriya and B. Mudgal, "Impact of urbanization on flooding: The thirusoolam sub watershed–a case study," *Journal of hydrology*, vol. 412, pp. 210–219, 2012.

[105] C. Yoo, E. Cho, W. Na, M. Kang, and M. Lee, "Change of rainfall–runoff processes in urban areas due to high-rise buildings," *Journal of Hydrology*, vol. 597, p. 126155, 2021.

[106] I. Douglas, "Urban ecology and urban ecosystems: understanding the links to human health and well-being," *Current Opinion in Environmental Sustainability*, vol. 4, no. 4, pp. 385–392, 2012.

[107] D. Zhou, S. Zhao, L. Zhang, G. Sun, and Y. Liu, "The footprint of urban heat island effect in china," *Scientific reports*, vol. 5, no. 1, pp. 1–11, 2015.

[108] Y. A. Phillis, V. S. Kouikoglou, and C. Verdugo, "Urban sustainability assessment and ranking of cities," *Computers, Environment and Urban Systems*, vol. 64, pp. 254–265, 2017.

[109] C. Cleophas, C. Cottrill, J. F. Ehmke, and K. Tierney, "Collaborative urban transportation: Recent advances in theory and practice," *European Journal of Operational Research*, vol. 273, no. 3, pp. 801–816, 2019.

[110] R. Lei, S. Feng, A. Danjou, G. Broquet, D. Wu, J. C. Lin, C. W. O'Dell, and T. Lauvaux, "Fossil fuel co2 emissions over metropolitan areas from space: A multi-model analysis of oco-2 data over lahore, pakistan," *Remote Sensing of Environment*, vol. 264, p. 112625, 2021.

[111] K. C. Seto and J. M. Shepherd, "Global urban land-use trends and climate impacts," *Current Opinion in Environmental Sustainability*, vol. 1, no. 1, pp. 89–95, 2009.

[112] S. Angel, A. M. Blei, D. L. Civco, and J. Parent, *Atlas of urban expansion*. Lincoln Institute of Land Policy Cambridge, MA, 2012.

[113] A. Glazener and H. Khreis, "Transforming our cities: best practices towards clean air and active transportation," *Current environmental health reports*, vol. 6, no. 1, pp. 22–37, 2019.

[114] T. Tingsanchali, "Urban flood disaster management," *Procedia engineering*, vol. 32, pp. 25–37, 2012.

[115] K. Burningham, J. Fielding, and D. Thrush, "'it'll never happen to me': understanding public awareness of local flood risk," *Disasters*, vol. 32, no. 2, pp. 216–238, 2008.

[116] N. Kapucu, "Collaborative emergency management: better community organising, better public preparedness and response," *Disasters*, vol. 32, no. 2, pp. 239–262, 2008.

[117] Y. Sermet and I. Demir, "Flood action vr: a virtual reality framework for disaster awareness and emergency response training," in *ACM SIGGRAPH 2019 Posters*, pp. 1–2, 2019.

[118] C. H. Green, S. Tunstall, and M. Fordham, "The risks from flooding: Which risks and whose perception?," *Disasters*, vol. 15, no. 3, pp. 227–236, 1991.

[119] R. Sacks, A. Perlman, and R. Barak, "Construction safety training using immersive virtual reality," *Construction Management and Economics*, vol. 31, no. 9, pp. 1005–1017, 2013.

[120] R. Lovreglio, V. Gonzalez, Z. Feng, R. Amor, M. Spearpoint, J. Thomas, M. Trotter, and R. Sacks, "Prototyping virtual reality serious games

for building earthquake preparedness: The auckland city hospital case study," *Advanced engineering informatics*, vol. 38, pp. 670–682, 2018.

[121] S. Gwynne, M. Amos, M. Kinateder, N. Benichou, K. Boyce, C. N. van Der Wal, and E. Ronchi, "The future of evacuation drills: Assessing and enhancing evacuee performance," *Safety science*, vol. 129, p. 104767, 2020.

[122] M. Simpson, L. Padilla, K. Keller, and A. Klippel, "Immersive storm surge flooding: Scale and risk perception in virtual reality," *Journal of Environmental Psychology*, vol. 80, p. 101764, 2022.

[123] R. Lovreglio, X. Duan, A. Rahouti, R. Phipps, and D. Nilsson, "Comparing the effectiveness of fire extinguisher virtual reality and video training," *Virtual Reality*, vol. 25, no. 1, pp. 133–145, 2021.

[124] Z. Feng, V. A. González, C. Mutch, R. Amor, A. Rahouti, A. Baghouz, N. Li, and G. Cabrera-Guerrero, "Towards a customizable immersive virtual reality serious game for earthquake emergency training," *Advanced Engineering Informatics*, vol. 46, p. 101134, 2020.

[125] K. Atli, W. Selman, and A. Ray, "A comprehensive multicomponent neurosurgical course with use of virtual reality: modernizing the medical classroom," *Journal of surgical education*, vol. 78, no. 4, pp. 1350–1356, 2021.

[126] M. B. O'Connor, S. J. Bennie, H. M. Deeks, A. Jamieson-Binnie, A. J. Jones, R. J. Shannon, R. Walters, T. J. Mitchell, A. J. Mulholland, and

D. R. Glowacki, "Interactive molecular dynamics in virtual reality from quantum chemistry to drug binding: An open-source multi-person framework," *The Journal of chemical physics*, vol. 150, no. 22, p. 220901, 2019.

[127] T. Fujimi and K. Fujimura, "Testing public interventions for flash flood evacuation through environmental and social cues: The merit of virtual reality experiments," *International Journal of Disaster Risk Reduction*, vol. 50, p. 101690, 2020.

[128] M. J. Castro, S. Ortega, M. De la Asuncion, J. M. Mantas, and J. M. Gallardo, "Gpu computing for shallow water flow simulation based on finite volume schemes," *Comptes Rendus Mécanique*, vol. 339, no. 2-3, pp. 165–184, 2011.

[129] R. Vacondio, A. Dal Palù, and P. Mignosa, "Gpu-enhanced finite volume shallow water solver for fast flood simulations," *Environmental modelling & software*, vol. 57, pp. 60–75, 2014.

[130] B. Kim, C. Oh, Y. Yi, and D.-H. Kim, "Gpu-accelerated boussinesq model using compute unified device architecture fortran," *Journal of Coastal Research*, no. 85 (10085), pp. 1176–1180, 2018.

[131] S. Tavakkol and P. Lynett, "Celeris base: An interactive and immersive boussinesq-type nearshore wave simulation software," *Computer Physics Communications*, vol. 248, p. 106966, 2020.

[132] G.-T. Yeh, H.-P. Cheng, J.-R. Cheng, H.-C. J. Lin, and W. D. Martin, "A numerical model simulating water flow and contaminant and sediment

transport in watershed systems of 1-d stream-river network, 2-d overland regime, and 3-d subsurface media (wash123d: Version 1.0)," tech. rep., ARMY ENGINEER WATERWAYS EXPERIMENT STATION VICKSBURG MS COASTAL HYDRAULICS LAB, 1998.

[133] S. K. Mishra, J. V. Tyagi, and V. P. Singh, "Comparison of infiltration models," *Hydrological processes*, vol. 17, no. 13, pp. 2629–2652, 2003.

[134] A. N. Kostiakov, "On the dynamics of the coefficient of water-percolation in soils and on the necessity of studying it from a dynamic point of view for purposes of amelioration," *Trans. 6th Cong. International. Soil Science, Russian Part A*, pp. 17–21, 1932.

[135] L. F. Huggins, *The mathematical simulation of the hydrology of small watersheds.* Purdue University, 1966.

[136] R. E. Horton, "The role of infiltration in the hydrologic cycle," *Eos, Transactions American Geophysical Union*, vol. 14, no. 1, pp. 446–460, 1933.

[137] D. Overton, *Mathematical refinement of an infiltration equation for watershed engineering.* Agricultural Research Service, US Department of Agriculture, 1964.

[138] V. P. Singh and F. X. Yu, "Derivation of infiltration equation using systems approach," *Journal of Irrigation and Drainage Engineering*, vol. 116, no. 6, pp. 837–858, 1990.

[139] L. Gowdish and R. Muñoz-Carpena, "An improved green–ampt infiltration and redistribution method for uneven multistorm series," *Vadose Zone Journal*, vol. 8, no. 2, pp. 470–479, 2009.

[140] P. K. Parhi, S. K. Mishra, and R. Singh, "A modification to kostiakov and modified kostiakov infiltration models," *Water resources management*, vol. 21, no. 11, pp. 1973–1989, 2007.

[141] W. H. Green and G. Ampt, "Studies on soil phyics.," *The Journal of Agricultural Science*, vol. 4, no. 1, pp. 1–24, 1911.

[142] J. R. Philip, "Evaporation, and moisture and heat fields in the soil," *Journal of Atmospheric Sciences*, vol. 14, no. 4, pp. 354–366, 1957.

[143] L. A. Richards, "Capillary conduction of liquids through porous mediums," *Physics*, vol. 1, no. 5, pp. 318–333, 1931.

[144] R. E. Smith, "The infiltration envelope: results from a theoretical infiltrometer," *Journal of hydrology*, vol. 17, no. 1-2, pp. 1–22, 1972.

[145] R.-M. Li, D. B. Simons, and M. A. Stevens, "Solutions to green-ampt infiltration equation," *Journal of the Irrigation and Drainage Division*, vol. 102, no. 2, pp. 239–248, 1976.

[146] G. Wei and J. T. Kirby, "Time-dependent numerical code for extended boussinesq equations," *Journal of waterway, port, coastal, and ocean engineering*, vol. 121, no. 5, pp. 251–261, 1995.

[147] K. Erduran, S. Ilic, and V. Kutija, "Hybrid finite-volume finite-difference

scheme for the solution of boussinesq equations," *International Journal for Numerical Methods in Fluids*, vol. 49, no. 11, pp. 1213–1232, 2005.

[148] M. Tonelli and M. Petti, "Hybrid finite volume–finite difference scheme for 2dh improved boussinesq equations," *Coastal Engineering*, vol. 56, no. 5-6, pp. 609–620, 2009.

[149] T. C. Wei, *Reciprocal Distance Squared Method, A computer technique for estimating areal precipitation*, vol. 8. US Department of Agriculture, Agricultural Research Service, North Central ..., 1973.

[150] R. G. Mein and C. L. Larson, "Modeling infiltration during a steady rain," *Water resources research*, vol. 9, no. 2, pp. 384–394, 1973.

[151] S. T. Chu, "Infiltration during an unsteady rain," *Water Resources Research*, vol. 14, no. 3, pp. 461–466, 1978.

[152] M. Esteves, X. Faucher, S. Galle, and M. Vauclin, "Overland flow and infiltration modelling for small plots during unsteady rain: numerical results versus observed values," *Journal of hydrology*, vol. 228, no. 3-4, pp. 265–282, 2000.

[153] R. V. Kale and B. Sahoo, "Green-ampt infiltration models for varied field conditions: A revisit," *Water resources management*, vol. 25, no. 14, pp. 3505–3536, 2011.

[154] J. Singh, M. S. Altinakar, and Y. Ding, "Numerical modeling of rainfall-generated overland flow using nonlinear shallow-water equations," *Journal of Hydrologic Engineering*, vol. 20, no. 8, p. 04014089, 2015.

[155] S.-Y. Hsu, V. Huang, S. W. Park, and M. Hilpert, "Water infiltration into prewetted porous media: Dynamic capillary pressure and green-ampt modeling," *Advances in water resources*, vol. 106, pp. 60–67, 2017.

[156] L. Dasallas, H. An, and S. Lee, "Developing an integrated multiscale rainfall-runoff and inundation model: Application to an extreme rainfall event in marikina-pasig river basin, philippines," *Journal of Hydrology: Regional Studies*, vol. 39, p. 100995, 2022.

[157] Y.-S. Fok, "Infiltration equation in exponential forms," *Journal of the Irrigation and Drainage Division*, vol. 93, no. 4, pp. 125–135, 1967.

[158] G. D. Salvucci and D. Entekhabi, "Explicit expressions for green-ampt (delta function diffusivity) infiltration rate and cumulative storage," *Water Resources Research*, vol. 30, no. 9, pp. 2661–2663, 1994.

[159] J. J. Stone, R. H. Hawkins, and E. D. Shirley, "Approximate form of green-ampt infiltration equation," *Journal of irrigation and drainage engineering*, vol. 120, no. 1, pp. 128–137, 1994.

[160] D. Barry, J.-Y. Parlange, L. Li, D.-S. Jeng, and M. Crapper, "Green–ampt approximations," *Advances in Water Resources*, vol. 28, no. 10, pp. 1003–1009, 2005.

[161] L. Chen and M. H. Young, "Green-ampt infiltration model for sloping surfaces," *Water resources research*, vol. 42, no. 7, 2006.

[162] S. Ali, N. C. Ghosh, R. Singh, and B. Sethy, "Generalized explicit models

for estimation of wetting front length and potential recharge," *Water resources management*, vol. 27, no. 7, pp. 2429–2445, 2013.

[163] J. Zhu, F. L. Ogden, W. Lai, X. Chen, and C. A. Talbot, "An explicit approach to capture diffusive effects in finite water-content method for solving vadose zone flow," *Journal of Hydrology*, vol. 535, pp. 270–281, 2016.

[164] W.-B. Nie, Y.-B. Li, L.-J. Fei, and X.-Y. Ma, "Approximate explicit solution to the green-ampt infiltration model for estimating wetting front depth," *Water*, vol. 9, no. 8, p. 609, 2017.

[165] Y. Bai and J. G. Duan, "Simulating unsteady flow and sediment transport in vegetated channel network," *Journal of Hydrology*, vol. 515, pp. 90–102, 2014.

[166] R. E. Horton, "An approach toward a physical interpretation of infiltration-capacity 1," *Soil science society of America journal*, vol. 5, no. C, pp. 399–417, 1941.

[167] J. Fernández-Pato, D. Caviedes-Voullième, and P. García-Navarro, "Rainfall/runoff simulation with 2d full shallow water equations: Sensitivity analysis and calibration of infiltration parameters," *Journal of hydrology*, vol. 536, pp. 496–513, 2016.

[168] V. Singh, "Kinematic wave modeling in water resources. surface-water hydrology, 1399 pp," 1996.

[169] K. W. King, J. Arnold, and R. Bingner, "Comparison of green-ampt and curve number methods on goodwin creek watershed using swat," *Transactions of the ASAE*, vol. 42, no. 4, p. 919, 1999.

[170] D. A. Vieira and W. Wu, "One-dimensional channel network model cche1d version 3.0: User's manual," *National Center for Computational Hydroscience and Engineering, University of Mississippi, Oxford, MS*, 2002.

[171] W. A. Blackmarr, "Documentation of hydrologic, geomorphic, and sediment transport measurements on the goodwin creek experimental watershed, northern mississippi, for the period 1982–1993, preliminary release," *Res. Rep*, vol. 3, 1995.

[172] S. R. Rojas, "Gis-based upland erosion modeling, geovisualization and grid size effects on erosion simulations with casc2d-sed.," 2003.

[173] H. F. Needham, B. D. Keim, and D. Sathiaraj, "A review of tropical cyclone-generated storm surges: Global data sources, observations, and impacts," *Reviews of Geophysics*, vol. 53, no. 2, pp. 545–591, 2015.

[174] Q. Wuxi, J. Li, and B. Nie, "Effects of tide-surge interaction and wave set-up/set-down on surge: case studies of tropical cyclones landing china's zhe-min coast," *Theoretical and Applied Mechanics Letters*, vol. 8, no. 3, pp. 153–159, 2018.

[175] K. A. Emanuel, "The dependence of hurricane intensity on climate," *Nature*, vol. 326, no. 6112, pp. 483–485, 1987.

[176] M. A. Saunders and A. R. Harris, "Statistical evidence links exceptional 1995 atlantic hurricane season to record sea warming," *Geophysical Research Letters*, vol. 24, no. 10, pp. 1255–1258, 1997.

[177] M. F. Karim and N. Mimura, "Impacts of climate change and sea-level rise on cyclonic storm surge floods in bangladesh," *Global environmental change*, vol. 18, no. 3, pp. 490–500, 2008.

[178] J. Yin, N. Lin, and D. Yu, "Coupled modeling of storm surge and coastal inundation: A case study in n ew y ork c ity during h urricane s andy," *Water Resources Research*, vol. 52, no. 11, pp. 8685–8699, 2016.

[179] M. Peng, L. Xie, and L. J. Pietrafesa, "A numerical study of storm surge and inundation in the croatan–albemarle–pamlico estuary system," *Estuarine, Coastal and Shelf Science*, vol. 59, no. 1, pp. 121–137, 2004.

[180] J.-J. Yoon and J.-S. Shim, "Estimation of storm surge inundation and hazard mapping for the southern coast of korea," *Journal of Coastal Research*, no. 65 (10065), pp. 856–861, 2013.

[181] A. Rahdarian and M. H. Niksokhan, "Numerical modeling of storm surge attenuation by mangroves in protected area of mangroves of qheshm island," *Ocean Engineering*, vol. 145, pp. 304–315, 2017.

[182] L. Xie, H. Liu, and M. Peng, "The effect of wave–current interactions on the storm surge and inundation in charleston harbor during hurricane hugo 1989," *Ocean modelling*, vol. 20, no. 3, pp. 252–269, 2008.

[183] S. Y. Kim, T. Yasuda, and H. Mase, "Wave set-up in the storm surge along open coasts during typhoon anita," *Coastal Engineering*, vol. 57, no. 7, pp. 631–642, 2010.

[184] Y. P. Sheng, Y. Zhang, and V. A. Paramygin, "Simulation of storm surge, wave, and coastal inundation in the northeastern gulf of mexico region during hurricane ivan in 2004," *Ocean Modelling*, vol. 35, no. 4, pp. 314–331, 2010.

[185] Z. He, Y. Tang, Y. Xia, B. Chen, J. Xu, Z. Yu, and L. Li, "Interaction impacts of tides, waves and winds on storm surge in a channel-island system: observational and numerical study in yangshan harbor," *Ocean Dynamics*, vol. 70, no. 3, pp. 307–325, 2020.

[186] E. Rusu and C. G. Soares, "Modeling waves in open coastal areas and harbors with phase-resolving and phase-averaged models," *Journal of Coastal Research*, vol. 29, no. 6, pp. 1309–1325, 2013.

[187] Deltares, "D-flow flexible mesh: D-flow fm in delta shell user manual, released for delft3d fm suite 2020, version: 1.5.0, revision:64974, december 14, 2019," 2019.

[188] V. V. Titov and C. E. Synolakis, "Numerical modeling of tidal wave runup," *Journal of Waterway, Port, Coastal, and Ocean Engineering*, vol. 124, no. 4, pp. 157–171, 1998.

[189] A. V. Dongeren and I. Svendsen, "Absorbing-generating boundary con-

dition for shallow water models," *Journal of waterway, port, coastal, and ocean engineering*, vol. 123, no. 6, pp. 303–313, 1997.

[190] J. Hinkel, D. Lincke, A. T. Vafeidis, M. Perrette, R. J. Nicholls, R. S. Tol, B. Marzeion, X. Fettweis, C. Ionescu, and A. Levermann, "Coastal flood damage and adaptation costs under 21st century sea-level rise," *Proceedings of the National Academy of Sciences*, vol. 111, no. 9, pp. 3292–3297, 2014.

[191] L. Bengtsson, K. I. Hodges, and E. Roeckner, "Storm tracks and climate change," *Journal of climate*, vol. 19, no. 15, pp. 3518–3543, 2006.

[192] S. Dasgupta, B. Laplante, S. Murray, and D. Wheeler, "Exposure of developing countries to sea-level rise and storm surges," *Climatic Change*, vol. 106, no. 4, pp. 567–579, 2011.

[193] T. Wahl, S. Jain, J. Bender, S. D. Meyers, and M. E. Luther, "Increasing risk of compound flooding from storm surge and rainfall for major us cities," *Nature Climate Change*, vol. 5, no. 12, pp. 1093–1097, 2015.

[194] T. Stocker, *Climate change 2013: the physical science basis: Working Group I contribution to the Fifth assessment report of the Intergovernmental Panel on Climate Change*. Cambridge university press, 2014.

[195] M. Vermeer and S. Rahmstorf, "Global sea level linked to global temperature," *Proceedings of the national academy of sciences*, vol. 106, no. 51, pp. 21527–21532, 2009.

[196] D.-S. R. Park, C.-H. Ho, J.-H. Kim, and H.-S. Kim, "Strong landfall typhoons in korea and japan in a recent decade," *Journal of Geophysical Research: Atmospheres*, vol. 116, no. D7, 2011.

[197] S. Nayak and T. Takemi, "Quantitative estimations of hazards resulting from typhoon chanthu (2016) for assessing the impact in current and future climate," *Hydrological Research Letters*, vol. 13, no. 2, pp. 20–27, 2019.

[198] J. L. Bamber, M. Oppenheimer, R. E. Kopp, W. P. Aspinall, and R. M. Cooke, "Ice sheet contributions to future sea-level rise from structured expert judgment," *Proceedings of the National Academy of Sciences*, vol. 116, no. 23, pp. 11195–11200, 2019.

[199] I.-I. Lin, G. J. Goni, J. A. Knaff, C. Forbes, and M. Ali, "Ocean heat content for tropical cyclone intensity forecasting and its impact on storm surge," *Natural Hazards*, vol. 66, no. 3, pp. 1481–1500, 2013.

[200] N. Bernier and K. Thompson, "Tide-surge interaction off the east coast of canada and northeastern united states," *Journal of Geophysical Research: Oceans*, vol. 112, no. C6, 2007.

[201] H. Ikeuchi, Y. Hirabayashi, D. Yamazaki, S. Muis, P. J. Ward, H. C. Winsemius, M. Verlaan, and S. Kanae, "Compound simulation of fluvial floods and storm surges in a global coupled river-coast flood model: Model development and its application to 2007 c yclone s idr in b angladesh," *Journal of Advances in Modeling Earth Systems*, vol. 9, no. 4, pp. 1847–1862, 2017.

[202] Y. Krien, L. Testut, A. Islam, X. Bertin, F. Durand, C. Mayet, A. Tazkia, M. Becker, S. Calmant, F. Papa, *et al.*, "Towards improved storm surge models in the northern bay of bengal," *Continental Shelf Research*, vol. 135, pp. 58–73, 2017.

[203] F. L. Santiago-Collazo, M. V. Bilskie, and S. C. Hagen, "A comprehensive review of compound inundation models in low-gradient coastal watersheds," *Environmental Modelling & Software*, vol. 119, pp. 166–181, 2019.

[204] J. J. Westerink, R. A. Luettich, J. C. Feyen, J. H. Atkinson, C. Dawson, H. J. Roberts, M. D. Powell, J. P. Dunion, E. J. Kubatko, and H. Pourtaheri, "A basin-to channel-scale unstructured grid hurricane storm surge model applied to southern louisiana," *Monthly weather review*, vol. 136, no. 3, pp. 833–864, 2008.

[205] W.-B. Chen and W.-C. Liu, "Modeling flood inundation induced by river flow and storm surges over a river basin," *Water*, vol. 6, no. 10, pp. 3182–3199, 2014.

[206] J.-C. Huang, T.-Y. Lee, and J.-Y. Lee, "Observed magnified runoff response to rainfall intensification under global warming," *Environmental Research Letters*, vol. 9, no. 3, p. 034008, 2014.

[207] H. R. Moftakhari, G. Salvadori, A. AghaKouchak, B. F. Sanders, and R. A. Matthew, "Compounding effects of sea level rise and fluvial flooding," *Proceedings of the National Academy of Sciences*, vol. 114, no. 37, pp. 9785–9790, 2017.

[208] E. Tromble, R. Kolar, K. Dresback, Y. Hong, B. Vieux, R. Luettich, J. Gourley, K. Kelleher, and S. Van Cooten, "Aspects of coupled hydrologic-hydrodynamic modeling for coastal flood inundation," in *Estuarine and Coastal Modeling (2009)*, pp. 724–743, 2010.

[209] J. Maskell, K. Horsburgh, M. Lewis, and P. Bates, "Investigating river–surge interaction in idealised estuaries," *Journal of Coastal Research*, vol. 30, no. 2, pp. 248–259, 2014.

[210] L. H. Erikson, A. C. O'Neill, and P. L. Barnard, "Estimating fluvial discharges coincident with 21st century coastal storms modeled with cosmos," *Journal of Coastal Research*, no. 85 (10085), pp. 791–795, 2018.

[211] C. Svensson and D. A. Jones, "Dependence between extreme sea surge, river flow and precipitation in eastern britain," *International Journal of Climatology: A Journal of the Royal Meteorological Society*, vol. 22, no. 10, pp. 1149–1168, 2002.

[212] C. Svensson and D. A. Jones, "Dependence between sea surge, river flow and precipitation in south and west britain," *Hydrology and Earth System Sciences*, vol. 8, no. 5, pp. 973–992, 2004.

[213] J. Christian, Z. Fang, J. Torres, R. Deitz, and P. Bedient, "Modeling the hydraulic effectiveness of a proposed storm surge barrier system for the houston ship channel during hurricane events," *Natural Hazards Review*, vol. 16, no. 1, p. 04014015, 2015.

[214] M. Karamouz, A. Razmi, S. Nazif, and Z. Zahmatkesh, "Integration of

inland and coastal storms for flood hazard assessment using a distributed hydrologic model," *Environmental Earth Sciences*, vol. 76, no. 11, pp. 1–17, 2017.

[215] T. Nose, J. M. Burston, D. Gee, and R. Tomlinson, "Potential for forecasting inundation from flooding and storm surge: A case study of a small urban catchment during ex tropical cyclone oswald," in *Coasts and Ports*, vol. 2013, p. 21st, 2013.

[216] H. V. Wang, J. D. Loftis, Z. Liu, D. Forrest, and J. Zhang, "The storm surge and sub-grid inundation modeling in new york city during hurricane sandy," *Journal of Marine Science and Engineering*, vol. 2, no. 1, pp. 226–246, 2014.

[217] A. F. Blumberg, N. Georgas, L. Yin, T. O. Herrington, and P. M. Orton, "Street-scale modeling of storm surge inundation along the new jersey hudson river waterfront," *Journal of Atmospheric and Oceanic Technology*, vol. 32, no. 8, pp. 1486–1497, 2015.

[218] T. Yasuda, H. Mase, and N. Mori, "Projection of future typhoons landing on japan based on a stochastic typhoon model utilizing agcm projections," *Hydrological Research Letters*, vol. 4, pp. 65–69, 2010.

[219] R. Nakamura, T. Shibayama, M. Esteban, and T. Iwamoto, "Future typhoon and storm surges under different global warming scenarios: case study of typhoon haiyan (2013)," *Natural Hazards*, vol. 82, no. 3, pp. 1645–1681, 2016.

[220] S. Kim, J. Oh, K.-D. Suh, and H. Mase, "Estimation of climate change impact on storm surges: application to korean peninsula," *Coastal Engineering Journal*, vol. 59, no. 2, pp. 1740004–1, 2017.

[221] M. V. Bilskie, S. Hagen, and J. Irish, "Development of return period stillwater floodplains for the northern gulf of mexico under the coastal dynamics of sea level rise," *Journal of Waterway, Port, Coastal, and Ocean Engineering*, vol. 145, no. 2, p. 04019001, 2019.

[222] N. A. Phillips, "A coordinate system having some special advantages for numerical forecasting," *J. Meteorol.*, vol. 14, pp. 184–195, 1957.

[223] H. Kiri, E. Shiratani, H. Tanji, and K. Ishita, "Tidal current simulation of the ariake sea using the sigma-coordinate finite element model," in *Asian And Pacific Coasts 2011*, pp. 1338–1345, World Scientific, 2012.

[224] A. D. Feldman, *Hydrologic modeling system HEC-HMS: technical reference manual*. US Army Corps of Engineers, Hydrologic Engineering Center, 2000.

[225] KMA, "Korea climate change report (in korean)," 2012.

[226] W. Collins, N. Bellouin, M. Doutriaux-Boucher, N. Gedney, P. Halloran, T. Hinton, J. Hughes, C. Jones, M. Joshi, S. Liddicoat, *et al.*, "Development and evaluation of an earth-system model–hadgem2," *Geoscientific Model Development*, vol. 4, no. 4, pp. 1051–1075, 2011.

[227] S. M. Oh and I.-J. Moon, "Typhoon and storm surge intensity changes

in a warming climate around the korean peninsula," *Natural hazards*, vol. 66, no. 3, pp. 1405–1429, 2013.

[228] S. Nakajo, N. Mori, S. Kim, T. Yasuda, and H. Mase, "Consideration of applicability of stochastic tropical cyclone model for probability assessment of storm surge," in *Proceedings of 7th International Conference on Asian Pacific Coasts September 24*, vol. 26, pp. 613–619, 2013.

[229] T. Yasuda, S. Nakajo, S. Kim, H. Mase, N. Mori, and K. Horsburgh, "Evaluation of future storm surge risk in east asia based on state-of-the-art climate change projection," *Coastal Engineering*, vol. 83, pp. 65–71, 2014.

[230] W. Mei, S.-P. Xie, F. Primeau, J. C. McWilliams, and C. Pasquero, "Northwestern pacific typhoon intensity controlled by changes in ocean temperatures," *Science advances*, vol. 1, no. 4, p. e1500014, 2015.

[231] A. H. Sobel, S. J. Camargo, T. M. Hall, C.-Y. Lee, M. K. Tippett, and A. A. Wing, "Human influence on tropical cyclone intensity," *Science*, vol. 353, no. 6296, pp. 242–246, 2016.

[232] X. Feng and M. N. Tsimplis, "Sea level extremes at the coasts of china," *Journal of Geophysical Research: Oceans*, vol. 119, no. 3, pp. 1593–1608, 2014.

[233] K. Emanuel, "Increasing destructiveness of tropical cyclones over the past 30 years," *Nature*, vol. 436, no. 7051, pp. 686–688, 2005.

[234] A. Ali, "Climate change impacts and adaptation assessment in bangladesh," *Climate research*, vol. 12, no. 2-3, pp. 109–116, 1999.

[235] S. Gualdi, E. Scoccimarro, and A. Navarra, "Changes in tropical cyclone activity due to global warming: Results from a high-resolution coupled general circulation model," *Journal of climate*, vol. 21, no. 20, pp. 5204–5228, 2008.

[236] G. Villarini, D. A. Lavers, E. Scoccimarro, M. Zhao, M. F. Wehner, G. A. Vecchi, T. R. Knutson, and K. A. Reed, "Sensitivity of tropical cyclone rainfall to idealized global-scale forcings," *Journal of climate*, vol. 27, no. 12, pp. 4622–4641, 2014.

[237] E. Scoccimarro, S. Gualdi, G. Villarini, G. A. Vecchi, M. Zhao, K. Walsh, and A. Navarra, "Intense precipitation events associated with landfalling tropical cyclones in response to a warmer climate and increased co 2," *Journal of climate*, vol. 27, no. 12, pp. 4642–4654, 2014.

[238] D. B. Wright, T. R. Knutson, and J. A. Smith, "Regional climate model projections of rainfall from us landfalling tropical cyclones," *Climate dynamics*, vol. 45, no. 11, pp. 3365–3379, 2015.

[239] C. M. Patricola and M. F. Wehner, "Anthropogenic influences on major tropical cyclone events," *Nature*, vol. 563, no. 7731, pp. 339–346, 2018.

[240] J. Choi, J. Lee, and S. Kim, "Impact of sea surface temperature and surface air temperature on maximizing typhoon rainfall: focusing on typhoon maemi in korea," *Advances in Meteorology*, vol. 2019, 2019.

[241] F. Zheng, S. Westra, and S. A. Sisson, "Quantifying the dependence between extreme rainfall and storm surge in the coastal zone," *Journal of hydrology*, vol. 505, pp. 172–187, 2013.

[242] Y. Shen, M. M. Morsy, C. Huxley, N. Tahvildari, and J. L. Goodall, "Flood risk assessment and increased resilience for coastal urban watersheds under the combined impact of storm tide and heavy rainfall," *Journal of Hydrology*, vol. 579, p. 124159, 2019.

[243] S.-C. Hsiao, W.-S. Chiang, J.-H. Jang, H.-L. Wu, W.-S. Lu, W.-B. Chen, and Y.-T. Wu, "Flood risk influenced by the compound effect of storm surge and rainfall under climate change for low-lying coastal areas," *Science of the total environment*, vol. 764, p. 144439, 2021.

[244] M. A. Imaz-Lamadrid, J. Wurl, E. Ramos-Velázquez, and J. Rodríguez-Trasviña, "Integrated runoff-storm surge flood hazard mapping associated with tropical cyclones in the suburbs of la paz, baja california sur, méxico," *GeoHazards*, vol. 3, no. 1, pp. 1–15, 2021.

[245] Y. Qiang, L. Zhang, J. He, T. Xiao, H. Huang, and H. Wang, "Urban flood analysis for pearl river delta cities using an equivalent drainage method upon combined rainfall-high tide-storm surge events," *Journal of Hydrology*, vol. 597, p. 126293, 2021.

[246] Y. Shen, N. Tahvildari, M. M. Morsy, C. Huxley, T. D. Chen, and J. L. Goodall, "Dynamic modeling of inland flooding and storm surge on coastal cities under climate change scenarios: Transportation infras-

tructure impacts in norfolk, virginia usa as a case study," *Geosciences*, vol. 12, no. 6, p. 224, 2022.

[247] A. Jarvis, H. I. Reuter, A. Nelson, E. Guevara, *et al.*, "Hole-filled srtm for the globe version 4," *available from the CGIAR-CSI SRTM 90m Database (http://srtm. csi. cgiar. org)*, vol. 15, no. 25-54, p. 5, 2008.

[248] T. Neumann and K. Ahrendt, "Comparing the" bathtub method" with mike 21 hd flow model for modelling storm surge inundation," *Ecologic Institute, Berlin, Germany*, 2013.

[249] J. E. Schubert and B. F. Sanders, "Building treatments for urban flood inundation models and implications for predictive skill and modeling efficiency," *Advances in water resources*, vol. 41, pp. 49–64, 2012.

[250] B. Kim, B. F. Sanders, J. E. Schubert, and J. S. Famiglietti, "Mesh type tradeoffs in 2d hydrodynamic modeling of flooding with a godunov-based flow solver," *Advances in Water Resources*, vol. 68, pp. 42–61, 2014.

[251] B. F. Sanders and J. E. Schubert, "Primo: Parallel raster inundation model," *Advances in Water Resources*, vol. 126, pp. 79–95, 2019.

[252] W. Li, B. Liu, P. Hu, Z. He, and J. Zou, "Porous shallow water modeling for urban floods in the zhoushan city, china," *Frontiers in Earth Science*, vol. 9, p. 687311, 2021.

[253] M.-H. Hsu, S.-H. Chen, and T.-J. Chang, "Inundation simulation for urban drainage basin with storm sewer system," *Journal of hydrology*, vol. 234, no. 1-2, pp. 21–37, 2000.

[254] B. Jongman, H. Kreibich, H. Apel, J. Barredo, P. Bates, L. Feyen, A. Gericke, J. Neal, J. Aerts, and P. Ward, "Comparative flood damage model assessment: towards a european approach," *Natural Hazards and Earth System Sciences*, vol. 12, no. 12, pp. 3733–3752, 2012.